



# Study of degradation mechanisms in halide perovskite films and in perovskite solar cells using electrical and synchrotron-based characterization

Haeyeon Jun

## ► To cite this version:

Haeyeon Jun. Study of degradation mechanisms in halide perovskite films and in perovskite solar cells using electrical and synchrotron-based characterization. Physics [physics]. Institut Polytechnique de Paris; Synchrotron SOLEIL, 2022. English. NNT : 2022IPPAX103 . tel-04461265

**HAL Id: tel-04461265**

<https://theses.hal.science/tel-04461265v1>

Submitted on 16 Feb 2024

**HAL** is a multi-disciplinary open access archive for the deposit and dissemination of scientific research documents, whether they are published or not. The documents may come from teaching and research institutions in France or abroad, or from public or private research centers.

L'archive ouverte pluridisciplinaire **HAL**, est destinée au dépôt et à la diffusion de documents scientifiques de niveau recherche, publiés ou non, émanant des établissements d'enseignement et de recherche français ou étrangers, des laboratoires publics ou privés.

# Contents

<b>1. Introduction.....</b>	<b>9</b>
<b>1.1 Global Energy Issues and Photovoltaics .....</b>	<b>9</b>
1.1.1 Global Energy Issues and Trends of Renewable Energy.....	9
1.1.2 Trend in Photovoltaics .....	11
<b>1.2 Organic-inorganic Halide Perovskite Solar Cells.....</b>	<b>13</b>
1.2.1 Solar Cells based on Organic-inorganic Halide Perovskites .....	13
1.2.2 Stability Issues of Halide Perovskite Solar Cells .....	15
<b>1.3 Characterization Techniques for Perovskite Solar Cells.....</b>	<b>20</b>
1.3.1 Potential of Impedance Spectroscopy towards Analysis of Photovoltaics .....	20
1.3.2 Applications of Electrochemical Impedance Spectroscopy to Perovskite Solar Cells .....	21
1.3.3 Synchrotron-based X-ray Techniques in Materials Characterization.....	23
1.3.4 Application of Synchrotron-based Characterizations to Perovskite Solar Cells .....	25
<b>1.4 Motivation of the Research and Thesis Overview.....</b>	<b>28</b>
<b>2. Fundamental Theory .....</b>	<b>31</b>
<b>2.1 Introduction .....</b>	<b>31</b>
<b>2.2 Basic Concepts of Solar Cells .....</b>	<b>32</b>
2.2.1 Working Principle of Solar Cells .....	32
2.2.2 P-I-N Junction and Thin Film Solar Cells .....	33
2.2.3 Solar Cell Parameters under Light .....	36
2.2.4 J-V Characteristics under Dark .....	37
<b>2.3 Organic Inorganic Halide Perovskite Solar Cells .....</b>	<b>38</b>
2.3.1 Crystal Structure of Halide Perovskite and its Properties .....	38
2.3.2 Architecture of Perovskite Solar Cells .....	41
2.3.3 Ion Migration .....	44
<b>2.4 Characterization of Perovskite Solar Cells using Impedance Spectroscopy .....</b>	<b>48</b>
2.4.1 Dielectric Properties and Charge Dynamics.....	48
2.4.2 Impedance Spectroscopy.....	50
2.4.3 Ionic Conductivity of Halide Perovskites: Low Frequency Dielectric Response of Perovskite .....	54
<b>2.5 Characterization of Perovskite using Scanning Transmission X-ray Microspectroscopy .....</b>	<b>56</b>
2.5.1 Principle of Synchrotron Radiation .....	56
2.5.2 X-ray Interaction with Materials .....	59
2.5.3 Scanning Transmission X-ray Microscopy .....	60
<b>3. MAPbI<sub>3</sub> Perovskite Solar Cells by Co-evaporation.....</b>	<b>65</b>
<b>3.1 Introduction .....</b>	<b>65</b>
<b>3.2 Experimental Details.....</b>	<b>66</b>
3.2.1 Evaporation of MAPbI <sub>3</sub> Film based on Co-evaporation.....	66
3.2.2 Fabrication of MAPbI <sub>3</sub> Solar Cells.....	68
3.2.3 Perovskite Film Characterization .....	71
3.2.4 Perovskite Solar Cells Characterization .....	72
<b>3.3 Optimization of MAPbI<sub>3</sub> Film.....</b>	<b>73</b>
3.3.1 Impact of Deposition Rate Ratio of PbI <sub>2</sub> and MAI on MAPbI <sub>3</sub> Film Properties.....	74
3.3.2 Impact of Rate of PbI <sub>2</sub> on MAPbI <sub>3</sub> Film Properties .....	76
3.3.3 Impact of Hole Transport Layers on MAPbI <sub>3</sub> Film Properties.....	78
<b>3.4 Photovoltaic Performances of MAPbI<sub>3</sub> Solar Cells.....</b>	<b>82</b>
3.4.1 Photovoltaic Performance of Reference Solar Cells .....	82
3.4.2 Impact of Electron Transport Materials on Photovoltaic Performance .....	85
3.4.3 Impact of Hole Transport Materials on Photovoltaic Performance .....	88
<b>4. Degradation in PSCs Caused by Electric Field and Exposure to Air Investigated with Impedance Spectroscopy.....</b>	<b>91</b>

<b>4.1 Introduction .....</b>	<b>91</b>
<b>4.2 Experimental Details.....</b>	<b>92</b>
4.2.1 Fabrication of Solar Cells for EIS measurement .....	92
4.2.2 Impedance Spectroscopy Measurement .....	95
4.2.3 Equivalent Circuit Modeling .....	96
<b>4.3 Analysis of Electric Field Induced Degradation.....</b>	<b>98</b>
4.3.1 EIS Results of the Reference MAPbI <sub>3</sub> PSCs .....	98
4.3.2 EIS Results by Applying the Electric Field.....	100
4.3.3 Presentation of the Hypothesis of Generation of Second Capacitance Caused by Electric Field.....	106
<b>4.4 Analysis of Degradation Caused by Air-Exposure.....</b>	<b>107</b>
4.4.1 EIS Results by Air Exposure .....	107
4.4.2 Application of Dielectric Modulus Spectroscopy to Study Degradation in PSCs.....	109
4.4.3 Discussion of Air Exposure Phenomena in the Reference PSCs .....	111
<b>5. <i>Study of Electric Field-induced Degradation in Perovskite Films and Solar Cells with Scanning Transmission X-ray Microscopy.....</i></b>	<b>115</b>
<b>5.1 Introduction .....</b>	<b>115</b>
<b>5.2 Experimental Details.....</b>	<b>116</b>
5.2.1 Preparation of Films of Components Forming Halide Perovskites and PSCs.....	116
5.2.2 Instruments for Synchrotron-based Characterization .....	119
5.2.3 Specialized In-situ Electric Biasing System from Norcada Inc.....	120
<b>5.3 Utility of STXM for Chemical Characterization of Halide Perovskites.....</b>	<b>122</b>
5.3.1 Identification of Components and By-products in Halide Perovskites.....	122
5.3.2 Characterization of MAPbI <sub>3</sub> using STXM .....	125
5.3.3 Evaluation of Homogeneity of MAPbI <sub>3</sub> based on STXM .....	128
<b>5.4 Degradation of Halide Perovskite Film and Solar Cells under In-situ Biasing .....</b>	<b>129</b>
5.4.1 Degradation of MAPbI <sub>3</sub> Film under In-situ Electric Bias .....	129
5.4.2 Degradation of MAPbI <sub>3</sub> Solar Cells Induced by Ex-situ Electric Field .....	134
5.4.3 Proposal to Explain Electric Field-induced Degradation Mechanism in MAPbI <sub>3</sub> Solar Cells through the Correlation between STXM and EIS Results .....	139
<b>6. General Conclusion and Perspectives .....</b>	<b>142</b>
<b>Appendix A. List of Publication.....</b>	<b>144</b>
<b>Appendix B. Conferences, Training, and Scholarships .....</b>	<b>145</b>
<b>Bibliography.....</b>	<b>147</b>

# **Chapter 1.**

## **Introduction**

---

<b>1.1 Global Energy Issues and Photovoltaics .....</b>	<b>9</b>
1.1.1 Global Energy Issues and Trends of Renewable Energy.....	9
1.1.2 Trend in Photovoltaics .....	11
<b>1.2 Organic-inorganic Halide Perovskite Solar Cells.....</b>	<b>13</b>
1.2.1 Solar Cells based on Organic-inorganic Halide Perovskites .....	13
1.2.2 Stability Issues of Halide Perovskite Solar Cells .....	15
<b>1.3 Characterization Techniques for Perovskite Solar Cells.....</b>	<b>20</b>
1.3.1 Potential of Impedance Spectroscopy towards Analysis of Photovoltaics .....	20
1.3.2 Applications of Electrochemical Impedance Spectroscopy to Perovskite Solar Cells .....	21
1.3.3 Synchrotron-based X-ray Techniques in Materials Characterization.....	23
1.3.4 Application of Synchrotron-based Characterizations to Perovskite Solar Cells .....	25
<b>1.4 Motivation of the Research and Thesis Overview.....</b>	<b>28</b>

---

### **1.1 Global Energy Issues and Photovoltaics**

#### **1.1.1 Global Energy Issues and Trends of Renewable Energy**

The increase in world population and the progress of civilization have led to world energy growth in demand. As shown in Fig. 1.1, Fossil fuels, including coal, natural gas, and oil, account for the largest portion of the energy sector which people consume (over 80 %). However, they are not sustainable, and the combustion process of fossil fuels results in the emission of greenhouse gases such as methane, carbondioxide, and nitrous oxide [1], [2]. The emission of greenhouse gases due to fossil fuels resulted in the increase in average world temperature, which leads to climate change with sea-level rise, changes in the ecosystem, etc. [3]. Furthermore, some exporters of fossil fuels misuse them for political purposes. For example, Russia has threatened to cut natural gas to western European

countries since Russo-Ukrainian War which implies energy weaponization. Due to such climate changes and energy crises caused by fossil fuels, alternative energies are required to be explored.

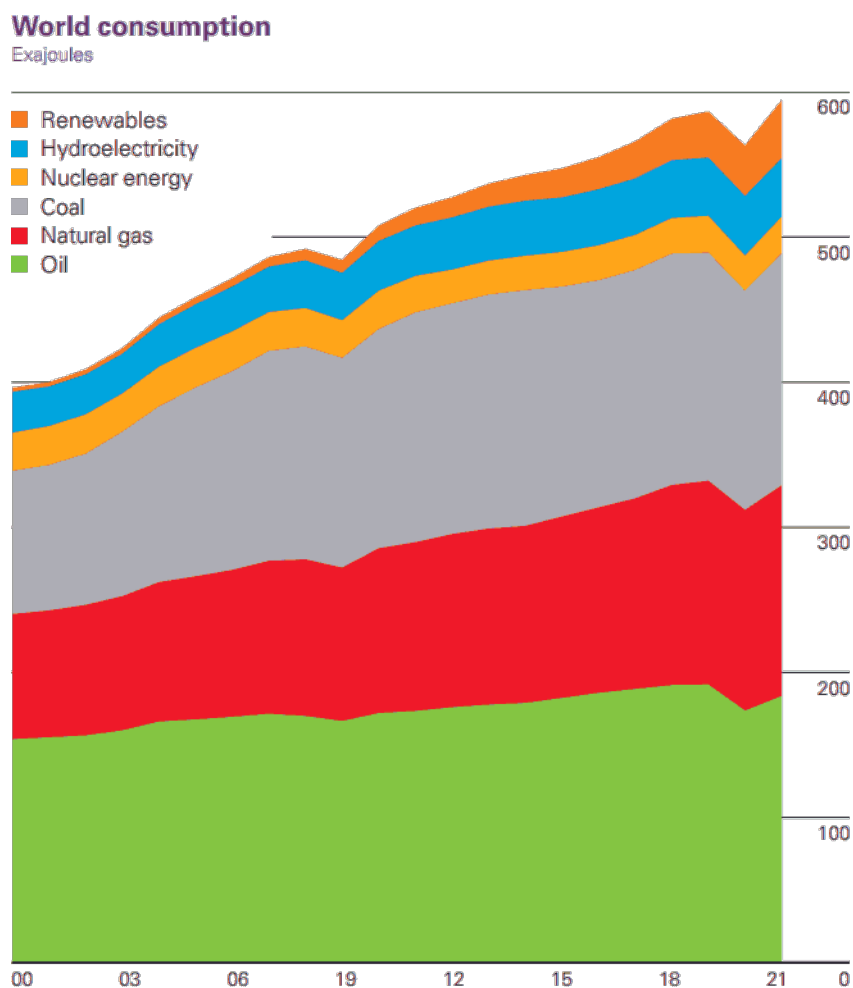


**Figure 1.1** Energy consumption in the world from 2000 to 2021 [4].

To reduce energy-related problems, governments around the world have accelerated the development of renewable energy as an alternative energy source. Renewable energy is more environment-friendly with respect to greenhouse emissions, and it is regarded as the long-term solution for a reliable and infinite supply of electricity. There are many different types of renewable energy, including renewable heat, hydropower, solar photovoltaic, wind power, etc. Renewable thermal energy is a technology that provides energy from sources, including geothermal, solar thermal energy, and biomass, that replenish themselves for immediate use or battery charging. Solar photovoltaic is a way of harvesting energy through the conversion of light energy from the sun into electrical energy. Wind power is a method of producing electric power from kinetic energy. From a financial point of view while REN21 has reported that the share of fossils has gradually decreased over ten years (2009-2020) [5] (Fig 1.2), the share of renewable energy has increased. Furthermore, it is worth noting that the share of renewable energy in 2020 increased from 11.7 % to 12.6 % compared with that in 2019 despite a temporary reduction in global energy demand related to COVID-19 (Fig. 1.2). With this trend, we

can anticipate that renewable energy will grow to 22 % in 2060 and contribute to reducing a significant amount of greenhouse gases.

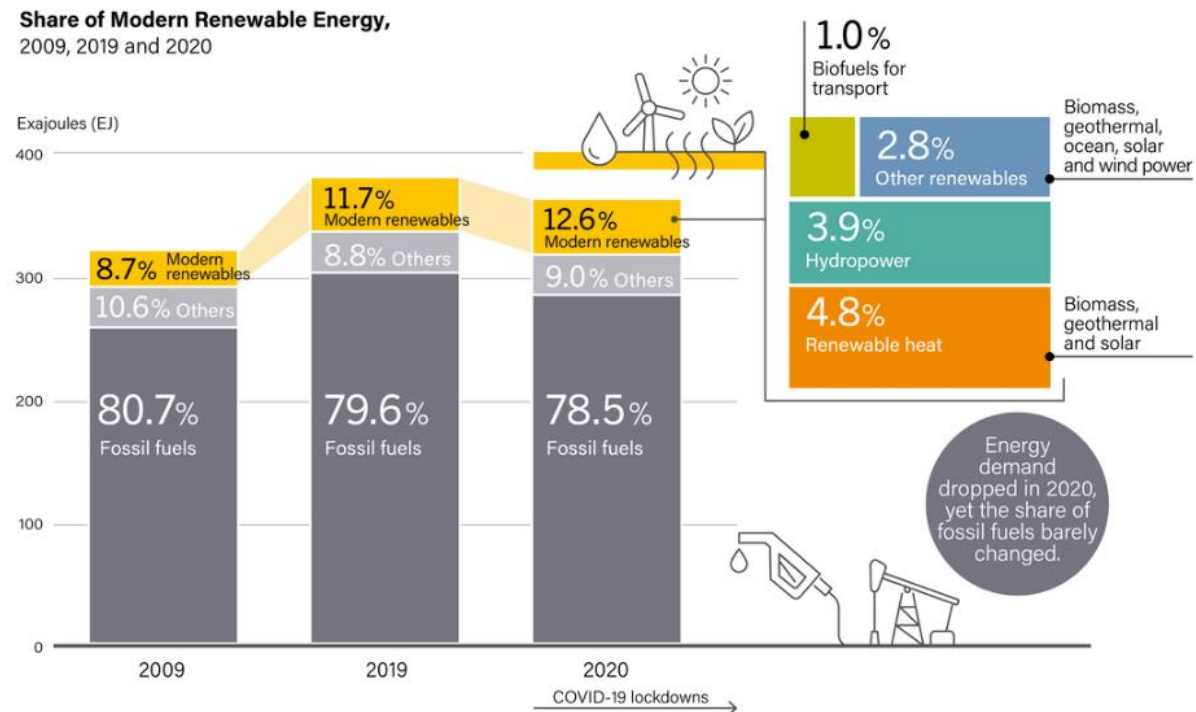


**Figure 1.2** Total final energy consumption and share of renewable energy in 2009, 2019, and 2020 [5].

### 1.1.2 Trend in Photovoltaics

Among various renewable energy resources, solar energy is an infinite resource, and it can be the optimal energy source that humans need on the Earth today [6], [7]. Initially the first solar cells were used for space application during 1960s [8]. Photovoltaic (PV) is the best-known solar energy conversion technology by directly converting from solar energy into electrical energy. Fig. 1.3 (a) shows the annual global capacity of solar PV with additions for 10 years [5]. Both, PV capacity and the overall annual additions can be seen to have gradually increased during the last 10 years. The PV markets continued record-breaking peak of PV capacity and its additions. The global PV capacity and its additions in 2021 are 942 gigawatts (GW) and 175 GW, respectively. Furthermore, it is noticeable that the capacity increment of PV is the largest in renewable energies (Fig 1.3 (b)). Additionally, the capacity additions of PV have continued to increase from 2016 to 2021 compared to other energies. The data from REN21 2022 report imply that solar PV has received a lot of attention and is being developed actively.

Photovoltaics are safer, cleaner, and more efficient than other ways of using solar energy, such as solar thermal and photochemical reactions. In addition, the direct conversion of solar energy into electrical energy enables a more efficient energy transportation and storage process. Furthermore, PV is more applicable to real life. For example, it can be integrated from rooftops to the windows and even on cars, ships and planes [9].

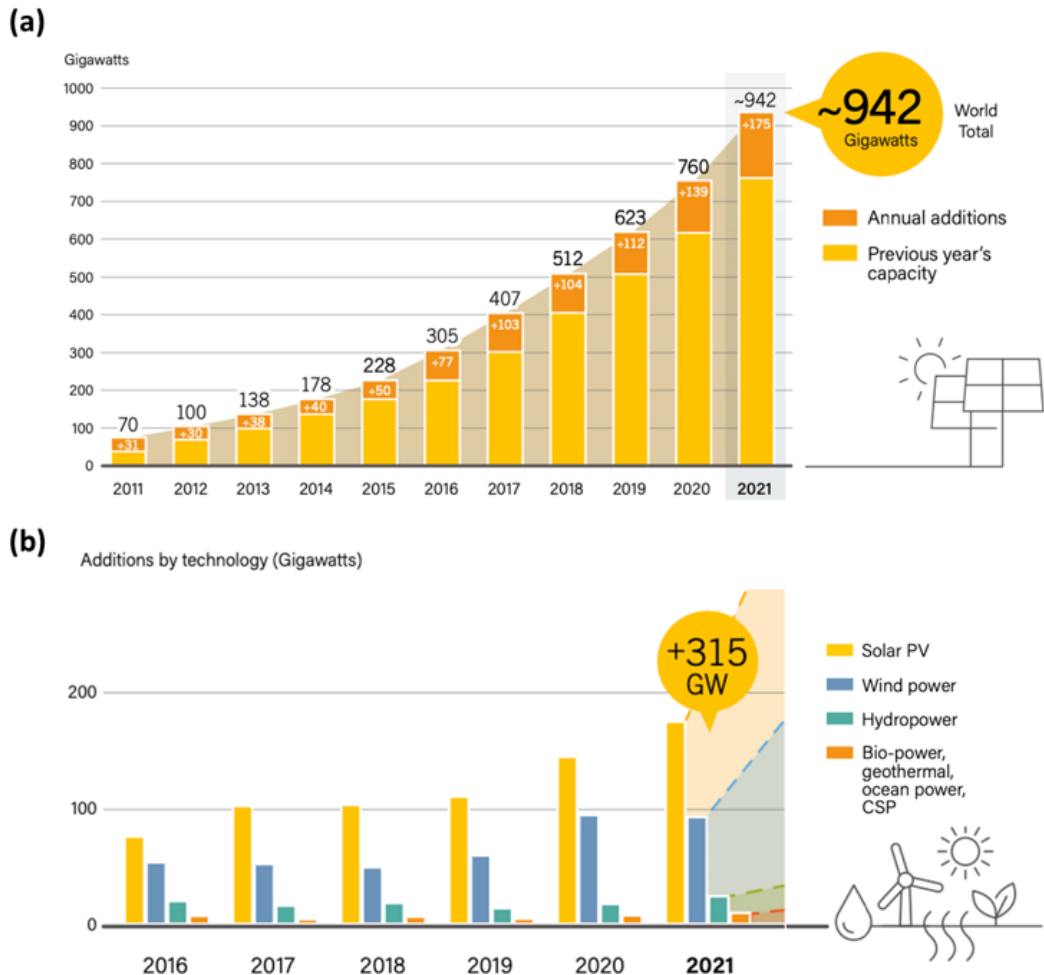


**Figure 1.3** (a) Annual solar PV capacity and increases from 2011 to 2021. (b) Annual increases in renewable power capacity from 2016 to 2021 [5].

In general, photovoltaic performance is influenced by semiconductor materials. The first solar cell was fabricated with a thin selenium-coated gold layer by Charles Fritts in 1883 [10]. 1 % of power conversion efficiency (PCE) was achieved. The research on photovoltaics stopped due to low efficiency and material costs. After around 70 years, the first practical silicon-based solar cells with 6 % of PCE were developed at Bell Laboratories in 1954 [11]. Since then, photovoltaic technologies have received attention from researchers, and research on photovoltaics has been actively proceeding. For the last 60 years, device engineering with a fundamental physical understanding of silicon-based solar cells has led to the achievement of high efficiency of 26.7 % and the highest market share in the solar panel [12].

Meanwhile, other absorber materials such as CIGS, CdTe, and GaAs have been spotlighted as thin film solar cells because it is appropriate for flexible solar cells compared to Si solar cells [13]. GaAs single-junction thin film solar cells have achieved 29.1 % [14]. In addition, organic photovoltaics (OPVs) [15], dye-sensitized solar cells (DSCs) [16] and quantum-dot solar cells (QDSCs) [17] emerged as next-generation solar technologies. The common advantages of these photovoltaic technologies are low-temperature processes, simple solution processes such as spin-coating and roll-to-roll printing, and thus low cost.

## 1.2 Organic-inorganic Halide Perovskite Solar Cells

### 1.2.1 Solar Cells based on Organic-inorganic Halide Perovskites

Apart from the thin film and next-generation solar cells, as mentioned in section 1.1.2, organic-inorganic halide perovskite solar cells (PSCs) have attracted much attention from the photovoltaic community. Organic-inorganic halide perovskites formed by the  $ABX_3$  structure have emerged as an innovative material with excellent optoelectrical properties. The bandgap of the halide perovskites is widely tunable by finely tuning the composition of cations ( $MA^+$ ,  $Cs^+$ ,  $FA^+$ ,  $Rb^+$ , etc.) and anions ( $Cl^-$ ,  $Br^-$ ,  $I^-$ ). In  $ABX_3$  structures, the bandgap energy generally decreases as X goes from Cl to Br to I because of the increase in the halide ionic radius size. Additionally, bandgap energy can be changed by substituting cation positioned A of  $ABX_3$  structures. For example,  $FAPbI_3$  has lower bandgap energy than that of  $MAPbI_3$  because  $FA^+$  ions with a larger ion size expand the perovskite crystal and shorten the distance of the Pb-I bond. Fig. 1.4 presents bandgap energies of halide perovskites with respect to elemental composition. Additionally, we can control the bandgap energy by keeping the same composition but varying the size of nanoparticles in the form of quantum dot perovskites. All this flexibility and adjustability enables halide perovskite to be applied in various optoelectronic devices, including solar cells, light emitting diodes [18], photodetectors [19], field effect transistors [20], etc. (Fig. 1.5).

Organic-inorganic halide perovskites have been most actively researched in the area of photovoltaic among various areas of optoelectrical devices due to several advantageous properties of halide perovskites. Their high optical absorption coefficient [21], long carrier diffusion length ( $1 \mu m$ ) [22], low trap density ( $10^{16} - 10^{17} \text{ cm}^{-3}$ ), and small exciton binding energy [23] contributes to the high

photovoltaic performance of perovskite solar cells. Furthermore, the manufacturing cost of halide perovskite solar cells is less than silicon-based solar cells. Meng *et al.* estimated that the manufacturing cost of perovskite solar modules is less than half of 0.30 \$/W for Si-based solar modules [24]. The lower manufacturing cost of perovskite solar modules is strongly influenced by lower material costs [25]. Because of these properties, PSCs have shown comparatively marked improvement in their performance in the past 12 years. The initial PCE of PSCs was only 3.8% in 2009 [26] but increased to 14.1% in 2013 for the first certified PCE [27], followed by a PCE of 25.7 % in 2022, much closer to GaAs-based and Si-based technologies (Fig. 1.6) [14]. The achievement of high PCE is more impressive considering the short period compared with other inorganic or organic PV technologies.

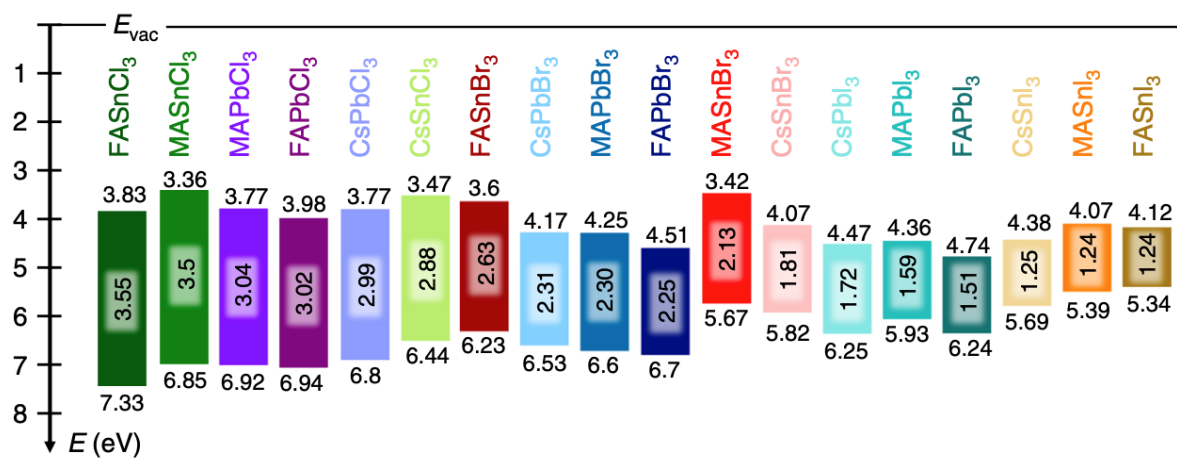


Figure 1.4 Schematic energy level diagram of halide perovskites with different chemical components.

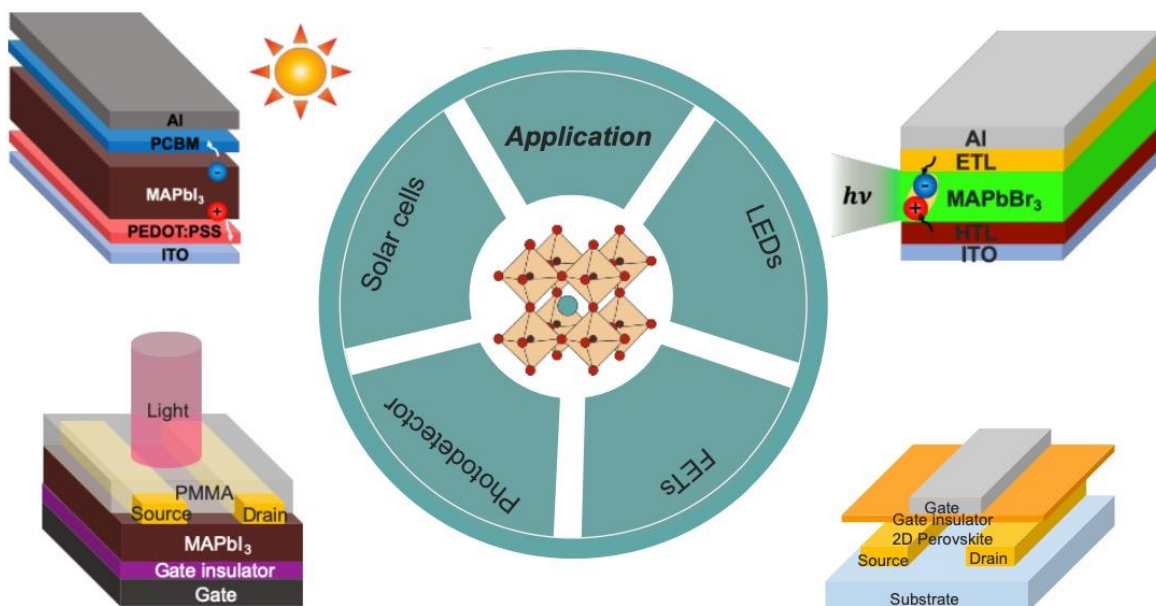
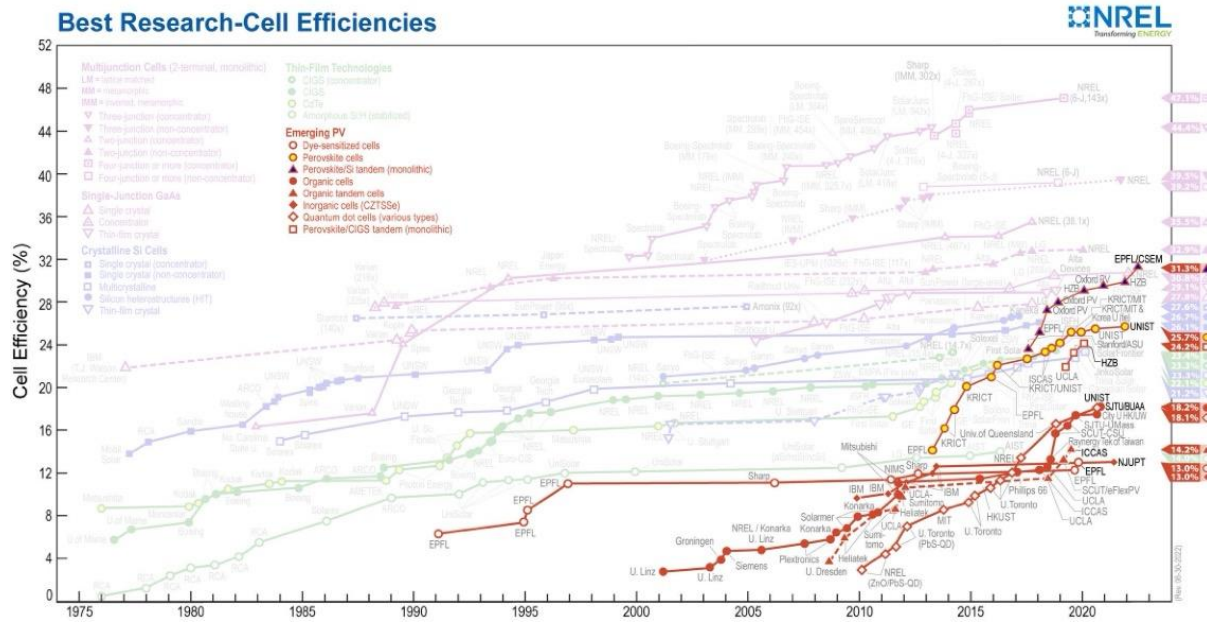


Figure 1.5 Schematic diagram of the potential optoelectrical applications: solar cells, photodetectors, field effect transistors (FETs), and light-emitting diodes (LEDs).



**Figure 1.6** Best efficiency of the perovskite-based solar cell compared with other material-based solar cells [14].

There were several events that contributed to important breakthroughs in PSCs from 2013 to 2022. To increase the photocurrents in PSCs, researchers substituted  $\text{FA}^+$  for  $\text{MA}^+$  in  $\text{MAPbI}_3$ . However, the photoactive black  $\alpha$ -phase  $\text{FAPbI}_3$  is unstable and tends to easily transform the yellow  $\delta$ -phase  $\text{FAPbI}_3$ , which leads to the decline of photovoltaic performance. Jeon *et al.* incorporated  $\text{MAPbBr}_3$  in  $\text{FAPbI}_3$  to stabilize the  $\alpha$ -phase  $\text{FAPbI}_3$  and achieved 18.4 % in 2015 [28]. Afterward, Saliba *et al.* mixed  $\text{FA}^+$ ,  $\text{MA}^+$ , and  $\text{Rb}^+$  at A site cation to remove the residual  $\delta$ -phase  $\text{FAPbI}_3$ . Through this strategy, 21 % of PCE was achieved in FA-based PSCs with small amounts of  $\text{MA}^+$  and  $\text{Rb}^+$  [29]. However, FA-based perovskites with  $\text{MA}^+$  and  $\text{Rb}^+$  increases bandgap energy consequently reducing PCE. Therefore, Jeong *et al.* proposed to passivate  $\text{I}^-$  vacancy defect in  $\text{FAPbI}_3$  with the pseudo halide anion ( $\text{HCOO}^-$ ), which lead to an achievement of 25.6 % PCE in 2021 [30]. The aforementioned results are mostly achieved by controlling the chemical compositions of halide perovskite. In addition to the above mentioned strategies, modification of the structures of PSCs, other deposition techniques, or engineering of interfaces between halide perovskite layers and charge transport layers also contribute to improving the efficiency.

## 1.2.2 Stability Issues of Halide Perovskite Solar Cells

Despite the high photovoltaic performance in halide PSCs, one of the challenging issues for the successful commercialization of PSCs is still low operational stability. The mechanisms of

degradation in a bulk perovskite layer and interfaces between perovskite and charge transport layers are caused by various factors of the operational environment such as oxygen, moisture, heat, light, and electrical field. Degradation is divided mainly into extrinsic and intrinsic degradation. Extrinsic degradation is a consequence of external factors, such as moisture, oxygen, and heat. On the other hand, intrinsic degradation results from intrinsic factors required or generated during operation (light illumination and electric field) [31].

To improve the stability, many researchers have tried to investigate them in different ways and have observed the degradation phenomena under varied conditions [32], [33]. Among various degradation phenomena, degradation caused by extrinsic factors has been studied well. For example, the  $\text{MAPbI}_3 \cdot \text{H}_2\text{O}$  complex is formed, or the  $\text{H}_2\text{O}$  molecule diffuses into the  $\text{CH}_3\text{NH}_3^+$  site when  $\text{MAPbI}_3$  is exposed to moisture [34]. The diffused  $\text{H}_2\text{O}$  molecule acts as the charge trap center and causes the non-radiative recombination. In the case when  $\text{MAPbI}_3$  is exposed to oxygen in the dark, oxygen has a negligible effect on film morphology and PL lifetime [35]. However, in the presence of both oxygen and light (photo-oxidation), oxygen diffuses into  $\text{MAPbI}_3$  through iodide vacancies at the surface and in bulk leading to degradation in a short time. Heat promotes the diffusion of mobile ions in halide perovskite and the reaction of the mobile ions with the contact layer [36].

As mentioned above, degradation caused by extrinsic factors has been studied and understood well. Many researchers systematically investigated the degradation mechanism and divided them in detail according to the device structure and the kind of halide perovskite (i.e., lead-based halide perovskite, tin-based halide perovskite, etc.). Furthermore, the proper encapsulation technique is employed in order to avoid the degradation triggered by moisture, oxygen, and heat. Due to the packing techniques, PSCs are prevented from being decomposed, and the stability issues can be addressed.

Although the light and the electric field are necessary or always exist for the operation of PSCs, these two intrinsic factors also cause the decomposition of halide perovskite. Understanding of the intrinsic degradation attributed to these two intrinsic factors had remained vague due to the complexity of these materials. However, recently several researchers have vigorously studied the degradation caused by light between the two intrinsic factors. During illumination, the changes, including halide segregation (Hoke effect), cation segregation, and photochemical reaction, occur [36], [37].

However, there are fewer studies about the degradation of perovskite caused by electric fields than about the degradation attributed to other factors. Researchers have difficulty studying the degradation caused by an electric field because the in-situ electric biasing system for the measurement is not well equipped compared with other environmental systems. Ex-situ measurement, which can be a substitute for in-situ measurement, is performed near equilibrium. It is conducted after applying bias,

so during the transportation of the sample from applying a bias to the measurement system. The sample can be exposed to oxygen, or ions move back to their original position at the equilibrium [38]. For studying electric field-induced degradation of PSCs, the measurement is required to be performed in real-time, excluding other environmental parameters. Table 1.1 summarizes the observation of the degradation of halide perovskite film and PSCs caused by the electric field. The summarized measurements were performed under a pure electric field and were not affected by air, moisture (in a vacuum), and sun illumination.

**Table 1.1** Summary of reported studies of degradation of perovskite film and PSCs caused by electric bias. Q-perovskite means quadruple cation perovskite ( $\text{Rb}_{0.05}(\text{Cs}_{0.1}\text{MA}_{0.15}\text{FA}_{0.75})_{0.95}\text{PbI}_2\text{Br}_3$ ).

Sample	Measurement	Electric field	Distance between electrodes	Ref
$\text{CH}_3\text{NH}_3\text{PbI}_{3-x}\text{Cl}_x$	XPS	1 V	200 $\mu\text{m}$	[39]
$\text{MAPbI}_3$	PL & EIS	$1*10^5 \text{ V/m}$	200 $\mu\text{m}$	[40]
$\text{MAPbBr}_3$	n-XRF	$\pm 2 \text{ V}$	10 $\mu\text{m}$	[41]
$\text{MAPbBr}_3$	TOF-SIMS	5 – 15 V	100 $\mu\text{m}$	[42]
ITO/ETL/ $\text{MAPbI}_3$ /HTL/Au	TEM	$1*10^5 \text{ V/m}$	400 nm	[43]
FTO/cp-TiO <sub>2</sub> /m-TiO <sub>2</sub> /Q-Perovskite/spiro-MeOTAD/Au	Micro PL	1.2 V, -1 V	300 nm	[44]
ITO/ETL/ $\text{MAPbI}_3$ /HTL/Au	HRTEM	1 V	500 nm	[45]

Li *et al.* measured XPS of  $\text{CH}_3\text{NH}_3\text{PbI}_{3-x}\text{Cl}_x$  with lateral electrodes to investigate the redistribution of ions after long-term electric biasing. Through the measurement, they observed that the ratio of I/Pb, which is constant everywhere before biasing, gets higher at the positive electrode and lower at the ground electrode (Fig. 1.7 (a)) [39]. Furthermore, they also visualized the ion migration of  $\text{MAPbI}_3$  under an electric field using PL imaging microscopy (Fig. 1.7 (b)) [40]. Luo and his co-workers used nano-XRF (n-XRF) to analyze ion migration in  $\text{MAPbBr}_3$  monocrystal quantitatively and study intrinsic point defects in relation to optoelectrical properties at the nanometer scale (Fig. 1.7 (c)) [41].

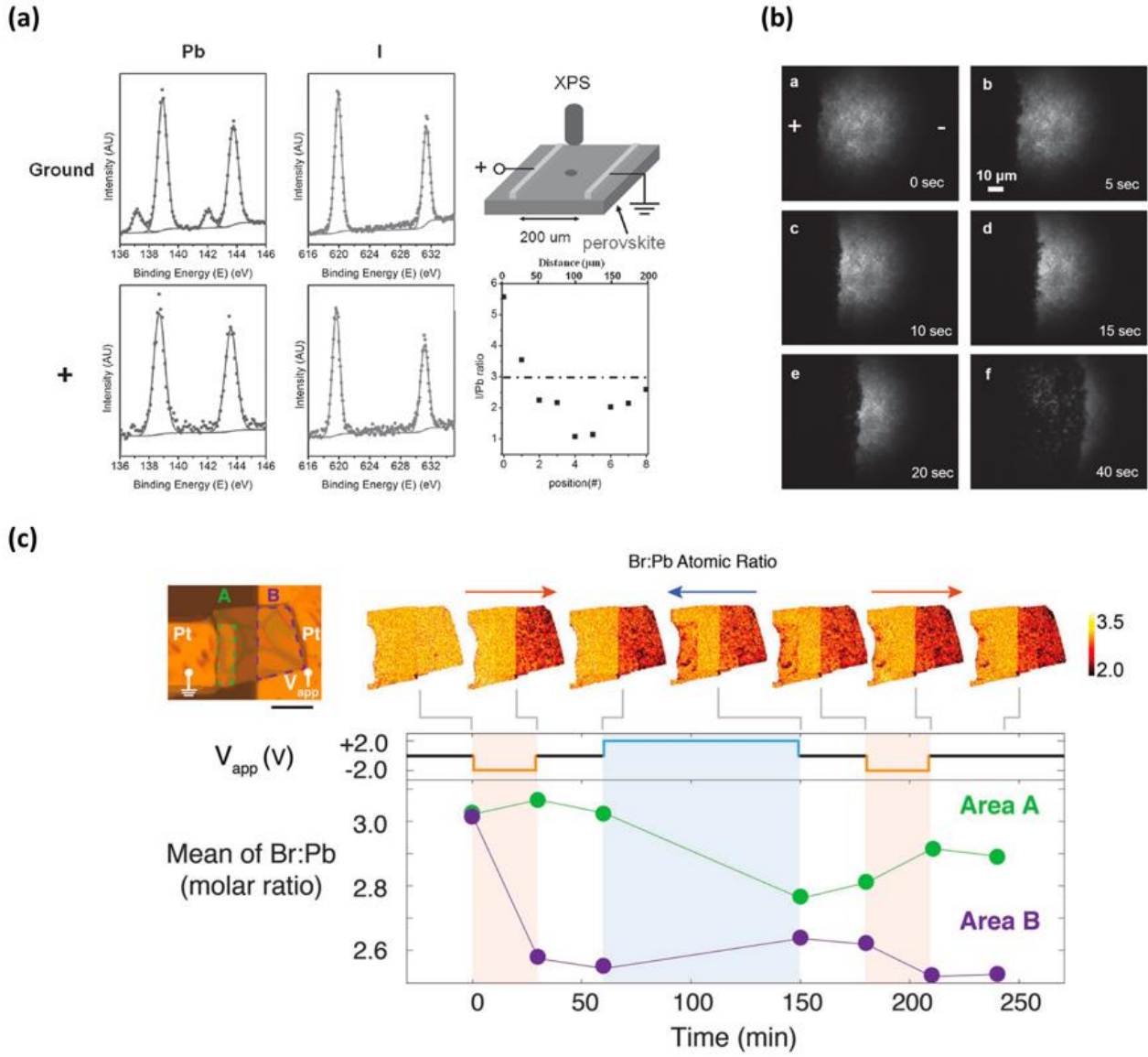


**Figure 1.7** (a) X-ray photoemission spectroscopy (XPS) spectra of Pb and I of a lateral  $\text{CH}_3\text{NH}_3\text{PbI}_{3-x}\text{Cl}_x$  near the ground and the positive electrode and distribution of the ratio of I/Pb between the two electrodes after applying bias 1 V for 30 min [39]. (b) Time-dependent photoluminescence (PL) images of MAPbI<sub>3</sub> film under electric bias [40]. (c) Nanoprobe X-ray fluorescence (n-XRF) measurement of the changes in Br:Pb element ratio in MAPbBr<sub>3</sub> single crystal under bias, and the mean Br:Pb ratio of area A and B during the bias sequence with the corresponding bias condition. The red and blue arrows indicate the direction of the electric field [41].

Researchers have put their effort towards investigating the influence of electric field on the bulk of halide perovskite and the interfaces between halide perovskite and the charge transport layer in PSCs. Jeangros *et al.* used the FIB section of PSCs with TEM and carried out in-situ characterization. They observed the formation of PbI<sub>2</sub> nanoparticles and voids near the interfaces in PSCs, which deteriorate the photovoltaic performances of PSCs (Fig. 1.8 (a)) [43]. In addition, phase segregation of MAPbI<sub>3</sub> in PSCs was observed using micro-PL by Duong *et al.* [42]. Under forward bias, there is a dramatic change in PL intensity however, the shift in PL is not observed under reverse bias. The results are caused by the relation of carrier concentration with the applied voltage based on the electron-phonon

theory [44]. At the forward bias above the built-in potential, the charge concentration significantly increases, which generates lattice strain and then promotes phase segregation.

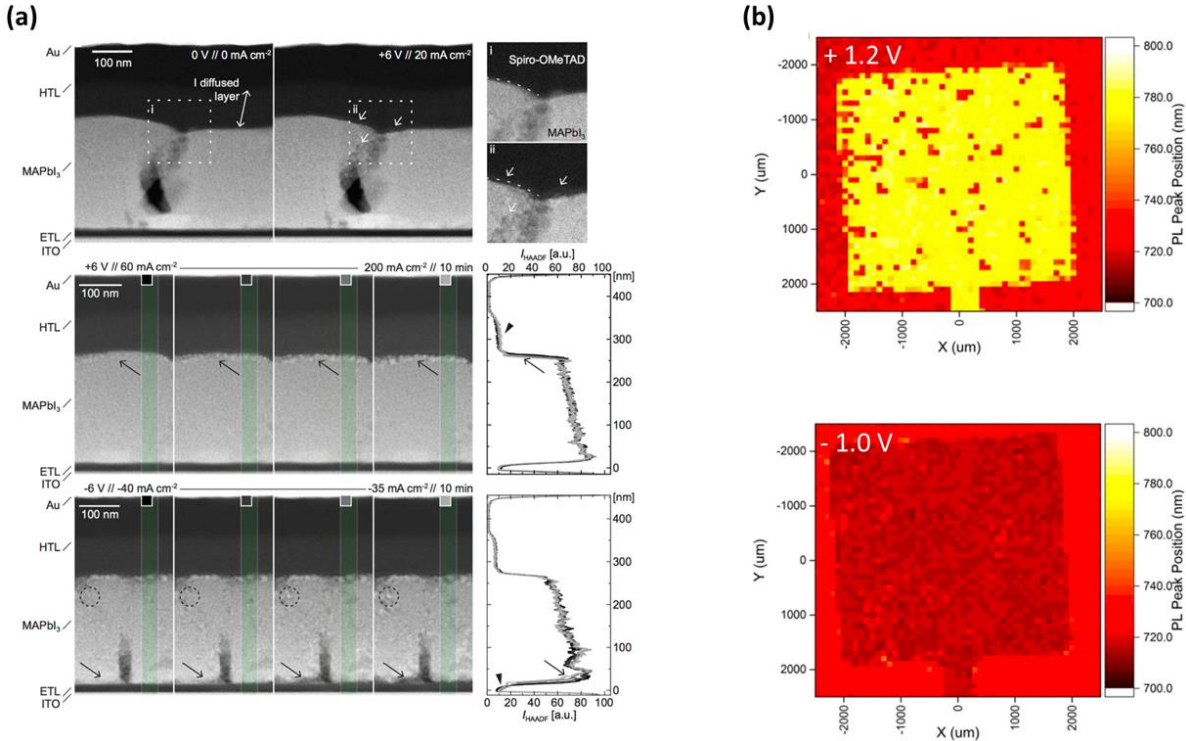


**Figure 1.8** (a) Scanning transmission microscope (STEM) with a high-angle annular dark-field (HAADF) micrographs showing changes in the morphology of the MAPbI<sub>3</sub> with applying  $\pm 6$  V to PSCs. Arrows and circles highlight the formation of nanoparticles and the resulting shrinkage of the MAPbI<sub>3</sub> phase during biasing [43]. (b) Micro-PL scan images showing the perovskite material in PSCs after applying the electric bias of  $+1.2$  V and  $-1$  V. All measurements were performed in the dark [44].

In the precedent studies, they have visualized the change in perovskite film or PSCs under an electric field. Furthermore, they quantified the change of mobile halide ions in the perovskite layers and the interfaces in PSC and tried to understand the parameters that affect the stability of PSCs. However, there is still a lack of deeper understanding of the degradation of PSC caused by an electric field. In the studies, they have analyzed the change of lead cation and halide anions, but they have not investigated organic cations and the change of the chemical bonds in detail. For a better understanding of the detailed mechanism of the phenomena, advanced characterizations are required, which provide insights into nano- and microscale details with respect to the chemical, electronic and ionic parameters (or compositional and structural heterogeneities), as these parameters have a decisive influence on not only performance but also stability of PSCs.

## 1.3 Characterization Techniques for Perovskite Solar Cells

### 1.3.1 Potential of Impedance Spectroscopy towards Analysis of Photovoltaics

Optoelectronic devices generally consist of several different functional layers, including the active layer and charge extraction/transport layers. For the deposition of the layers, various fabrication processes such as spin-coating, metal-organic chemical/physical vapor deposition, ion implantation, and epitaxial growth are employed [46]–[48]. In terms of devices, the interfaces between layers deposited by the mentioned processes are non-ideal, which strongly affects the electronic properties and the performance of devices. Observing interfacial reactivity during operation is difficult because the interface is buried inside devices, and the reaction occurs in the range of nanometers near the contact. In order to investigate the interface and the influence of non-ideal on the performance of the device, chemical spatially resolved measurement with ion milling has been used so far, which is a destructive technique [49], [50].

Among optoelectronic devices, the efficiency of solar cells is generally evaluated with parameters such as power conversion efficiency, series and shunt resistance, ideality factor, and built-in potential. These parameters can be achieved by DC techniques. Current (J) – voltage (V) measurement is the most conventional DC measurement. They are useful for correlating the performance with thin film properties, such as crystallinity, morphology, microstructure, and optical stability. However, J-V measurement is insufficient to understand dominating mechanisms fully and whether the mechanisms occur at interface or bulk. In addition, it alone cannot provide resistive or capacitive parameters indicating the interface change.

Impedance spectroscopy (IS) is a versatile technique that can help to monitor electrical and electrochemical processes under operando conditions and describe the electronic structure in electrochemical and solid-state devices [51]. In general, IS can be mainly divided into two categories: IS for dielectric materials and electrochemical impedance spectroscopy (EIS). The first IS is employed for dielectric materials such as solid/liquid nonconductors, single-crystal/amorphous semiconductors, glasses, polymers, etc. On the contrary, EIS is applied to investigate ion conductive materials, such as ionic conducting glasses, solid and liquid electrolytes, polymers, and nonstoichiometric ionically bonded single crystals [52], [53].

In IS experiments, the response of the samples to small-signal sinusoidal variation (AC characterization) is probed as a function of the frequency. The electrical energy of the signal is dissipated or stored by the device, which depends on the dynamical characteristics being detected. The dynamic or relaxation behavior can be differentiated depending on their unique relaxation time. IS complements the standard electrical characterization and can be easily measured without damaging the device structure [51].

This AC characterization technique enables quantitative analysis of various physical processes occurring at interface or bulk in solar cells, which cannot be elucidated by the DC measurements. IS can examine the kinetics of physical and chemical processes in semiconductor materials [54]. In addition, resistive and capacitive components can be achieved separately using IS according to the kinetics of the processes such as charge transfer, transport, and accumulation in solar cells that occur simultaneously.

### 1.3.2 Applications of Electrochemical Impedance Spectroscopy to Perovskite Solar Cells

As mentioned in section 1.2.2, low operational stability is the main issue in PSCs where high efficiency and reproducibility are achieved. The efficiency drop during continuous operation is mainly associated with the change in the bulk of the halide perovskite layer and ion migration [55]. Ion migration is an intrinsic effect of halide perovskite because perovskites are partially ionic compounds. In the ionic compounds, loose crystals, vacancies, and other defects exist. When an electric field is applied, ions migrate within the perovskite layer and can be accumulated at the interfaces between halide perovskite and contact layers which leads to hysteresis and degradation of PSCs [56], [57]. In order to alleviate the issues of stability, the changes in the perovskite materials and interfaces in the device need to be understood in more detail [58], [59]. To get insight into these issues, it is vital to employ characterization techniques that can provide information about the degradation processes in bulk and the interfaces of the devices.

EIS is an appropriate characterization technique for studying various processes taking place in PSCs and how they are affected by other contact layers, and it has been gaining increasing attention recently by researchers. The reason why EIS is a well-suited technique for studying PSCs is that PSCs have both electronic and ionic carriers whose motions are fast and slow processes, respectively. Due to the

two carriers, a wide range of electrical and electrochemical processes happen at the device interfaces. EIS can distinguish the results of the electronic and ionic charge dynamics in the absorber layer and at the interfaces in the form of resistance and capacitance.

There are several examples of studying phenomena in PSCs based on EIS. Sanchez *et al.* applied EIS to identify a slow dynamic process in PSCs according to hysteresis [60], [61]. They observed three arc features in the complex impedance plot at high-, intermediate-, and low frequency (Fig. 1.9 (a)). The arcs at high- and intermediate-frequency are related to selective contacts and chemical capacitance, respectively. They found that the feature at low frequency is attributed to the polarizability of MA cation in perovskites. Dhar *et al.* studied ion displacement in single crystalline and polycrystalline  $\text{MAPbI}_3$  using EIS. Fig. 1.9 (b) presents impedance spectra of single crystal and polycrystals with silver and graphite electrodes. They found that the Warburg feature, which is affected by ion transfer to the electrode, decreases when silver is replaced with a graphite electrode.

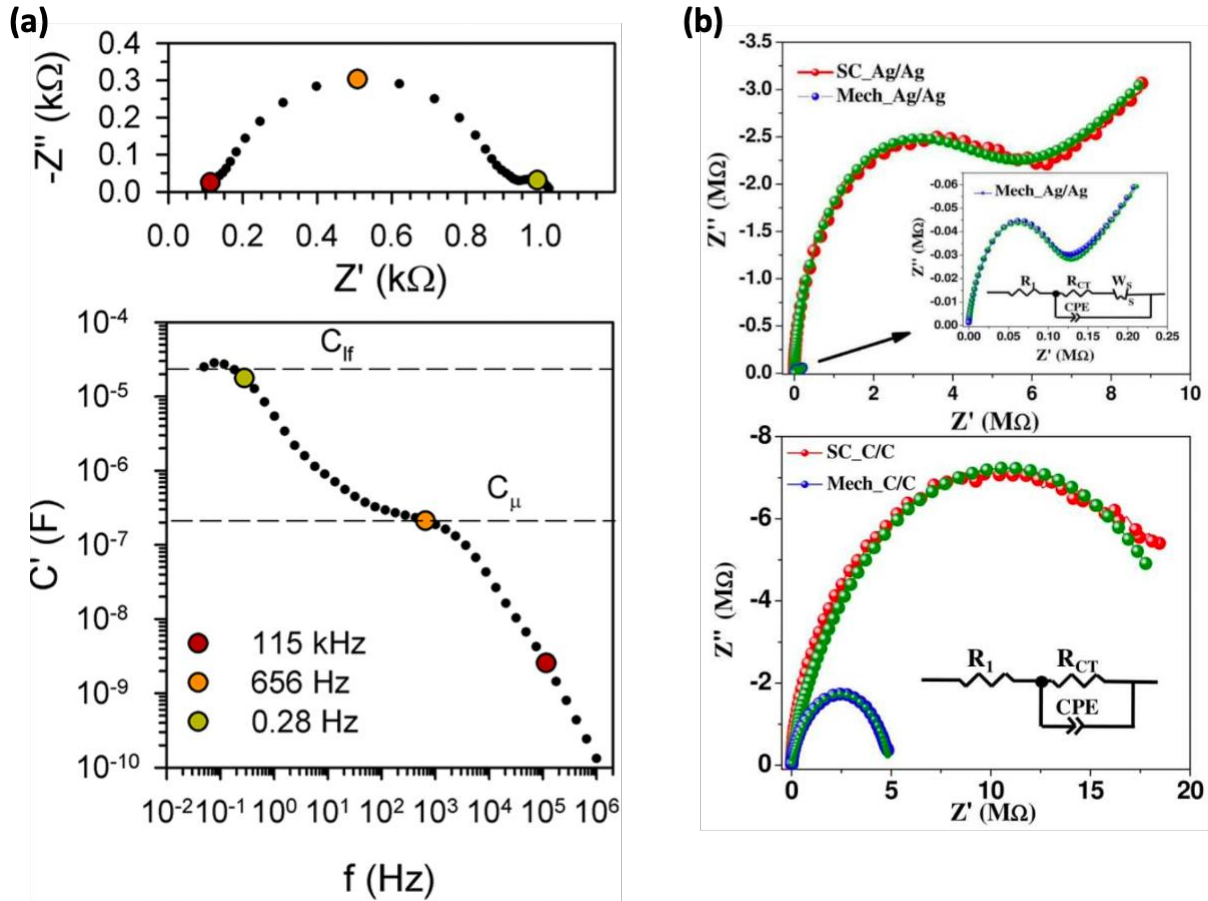


**Figure 1.9** (a) Complex impedance plot and Bode plot of the real part of the capacitance of Sing-MA/I-Cl sample under the dark condition at DC bias of 0.9 V [61]. (b) Complex impedance plot of single crystal and polycrystals  $\text{MAPbI}_3$  according to silver and graphite electrodes [62].

In addition to ion migration, the effect of hole and electron transport layers on the performance of  $\text{MAPbI}_3$  PSC was studied using EIS [63]. The Nyquist plots of the original full device, an electron-

only device with  $\text{TiO}_2$ , and a hole-only device with spiro-OMeTAD are shown in Fig 1.10 (a). In the impedance spectra, two impedance features exist at high and low frequencies. The arc at high frequency is related to selective contacts, and the arc at low frequency is influenced by the perovskite layer. In addition, the influence of doping or oxidation of hole transport materials on the impedance response was also studied by Juárez-Pérez and his co-workers [64]. Fig 1.10 (b) shows Nyquist plots of doped, oxidized, and undoped spiro-OMeTAD-based PSCs measured at 0 V. They found that the relaxation time of hole transport materials decreases by employing doped and oxidized spiro-OMeTAD and perovskite/HTM interfaces are highly improved.

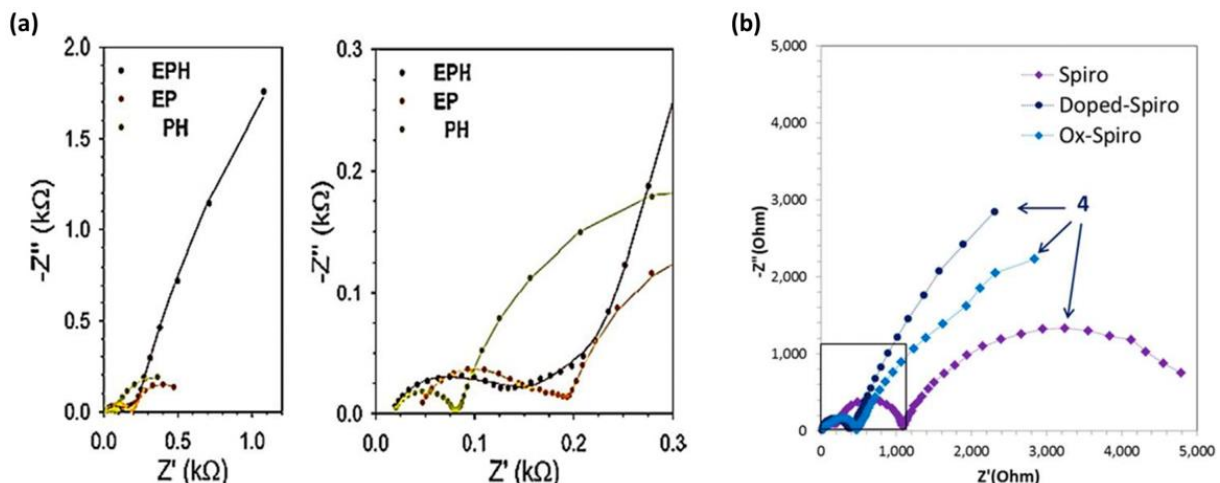


**Figure 1.10** (a) Full and zoomed Nyquist plot of PSCs (FTO/TiO<sub>2</sub>/perovskite/spiro-OMeTAD/Au), electron-only device with TiO<sub>2</sub>, and hole-only device with spiro-OMeTAD [63]. (b) Complex impedance plot of undoped, doped and oxidized spiro-OMeTAD based PSCs [64].

Through the examples described above, we can confirm that IS measurements have shown great success in observing behavior occurring in the bulk of perovskite and the interface in PSCs due to its good adaptability and high sensitivity and there is still much potential to discover the various phenomena in PSCs using EIS.

### 1.3.3 Synchrotron-based X-ray Techniques in Materials Characterization

The development of new functional materials has brought about technical and scientific impacts in engineered structures, sustained energy sources, and a host of other applications. In order to improve the performance of the new materials, it is important to explore, understand them and further modify the synthesis and manufacturing process. A more systematic approach is necessary for obtaining information about the probable imperfection and hidden properties in the materials. In general,

laboratory-based characterization, including X-ray diffraction (XRD), scanning electron microscopy (SEM), and UV-Visible absorption spectroscopy, is conventional and useful for the characterization of materials. However, they have limitations in analyzing the material on the nanoscale.

Synchrotron radiation-based characterization is one of the effective solutions for dealing with the constraints of conventional characterization techniques. Since the appearance of the third-generation synchrotron radiation beamline, which provides high X-ray brightness up to  $10^{18}$  photons/s [65], [66], the gigantic X-ray source has attracted attention as one of the mainstream scientific tools for getting insight into nanoscale details of the materials which couldn't be founded by conventional characterization techniques. Synchrotron radiation is electromagnetic radiation resulting from the acceleration of electrons close to the speed of light. Synchrotron generates monochromatic, collimated, and highly brilliant beam, which contributes to a higher spatial and spectral resolution with a micro-sized beam size. Additionally, synchrotron X-ray-based techniques are non-destructive.

As a result of the advantages of synchrotron radiation-based X-rays, they have been one of the most crucial components of research in various fields of materials science including nanomaterials, biomaterials, and energy materials. It is possible to apply synchrotron-based characterization techniques to diverse types of materials such as powders, thin films, and bulk forms with complex crystalline or amorphous structures. Furthermore, varied characterization techniques can be performed with synchrotron radiation, such as grazing-incidence X-ray diffraction (XRD), X-ray imaging, X-ray photoelectron spectroscopy (XPS), and X-ray absorption spectroscopy (XAS) [67].

A variety of crystalline structures of the material exists, from single crystals to nanocrystals. Due to the various crystalline properties of the material, different techniques of diffraction, including X-ray powder diffraction, grazing-incidence XRD, and small-angle X-ray scattering, wide-angle X-ray scattering, have been developed depending on the purpose. X-ray imaging is a technique to achieve 3D reconstruction images and perform phase-contrast microscopy with high resolution. XPS is a measurement to obtain detailed information about the surface of the materials. Through the measurement, quantitative elemental analysis with the bonding and oxidation state can be achieved. XAS is a measurement technique of absorbed X-rays of materials with different energies. The absorption coefficient, which is affected by the atomic types and nature of the bond, can be determined by the measurement. By applying these different techniques, complementary information about the surface and depth of the materials can be achieved, which is helpful to deeper insight into the nature of new materials.

### 1.3.4 Application of Synchrotron-based Characterizations to Perovskite Solar Cells

Based on the properties of synchrotron radiation mentioned in section 1.3.3, the application of synchrotron-based characterization to study PSCs has been active recently. In the synchrotron-based characterization techniques, which span from X-ray imaging, spectroscopy, and scattering microscopies, their properties such as X-ray spot size, coherence, intensity etc. enables obtaining optical and chemical information at subgrain resolution leading to the correlation of electrical performance with elemental composition for PSCs with polycrystalline perovskite layer. In addition, these techniques help explain phenomena that govern PSCs from the chemical and electrical points of view and how they affect photovoltaic performance [68]. Currently, the application of synchrotron-based measurements for the characterization of PSCs is still in its infancy and leaves possibilities to suggest various new experiments with ptychographic, multimodal, *in situ*, and *operando* measurements. In this section, several studies on PSCs using synchrotron-based characterization are described, which have proven that the characterizations are valuable tools for understanding the role of defects, impurities, and the change in the perovskite materials and interfaces in PSCs.

Oesinhaous *et al.* employed grazing-incidence wide-angle X-ray scattering (GISAXS) to study the crystallization of  $\text{MAPbI}_3$  based on a 2-step deposition process. When the MAI precursor solution is spin-coated on the  $\text{PbI}_2$  layer, not only (002) orientation (face-up) but also corner-up orientation is discovered (Fig. 1.11 (a)) [69]. The corner-up orientation is a distinct property of  $\text{MAPbI}_3$  formed by a 2-step deposition process compared with the 1-step deposition method showing only the preference (002) plane. The GIWAXS results show that the crystalline orientation is affected by the deposition methods of halide perovskite. Grain boundaries play an important role in the photovoltaic performance of PSCs. In order to prove it, the crystalline properties of grain boundary are studied at the nanoscale using nano-XRD by Adhyaksa and his co-workers. Fig. 1.11 (b) presents SEM and nano X-ray diffraction (n-XRD) images of a polycrystalline  $\text{MAPbBr}_3$  film. In the SEM image of the film, the grain size of a few tens of micrometers is shown. The nano-XRD map indicates that the scattering intensity of the characteristic (002) is very low in the grain-boundary region. It implies that grain boundaries in halide perovskite film are amorphous [70].

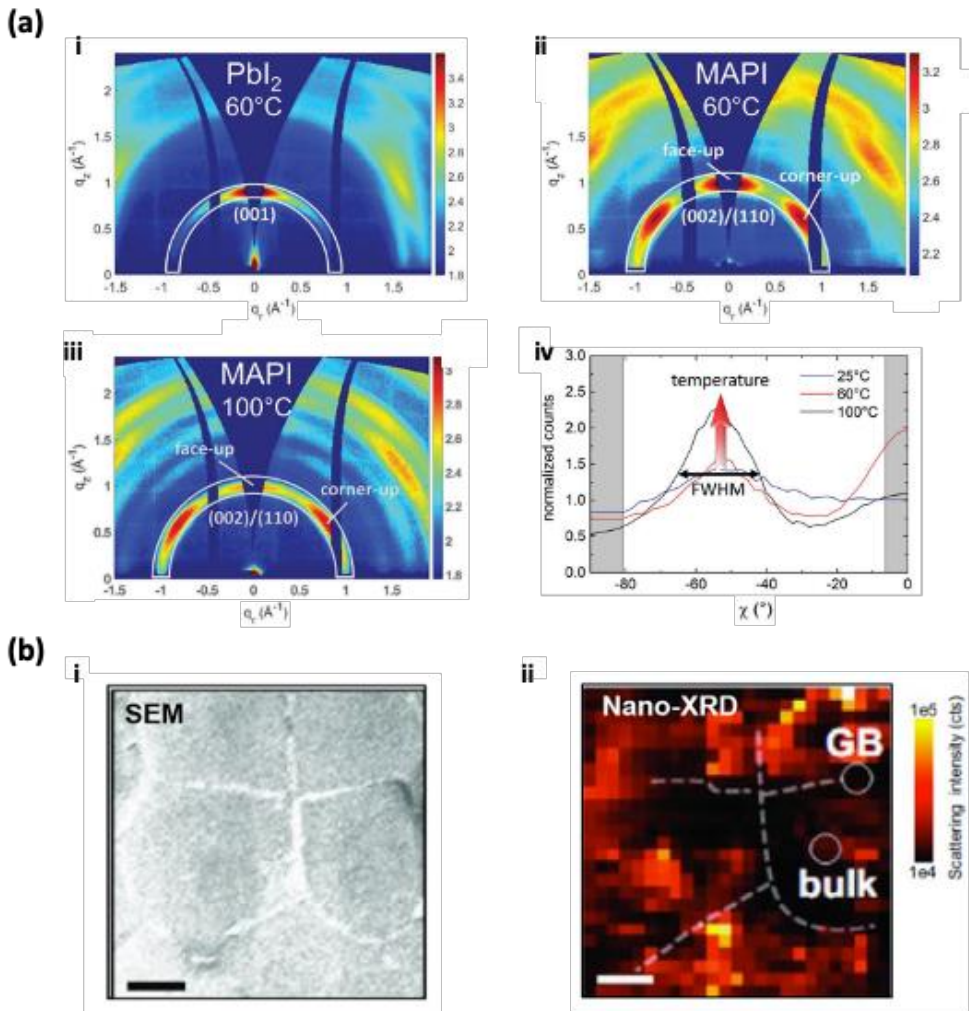


**Figure 1.11** (a) GIWAXS data of conversion of  $\text{PbI}_2$  into  $\text{MAPbI}_3$ , GIWAXS data of i)  $\text{PbI}_2$ , ii)  $\text{MAPbI}_3$  produced at 60 °C and 100 °C, and azimuthal cuts performed on GIWAXS data of  $\text{MAPbI}_3$  according to the temperature for crystallization [69]. (b) n-XRD data of  $\text{MAPbBr}_3$  region covering grain and grain boundaries i) SEM, correlated ii) nano-XRD map. The scale bars are 4  $\mu\text{m}$  [70].

X-ray fluorescence microscopy is a useful technique for analyzing the presence of elements at the nanoscale. For example, Unger *et al.* applied n-XRF to identify the presence of I and Cl in  $\text{MAPbI}_{3-x}\text{Cl}_x$  perovskite films [71]. The elemental distribution of I and Cl in the perovskite film was spatially resolved by n-XRF in Fig. 1.12 (a). The maps of local halide content and halide ratio show that Cl clusters were localized outside of iodine-rich grains, which induces that Cl remained at grain boundaries. Meanwhile, n-XRF can be performed with XRF with X-ray beam-induced current (XBIC) to study recombination properties of perovskite simultaneously. Correa-Baena and his co-workers measured n-XRF and XBIC of  $(\text{FAPbI}_3)_{0.83}(\text{MAPbBr}_3)_{0.17}$  with different doping concentrations of RbI [72]. Incorporation of alkali cations like  $\text{Cs}^+$  and  $\text{Rb}^+$  onto the A-site of  $\text{ABX}_3$  structure on behalf of larger organic cations leads to enhancement of the stability in the perovskite film [73]. As shown in the n-XRF mapping (Fig. 1.12 (b)), Rb-rich clusters increase as the concentration of RbI increases. Furthermore, higher photocurrent in Rb-rich perovskite film is observed by XBIC, implying that non-radiative recombination in Rb-rich perovskite film is weak. These results propose that further

optimization of perovskite chemistry for enhancement of both photocurrent and voltage is available with the n-XRF measurements.

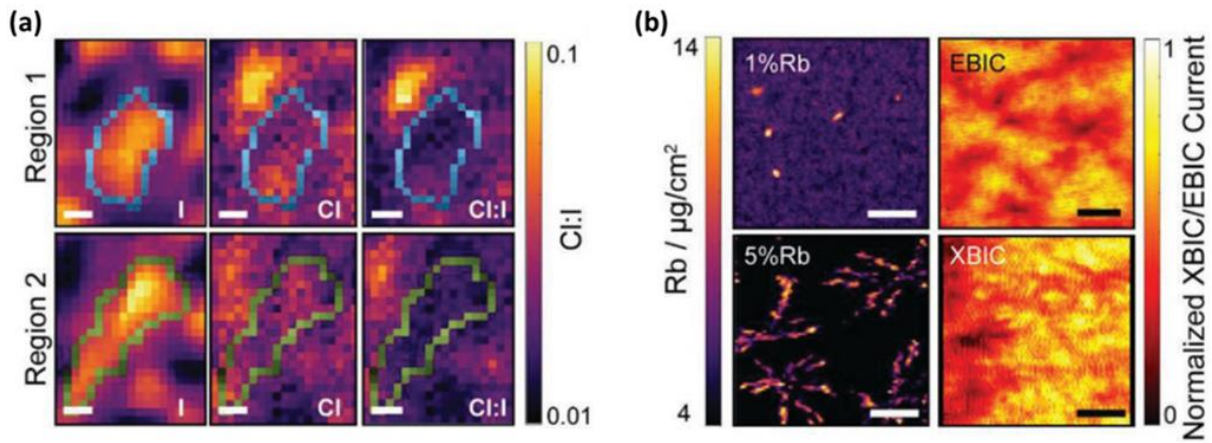


**Figure 1.12** (a) n-XRF maps of Cl, I, and Cl:I ratio in  $\text{MAPbI}_{3-x}\text{Cl}_x$  with the scale bar of 100 nm [71]. (b) n-XRF maps of Rb in  $(\text{FAPbI}_3)_{0.83}(\text{MAPbBr}_3)_{0.17}$  with doping of 1 % and 5 % RbI and their corresponding XBIC measurements. The length of the scale bar is 5  $\mu\text{m}$  [72].

X-ray photoemission electron microscopy (XPEEM) is an excellent technique to study surface chemistry and defect states in semiconductor devices. In XPEEM, unbound energetic electrons are emitted from the surface of the samples, and the collected electrons by detectors form the surface image with chemical shifts. Furthermore, it can be used to spatially resolve band bending between charge transport layers and the perovskite layer. Appropriate band alignment between the charge transport layers and perovskite layers leads to the performance of PSCs [74]. For example, Hartman *et al.* employed PEEM to investigate the valence band maximum of defects formed in  $\text{MAPbI}_{(3-x)}\text{Cl}_x$  on  $\text{TiO}_2$  (Fig. 1.13 (a)) [74]. The local composition of the perovskite surface can be identified using X-ray photoelectron spectroscopy (XPS) –PEEM. In the XPS-PEEM spectra, the Pb 4f binding energy of the incomplete region of perovskite is lower than the bulk of perovskite, indicating a downward band bending from perovskite to the interface between perovskite and  $\text{TiO}_2$  up to 450 meV.

X-ray absorption spectroscopy (XAS) can be used to identify elements and understand the chemical state. Stuckelberger and his coworkers analyzed the distribution of halide in  $\text{MAPb}(\text{Br}_x\text{I}_{1-x})$  using high-energy resolution fluorescence detection (HERFD) XAS [75]. XAS spectra of  $\text{MAPb}(\text{Br}_x\text{I}_{1-x})$  with different ratios of Br and I at  $\text{Pb-L}_{\beta 5}$  are shown in Fig. 1.13 (b). In the spectra, there are two distinct features in the middle of the rising absorption edge and at the top of the main edge. As the Br content increases ( $x$  increases), the two spectral features blue shift with the shifts of the rising edge from 13039.9 eV to 13040.8 eV and the main edge from 13044.7 eV to 13046.2 eV for  $\text{MAPbI}_3$  and  $\text{MAPbBr}_3$ . However, spectra of intermediate compositions cannot be explained by using a linear combination of the spectra of  $\text{MAPbI}_3$  and  $\text{MAPbBr}_3$ . With additional analysis of the spectra using DFT calculation, the results indicate that the mixed halide materials form well-mixed single phases

rather than segregated pure halide phases.

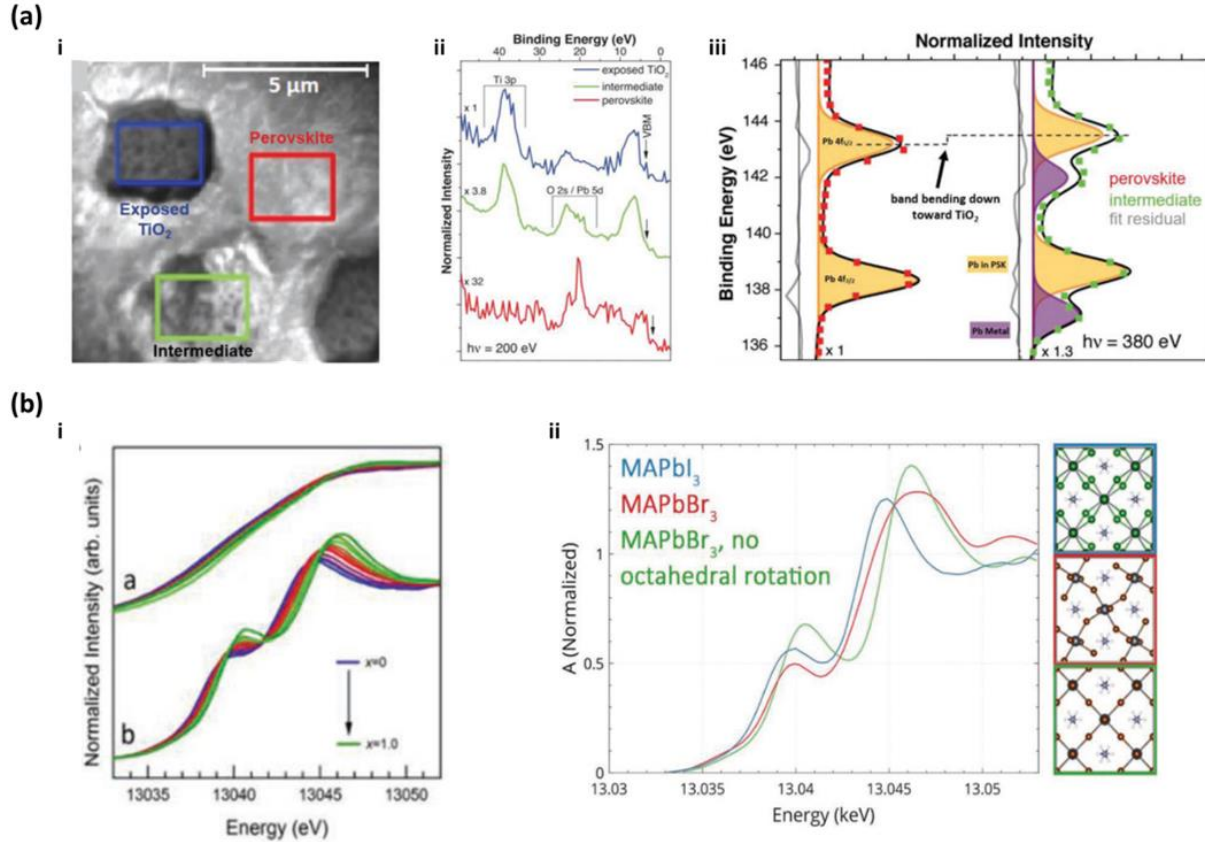


**Figure 1.13** (a) i) PEEM image of  $\text{MAPbI}_{(3-x)}\text{Cl}_x$  on planar compact  $\text{TiO}_2$ , ii) XPS-PEEM spectra at the energy region of valence band maximum (VBM) and shallow core levels (Ti 3p, O 2s, and Pb 5d), iii) Pb 4f XPS-PEEM spectra of bulk perovskite and perovskite near the interface [74]. (b) i) HERFD (bottom) XAS spectra of  $\text{MAPb}(\text{Br}_x\text{I}_{1-x})_3$  at a Pb L-edge region, ii) DFT-calculated  $\text{Pb}_{\text{L}3}$  HERFD-XANES spectra of  $\text{MAPbBr}_3$  according to octahedral tilting and  $\text{MAPbI}_3$  [75].

The examples described above imply that synchrotron-based characterization can offer an observation of nanoscale compositional and structural features of perovskite films and PSCs and the potential to achieve a more comprehensive understanding of the degradation mechanisms in PSCs.

## 1.4 Motivation of the Research and Thesis Overview

This thesis is titled ‘Study of degradation mechanisms in halide perovskite films and PSCs using electrical and synchrotron-based characterization’. The title implies that we aim to investigate the degradation mechanism of the bulk of perovskite and interfaces in PSCs. For this goal, not only laboratory-based characterization but also synchrotron-based characterization is employed.

This chapter (chapter 1) is presented as background information to assist with an understanding of

the motivation of this research. Organic-inorganic halide perovskite solar cells have been the most promising candidates for next-generation solar cells due to their excellent optoelectrical properties and high efficiency. However, the current understanding of degradation mechanisms caused by various environments is inadequate. Among various degradations, there isn't a lot of definitive research about the degradation of perovskite caused by an electric field. In order to fully understand the degradation mechanism, electrochemical impedance spectroscopy (EIS) and scanning transmission X-ray microscopy (STXM) are employed in this thesis. Before the experiments with EIS and STXM, several fundamental concepts about PSC, EIS, and STXM and the preparation of optimized perovskite film and PSCs required to be explained.

This thesis covers many concepts, including solar cells, halide perovskite, EIS, and STXM. In chapter 2, the fundamental theories for this thesis are explained for all of them. First of all, the principle of photovoltaics and the properties of halide perovskite and PSCs are described. After that, the concept of EIS and its necessity for studying halide perovskites are explained. Lastly, the synchrotron radiation and STXM on that basis are introduced in detail.

Chapter 3 deals with the overall process necessary for the fabrication of solar cells and the photovoltaic performance of the fabricated PSCs. The optimized perovskite film and solar cells are employed to study of electric field-induced degradation. Firstly, the optimization process of  $\text{MAPbI}_3$  film deposited by co-evaporation is explained with different conditions of the ratio of  $\text{PbI}_2$  and MAI and the rate of  $\text{PbI}_2$  with the same ratio. Secondly, photovoltaic performances of PSCs based on  $\text{MAPbI}_3$  deposited under the optimized condition are evaluated. In addition, the performance of reference PSC is compared to that of other PSCs with different hole /electron transport layers.

Chapter 4 reports the EIS results of PSCs with different perovskite layers and different conditions. At first, the EIS properties according to different halide perovskites, including  $\text{MAPbI}_3$  based on co-evaporation and spin-coating processes, and  $\text{FAMACs}_{0.05}\text{Pb}(\text{I}_{0.83}\text{Br}_{0.17})_3$  prepared by spin-coating, are described. Then, the influence of the electric field on EIS properties of PSCs is studied, which contributes to studying electric field-induced degradation in PSCs. Additionally, the EIS of the reference sample of PSCs is measured under ageing in the air. After that, the degradation mechanism in the air is explained.

Chapter 5 reports the effect of electric field on  $\text{MAPbI}_3$  film and solar cells as investigated using STXM. Before studying the effect, we demonstrated that STXM is a useful technique for exploring phenomena in PSCs by verifying the sensitivity of STXM to various elements. Secondly, an electric field is applied to  $\text{MAPbI}_3$  film on a customized electric biasing system, and the chemical change in bulk  $\text{MAPbI}_3$  is analyzed. Thirdly, the focused ion beam (FIB) section of the reference PSCs with

different conditions of applying electric bias is measured by STXM, and chemical changes in the interfaces between perovskite and transport layers are analyzed at the nanoscale. In the end, the mechanism of the electric field-induced degradation in  $\text{MAPbI}_3$  solar cells is hypothesized by correlating the results of STXM with EIS results.

Chapter 6 gives a short conclusion outlining what was done and what remains to be done in subsequent studies.

# **Chapter 2.**

# **Fundamental Theory**

---

<b>2.1 Introduction .....</b>	<b>31</b>
<b>2.2 Basic Concepts of Solar Cells .....</b>	<b>32</b>
2.2.1 Working Principle of Solar Cells .....	32
2.2.2 P-I-N Junction and Thin Film Solar Cells .....	33
2.2.3 Solar Cell Parameters under Light .....	36
2.2.4 J-V Characteristics under Dark .....	37
<b>2.3 Organic Inorganic Halide Perovskite Solar Cells .....</b>	<b>38</b>
2.3.1 Crystal Structure of Halide Perovskite and its Properties .....	38
2.3.2 Architecture of Perovskite Solar Cells .....	41
2.3.3 Ion Migration .....	44
<b>2.4 Characterization of Perovskite Solar Cells using Impedance Spectroscopy .....</b>	<b>48</b>
2.4.1 Dielectric Properties and Charge Dynamics.....	48
2.4.2 Impedance Spectroscopy.....	50
2.4.3 Ionic Conductivity of Halide Perovskites: Low Frequency Dielectric Response of Perovskite .....	54
<b>2.5 Characterization of Perovskite using Scanning Transmission X-ray Microspectroscopy .....</b>	<b>56</b>
2.5.1 Principle of Synchrotron Radiation .....	56
2.5.2 X-ray Interaction with Materials .....	59
2.5.3 Scanning Transmission X-ray Microscopy .....	60

---

## **2.1 Introduction**

In chapter 1, we explained that renewable energy sources, including photovoltaics, are uprising to solve the problems of exhaustion of energy and reduce greenhouse gas. In photovoltaics, organic-inorganic halide perovskite solar cells are a promising candidate for scalable, low-cost, and high-efficiency photovoltaics because of their good optoelectronic properties. However, the degradation mechanism needs to be studied due to their instability in various environments. In this thesis, the degradation mechanism under an electric field is investigated using EIS and STXM. Before studying and analyzing the results achieved by EIS and STXM, various background knowledge is required to

be learned and understood for this research.

In this chapter, the fundamental theories related to photovoltaics, halide perovskites, EIS and STXM are explained. Firstly, the operation principle of photovoltaics and P-I-N junction appropriate for thin film solar cells are explained. In addition, electrical characteristics in the solar cells under dark and illuminations and the element of performance evaluation are described. Secondly, the basic concept of halide perovskite and PSCs are accounted for. Thirdly, the concepts of impedance spectroscopy and dielectric properties in halide perovskite. Lastly, synchrotron radiation and interaction between X-rays and materials are covered. Based on them, various applications of synchrotron characterizations for studying PSCs are described.

## 2.2 Basic Concepts of Solar Cells

### 2.2.1 Working Principle of Solar Cells

A solar cell is a semiconductor device that converts light energy into electrical energy. The working principle of solar cells is based on the photovoltaic (PV) effect. The PV effect is the direct conversion of optical energy (i.e., energy from light, including infrared (IR), visible, and ultraviolet). The following steps are essential for the operation of solar cells: 1) Absorption of photons that leads to an excited state of the absorber, which can generate either a free electron-hole pair or an exciton (bound electron-hole pair (EHP)), 2) Separation of photogenerated charge carriers at the junction by a built-in field designed to break symmetry, 3) Collection of the charge carriers at the electrodes. After these steps, the electron dissipates in the external circuit in order to produce an electrical current (Fig. 2.1).

Semiconductor materials in the form of the p-n junction usually are used for photovoltaic energy conversion. The conventional solar cell is a typical p–n junction consisting of two layers of differently doped semiconductors. Without light, the cell functions as a p–n junction diode with current (I)–voltage (V) characteristics, as shown below following the Shockley equation.

$$I_d = I_s \left[ \exp \left( \frac{qV}{nkT} \right) - 1 \right] \quad (2.1)$$

where  $I_d$ ,  $I_s$ ,  $q$ ,  $k$ , and  $T$  are predicted diode current, dark saturation current, electron charge ( $1.602 \times 10^{-19}$  C), Boltzmann's constant, and absolute temperature, respectively. When the cell is exposed to solar

radiation, photons with energy equal to or larger than the bandgap ( $E_g$ ) of the semiconductor are absorbed, and EHPs are generated [76]. If the electron and hole are not separated within their lifetime, they will recombine. Recombination of generated EHPs by light is a mechanism for loss in solar cells, and hence, if they recombine, no current can be generated. One of the ways to separate the EHPs is to make use of the electric field existing in a p–n junction. EHPs are created in the n-type, depletion, and p-type regions, and due to the built-in potential and electric field, electrons move to the n region and holes to the p region. The resulting electrical current due to the PV effect is called the light-generated current or photocurrent. Thereby, an illuminated cell can be described as a current source paralleled by a p–n junction diode [77].

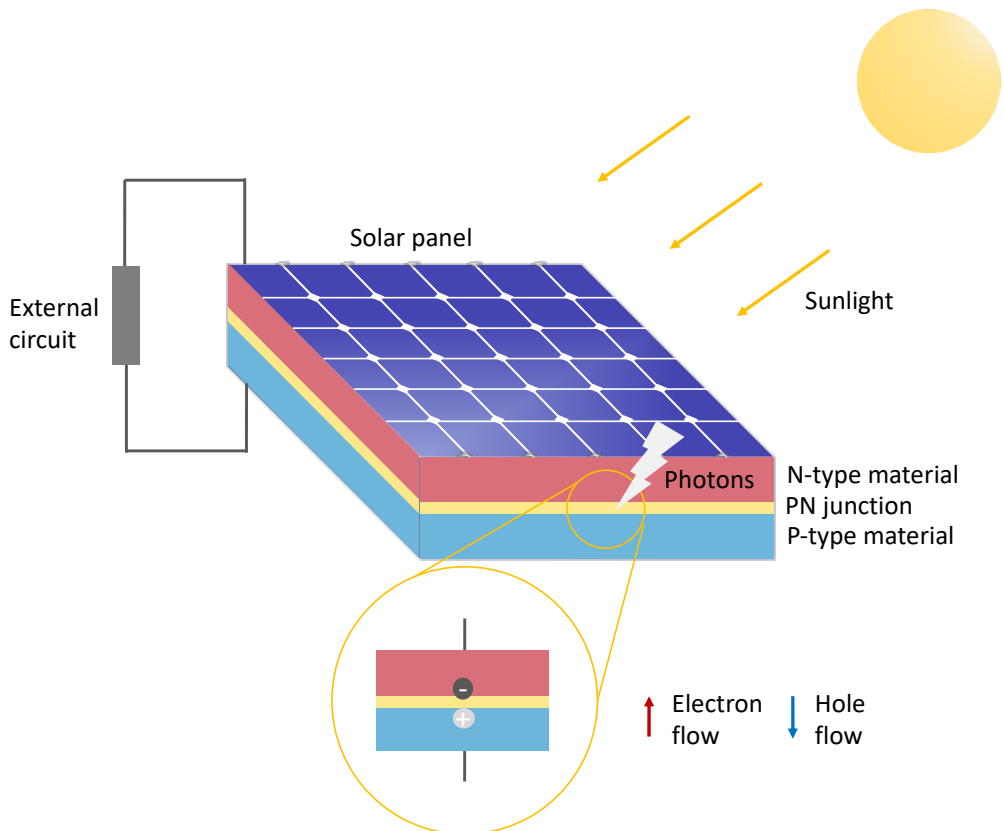


**Figure 2.1** Schematic of the photovoltaic effect in solar panel.

## 2.2.2 P-I-N Junction and Thin Film Solar Cells

The charge transport mechanisms in solar cells can be divided into diffusion and drift. Diffusion is a process where charge carriers tend to spread out from regions of high particle concentration into regions of low particle concentration.

This equation describes the current density caused by electron diffusion

$$J_e = qD_e \frac{dn}{dx} \quad (2.2)$$

where  $q$  is an electronic charge ( $1.6 \times 10^{-19}$  C),  $D_e$  is the electron diffusion coefficient,  $n$  is the electron concentration, and  $\frac{dn}{dx}$  is the concentration gradient. The other mechanism for carrier charge transport is drift. Drift is charge carrier motion in the presence of an electric field. Principally, when a negative charge is placed in an electric field, it will experience a flux in the opposite direction of the electric field. On the other hand, a positive charge will experience a flux in the direction of the electric field.

The current density resulting from the electron drift is described by this equation.

$$J_e = qn\mu_e E \quad (2.3)$$

where  $n$ ,  $\mu_e$ , and  $E$  are the electron concentration, electron mobility, and electric field, respectively. The diffusion length ( $L$ ) of the minority carrier is defined as

$$L = \sqrt{D \cdot \tau} \quad (2.4)$$

The diffusion length can be interpreted as the average distance that excited minority carriers travel before recombining with a majority charge carrier.

Therefore, the thickness of the absorber layer is required to have the same order of magnitude as the diffusion lengths so that electrons and holes farthest from the depletion region can be collected. In general, the thickness of a c-Si absorber layer is limited to 300  $\mu\text{m}$  because the diffusion length of crystalline silicon (c-Si) is about 300  $\mu\text{m}$  [78]. On the other hand, amorphous silicon, organic semiconductor, or halide perovskite have a much higher defect density than crystalline silicon, and therefore the diffusion length is much shorter. For example, the diffusion length of amorphous silicon (a-Si) is 100 – 300 nm [79]. The diffusion length of an organic semiconductor is 3-10 nm [80]. The diffusion length of halide perovskite is from 100 nm to 1  $\mu\text{m}$  [81].

The charge carrier transport in a thick absorber cannot depend on diffusion but on the drift because  $\tau_n$  and  $\tau_p$  are insignificant. Hence materials for absorbers, including a-Si, organic semiconductor, and halide perovskite, as mentioned earlier, are not based on a p-n junction but rather on a p-i-n junction where an undoped semiconductor layer is located between thin p-doped and n-doped layers. The thickness of the intrinsic layer is typically several hundreds of nanometers, while those of doped layers are several tens of nanometers.

Fig. 2.2 presents the band diagram of the p-i-n structure with p, i, and n-layers (a) being physically separate and (b) after the junction is formed. In Fig. 2.2, a built-in electric field is formed across the intrinsic layer between the p- and n-doped layers. When the layers are separate (Fig. 2.2 (a)), the Fermi level ( $E_F$ ) in the p-layer is placed near the valence band edge, and the Fermi level in the n-layer is closer to the conduction band edge. The Fermi level of the intrinsic layer is in the middle of the bandgap. When the layers are in contact (Fig. 2.2 (b)), the Fermi levels in each layer align on the same energy under thermal equilibrium in the dark. It generates a slope over the electronic bands in the intrinsic film because there is no change in the intrinsic layer. The potential difference from the slope across the intrinsic layer is called built-in potential ( $V_{Bi}$ ). The built-in potential equals the difference of bandgap energy of the intrinsic layer and the sum of the energy of Fermi levels in the doped region. There are no majority or minority carriers in the intrinsic layer, and therefore drift is dominant for charge carrier transport in the absorber layer of the p-i-n structure. Electrons of EHPs generated due to light absorption move down the slope in the conduction band, and holes move up the slope of the valence band toward the p-doped layer. In n- and p-doped layers, each electron and hole are the majority carrier, so diffusion is responsible for charge carrier transport. However, the diffusion length of the doped layers is low, which makes the thickness of the layers thin. The doped layer for high-efficiency solar cells should be transparent to incident photons to minimize the parasitic absorption by the doped layer. In order to be transparent, the bandgap energy of the doped layer should be high. Furthermore, it is important to achieve the doped layer with high conductivity and adjust the balance of conductivity of the two doped layers. Balancing the optical and electrical properties of the doped layer is a delicate process that can strongly influence the performance of the device.

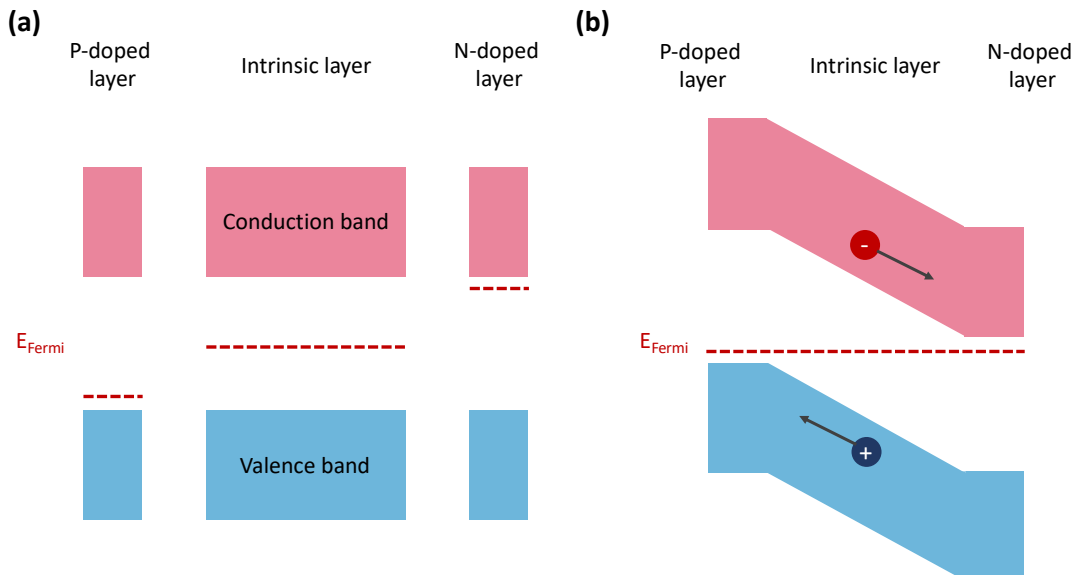


**Figure 2.2** Schematic energy band diagram of p-i-n structure with p, i, and n-layers (a) being separate and (b) after the junction is formed.

## 2.2.3 Solar Cell Parameters under Light

Solar cells are a form of photosynthesis cell, defined as a device whose electrical characteristics, such as current, voltage, or resistance, vary when exposed to light.

The I-V characteristics of an ideal solar cell under illumination are characterized by the following equation (Eq. 2.5)

$$I = I_{ph} - I_s [\exp\left(\frac{qV}{nkT}\right) - 1] \quad (2.5)$$

The photocurrent ( $I_{ph}$ ) in the equation arises from the generation of excess carriers by solar radiation. We can obtain open circuit voltage by setting  $I=0$  (Eq. 2.6)

$$V_{OC} = \frac{nKT}{q} \ln\left(\frac{I_{ph}}{I_s} + 1\right) \approx \frac{nKT}{q} \ln\left(\frac{I_{ph}}{I_s}\right) \quad (2.6)$$

The maximum open circuit voltage ( $V_{oc}$ ) is the built-in potential of the junction, and the maximum built-in potential is close to the band gap. We should add the effect of series resistance  $R_S$  and shunt resistance  $R_{SH}$  in parallel with the semiconductor device, which causes current leakage. Now, the net output current of the cell, considering both of them, is given by Eq. 2.7 with the circuit model (Fig. 2.3 (a)).

$$I = I_{ph} - I_s \left[ \exp\left(\frac{q(V+IR_S)}{nkT}\right) - 1 \right] - \frac{V+IR_S}{R_{SH}} \quad (2.7)$$

The current-voltage characteristics of a solar cell are shown in Fig. 2.3 (b). The fill factor (FF) is a measure of how close the characteristic is to conforming to the ideal rectangular I-V shape and is defined as

$$FF = \frac{V_{max} \times I_{max}}{V_{oc} \times I_{sc}} \quad (2.8)$$

The ideal power conversion efficiency (PCE) is the ratio of the maximum power output to the incident power  $P_{in}$ .

$$\eta = \frac{P_m}{P_{in}} = \frac{V_{max} \times I_{max}}{P_{in}} = \frac{V_{oc} \times I_{sc}}{P_{in}} \times FF \quad (2.9)$$

When defining the PCE, it is important to use a well-defined and reproducible light spectrum. The air mass (AM)-solar spectra are the standard light spectra for outdoor PV applications and define the degree to which the atmosphere affects the sunlight received at the earth's surface. The secant of the

angle between the sun and the zenith ( $\sec \theta$ ) is defined as the AM number, and it measures the atmospheric path length relative to the minimum path length when the sun is directly overhead. The global AM 1.5 spectrum is used as a reference spectrum for PV applications. The global AM 1.5-spectrum combines a direct AM 1.5 spectrum and a standard scattered light spectrum [76], [82].

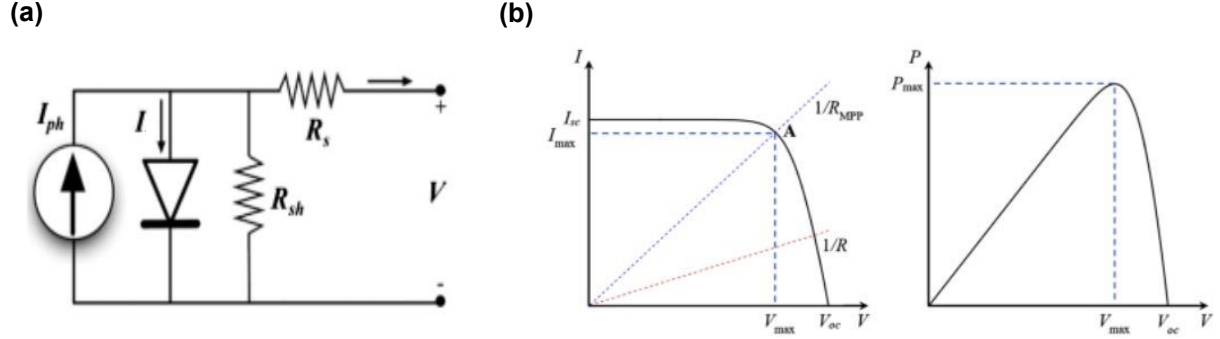


**Figure 2.3** (a) Equivalent circuit of a solar cell where the current source ( $I_{ph}$ ). (b) The I-V characteristic curve (showing the maximum power point A) and power-voltage curve of a solar cell.

## 2.2.4 J-V Characteristics under Dark

J-V characteristics of solar cells under dark are essential for evaluating the diode behavior. Fig. 2.4 presents the typical dark current density-voltage (J-V) characteristic curves. In the curves, three specific regions can be observed: (I) a shunt resistance region, (II) an exponential behavior region, and (III) a series resistance region. The shunt resistance region is the linear region with low negative and positive potential. The shunt resistance ( $R_{SH}$ ) strongly impacts the current density in the region. For high photovoltaic performance, the leakage current should be low.

The J-V curve shows exponential growth, and the ideality factor ( $n$ ) is the most critical parameter of diode operation in the exponential region. It can be calculated from the diode equation (Eq. 2.1), and the value is between 1 and 2. It is assumed that all the recombination occurs via band to band or via traps in bulk in the ideal diode. Ideality factor is used to identify the dominant recombination type in the solar cell. The series resistance ( $R_s$ ) region is another linear region at a large positive bias region.  $R_s$  dominates the current, and it should be small in order to achieve higher current and FF.

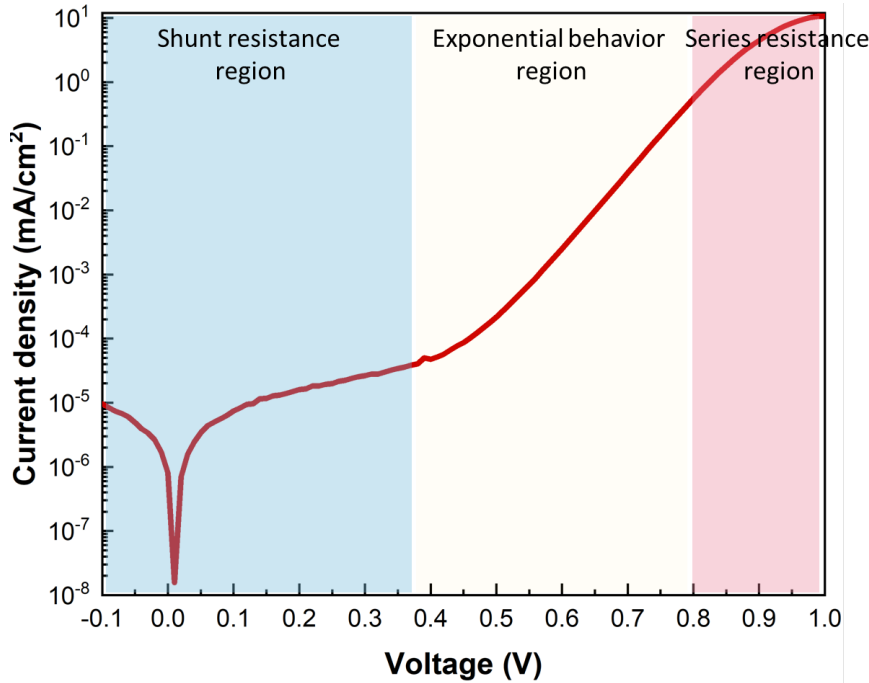


**Figure 2.4** Dark J-V curve of perovskite solar cell with three distinct regions.

## 2.3 Organic Inorganic Halide Perovskite Solar Cells

### 2.3.1 Crystal Structure of Halide Perovskite and its Properties

“Perovskite” is defined as any material with a specific crystal structure. The specific crystal structure was first found in an inorganic mineral  $\text{CaTiO}_3$  ( $\text{ABX}_3$ ) with a cubic unit cell. The compound was first discovered by Gustav Rose in 1839 and is named after L.A. Perovski, a Russian mineralogist [83], [84]. A perovskite structure can be described as a network of corner-sharing  $\text{BX}_6$  octahedra surrounding a larger A-site cation which crystallize with a general  $\text{ABX}_3$  stoichiometry (Fig. 2.5) [85]. In the lattice, A is a large atomic or molecular cation located in the center of a cube. Atom B is located at the corner of the cube, and smaller X anions occupy the edge of the cube. Silicate, including  $(\text{Mg}, \text{Fe})\text{SiO}_3$ , is the perovskite mostly seen in nature, and other perovskites such as fluoride, hydroxide, and intermetallic compounds also exist. However, the number of perovskite minerals in nature is limited, so other perovskites are synthesized with various components across the periodic table to serve a variety of objectives.

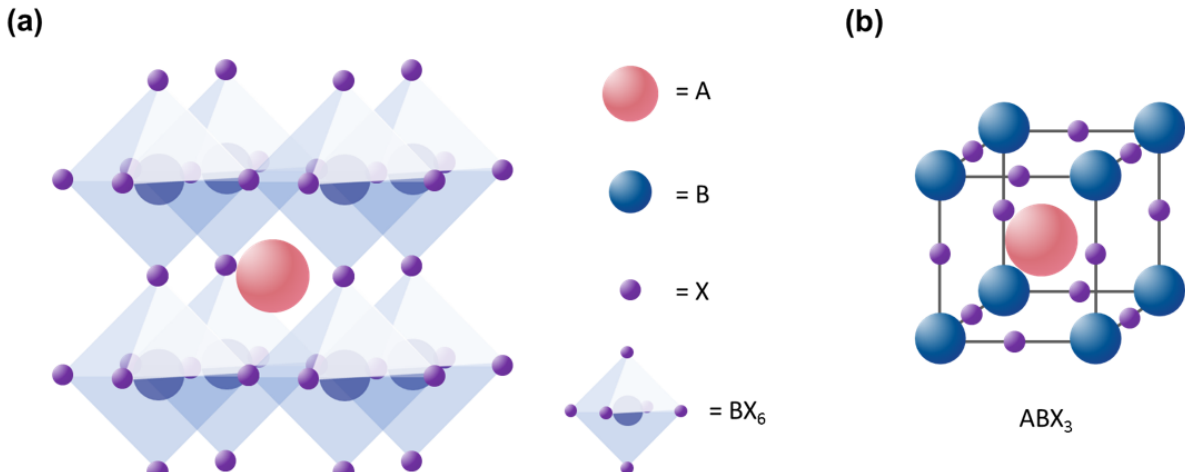


**Figure 2.5** (a) Extended crystal structure of perovskite connected by  $[BX_6]^{4-}$  octahedral. (b) Unit cell  $ABX_3$  of perovskite.

Halide perovskites used for solar cells also have the same stoichiometry as  $ABX_3$  but include halide anions. In the lattice of halide perovskites, A is the cation, including methylammonium (MA), formamidinium (FA), and butylammonium (BA), to create organic–inorganic hybrid materials. It can also be cesium (Cs) and rubidium to form all-inorganic materials. The cation B with divalent metal ions such as lead (Pb), tin (Sn), or copper (Cu) is stabilized in an octahedral site shared with six X anions which can be halides (Cl, Br, and I). All-inorganic perovskite  $CsPbI_3$  is the first reported case concerning halide perovskite semiconductors for optoelectronic devices in the late 1950's by Möller [86]. In 1978, Dieter Weber formed  $MAPbX_3$  compounds by replacing inorganic cation Cs with organic cation ( $MA^+$ ), the first three-dimensional organic-inorganic hybrid halide perovskite. Furthermore, Mitzi *et al.* demonstrated the field-effect transistors (FETs) based on organic-inorganic perovskite in the late 1990s [87]. It was the first time organic-inorganic hybrid halide perovskite with such promising properties was introduced for electronic devices.

The crystallographic stability and apparent perovskite structure can be deduced by considering a Goldschmidt tolerance factor designated as t and an octahedral factor  $\mu$  (Fig. 2.6). Here, t is defined as the ratio of distance A-X to the distance B-X in an idealized solid sphere model. TF is given by

$$t = \frac{(R_A + R_X)}{\sqrt{2}(R_B + R_X)} \quad (2.10)$$

In addition, an octahedral factor  $\mu$  is defined as

$$\mu = \frac{R_B}{R_X} \quad (2.11)$$

where  $R_A$ ,  $R_B$ , and  $R_X$  correspond to the atomic radius of A, B, and X, respectively. By varying the cation or anion in each lattice site, bandgap energy can be tuned easily.

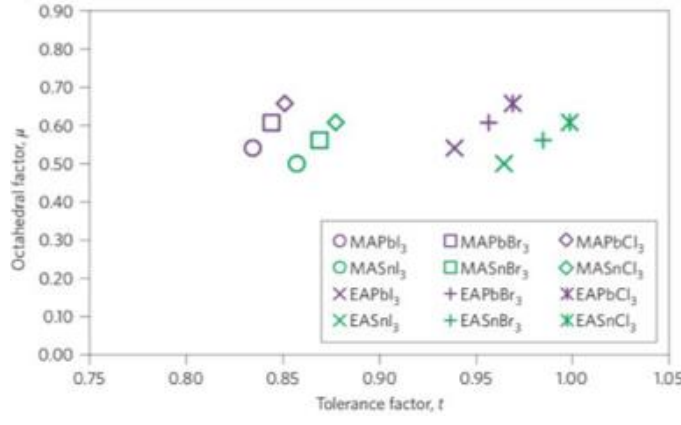


**Figure 2.6** Calculated  $t$  and  $\mu$  factors for 12 halide perovskites [84].

$\text{MAPbI}_3$  is the most representative material used for PSCs. Although its attractive properties were already known for more than 20 years, liquid-electrolyte-based dye-sensitized solar cells based on  $\text{MAPbI}_3$  were fabricated about 12 years ago, which was the first time for application of organic-inorganic hybrid halide perovskite for photovoltaics [26], [88].  $\text{MAPbI}_3$  has a direct bandgap with high absorption coefficient. In theory, the bandgap energy of  $\text{MAPbI}_3$  is around 1.7 eV, calculated by several state-of-art flavors of many-body perturbation theory [89]. However, the bandgap value obtained from optical measurement is around 1.55 eV with an absorption onset of 800 nm [90]. The energy is a fulfilling value for the Shockley-Queisser limit theory, where a single junction solar cell is required to have a bandgap of 1.1-1.5 eV under AM1.5G solar illumination (Fig. 2.7 (a)) [91]. In Fig. 2.7 (b), the absorption coefficient of perovskites is higher than those of GaAs and c-Si, which confirms that the thickness of the absorber layer can be effectively reduced to 500 nm [92]. An Urbach energy calculated from the sharp absorption onset is 15 meV which is very small and indicates that the perovskite is a semiconductor with tiny impurity and without deep trap states [93]. These above-mentioned properties of  $\text{MAPbI}_3$  contribute to the high performance of solar cells with high  $V_{\text{OC}}$  and FF.

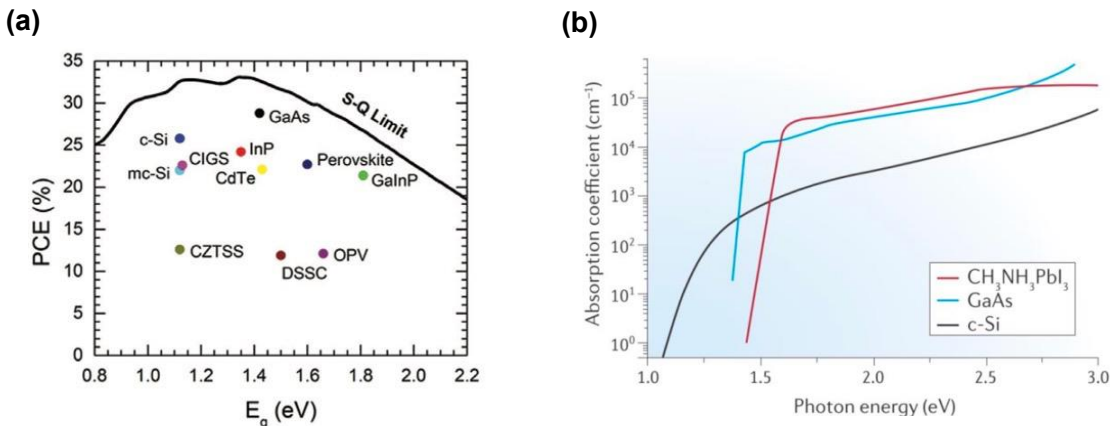


**Figure 2.7** (a) Shockley-Queisser limit (limit of maximum PCE depending on absorber materials) for a solar cell operated under AM 1.5G illumination at room temperature as a function of bandgap energy [92]. (b) Absorption coefficient spectrum of  $\text{MAPbI}_3$ , GaAs, and c-Si as a function of photon energy [93].

Carrier mobility of  $\text{MAPbI}_3$  is high because of the small effective masses of electrons and holes. The electron mobility is  $7.5 \text{ cm/V}\cdot\text{s}$  [94], and the hole mobility is  $12.5 - 6.6 \text{ cm/V}\cdot\text{s}$  [95]. Furthermore, the exciton binding energy is around  $0.03 \text{ eV}$  indicating that most of EHPs dissociate very rapidly into free carriers at room temperature [96]. The diffusion length of a single crystal of  $\text{MAPbI}_3$  is  $\sim 175 \mu\text{m}$ , which is even longer than those of other semiconductors used in photovoltaics. Therefore, the long carrier diffusion length of perovskite allows for the application of halide perovskite to a planar hetero junction with charge-selective interfaces. In the planar heterojunction, the perovskite layer is placed between a p-type and n-type layer forming a planar p-i-n or n-i-p structure.

In addition, perovskite with high crystallinity can be formed at low temperatures (below  $140^\circ\text{C}$ ) because of the low energetic barrier for crystal formation. The low-temperature thermal treatment fully ensures scalability and high throughput for the process, which reduces cost in both material and fabrication.

### 2.3.2 Architecture of Perovskite Solar Cells

In photovoltaics, halide perovskite was first applied to dye-sensitized solar cells (DSSCs) in 2009 by Miyasaka and co-workers (Fig 2.8 (a)) [26]. They replaced the dye with  $\text{MAPbI}_3$  and  $\text{MAPbBr}_3$  in the DSSCs and achieved a PCE of 3.8 % and 3.4 %, respectively, with the iodine/ triiodide redox liquid electrolyte as the hole-transport layer (HTL) material. However, the halide perovskite is unstable in the electrolytes. In 2012, Park *et al.* deposited a solid HTL instead of the liquid electrolyte and fabricated all-solid-state  $\text{MAPbI}_3$  solar cells with a PCE of 9.7% and a higher stability [97]. Lee and co-workers demonstrated that solar cells with  $\text{Al}_2\text{O}_3$  mesoporous scaffold have a similar performance to those with  $\text{TiO}_2$ , indicating that perovskite itself is an excellent electronic conductor (Fig 2.8 (b)). Furthermore, the structure got simpler with a thinner thickness than  $1 \mu\text{m}$ . Liu *et al.* achieved a PCE of 15.4% by fabricating the more straightforward planar-type device structure without any mesoporous metal oxide layer [98].

Etgar confirmed that  $\text{MAPbI}_3$  solar cells without HTL operate properly because  $\text{MAPbI}_3$  has an efficient hole conductivity [99]. Despite the property of  $\text{MAPbI}_3$ , both electron and hole transport layers contribute to charge extraction and the enhancement of the fill factor. Especially hole transport layer not only transports holes efficiently but also blocks electrons. These properties minimize interfacial charge recombination processes and enhance open-circuit voltage.

Up to now,  $\text{TiO}_2$  mesoporous layer has been used in almost reported high-efficiency devices (Fig 2.8 (c)). However, a high-temperature process is required to form  $\text{TiO}_2$  mesoporous layer. Perovskite scientific community pursues simple processes at low temperatures with cheap materials, further reducing costs by producing large areas for commercialization. The planar structure of PSCs is divided into n-i-p and p-i-n structures. In the n-i-p structure, the solar cell is illuminated from the ETL side, and ETL is deposited before perovskite deposition (Fig 2.8 (d)). On the other hand, illumination occurs from the HTL side, and HTL is firstly formed before the deposition of halide perovskite in the p-i-n structure (Fig 2.8 (e)).

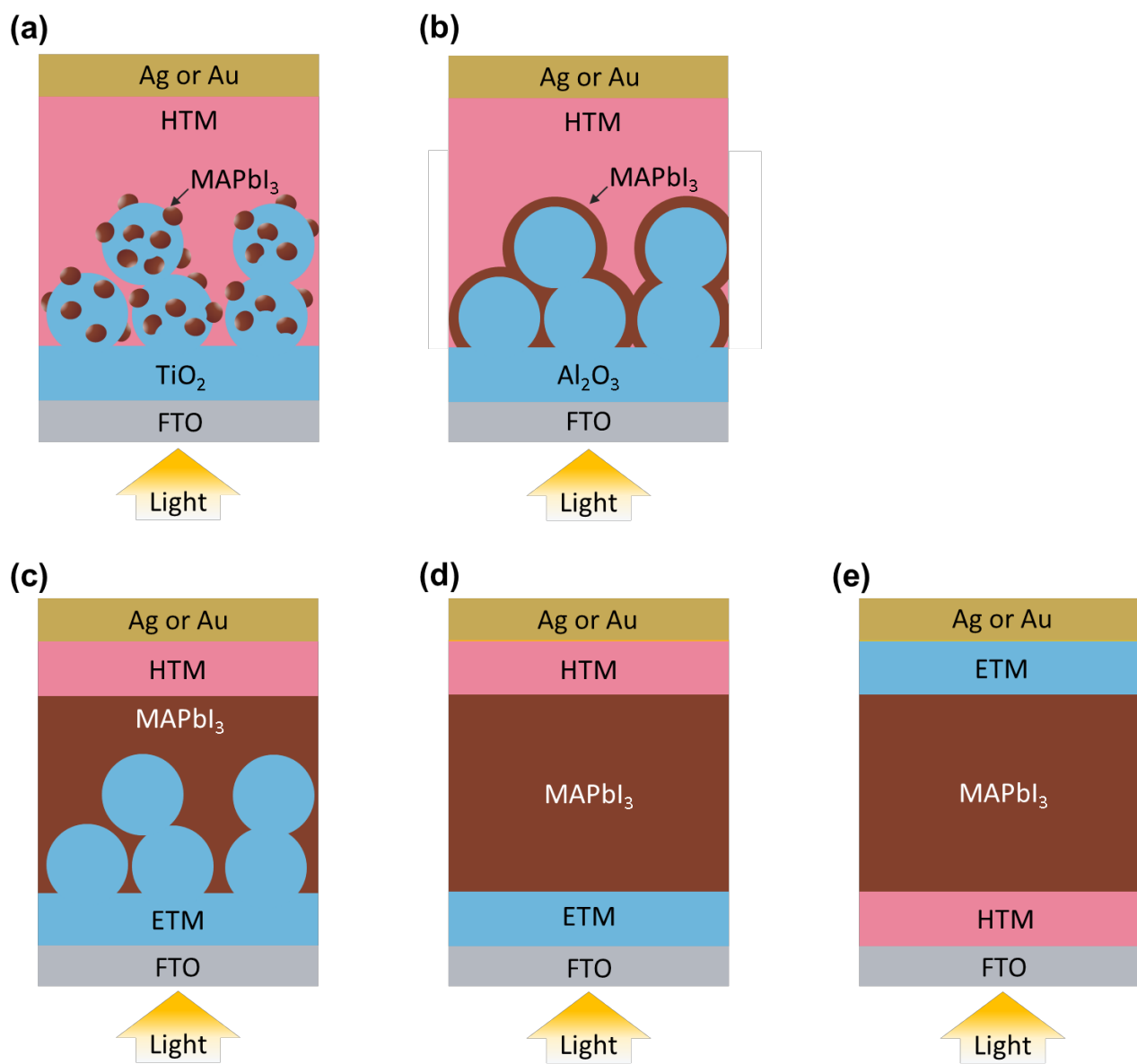


**Figure 2.8** Evolution of PSC structure. (a) Sensitization solar cells. (b) Meso-super structure with scaffold  $\text{Al}_2\text{O}_3$ . (c) Conventional n-i-p structure with mesoporous ETL. (d) Conventional n-i-p planar structure. (e) Inverted p-i-n planar structure.

In the n-i-p planar structure,  $\text{TiO}_2$  and spiro-MeOTAD are generally used for the bottom electron

transport layer and top hole transport layer, respectively [100]. However, the electron mobility of TiO<sub>2</sub> (0.1-4 cm<sup>2</sup>/Vs) [101] is low compared with those in halide perovskite (10-100 cm<sup>2</sup>/Vs) [102]. In addition, TiO<sub>2</sub> is vulnerable to ultraviolet which causes degradation of the perovskite [103]. Therefore, hysteresis in J-V characteristics occurs in the PSCs with TiO<sub>2</sub>. Hence, other electron transport materials with higher electron mobility and stability for n-i-p PSCs have been investigated. Hwang et al. spin-coated a film of ZnO nanoparticles for ETL and achieved a PCE of 15.7 % [104]. The electron mobility of ZnO is orders of magnitude higher than that of TiO<sub>2</sub>. Ke and coworkers also applied nanocrystalline SnO<sub>2</sub> for ETL through spin-coating, and the PCE of the solar cell is 16.0 % [105]. SnO<sub>2</sub> is stable, and it has a deeper conduction band which enables injecting electrons efficiently and reducing the Schottky barrier at the interface between FTO and SnO<sub>2</sub> with higher V<sub>OC</sub>. In addition to ZnO and SnO<sub>2</sub>, other metal oxides, including WO<sub>x</sub> and In<sub>2</sub>O<sub>3</sub> [106] or Metal sulfide [107], have been investigated to enhance the photovoltaic performance.

In the p-i-n structure called inverted planar structure in PSCs, ETL is deposited on the perovskite layer. In the structure, ETL materials used in the n-i-p structure cannot be applied in the p-i-n structure because the heat of the thermal treatment could damage the organic cation on the A site of organic-inorganic hybrid perovskites. Therefore, the first p-i-n structure, called the inverted planar structure in PSCs followed the structure of the organic solar cells. Poly(3,4-ethylenedioxythiophene) polystyrene sulfonate (PEDOT:PSS) and fullerene (C<sub>60</sub>) are used as the hole transport layer and electron transport layer, respectively. In addition, to prevent holes from transporting in ETL, bathocuproine (BCP) was deposited on ETL. Using this structure, Jeng *et al.* achieved a PCE of 3.9 % [108].

In addition to C<sub>60</sub>, fullerene derivative [6,6]-phenyl-C<sub>61</sub>-butyric acid methyl ester (PCBM) is also commonly used ETL material because of its appropriate mobility and availability of solution process. Through crystal engineering of halide perovskite and interface engineering, a PCE of 18.2 % was achieved in 2015 [109]. PEDOT:PSS is a typical hole transport material in the inverted structure. However, a high energy barrier between PEDOT:PSS and perovskite exists, and PEDOT:PSS in solution has high acidity. Hence, other researchers have tried to deposit hole transport material with higher mobility and stability. In 2019, Zhao et al. reported the inverted planar structure of PSCs with Poly[bis(4-phenyl)(2,5,6-trimethylphenyl)]amine (PTAA) as the hole transport layer and PCBM as the electron transport layer [110]. They achieved 18.11 % of PCE and 1.10 V of V<sub>OC</sub> with the structure. Many researchers have also used inorganic hole transport materials to improve stability. Yu and co-workers first applied Cu<sub>2</sub>O film to an inverted PSC and achieved 11 % of PCE [111]. Furthermore, Rao et al. enhanced the PCE of the solar cells to 19 % through morphology control of the perovskite film [112]. Improvement of morphology increases hole mobility and reduces intrinsic defects. NiO

has been used for HTL because it has a deep valence band and high chemical stability. In 2017, Xie et al. fabricated the PSCs with FTO/NiO/FAMAPbIxCl<sub>3-x</sub>/PCBM/TiO<sub>x</sub>/Ag. In FAMAPbIxCl<sub>3-x</sub>, methylammonium chloride (MACl) helps halide perovskite film recrystallize vertically. With the HTL and the perovskite, they achieved 20.65 % of the PCE [113].

### 2.3.3 Ion Migration

Not only charged electron and hole carriers but also charged ions in organic-inorganic halide perovskite are mobile under various environments, including applied electric field and illumination. The ion migration has received attention as one possible origin of the J-V hysteresis in halide PSCs [56], [114]. In addition, giant dielectric constant [115] at low frequency or light-induced self-poling effect (LISP) are caused by ion migration [116]. It is essential to understand ion migration in the lattice of halide perovskite for an in-depth understanding of the physical phenomena in PSCs. In solid-state materials, the activation energy ( $E_A$ ) is the most important factor determining ion migration. The migration rate ( $r_m$ ) is exponentially proportional to the activation energy, as shown below

$$r_m \propto e^{(-\frac{E_A}{k_B T})} \quad (2.12)$$

where  $K_B$  and  $T$  are the Boltzmann constant and temperature, respectively.

The concentration of mobile ions ( $N_i$ ) is mediated by temperature-independent defects and temperature-dependent defects. Temperature-independent defect includes extrinsic defects of impurities or nonstoichiometric compound. Temperature-dependent defects indicate thermal-excited point defect formation energy of  $E_D$ , which indicates intrinsic defects (e.g., Schottky defects). Hence, the conductivity of mobile ions caused by intrinsic defects can be expressed as

$$\sigma_i \propto e^{(-\frac{E_A}{k_B T})} e^{(-\frac{E_D}{2k_B T})} \quad (2.13)$$

The conductivity of extrinsic case can be described as

$$\sigma_i \propto e^{(-\frac{E_A}{k_B T})} \quad (2.14)$$

Here, the value of  $E_A$  and  $E_A+E_D/2$  can be obtained from the slope of the conductance, which scales logarithmically with  $T^{-1}$  (Fig. 2.9) [117]. The ions with the lowest  $E_A$  can easily migrate in the crystal with various ions. The value of the activation energy can be determined by several factors, including

crystal structure, ion radius, and the valence state of the ions.

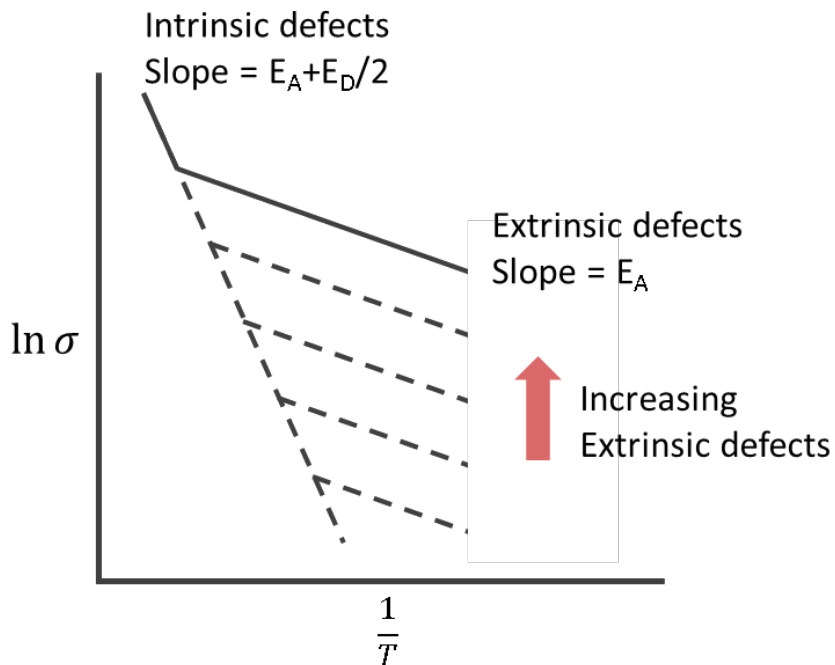


**Figure 2.9**  $\ln\sigma$ - $1/T$  curves for ion conduction where  $E_A$  is the activation energy for ion migration and  $E_D$  is formation energy for point defects.

The crystal structure impacts the distance between the nearest neighbor ions and the connection of the ion migration path, which affects  $E_A$  for ion migration. For instance, the migration path of  $O^{2-}$  ions in  $ABO_3$  perovskite oxide structure such as  $La_{1-x}Sr_xBO_{3-\delta}$  (B can be Mg, Ga, Co, or Fe) is along the O-O edge of the  $BO_{3-\delta}$  octahedron ( $a/\sqrt{2}$ ). In another case, the ion migration path of cubic perovskite structures such as the  $La_{1-x}Sr_xBO_{3-\delta}$  family is a three-dimensional network [118]. In contrast, the migration path of the tetragonal perovskite structure, including  $La_{0.64}Ti_{0.92}Nb_{0.08}O_{2.99}$  is a two-dimensional network. The ionic radius is another factor that determines the  $E_A$ . As the ionic radius is smaller, it usually is easier for ions to move. For example, cations such as  $H^+$ ,  $Li^+$ ,  $Cu^+$ , and  $Ag^+$  are mobile, but mobile anions are limited (e.g.,  $O^{2-}$  and  $F^-$ ). Moreover,  $E_A$  is affected by the valence state of the ion. Highly charged ions are confined in the crystal lattice because of their strong Coulombic attraction with their adjacent ions with opposite charges. For instance, a cation with a valence of more than two (e.g.,  $Ga^{3+}$  and  $Co^{3+}$ ) has difficulty migrating despite a small ionic radius.

In  $MAPbI_3$  perovskite,  $MA^+$ ,  $Pb^{2+}$ ,  $I^-$  ions, and other hydrogen-related defects such as  $H^+$ ,  $H^0$ , and  $H^-$  can be mobile ion candidates. The radius of  $I^-$  ions is 206 pm which is comparatively large. However, iodine migration in halide perovskite has been frequently observed [119]. The distance between  $I^-$  ions in the edge of the  $PbI_6$  octahedron and their closest neighbor is 4.46 Å which is longer than  $MA^+$  and  $Pb^{2+}$  ions. As noted earlier, the shortest distance between  $I^-$  ions and their neighbors contributes to the low activation energy, and  $I^-$  ions are the most easily mobile in  $MAPbI_3$  [120]. Eames et al.

explained the migration pathways of  $\text{I}^-$ ,  $\text{Pb}^{2+}$ , and  $\text{MA}^+$  ions in  $\text{MAPbI}_3$  and theoretically calculated their activation energies for the migration of each ion [120]. In  $\text{MAPbI}_3$  structure,  $\text{I}^-$  ions migrate along the I-I edge of the  $\text{PbI}_6$  octahedron, as shown in Fig. 2.10 (a), and the activation energy of iodine in bulk  $\text{MAPbI}_3$  is theoretically 0.58 eV. In the case of  $\text{MA}^+$  ions, it moves through the unit cell face consisting of  $\text{I}^-$  ions (Fig. 2.10 (b) path D), and it has a higher activation energy of 0.84 eV.  $\text{Pb}^{2+}$  ions with the activation energy of 2.31 eV migrate in a diagonal direction of the cubic unit cell (Fig. 2.10 (b) path B).

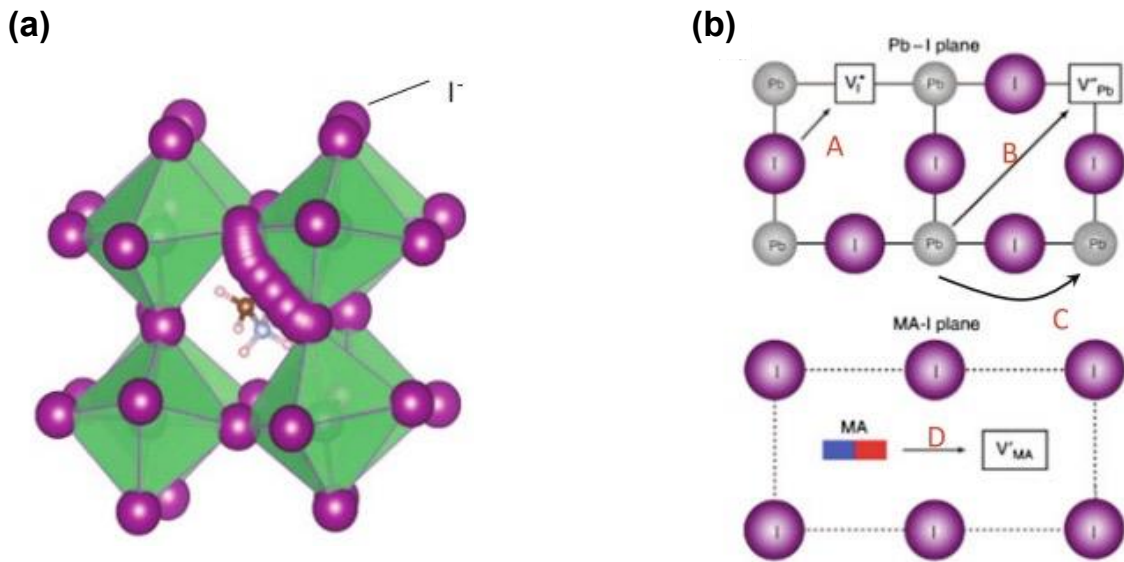


**Figure 2.10** Illustration of (a) migration path of  $\text{I}^-$  Ion in the unit cell of  $\text{MAPbI}_3$  and (b) migration path for the vacancy of iodine (path A), lead (path B or C) in the  $\text{Pb}-\text{I}$  plane, and methylammonium (path D) in  $\text{MA}-\text{I}$  plane [120].

$\text{MA}^+$  ions as well as  $\text{I}^-$  ions are supposed to be movable, which has been proved by several experimental measurements. Yuan and his co-workers applied electrical bias to  $\text{MAPbI}_3$  solar cells with lateral structure and investigated the concentration of  $\text{MA}^+$  ions through photothermal induced resonance (PTIR) microscopy. They observed the migration of  $\text{MA}^+$  ions on the anode and the center part into the cathode (Fig. 2.11) [121].

Hydrogenic impurities including  $\text{H}^+$ ,  $\text{H}^0$ , and  $\text{H}^-$  are also required to be considered carefully. They can be generated by the absorption of moisture during the fabrication process or by the decomposition of perovskite. We can confirm that the electrons are captured or lost by hydrogen-related defects through density functional theory (DFT) calculations [57].  $\text{H}^+$  can migrate along the I-I path, and the activation energy is 0.17-0.29 eV, suggesting that mobile hydrogenic impurities are easily formed in  $\text{MAPbI}_3$  film.

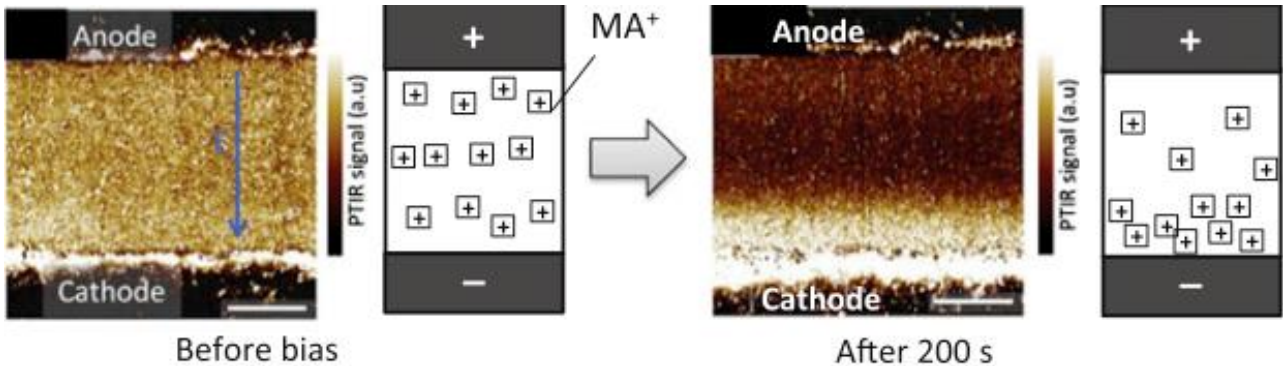


**Figure 2.11** PTIR images and their schematics of the distribution of  $\text{MA}^+$  ions before and after electrical biasing with the electric field of  $1.6 \text{ V}/\mu\text{m}$  for 200 s, respectively [121].

Based on these properties of ions in  $\text{MAPbI}_3$ , ion migration caused by the electric field is closely related to the presence of defects. The defects in halide perovskite can be point defects in a bulk crystal, lattice distortion, or grain boundary in polycrystalline perovskite film. They are generated for various reasons. The first reason is nonideal stoichiometry in perovskite film. Yu et al. investigated a degree of ion migration according to the stoichiometric ratio [122]. As  $\text{PbI}_2$  concentration increases, ion migration increases, meaning that MA vacancies act as a pathway for ion migration. Secondly, halide perovskites are easily decomposed because they are soft materials whose defects have low formation energy. Buin *et al.* suggested the energy of 0.1 eV is required for  $\text{MAPbI}_3$  to be decomposed into MAI and  $\text{PbI}_2$ , which is small [123]. In addition, Walsh et al. calculated the formation energy of Schottky defects in  $\text{MAPbI}_3$  [124]. The Schottky defect is a point defect caused by oppositely charged ion vacancy formed in its sites. The energy is higher than 0, which is coherent with the decomposition energy. Furthermore, a grain boundary in polycrystalline perovskite contributes to ion migration (Fig. 2.12). Xiao et al. confirmed that solar cells with large grains were more stable than those with smaller grains. The density of vacancies at grain boundaries is higher compared to the grains because of defect segregation, dangling bond, and lattice dislocation [125]. Moreover, point defects in grain occur a lot because of grain disorientation, inhomogeneous bonding, or tensile strain.

Ion migration in halide PSCs causes carrier localization leading to J-V hysteresis. Furthermore, the ion migration brings about a change in the chemical and physical properties of perovskite film under operating conditions that affect the stability of the solar cells. Snaith and his co-workers suggested that positive and negative charged ions in  $\text{MAPbI}_3$  are accumulated at the interfaces near the electron and hole transport layer under forward electric bias, respectively, [126]. In addition, they calculated the activation energy for the diffusion of each ion in  $\text{MAPbI}_3$  based on hysteretic change according to temperature. They concluded that  $\text{I}^-$  has the lowest activation energy and highest mobility [127]. Meanwhile, the migration properties in halide perovskite can deteriorate the device performance by forming a charge trap. For example, Hoke *et al.* confirmed that the XRD peak of  $\text{MAPbBr}_{x}\text{I}_{3-x}$  is

divided into two peaks under illumination by forming I-enriched and Br-enriched perovskite regions with different lattice constants [128]. The bandgap of the I-enriched region is smaller than that of the Br-enriched region, which serves as a charge trap. The light-induced charge trap leads to poor Voc and PCE in the  $\text{MAPbBr}_x\text{I}_{3-x}$  solar cells.

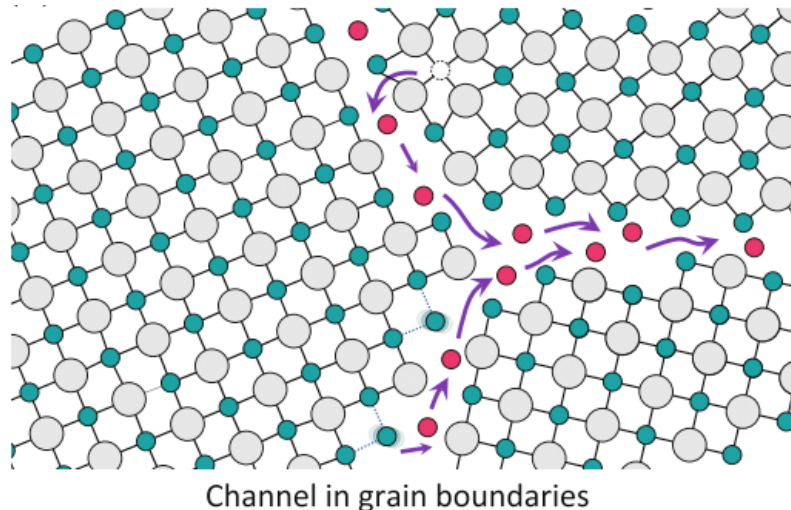


**Figure 2.12** Illustration of the ion migration channels comprising of wrong bonds and open spaces at grain boundaries [117].

## 2.4 Characterization of Perovskite Solar Cells using Impedance Spectroscopy

### 2.4.1 Dielectric Properties and Charge Dynamics

Dielectrics do not have free charges for conduction. However, they show conductive properties under an electric field. When a dielectric material is placed in an electric field, the positive charges are arranged in the direction of the electric field, and negative charges are arranged in the opposite direction, which is called polarization and causes the conductive properties. Polarization is generally classified into ionic, interfacial, dipolar, atomic, and electronic polarization [129].

In the case of ionic, interfacial, and dipolar polarization, dipoles try to align in the direction of the electric field, and the alignment changes when the direction of the field is reversed. The time the charges following the changing field take is called the relaxation time. Therefore, when the frequency changes, the time for the alignment of charges decreases, and the alignment fails to keep up. The

frequency is called relaxation frequency [130].

If we consider an electric field (E)

$$E = E_{max} \sin \omega t \quad (2.15)$$

With the electric field, the polarization field is given by Eq.2.16.

$$P = P_{max} \sin(\omega t - \varphi) \quad (2.16)$$

where  $E_{max}$  and  $P_{max}$  are constant, and  $\varphi$  is the phase difference between E and P vectors.

The polarization current is formulated as Eq. 2.17

$$\frac{\partial P}{\partial t} = \omega P_{max} \cos(\omega t - \varphi) \quad (2.17)$$

and the average power is written by Eq. 2.18.

$$P_{av} = \frac{1}{2} E_{max} P_{max} \omega \sin \varphi \quad (2.18)$$

If the phase difference is zero, no power is dissipated in the dielectric, and energy is stored like in a capacitor. When loss of electromagnetic energy in dielectrics due to conduction and polarization of charges in dielectrics is considered, permittivity obtains the complex form of  $\varepsilon^*$  depending on frequency and relaxation time ( $\tau$ ).

$$\varepsilon^* = \varepsilon' - i\varepsilon'' = \varepsilon_\infty + \frac{\varepsilon_s - \varepsilon_\infty}{1 + i\omega\tau} \quad (2.19)$$

where  $\varepsilon'$  is the real part of permittivity, and  $\varepsilon''$  is the loss factor ascribed to polarization losses.  $\varepsilon_s$  and  $\varepsilon_\infty$  are dielectric constants at low and at very high frequencies, respectively. Each real and imaginary part of permittivity is given by Eq. 2.20 and Eq. 2.21.

$$\varepsilon' = \varepsilon_\infty + \frac{\varepsilon_s - \varepsilon_\infty}{1 + \omega^2\tau^2} \quad (2.20)$$

$$\varepsilon'' = \frac{(\varepsilon_s - \varepsilon_\infty)\omega\tau}{1 + \omega^2\tau^2} \quad (2.21)$$

In Eq. 2.18, only one type of polarization mechanism is considered. Each polarization mechanism generally has its own relaxation time, and Eq. 2.22 considers it.

$$\varepsilon^* = \varepsilon_\infty + \frac{\varepsilon_s - \varepsilon_\infty}{1 + i\omega\tau_i} + \frac{\varepsilon_s - \varepsilon_\infty}{1 + i\omega\tau_{MW}} + \frac{\varepsilon_s - \varepsilon_\infty}{1 + i\omega\tau_d} + \frac{\varepsilon_s - \varepsilon_\infty}{1 + i\omega\tau_a} + \frac{\varepsilon_s - \varepsilon_\infty}{1 + i\omega\tau_e} \quad (2.22)$$

where  $\tau_i$ ,  $\tau_{MW}$ ,  $\tau_d$ ,  $\tau_i$ , and  $\tau_i$  are the relaxation times of ionic, interfacial, dipolar, atomic, and electronic polarizations, respectively. The inverse of relaxation time is relaxation frequency, shown in Fig. 2.13 (a) and Eq. 2.23.

$$f_r = \frac{1}{\tau'} \quad (2.23)$$

In Fig. 2.13 (a), the frequency is seen as a fall in the real part of permittivity ( $\epsilon'$ ) and a peak in the imaginary part of permittivity ( $\epsilon''$ ). The other cases, including atomic and electronic polarization, have different dynamics of mechanisms. In the two polarizations, the electric field changes the distance between the charges and a restoring force act. The frequency when the behavior of a resonator occurs is called resonance frequency.

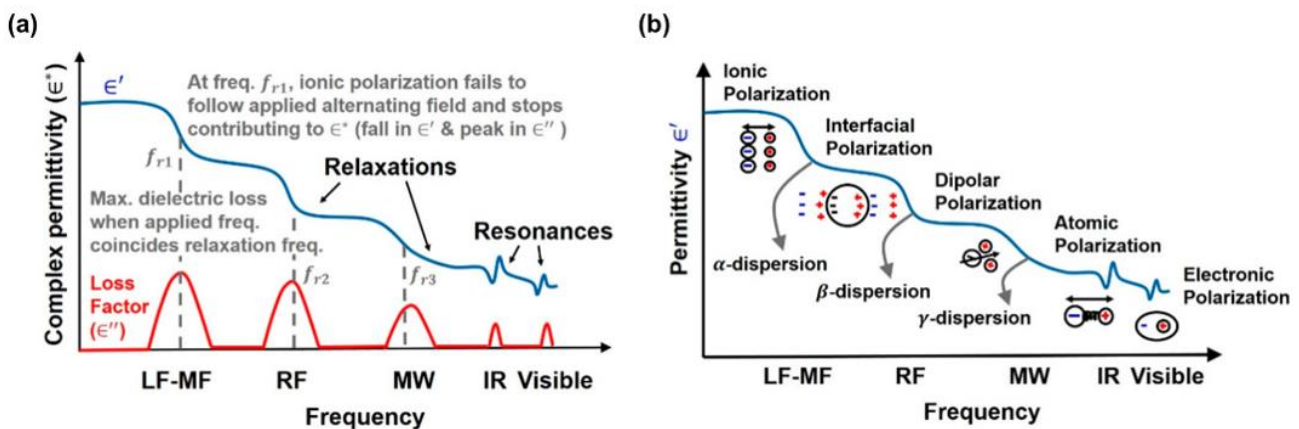


**Figure 2.13** (a) Real and imaginary part of permittivity as a function of frequency. (b) Polarization and relaxation processes observed under an alternating electric field [131].

Fig. 2.13 (b) shows a frequency-dependent permittivity spectrum with a relaxation process in dielectrics. At a very high frequency, changes in permittivity caused by electronic transition can be analyzed using transient optical spectroscopy. lattice polarization and dipolar rearrangement are studied with dielectric spectroscopy at a lower frequency ( $10^9$  Hz). At a very low frequency ( $10^{-2}$  Hz~), electronic and ionic conduction can be observed with electrical spectroscopy. The frequency-dependent permittivity spectra in semiconductors and electrochemical cells reflect processes including electrical and ionic transport and dipole alignment.

## 2.4.2 Impedance Spectroscopy

Immittance spectroscopy is a kind of technique such as impedance, admittance, capacitance, and dielectric spectroscopies. It is used to probe the permittivity and investigate the physical and chemical

properties of devices, interfaces, and materials. During an immittance measurement, the response of a sample to a time-varying electric field is measured. In addition, the fraction of electrical energy stored versus those dissipated by the sample and the relaxation time scale can be measured as a function of frequency. In immittance spectroscopy, the input signal is a small alternating voltage ( $V_{AC}$ ). During the small input signal measurement, the sample is perturbed but not irreversibly changed. Through the immittance spectroscopy, the relaxation processes, including lattice distortions, electrode polarization, dipole rearrangement, and electrical and ionic conduction, are sequentially probed by varying the frequency of  $V_{AC}$ .

In various measurements of the immittance spectroscopy, impedance spectroscopy (IS) is used to study the resistive and capacitive properties of solid-state devices and electrochemical cells. In IS, an alternating voltage  $V_{AC}$  is applied to a sample, and the current response  $I_{AC}$  is measured. In Fig. 2.14 (a),  $V_{AC}$  and  $I_{AC}$  are sinusoidal functions written by

$$V(t) = V_0 \sin(\omega t) = V_0 e^{i\omega t} \quad (2.24)$$

$$I(t) = I_0 \sin(\omega t + \varphi) = I_0 e^{i(\omega t + \varphi)} \quad (2.25)$$

where  $V_0$  and  $I_0$  are the amplitude of the voltage and current, and  $\varphi$  is a phase difference between  $V(t)$  and  $I(t)$ . With  $V(t)$  and  $I(t)$ , the impedance  $Z(t)$  is expressed as

$$Z(t) = \frac{V(t)}{I(t)} = Z_0 e^{-i\varphi} \quad (2.26)$$

where  $Z_0 = \frac{V_0}{I_0}$ .

The function of impedance  $Z$  relates the output current  $I_{AC}$  of the sample to the input voltage ( $V_{AC}$ ) as a function of frequency, indicating that  $Z$  is the transfer function. The impedance is a complex time-dependent equation.

Representation of dielectric function as a function of frequency (Fig. 2.14 (b)) has many advantages compared with the more intuitive time domain. All the information obtained in Fig. 2.14 (a) can be summarized into two quantities, including the magnitude of  $Z_0$  and the phase angle of  $\varphi$ . Change in the frequency of the  $V_{AC}$  results in a spectrum of  $Z$  as a function of frequency. In the complex domain,  $Z$  is given by

$$Z = Z' - iZ'' \quad (2.27)$$

where  $Z'$  is the real component of the impedance ( $\varphi=0$ ), and  $Z''$  is the imaginary component of  $Z$  ( $\varphi$

$= 90^\circ$ ). The magnitude of  $Z$  is written by  $Z = \sqrt{Z'^2 + Z''^2}$ . Physically,  $Z'$  is the resistance  $R$ , defined by Ohm's law, and it describes the resistance of a sample to current flow. On the other hand,  $Z''$  is the reactance that describes the resistance of the sample to changes in current flow.

$$Z' = Z_0 \cos(-\varphi) = Z_0 \cos(\varphi) \quad (2.28)$$

$$Z'' = Z_0 \sin(-\varphi) = -Z_0 \sin(\varphi) \quad (2.29)$$

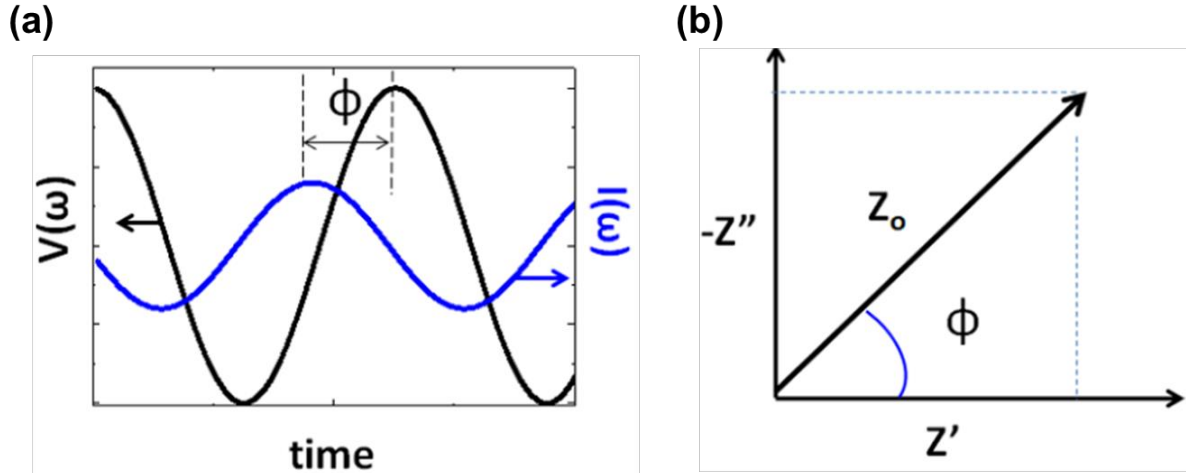


**Figure 2.14** (a) The input voltage and output voltage as a function of time, (b) complex impedance  $Z$  with  $Z_0 = \frac{V_0}{I_0}$  and phase angle of  $\varphi$  in the frequency domain.

The impedance can be expressed with ideal electrical circuit elements described in Table 2.1. The impedance of a resistor is the real part ( $\varphi = 0^\circ$ ) and is frequency-independent. The impedance of a capacitor that stores energy in an electric field is purely imaginary ( $\varphi = 90^\circ$ ), and it is in reverse proportion to the frequency. On the other hand, an impedance of the inductance, which stores energy in a magnetic field ( $\varphi = 90^\circ$ ), is proportional to frequency.

**Table 2.1** Circuit elements of the impedance of resistor, capacitor, and inductor.

Element	Unit	Symbol	Impedance
Resistor	$\Omega$	—~~~~—	$Z_R = R$
Capacitor	F	—  —	$Z_C = \frac{1}{i\omega C}$
Inductor	H	—~~~~—	$Z_L = i\omega L$

The equivalent circuit modeling with these circuit elements is used to analyze the impedance data from solar cells. Ideal relaxation in a device can be modeled in an RC circuit, which consists of resistance and capacitor in parallel. In Kirchhoff's current law

$$0 = I_R + I_C = \frac{V}{R} + C \frac{dV}{dt} \quad (2.30)$$

The solution of the equation is given by

$$V(t) = V_0 e^{-\frac{t}{RC}} \quad (2.31)$$

where  $V_0$  is the voltage at  $t = 0$ . The time  $t = RC$  is the characteristic time constant of the RC circuit and means the charging/discharging time of the capacitor in the ideal circuit. The time scale of the dielectric relaxation determines the time constant of the RC element in the dielectrics.

The impedance of the RC circuit is written by

$$Z_{RC} = \frac{R}{1+i\omega RC} \quad (2.32)$$

In the low-frequency limit,  $Z_{RC} \approx R$ . On the contrary,  $Z_{RC} \approx \frac{1}{i\omega RC} = Z_C$  in the high-frequency limit.

Fig. 2.15 (a) presents the impedance spectrum of an RC element. This spectrum in the shape of a semicircle in the complex domain is generally called Nyquist plot. Nyquist plot is generally used when equivalent circuit modeling is used to analyze data. In the Nyquist plot, the frequency increases toward the origin of the graph. The spectrum can be expressed by Eq. 2.32 with regard to the real and imaginary components in Eq. 2.27. The maximum of the semicircular spectrum is given at the peak frequency  $\omega_p = 2\pi f_p$  with  $\omega_p \tau = 1$ , where  $\tau$  is the RC time constant and the relaxation times. When individual relaxation time scales exist, the number of semicircles in the Nyquist plot indicates the number of relaxation processes in the spectrum. If the relaxation time scales are similar, the semicircles are overlapped, and they must be distinguished by modeling to achieve distinct relaxation processes.

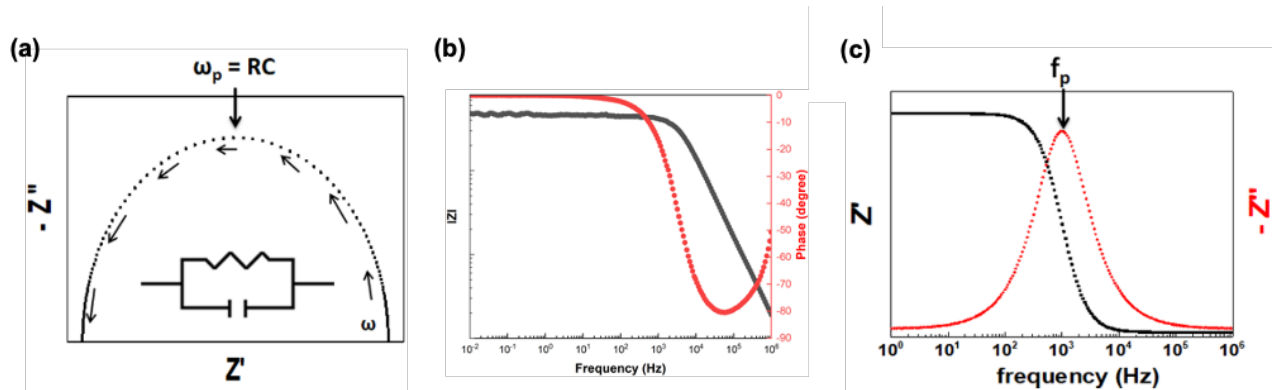


**Figure 2.15** (a) Nyquist plot. (b) Bode impedance-phase plot. (c) Bode  $Z'$ - $Z''$  plot of an R-C circuit.

Fig. 2.15 (b) and (c) show the Bode impedance-phase plot and the  $Z'$ - $Z''$  Bode plot, respectively. The Bode impedance-phase plot (Fig. 2.15 (b)) is used to identify circuit elements in the device. On the other hand, the Bode  $Z'$ - $Z''$  plot is applied to study the dielectric parameters affected by frequency (Fig. 2.15 (c)). In Fig. 2.15 (c), the frequency where the peak of  $-Z''$  exists corresponds to peak

frequency  $f_p$ . The RC circuit with a single time constant  $\tau$  is a fundamental unit for modeling the impedance data from physical samples. However, in real samples. However, relaxations with a distribution of time constants are shown in real samples.

In the case of the semi-infinite diffusion of particles, including ions, the impedance response at low frequency cannot be described with a simple RC element. The Warburg impedance  $Z_W$  is written by [132]

$$Z_W = \frac{A_W}{\sqrt{\omega}} - i \frac{A_W}{\sqrt{\omega}} \quad (2.33)$$

where  $A_W$  is the Warburg coefficient and is related to the AC diffusion coefficient of the particles. In Nyquist plot, the Warburg element is characterized by a linear Z value increase at low frequencies with  $\varphi = 45^\circ$ .

The constant phase element CPE is a generalization of the Warburg element, and the impedance of the CPE is expressed as

$$Z_{PCE} = \frac{1}{Q(i\omega)^n} \quad (2.34)$$

where n is a dispersion parameter that determines the physical meaning of  $Q$ . When n equals to 1, the CPE reduces to an ideal capacitor, and  $Q = C$ . If n = 0, the CPE gets to be a real resistor with  $Q = \frac{1}{R}$ .

When n is 0.5, the CPE reduces to a Warburg element with  $Q = \frac{1}{A_W}$ . The Warburg element is often used to explain relaxation processes with time-dependent processes. For example, the ideal capacitor with charge transfer at a nonhomogeneous electrode surface or carrier transport in amorphous semiconductors is substituted by a CPE element with  $Q = C$  and n > 0.5 in the circuit [133]. When  $0.5 < n < 1$ , the dispersed or distorted semicircle is shown in the Nyquist plot.

### 2.4.3 Ionic Conductivity of Halide Perovskites: Low Frequency Dielectric Response of Perovskite

As mentioned in chapter 2.2.3, ion migration occurs in the halide perovskite under operation conditions with an electric field and illumination. The ion migration is applied for the realization of devices, including memristors or batteries [134]–[136]. However, ion migration is associated with efficiency losses and degradation during operation [137]. Therefore, many efforts have been made to

prevent the negative effects caused by ion migration. It is important to understand the physical parameters, especially the conductivity of halide perovskite, to solve the problems caused by ion migration. Mizusaki *et al.* revealed that halide perovskites feature mixed ionic-electronic conductivities because not only electrons and holes but also ions migrate in PSCs. Ionic conductivity is influenced by stoichiometry, grain orientation, processing conditions, additives, or changing the dimensionality [138]. For example, iodide ion migration in  $\text{MAPbI}_3$  can account for a large fraction of the total electrical conductivity both in the dark and under an illumination [139]. Several researchers have observed halide conductivities in addition to the conductivity in  $\text{MAPbI}_3$  [140]. Yamada *et al.* also measured the conductivity in Ge- and Sn-based perovskite such as  $\text{MAGeCl}_3$ ,  $\text{CsSnI}_3$ , and  $\text{MASnI}_3$  [141], [142]. In addition, vacancy-mediated halide conductivity is observed at high temperatures ( $T > 573$  K) in all-inorganic perovskites, including  $\text{CsPbCl}_3$  and  $\text{CsPbBr}_3$  [119].

In chapter 2.2.3, ionic conductivity is explained with intrinsic and extrinsic defects (Eq. 2.13 and Eq. 2.14). The ionic conductivity can also be expressed by Eq. 2.35.

$$\sigma_i = q n_i \mu_i \quad (2.35)$$

where  $n_i$  is the concentration of ions and  $\mu_i$  is the mobility of mobile ions.

Based on the Einstein relation, mobility is written as the following Eq. 2.36.

$$\mu_i = \frac{q}{k_B T} D_i \quad (2.36)$$

where  $k_B$  is the Boltzmann constant and  $D_i$  is the ionic diffusion coefficient. In halide perovskites, the halide ions are the most mobile ion, and the migration happens through hopping between neighboring sites [120]. The ionic diffusion coefficient is given by an Arrhenius relationship defined in Eq. 2.37.

$$D = \frac{v_0 d^2}{6} \exp\left(-\frac{\Delta G}{k_B T}\right) = D_0 \exp\left(-\frac{E_A}{k_B T}\right) \quad (2.37)$$

where  $v_0$  is the attempt frequency of an ionic jump,  $d$  is the jump distance, and  $\Delta G$  is the Gibbs free energy during the jump of a mobile ion [143]. The diffusion coefficient represents the probability of an ion overcoming the energy barrier. Furthermore, the diffusion coefficient can be expressed with a temperature-independent perfector  $D_0$ , and the activation energy  $E_A$  affected by the temperature [144]. In the halide perovskites, the measured diffusion coefficient of halide ions ranges of around  $10^{-12}$   $\text{cm}^2/\text{s}$  [145]. On the other hand, the diffusion coefficient of  $\text{MA}^+$  ions is in the range of  $\sim 10^{-13}$   $\text{cm}^2/\text{s}$  [121], [146]. In Eq. 2.35, we can understand that ionic mobility is proportional to the diffusion coefficient. Therefore, halide ions are more mobile species than other ions in halide perovskites. In

addition, it is confirmed that it takes a few to hundreds of ms for halide ions to migrate, which restricts many measurement techniques from detecting ion migration [147].

As seen in Eq. 2.33, the ionic conductivity is affected by not only the mobility of ions but also the concentration of ions. However, the range of ionic conductivity reported in previous studies is wide (the value ranges from  $10^{-6}$  to  $10^{-9} \Omega \cdot \text{cm}$  [140]). IS has been used to quantify both the diffusion coefficient and the density of the mobile ions [148]. The ionic conduction is reported at a low frequency. For example, Sang-wan et al. observed a current fluctuation of  $\text{MAPbI}_3$  between the hole transport layer and electron transport layer in the low-frequency region. Based on the properties, the slow dynamics of ions observed at low frequency can be differentiated from the electronic conduction at high frequency by IS.

## 2.5 Characterization of Perovskite using Scanning Transmission X-ray Microspectroscopy

### 2.5.1 Principle of Synchrotron Radiation

Synchrotron radiation is the strong electromagnetic radiation emitted when relativistic charged particles with high energy and a speed close to those of light travel in curved paths (Fig 2.16 (a)). Because of relativistic particles, synchrotron radiation is emitted tangentially from the particle orbit and within a highly collimated angle equal to  $1/(1-(v/c)^2)^{-0.5}$ . The collimated angle is generally from 0.1 to 1 mrad, which is affected by electron beam energy. The intensity and brilliance of Synchrotron radiation are several orders of magnitude higher than the X-ray produced in the standard X-ray tube. In addition, a monochromatic X-ray beam can be chosen in the broad and continuous range of wavelengths from hard X-ray ( $10^{-11} \text{ m}$ ) to infrared ( $10^{-4} \text{ m}$ ) (Fig 2.16 (b)) with narrow angular divergence and a high degree of polarization. Lastly, synchrotron radiation has an important property, which is polarization. When the orbit plane of the circulating particles is observed, the projected movement is an oscillation which indicates that the emitted light is linearly polarized in the orbit plane [149]. Due to the advantages, the utilization of synchrotron radiation enables advanced investigation of matters, making it a useful characterization tool in various fields of basic and applied science, including material science, medical science, biology, chemistry, and physics.

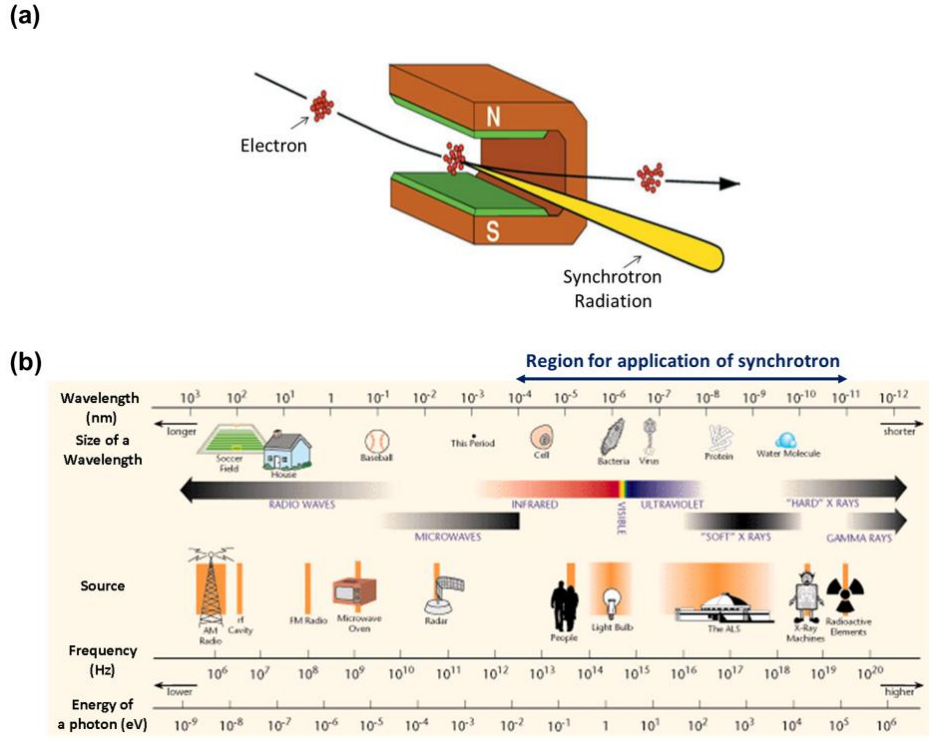


**Figure 2.16** (a) Schematic of mechanism of synchrotron radiation. (b) Electromagnetic spectrum with the broad distinction of photon wavelength inversely proportional to frequencies. The wavelength region of synchrotron radiation is from  $10^{-4}$  m to  $10^{-11}$  m [150].

Fig 2.17 (a) and (b) show a view of synchrotron SOLEIL and the fundamental components of synchrotron radiation facility, respectively. A synchrotron radiation facility is composed of a high vacuum storage ring, an electron accelerator, and magnetic field devices, such as wigglers, undulators, and bending magnets. Most synchrotron radiation sources are called storage rings today. A set of optical elements such as mirrors, slits, and monochromators are used to optimize the X-ray beam for the use of several experimental end-stations called “beamlines”.

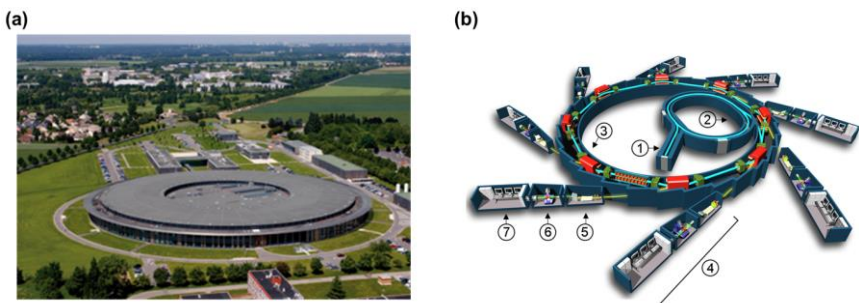


**Figure 2.17** (a) A view of the synchrotron facility, SOLEIL in France. (b) Structure of third-generation 2.75 GeV Soleil Light Source at Saint-Aubin, France. It consists of (1) the injector, (2) the booster ring, (3) the storage ring, (4) an experimental station called “beamline”, including (5) optics hutch, (6) experimental hutch, and (7) control room.

In the high vacuum storage ring, a beam of electrons is stored and kept on circular producing synchrotron radiation. The storage ring is not a perfect circle but a polygon because the insertion devices for the magnetic field, such as wigglers, undulates and bending magnet, are contained (Fig.

2.18). The wigglers and undulators comprise varying poles of many magnets in order to produce a periodically alternating field at the beam axis and provide curved transverse displacement of the beam [151]. In wigglers, the poles of the various magnets are used to have the electron beam wiggle, and synchrotron radiation is emitted at each wiggle so that a wide horizontal fan of X-ray provides more than one beamline with X-rays. Each beamline can take a portion of a slice of the fan for the research [152]. In the case of the undulator, the operation method is similar to the wiggler however, it has a shorter period between each magnetic pole, maintaining the curved beam within the original beam envelope. The radiation emitted at each pole causes a partially coherent, narrow X-rays beam with a higher brilliance [152]. On the other hand, the bending magnet has the electron beam forced to move in an arch through a magnetic field of the bending magnet leading to emission of radiation in a flattened cone [153].

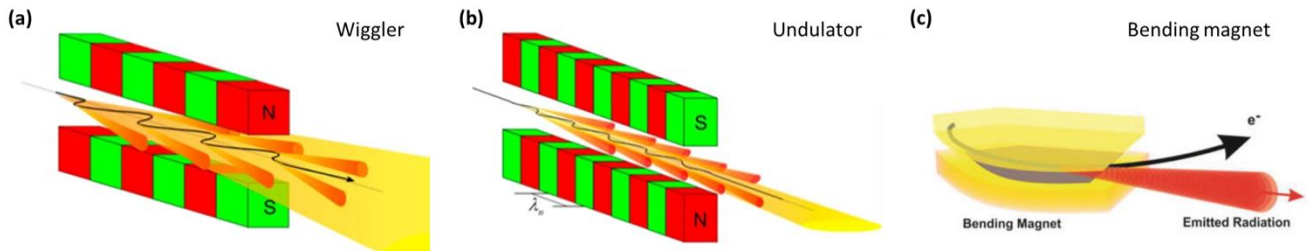


**Figure 2.18** Schematic of (a) a wiggler, (b) an undulator, and bending magnet [154], [153].

Optical elements used in each beamline depend on the range of synchrotron radiation used in the beamline, the resolution, etc. For example, Fig. 2.19 presents the optical layout of the HERMES beamline where halide perovskite is studied using STXM for this PhD work. In the optical system of the HERMES beamline, a set of three mirrors, including the collimating M1 mirror with specific angles, are optimized for the beam with energy from 70 eV to 2.5 keV emitted by undulators in the storage ring. The monochromator of the beamline is a plane-grating monochromator (PGM) with two types of gratings. One grating transmits a narrow selectable band of wavelengths of the radiation chosen from a range of low energy (70 eV to 1.6 keV), and the other grating chooses the wavelength of the radiation with high energy from 1 to 2.5 keV. After the beam exits from the slit of the monochromator, the beam is deflected by a set of two mirrors. A cylindrical mirror (M5) diverts the direction of the beam to the X-ray photoemission electron microscopy (XPEEM) branch. The other toroidal mirror sets the direction of the beam that came from the monochromatic to the STXM branch. After reflecting against each mirror, the two beams in each branch can operate alternatively and independently.

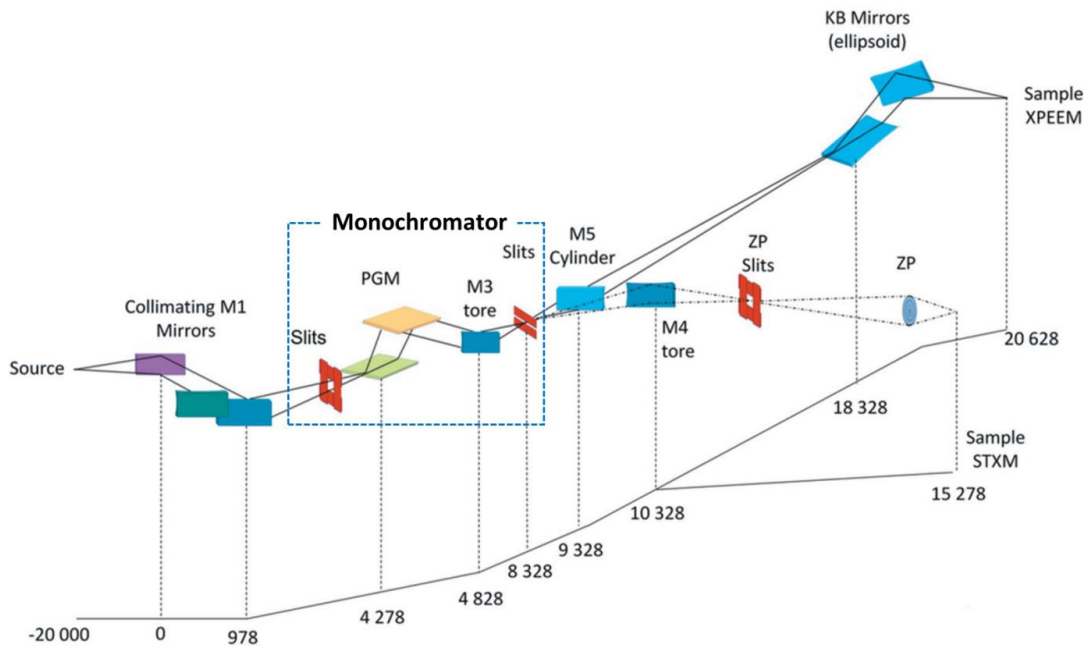


**Figure 2.19** Optical schematic of HERMES beamline in Synchrotron SOLEIL, France [155].

## 2.5.2 X-ray Interaction with Materials

X-ray is electromagnetic radiation with a wavelength ranging from  $10^{-11}$  to  $10^{-8}$  m. In terms of the magnitude of energy, X-rays are divided into hard X-rays with high photon energies (5 – 10 keV) and soft X-rays with lower energies (0.1 – 3 keV). The ways to generate X-rays are to apply an X-ray tube, nuclear decay by electron capture, or internal conversion of gamma rays. In addition, synchrotron radiation can also produce X-rays, as explained in section 2.5.1.

When X-rays approach matter, various interactions occur (Fig. 2.20 (a)). Parts of X-ray photons are absorbed in the matter. Absorption is a process by which energy is transferred from the X-rays to the atoms of matter. The absorbed energy is converted into the kinetic energy of the electron in the matter, and the kinetic energy causes electron excitation in the material. The excited photoelectrons can be transferred into bound or vacuum levels (Fig. 2.20 (b)). Meanwhile, when X-rays interact with the material, not only absorption but also scattering happens. The collision changes the direction of the X-rays, and it may or may not transfer energy from the incident X-rays to the material. Meanwhile, the photons which do not experience absorption or scattering are transmitted, and these X-ray photons, if counted by a detector, can be used to produce microscopy images.

When the X-rays are absorbed in the matter, photoelectron in an electron shell such as K or L shells is ejected, leaving behind a highly excited core-hole state. The excited state can relax by various

mechanisms, among which the emission of Auger electron and X-ray fluorescence is the most remarkable. Auger electron is ejected when an atom relaxes from a higher energy level to a former core-hole state resulting in the release of energy. The energy is transferred to this second electron. The emission of auger electrons is the primary relaxation process for lower energy excitation. On the other hand, X-ray fluorescence is released energy in the form of a photon when the electron excited by X-rays falls into the lower orbital to fill the hole. For higher-energy excitation, it is a prominent relaxation process with fluorescence yields approaching 1 (Fig. 2.20 (c)).

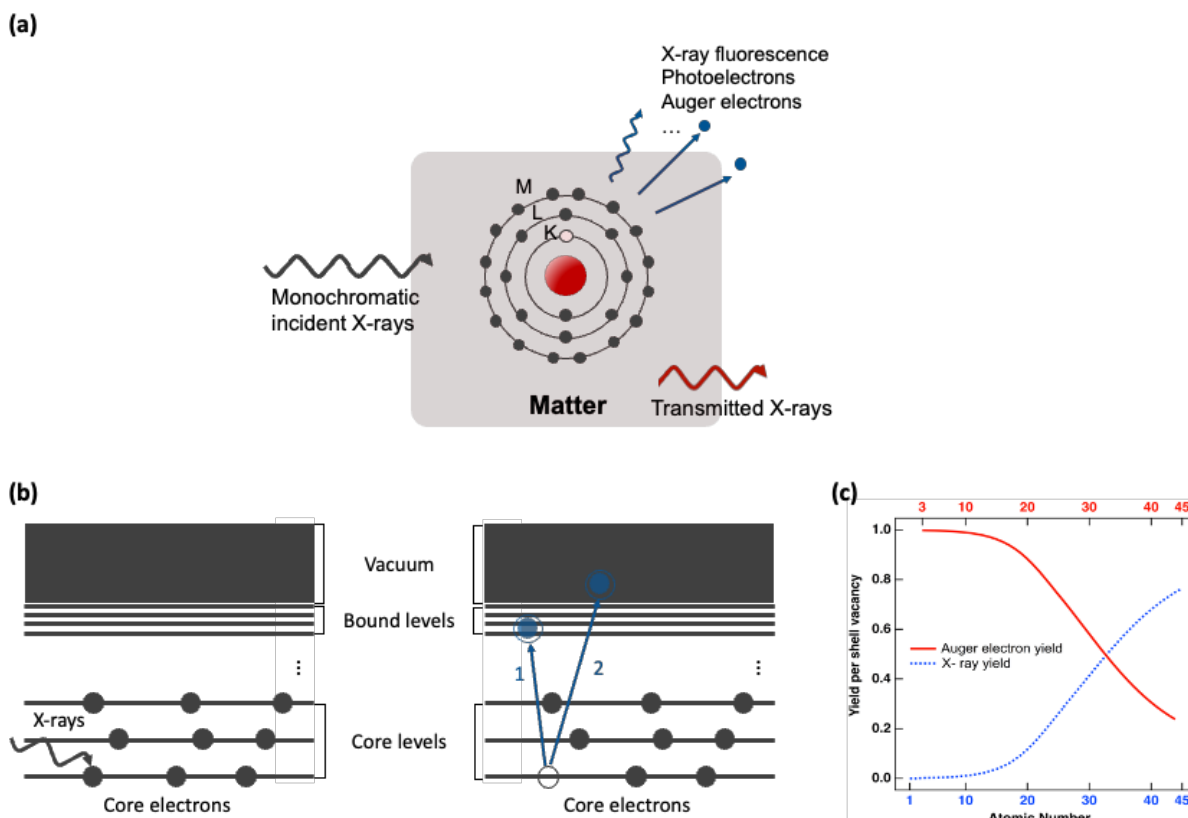


**Figure 2.20** Schematic of (a) interaction between X-rays and matter and (b) absorption process where processes 1 and 2 indicate the transfer of a photoelectron into a bound level and vacuum level, respectively. (c) Graph of Auger electron and fluorescence yield with respect to atomic number  $Z$  for the K shell. Courtesy of [http://www.wikiwand.com/en/Auger\\_electron\\_spectroscopy](http://www.wikiwand.com/en/Auger_electron_spectroscopy).

### 2.5.3 Scanning Transmission X-ray Microscopy

X-ray absorption spectroscopy (XAS) is a widely used technique for the measurement of transition from a core electronic state with a well-defined symmetry of the final state selected by quantum mechanical selection rules. When we regard the intensity of incident X-ray as  $I_0$ , the intensity of transmitted ray in the material with density  $\rho$  and thickness  $t$  follows Beer-Lambert law.

$$I_t = I_0 e^{-\mu(E)\rho t} \quad (2.38)$$

For quantitative analysis, the transmitted intensity can be converted into absorbance, a dimensionless quantity called optical density (OD) in the soft X-ray energy region.

$$OD = -\ln\left(\frac{I_t}{I_0}\right) = \mu(E)\rho t \quad (2.39)$$

where  $\mu(E)$  is the absorption coefficient. Through the conversion of the transmittance into OD, the absorption from a homogeneous substrate such as a silicon nitride membrane can be easily subtracted. Meanwhile, the absorption coefficient of an atom ( $\mu(E)$ ) varies as a function of energy as

$$\mu(E) \sim \frac{dz^4}{mE^3} \quad (2.40)$$

The absorption coefficient is affected by the incident photon energy (E) and atomic number (Z). Absorption coefficient decreases as the energy increases.

However, XAS spectra of any material are characterized by a sudden increase of absorption at specific X-ray photon energies. The sharp increase in absorption is called absorption edges. It is the energy for the ejection of a core electron into the unoccupied final state or to the continuum, and each absorption edge means a different core-electron binding energy. Following Bohr's model, absorption edges are named after the initial level of the transition. The absorption discontinuity is known as the K-edge when the photoelectron originates from the n=1 level (1s electron), an L-edge when the ionization is from the n=2 level (2s or 2p electron), and M-edge when ionization occurs from the n=3 level (3s, 3p or 3d electron).

Fig. 2.21 (a) shows a typical energy level diagram. As the energy of the state where ionized electrons are located increases, the spectroscopy of the edge is more sensitive to the electronic structure and the spin state changes of the material. In addition, the core-electron binding energy increase when the atomic number increases. For example, the energy of carbon (Z = 6) K-edge is 284 eV, and that of the uranium (Z = 92) K-edge is 115606 eV. When an absorption peak is observed closely, some absorption peaks consist of several distinct absorption edges. For instance, the L edge of Pb consists of three distinct L-edges, including L<sub>1</sub>, L<sub>2</sub>, and L<sub>3</sub>, as shown in Fig. 2.21 (b). L<sub>1</sub> indicates the excitation of a 2s electron. L<sub>2</sub> and L<sub>3</sub> are formed by spin-orbit coupling energy of 2p<sup>5</sup> configuration created when a 2p electron is excited. The higher energy of 2p<sup>5</sup> excited state is <sup>2</sup>P<sub>1/2</sub>, which causes the L<sub>2</sub> edge, and the lower energy of the excited state is <sup>2</sup>P<sub>3/2</sub>, which gives rise to the L<sub>3</sub> edge.

With the concept of the absorption edge, XAS can be explained as the measurement of X-ray absorption cross-section around the absorption edges. There are two main regions of absorption

spectra to be analyzed depending on the excited state: X-ray absorption near-edge structure (XANES) and extended X-ray absorption fine structure (EXAFS) (Fig. 2.22). XANES is a kind of absorption spectroscopy that shows characteristics in XAS due to absorption for electronic transitions from an atomic core level to final states in the energy region. On the other hand, a photoelectron wave after ionization of a core electron to the continuum propagates out from the absorbing atom, and the electrons in neighboring atoms backscatter the ionized electron. The phenomenon results in a modulation of the absorption coefficient referred to as EXAFS. The advantage of XAS is providing information on the local structure of the element of interest without interference [156], [157].

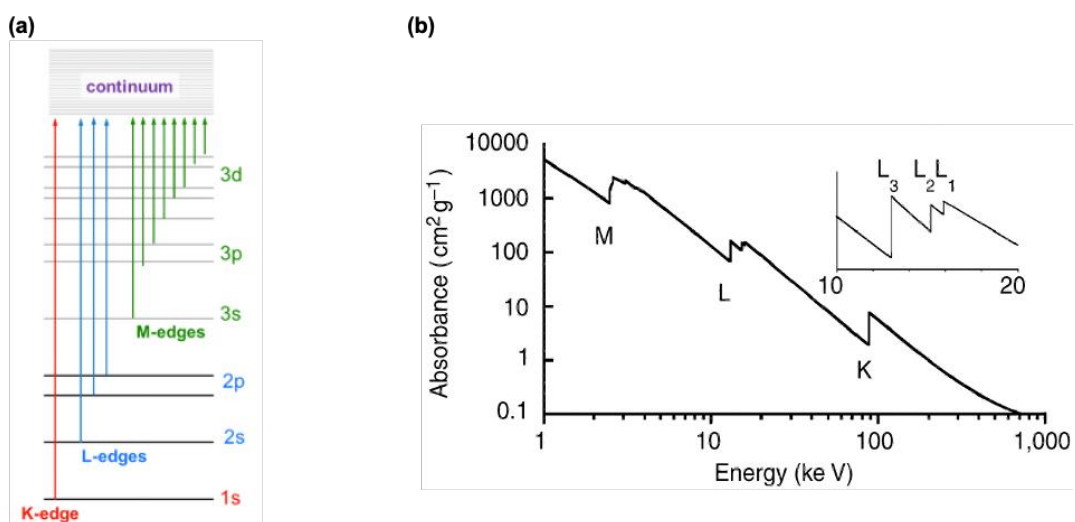


**Figure 2.21** (a) Transitions resulting from the excitation of a core electron and the corresponding XAS edges [156]. (b) X-ray absorption spectrum of Pb including three major absorption edges (M, L, K-edges). The inset image is a high-resolution XAS of split L-edges [158].

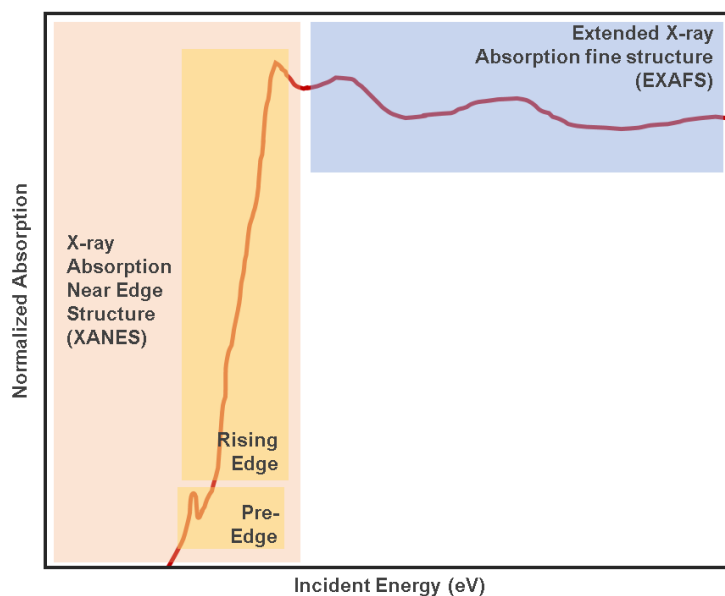


**Figure 2.22** XANES and EXAFS region of XAS spectra.

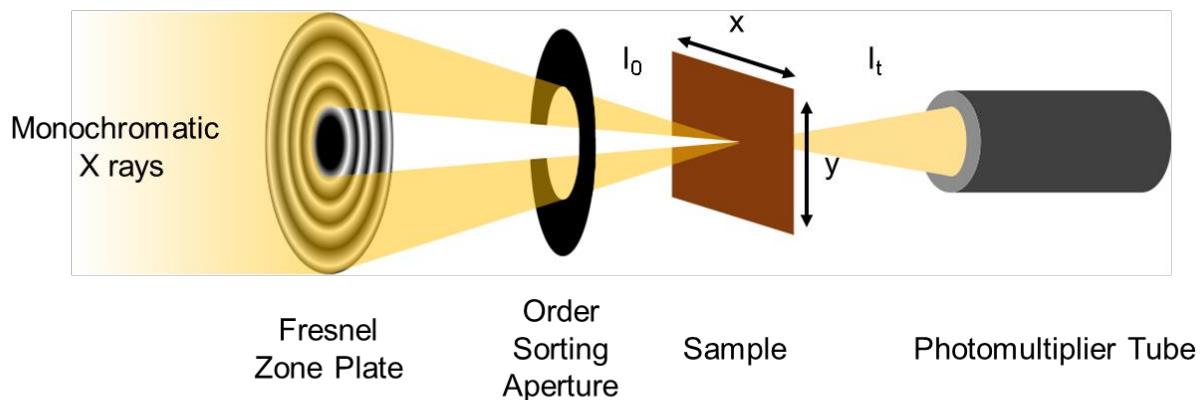
Scanning Transmission X-ray Microscopy (STXM) is a NEXAFS technique combined with X-ray

microscopy, and it is performed in transmission mode. Spatially resolved information on chemical bonding can be provided due to this combination. STXM instruments are shown in Fig. 2.23, and they consist of a Fresnel zone plate (FZP), order sorting aperture (OSA), and photodetector. The X-ray spot size at the focal point determines the spatial resolution of STXM. Because the wavelength of the soft x-ray used for STXM is short (1–10 nm), they can be focused to a smaller spot size using circular diffractive gratings called Fresnel zone plate (FZP). The incident X-rays are focused through constructive interference of the diffracted X-rays from each of the rings at the focal point. In addition, the FZP prevents unfocused incident X-rays, which have a negative influence on the sample. The Fresnel zone plate is made of gold rings with different ring widths on a silicon nitride membrane transparent for X-rays. As the distance of the ring from the center of FZP increases, the width of the gold zone decreases. The reported minimum spot size obtained using FZP is 7 nm [159], and many studies are in progress to achieve a smaller spot size. In general, the higher-order diffracted beam can degrade the spatial resolution and pollute the spectra. The incident X-ray beam on the FZP includes a considerable level of the higher-order diffracted beam. A pin-hole order sorting aperture (OSA) is used to eliminate higher order diffractions. When the OSA is placed in a decent position between the FZP and the sample, only first-order diffracted light is transmitted to the sample.

The focused X-ray beam is incident on the sample, and the transmitted beam is collected by a detector. Images are obtained at given photon energy by raster scanning the sample through the focal point while measuring the transmitted X-rays. A series of images at different energies are measured to acquire spatially resolved spectral information [155], [160]. The series of images is called “stack”. Through STXM measurement, not only a spectrum of a point in the sample but also a chemical map at specific energies can be achieved (Fig. 2.23 (b)).

Soft X-ray-based STXM has the advantage of being able to investigate the inner shells of light elements such as C, O, and N, as well as the outer shells of heavier elements. Soft X-ray STXM induces comparably less radiation damage as compared to hard X-ray tools. Furthermore, the thickness of the sample can be estimated in the spectra if the elemental composition is identified. Additionally, the normalized spectra of components can be used to quantify their composition in an unknown sample and to speculate what the material consists of [161].

(a)



(b)

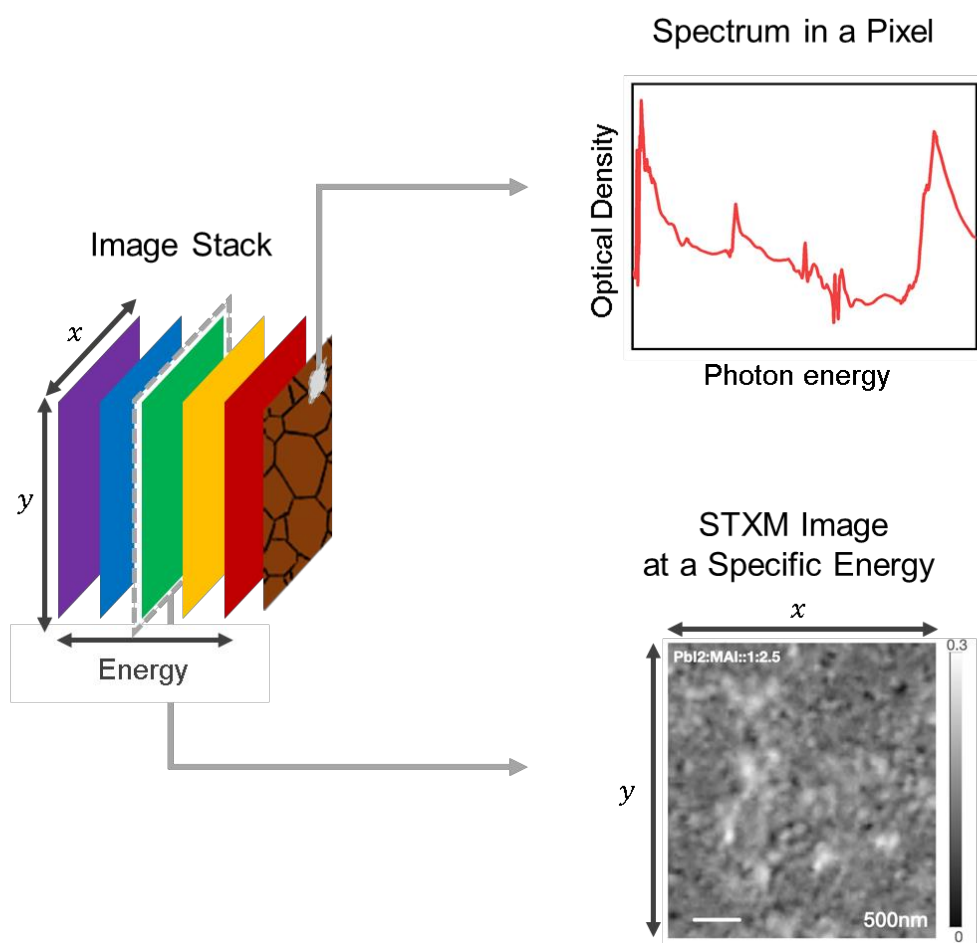


**Figure 2.23** (a) Experimental set-up for STXM. (b) Illustration of data acquired by STXM, including spatially resolved spectra (spectrum in a particular pixel) and STXM image at a specific energy.

# **Chapter 3.**

## **MAPbI<sub>3</sub> Perovskite Solar Cells by Co-evaporation**

---

<b>3.1 Introduction .....</b>	<b>65</b>
<b>3.2 Experimental Details.....</b>	<b>66</b>
3.2.1 Evaporation of MAPbI <sub>3</sub> Film based on Co-evaporation.....	66
3.2.2 Fabrication of MAPbI <sub>3</sub> Solar Cells.....	68
3.2.3 Perovskite Film Characterization .....	71
3.2.4 Perovskite Solar Cells Characterization .....	72
<b>3.3 Optimization of MAPbI<sub>3</sub> Film.....</b>	<b>73</b>
3.3.1 Impact of Deposition Rate Ratio of PbI <sub>2</sub> and MAI on MAPbI <sub>3</sub> Film Properties.....	74
3.3.2 Impact of Rate of PbI <sub>2</sub> on MAPbI <sub>3</sub> Film Properties .....	76
3.3.3 Impact of Hole Transport Layers on MAPbI <sub>3</sub> Film Properties.....	78
<b>3.4 Photovoltaic Performances of MAPbI<sub>3</sub> Solar Cells.....</b>	<b>82</b>
3.4.1 Photovoltaic Performance of Reference Solar Cells .....	82
3.4.2 Impact of Electron Transport Materials on Photovoltaic Performance .....	85
3.4.3 Impact of Hole Transport Materials on Photovoltaic Performance .....	88

---

### **3.1 Introduction**

As mentioned in the former chapter, halide PSCs have progressed by leaps and bound in a short period. The rapid improvement of efficiency in PSCs is attributed to the development of perovskite composition and process engineering. Wet processing technique, including spin-coating [27], [162], [163] and dip-coating [164], [165] is a typical fabrication technique for halide perovskite film, and it is a favored technique in the laboratory. However, the wet process has limitations in being used in large-scale fabrication for industrialization.

The vapor-based technique has attracted attention as an alternative technique. Vapor-based methods are a mature technology widely adopted in the coating and semiconductor industry. It has various advantages, including a solvent-free fabrication process, intrinsic purity of precursor, formation of pinhole-free perovskite film with superior uniformity, and scalability [166]. In addition, it enables

fine control over the thickness and stoichiometry of perovskite films and is substrate-independent for the deposition [167]–[169].

In this thesis, we fabricated PSCs based on the co-evaporation technique, one of the vapor-based techniques, and investigated various physical phenomena in solar cells. In this chapter, the optimization process of  $\text{MAPbI}_3$  film based on co-evaporation will be described by varying several parameters, such as the rate ratio of  $\text{PbI}_2$  and MAI and the rate of  $\text{PbI}_2$  with the same ratio. After that, PSCs with the optimized condition of  $\text{MAPbI}_3$  will be explained, and photovoltaic performance according to the charge transport layer will be investigated.

## 3.2 Experimental Details

### 3.2.1 Evaporation of $\text{MAPbI}_3$ Film based on Co-evaporation

Co-evaporation is a kind of deposition technique with more than two precursors in the vacuum chamber. Here,  $\text{MAPbI}_3$  was deposited on the HTL layer by co-evaporation of  $\text{PbI}_2$  (ultra-dry, 99.999% Sigma Aldrich) and MAI (>99.99 %, Greatcell Solar Materials). Fig. 3.1 shows a scheme of the co-evaporation system employed in our laboratory. The co-evaporation system consists of two crucibles of each precursor, one quartz crystal microbalance (QCM), a sample holder, a vacuum chamber, a primary pump, and a vacuum pump.

Two precursors in the crucibles are heated up where they start to sublime, and the rate of the precursor can be controlled by temperature. A pre-calibrated quartz crystal microbalance (QCM) sensor was used to monitor the rate of two precursors and the thickness of  $\text{MAPbI}_3$ . Therefore, the crystalline quality of  $\text{MAPbI}_3$  can be controlled by monitoring the temperature of MAI and  $\text{PbI}_2$ , the rate, and the thickness monitored by the QCM sensor (Fig. 3.2). At a specific temperature where  $\text{PbI}_2$  is sublimated,  $\text{PbI}_2$  in a high vacuum chamber travels in a straight line of sight as the mean free path. However, MAI tends to sublimate like a vapor gas in the vacuum due to its small molecular weight, which makes it difficult to control the rate using the conventional QCM [170]. To control the MAI deposition accurately, it is important to keep a close watch on an additional controllable parameter, especially the vapor pressure [170], [171].

In the optimized conditions for this chapter, each  $\text{PbI}_2$  and MAI was sublimated in the vacuum

chamber at 300 °C and 180 °C, with the deposition rate of 1 Å/s and 2.5 Å/s, respectively. During the evaporation, the vacuum level was  $5.5 \times 10^{-5}$  mbar. Fig. 3.3 presents the average and standard deviation of the temperature of PbI<sub>2</sub> and MAI, the rate of MAPbI<sub>3</sub> by QCM, and vacuum pressure. After deposition, the film was annealed at 70 °C for 10 min in an N<sub>2</sub>-filled glove box. The optimal thickness for the PSC is 500 nm.

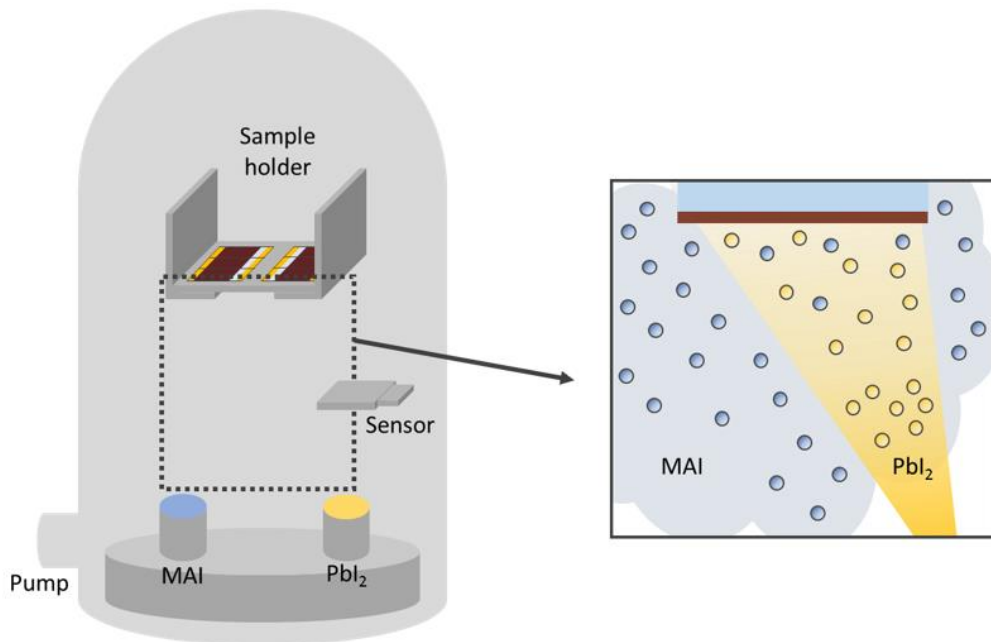


**Figure 3.1** Schematic illustration of the vacuum chamber for co-evaporation (left) and molecular motion of MAI and PbI<sub>2</sub> in the vacuum chamber (right).

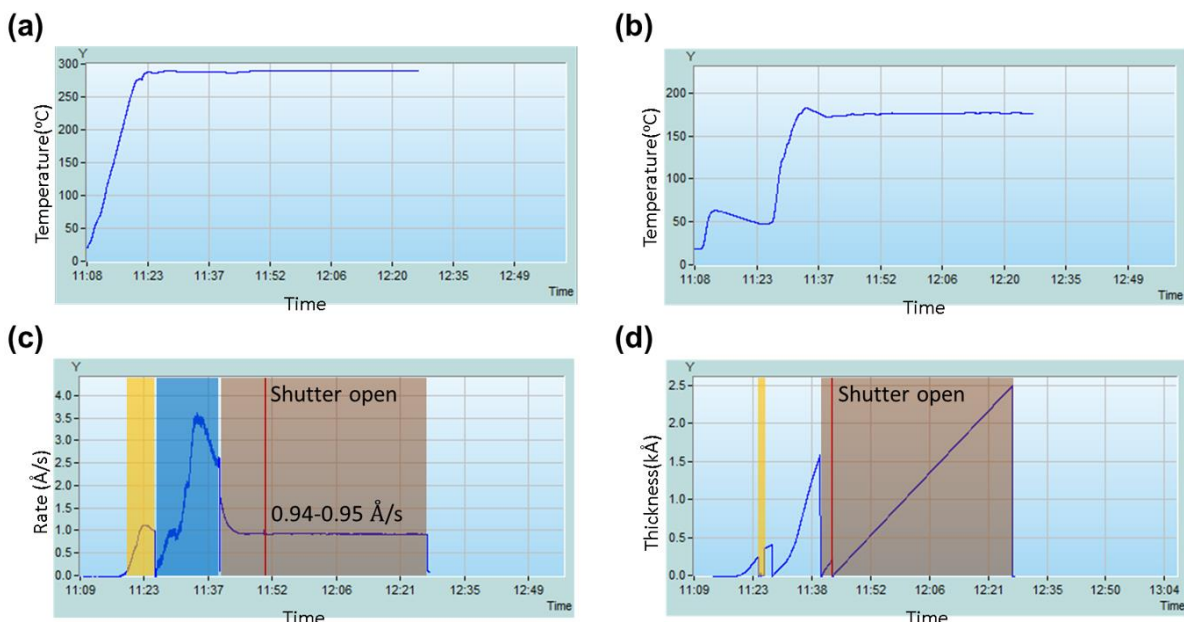


**Figure 3.2** Monitoring each parameter for evaporation of MAPbI<sub>3</sub>. Temperature of target material including (a) PbI<sub>2</sub>, (b) MAI. (c) Rate. (d) Thickness monitored by QCM.

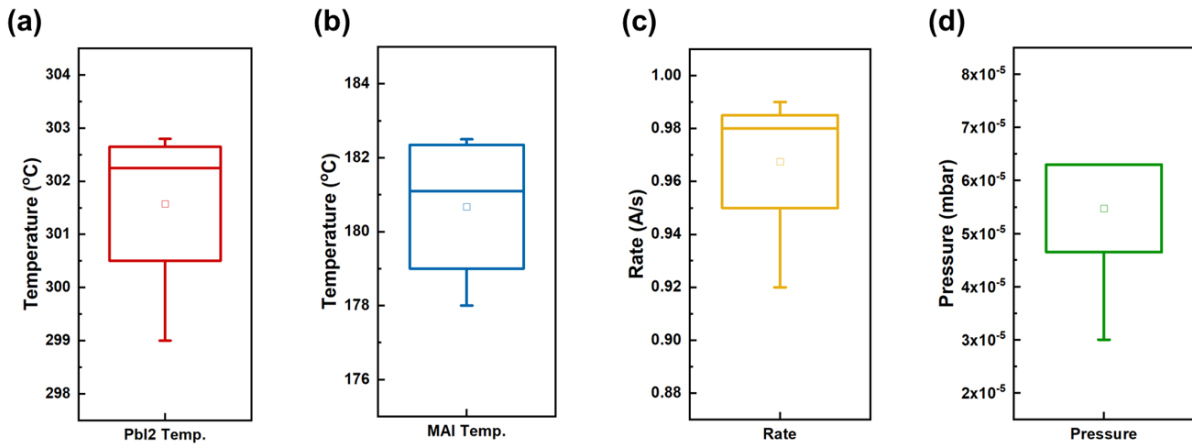


**Figure 3.3** Average temperature of (a) PbI<sub>2</sub> and (b) MAI, (c) rate of MAPbI<sub>3</sub>, and vacuum pressure with standard deviation.

### 3.2.2 Fabrication of MAPbI<sub>3</sub> Solar Cells

The fabrication processes of each of the electron and hole transport layers in co-evaporated PSCs are described below.

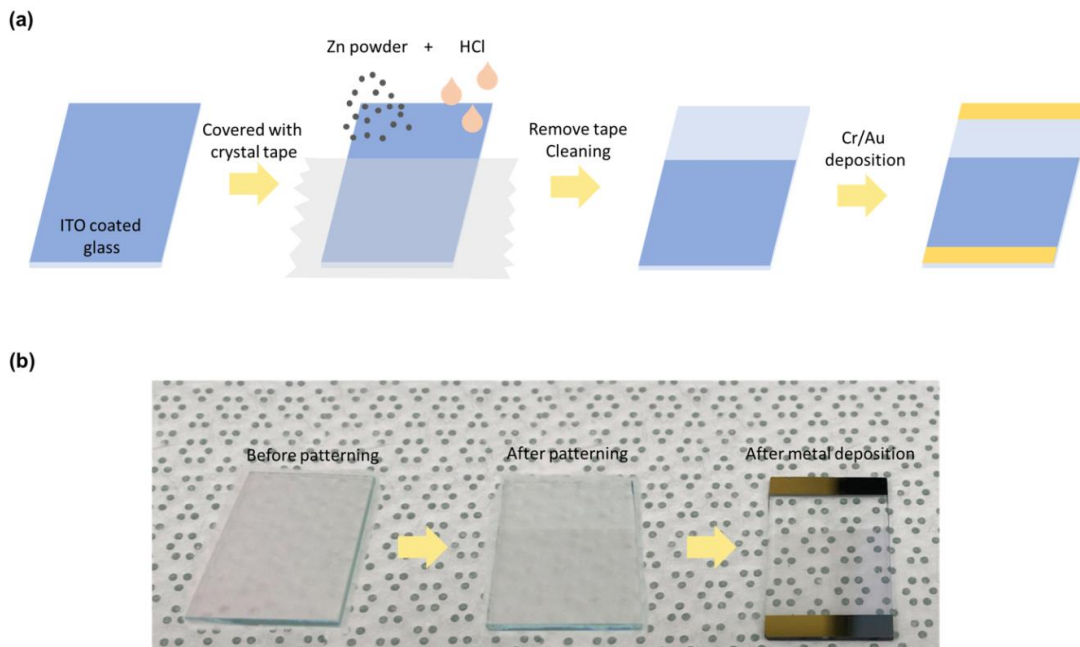


**Figure 3.4** (a) Illustration of ITO etching and Cr/Au deposition process for the substrate of solar cells. (b) Real image of ITO-coated glass before and after patterning, completed substrate with Cr/Au contact.

Substrate with anode Before fabrication of PSCs, patterned Indium tin oxide (ITO) etched by the wet process was employed as anode and substrate. Fig. 3.4 describes the chemical etching and metal deposition process for the preparation of the substrate. Firstly, the part of ITO-coated glass substrates (20ohm/sq, Xinyan Technologies), which needs to be protected for etching, was covered with 3M

crystal clear tape. Uncovered ITO was removed using hydrochloric acid (HCl) and zinc powder (Zn). The etched substrate was cleaned in ultrasonic baths of deionized water with 1% diluted detergent (Liqui-Nox Phosphate-Free Liquid Detergent, Alconox, Inc.) for 15 min, pure deionized water for 30 min, acetone for 15 min, and 2-propanol (IPA) for 15 min, in sequence. To reduce the contact resistance between ITO and the measurement system, chromium (Cr) and gold (Au) were deposited on edge of glass and ITO by thermal evaporation (Fig. 3.5 (a)) under a vacuum of  $1 \times 10^{-6}$  mbar. Here, Cr (5 nm) is used to improve adhesion between glass and Au.

Hole transport layer (HTL) In this study, three kinds of hole transport material including PEDOT:PSS, PTAA, and NiO were used for HTL in PSCs.

Before deposition of PEDOT:PSS, the surface of patterned ITO was treated with a UV-ozone chamber for 15 minutes. PEDOT:PSS solution (25 nm, AI 4083, Ossila) was filtered through a 0.45  $\mu$ m PVDF filter and deposited on UV-ozone activated ITO layer through spin-coating in air (Fig. 3.5 (b)). Meanwhile, poly(styrene sulfonate) (PSS) in PEDOT:PSS is used as the counter ion and charge compensator which masks PEDOT:PSS easily dispersible in water. However, PSS is an insulator causing low conductivity of the commercial PEDOT:PSS. To enhance its conductivity, 120  $\mu$ L of methanol was dropped during spin-coating. The methanol treatment removes the excess PSS from the film and improves the conductivity[172]. This was followed by thermal treatment at 120°C in air for 20 minutes.

In the case of PTAA, ITO coated glass also was treated with UV-O<sub>3</sub> for 10 minutes. PTAA (30 nm) was deposited on the ITO layer through spin-coating at 5000 rpm in air with thermal treatment at 100 °C in N<sub>2</sub> for 10 minutes. The PTAA solution was prepared with a concentration of 0.002 g/mL in toluene and filtered through a 0.45  $\mu$ m PTFE filter. PTAA was purchased from Ossila (M513, CAS: 1333317-99-9) and used as received.

Lastly, the sol-gel NiO solution was prepared and filtered through a 0.45  $\mu$ m PTFE filter. The NiO film was spin-coated at 4000 rpm followed by annealing at 300 °C in air for 1 hour. All experimental processes related with NiO were done in Institut Photovoltaïque d'Île-de-France (IPVF)

Methyl ammonium lead iodide (MAPbI<sub>3</sub>) MAPbI<sub>3</sub> deposited by co-evaporation was employed as an absorber layer. A detailed explanation of the deposition process is described in section 3.2.1.

Electron transport layer (ETL) PCBM and C<sub>60</sub> were applied to PSCs as ETL.

A PCBM thin film (40-50 nm thick) is spin-coated at 2000 rpm for 30 s onto the perovskite layer and dried for 20 minutes in an N<sub>2</sub> atmosphere. The spin coater in N<sub>2</sub> is shown in Fig. 3.5 (c). The PCBM solution of 40 mg/mL was prepared in anhydrous chlorobenzene solvent (Aldrich) and stirred overnight at room temperature in an N<sub>2</sub> atmosphere. PCBM powder was purchased from Ossila (99 %, CAS: 160848-22-6) and used as received.

$C_{60}$  thin film was deposited on  $MAPbI_3$  by thermal evaporation. The vacuum chamber (Fig. 3.5 (d)) was evacuated to a pressure of  $7.6 \times 10^{-7}$  mbar.  $C_{60}$  was sublimated at  $500^\circ C$  with a deposition rate of  $0.1 \text{ \AA/s}$ . The thickness of  $C_{60}$  deposited was  $25 \text{ nm}$ .  $C_{60}$  also was bought from Ossila (99.5 %, CAS: 99685-96-8).

Hole blocking layer (HBL) BCP was used for HBL to enhance charge separation and avoid the recombination of charges. The deposition process of BCP is divided into wet and dry processes depending on under layer.

On PCBM, BCP was also prepared by spin-coating at  $4000 \text{ rpm}$  in  $N_2$ . The  $0.0005 \text{ g/mL}$  of BCP was dissolved in 2-propanol and filtered through a  $0.45 \mu\text{m}$  PTFE filter. On the other hand, BCP was also deposited on  $C_{60}$  by thermal vapor deposition. The crucible of BCP is located in the same chamber of  $C_{60}$ . The vacuum conditions are the same as those of  $C_{60}$  deposition. BCP (> 99.5 %, Lumtech) was sublimated at  $100^\circ C$  with deposition rate of  $0.1\text{-}0.2 \text{ \AA/s}$ . BCP was purchased from Lumtec (> 99%, CAS: 4733-39-5).

Cathode Silver (Ag) of  $120 \text{ nm}$  thickness was deposited for a cathode. The equipment for thermal evaporation is the same as that for Au, so the vacuum conditions were the same. The active layer of PSCs is  $0.28 \text{ cm}^2$ .

In the thesis, the determined structure of the reference  $MAPbI_3$  PSCs is ITO/PEDOT:PSS/ $MAPbI_3/C_{60}/BCP/Ag$ .

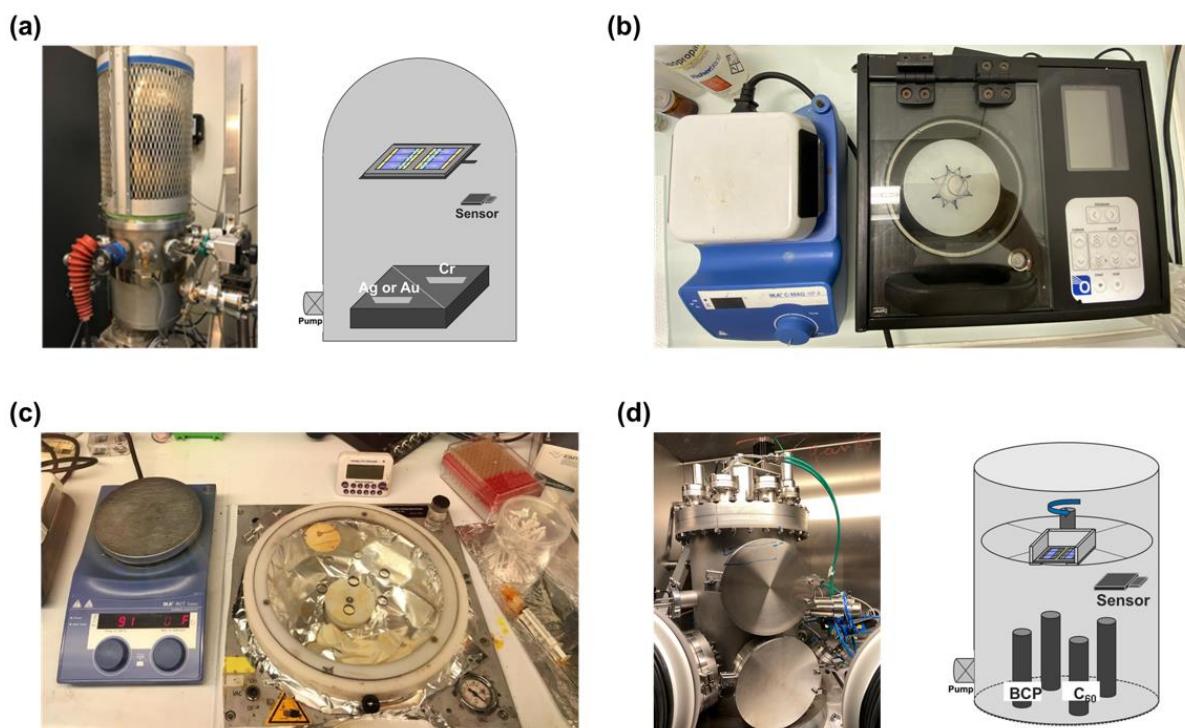


**Figure 3.5** (a) Real image and schematic illustration of thermal evaporator for contact metal, spin-coater, and heating plate in (b) air and (c)  $N_2$ . (d) Photograph of thermal evaporator for organic materials including  $C_{60}$  and BCP.

### 3.2.3 Perovskite Film Characterization

Profilometer A profilometer (Fig. 3.6 (a)) is an instrument used to measure the relief of a surface, such as to assess its roughness or microgeometry. Contact profilometers are based on the physical contact between a diamond tip and the surface to be measured. A sensor attached to the tip measures the vertical position Z when it is moved horizontally (X-axis) on the surface, thus establishing the profile  $Z=f(X)$  of the surface.

UV-Visible absorption spectroscopy In this thesis, UV-visible (UV-Vis) spectroscopy (UV-Vis spectrophotometer - Agilent Cary 50) (Fig. 3.6 (b)) is being used to study the optical bandgap and absorbance of halide perovskite film. To examine the intrinsic property of  $\text{MAPbI}_3$  and the property of interface between  $\text{MAPbI}_3$  and HTL,  $\text{MAPbI}_3$  films on glass, PEDOT:PSS/ITO, PTAA/ITO, and NiO/ITO were prepared.

X-ray diffraction (XRD) To investigate the crystalline quality of  $\text{MAPbI}_3$ , XRD was employed. XRD is a non-destructive analytical technique that reveal information about the crystal structure, chemical composition, and physical properties of materials and thin films (Fig. 3.6 (c)). It is based on observing the scattered intensity of an X-ray beam hitting a sample as a function of incident and scattered angle, polarization, and wavelength or energy. It is crucial to achieve highly crystalline  $\text{MAPbI}_3$  film for fabricating high-performance PSCs. The samples were prepared on glass. The standard XRD patterns were acquired using D8 Discover X-ray Diffractometer from Bruker with a Cu K- $\alpha$  X-ray source operating at 40 kV and 40 mA with a graphite monochromator. Multiple scans were collected between  $2\theta = 10^\circ$  and  $50^\circ$  with a step size of  $0.02^\circ$  and a scan speed of  $2^\circ/\text{sec}$ .

Scanning Electron microscopy (SEM) and energy dispersive spectrometer (EDX) SEM is a type of electron microscope that produces images of a sample by scanning the surface with a focused beam of electrons (Fig. 3.6 (d)). The electrons interact with atoms in the sample, producing various signals that contain information about the surface topography and composition of the sample. In the most common SEM mode, secondary electrons with an energy less than 50 eV, emitted by atoms excited by the electron beam are detected. The number of secondary electrons that can be detected, and thus the signal intensity, depends, among other things, on specimen topography. The imaging of the surface of perovskite film and cross-section of the film and device was carried out on Microscope MEB HITACHI. The film thickness was determined by cross-section imaging. The electron beam was accelerated at 10 kV, under a current of 4.3  $\mu\text{A}$ . The composition and element mapping of films and perovskite powder was obtained using an EDX (energy-dispersive X-ray microanalysis) system attached to the SEM.

Atomic force microscopy (AFM) AFM is a high-resolution non-imaging optical technique scanning probe microscopy (STM) ( $< 1 \text{ nm}$ ) (Fig. 3.6 (e)). STM is a microscopy-forming image of surfaces with a physical probe. In STM, which is based on quantum tunneling, applying a bias voltage between the conductive tip and the surface of the sample allows electrons to tunnel through a vacuum when the tip is closed to the surface. The surface information can be achieved through the measurement tunneling current between the STM tip and the surface. Compared to STM which is only able to measure conductive samples, AFM can achieve surface information of both conductive and nonconductive materials. Interface roughness between  $\text{MAPbI}_3$  and HTL layer can be obtained through AFM. The AFM measurement was recorded by PicoScan 3000.

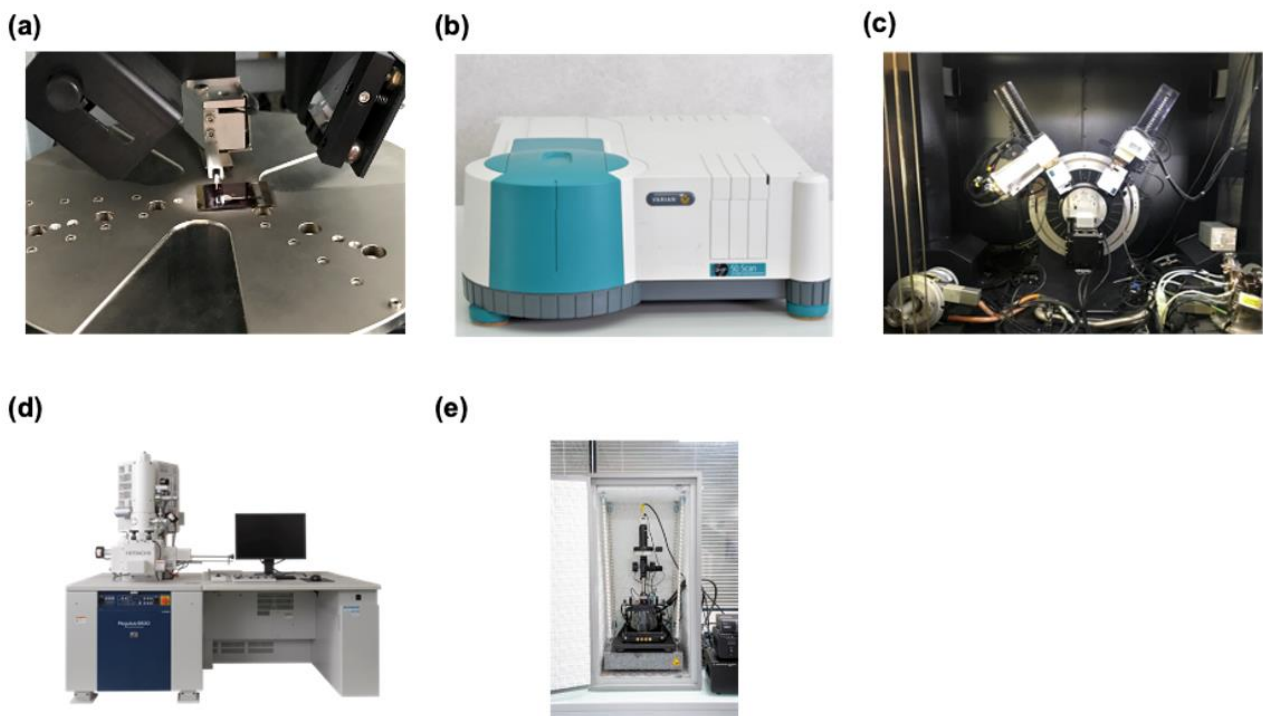


**Figure 3.6** Photographs of (a) profilometer, (b) UV-Visible spectrometer (Cary 50), (c) XRD (D8 Discover), (d) scanning emission microscope MEB HITACHI, (e) AFM (PicoScan 3000).

### 3.2.4 Perovskite Solar Cells Characterization

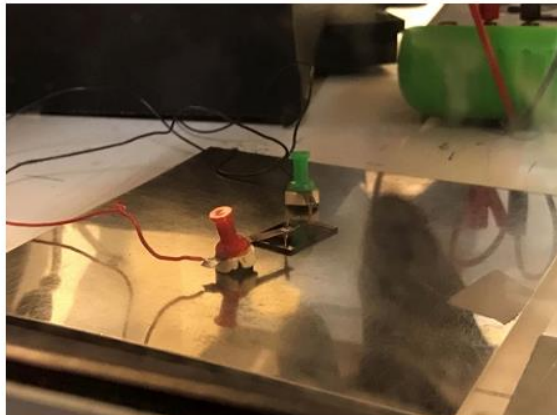
Current density-voltage (J-V) characterization The measurement of J-V characteristics is the simplest and most direct of the possible measurements. This measurement is ideally made under the same illumination as the sun ( $100 \text{ mW/cm}^2$ : a standard called AM1.5). In first-order and in most situations, relevant information can be extracted from measurements made with a lamp whose intensity corresponds to that of the AM1.5 spectrum. There are some parameters we are interested in: the open-

circuit voltage ( $V_{oc}$ ), the short-circuited current density ( $J_{sc}$ ), the fill factor (FF), the energy conversion efficiency ( $\eta$ ), the shunt resistance ( $R_{sh}$ ), and the series resistance ( $R_s$ ). The open circuit voltage is related to the bandgap of the semiconductor used, and the short-circuited current density can be related to the flow of absorbed photons. The fill factor characterizes the quality of the diode. The shunt resistance is obtained by the inverse of the slope at  $J_{sc}$  gives and indicates electrical leakage and recombination. Lastly, the series resistance is the resistance in the external circuit and is obtained by the inverse of the slope at  $V_{oc}$ . In order to estimate photovoltaic performance, the dark and photocurrent density-voltage (J-V) curves of PSCs were measured in the  $N_2$  glove box (Fig. 3.7 (a)) using Keithley model 2635. The condition of illumination was AM 1.5 G i. e.  $100\text{ mW/cm}^2$  simulated solar light from Solar Cell Test 575 of ATLAS MTT. The J-V curves were obtained by scanning along the forward scan direction and the reverse scan direction in the range of  $-0.1\text{ V}$  to  $1.1\text{ V}$ . The step voltage was set at  $1\text{ mV}$  for unit cells.

All photovoltaic parameters of PSCs, including  $V_{oc}$ ,  $J_{sc}$ , FF,  $V_{max}$ ,  $J_{max}$ , PCE,  $R_s$ , and  $R_{sh}$  are extracted from the J-V curve using Labview.

External quantum efficiency measurement (EQE) The external quantum efficiency (EQE) was measured with TSFC-Instrument's EQE with LED light source (Fig. 3.7 (b)). The light intensity was calibrated using a single-crystal Si photovoltaic cell as the reference. A 1-mm-diameter orifice was used for the EQE.

(a)



(b)

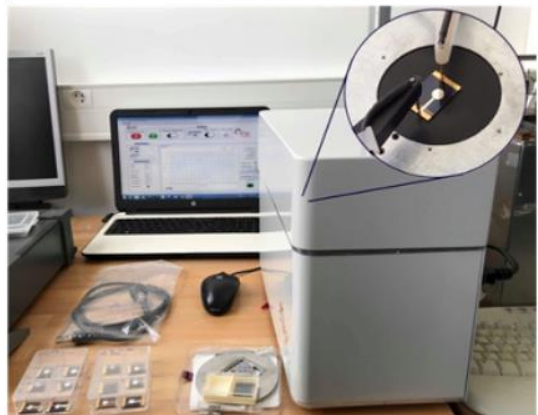


**Figure 3.7** (a) J-V measurement. (b) EQE measurement equipment with measurement software.

### 3.3 Optimization of $\text{MAPbI}_3$ Film

### 3.3.1 Impact of Deposition Rate Ratio of PbI<sub>2</sub> and MAI on MAPbI<sub>3</sub> Film Properties

In order to achieve a good photovoltaic performance of halide perovskite solar cells, it is important to obtain perovskite film with high crystallinity, full coverage, large grain size, and favorable grain orientation. By controlling the individual evaporation rate of PbI<sub>2</sub> and MAI, the crystalline quality and the stoichiometry of MAPbI<sub>3</sub> are determined. The crystalline quality was determined using XRD. MAPbI<sub>3</sub> films were deposited with various PbI<sub>2</sub> to MAI evaporation rate ratios including PbI<sub>2</sub>:MAI = 1:0 (pure PbI<sub>2</sub>), 1:1, 1:2.5, and 1:4 to optimize the conditions for high-quality perovskite film. Fig. 3.8 (a) shows optical absorption spectra of perovskite films with different deposition rates. 2.41 eV of bandgap offset of PbI<sub>2</sub> is obtained through drawing Tauc's plot. In MAPbI<sub>3</sub> film with a deposition ratio of 1:1, the absorption onset occurs around 780 nm and it corresponds to the bandgap wavelength of MAPbI<sub>3</sub>. The absorbance peak in the region of around 514 nm, which corresponds to the absorbance of PbI<sub>2</sub>, still remains a pure phase indicating that parts of PbI<sub>2</sub> have not reacted with MAI. As the amount of MAI increases, the absorbance of MAPbI<sub>3</sub> increases until the rate of MAI increases with the ratio (1:2.5). The peak of PbI<sub>2</sub> disappears which implies good quality perovskite film is obtained. In MAPbI<sub>3</sub> with the ratio of 1:4, overall absorbance is lower than those with 1:2.5. Notably, the absorbance in the shorter-wavelength region than 514 nm drastically decreased. It implies that the excess MAI damages the crystallinity of perovskite.

XRD patterns of MAPbI<sub>3</sub> with various deposition ratios are shown in Fig. 3.8 (b). In addition, detailed XRD peak information is described in Table 3.1. In MAPbI<sub>3</sub> with the deposition ratio of 1:1, a set of preferred orientations at 14.08 °, 28.44 °, 43.19 °, and 58.34 ° of tetragonal perovskite structure was observed, which was assigned to the (110), (220), (314) and (440) planes of the MAPbI<sub>3</sub> perovskite. The peak at 12.6 ° exists, and it corresponds to the (001) plane of PbI<sub>2</sub>, which indicated that residual PbI<sub>2</sub> not reacted with MAI remains. The results are coherent with those of absorption spectra. As the amount of MAI increases, the full width at half maximum (FWHM) of the (110) plane at 14.08 ° decreases, and the ratio of (110) to (220) in MAPbI<sub>3</sub> gradually increases. Furthermore, when the MAI rate increases until that the ratio of PbI<sub>2</sub> to MAI approaches 1:2.5, the (001) plane of PbI<sub>2</sub> becomes negligible while the pure plane of MAPbI<sub>3</sub> perovskite remains. In addition, MAPbI<sub>3</sub> has preferentially oriented along (110). However, MAI-rich films exhibit overlapping diffraction peaks between 11.3 ° and 11.7 °.

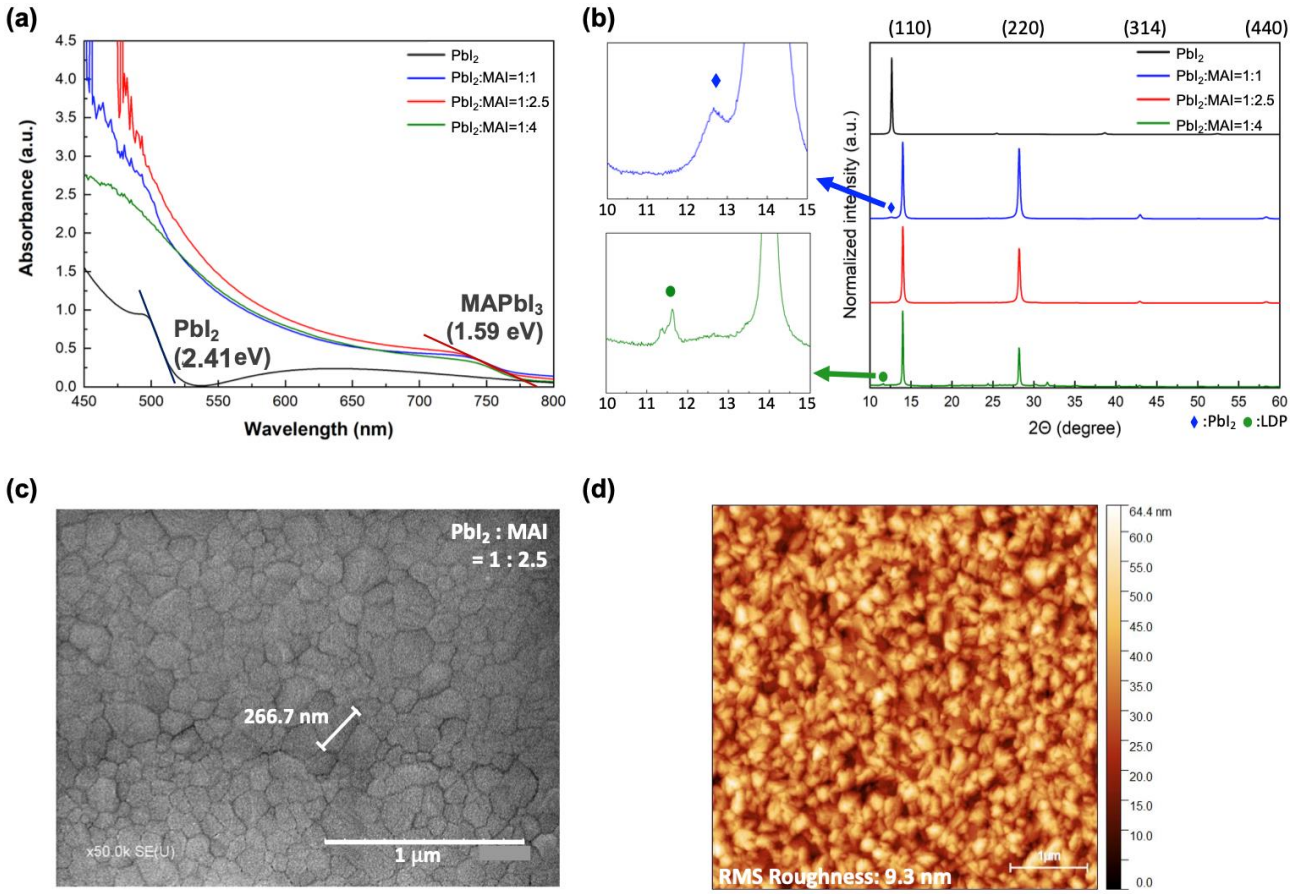


**Figure 3.8** (a) Absorbance graph and (b) XRD patterns of  $\text{PbI}_2$  and perovskite thin films deposited by co-evaporation with the deposition ratio of 1:1, 1:2.5, and 1:4. (c) SEM and (d) AFM image of  $\text{MAPbI}_3$  film prepared with optimized condition (1:2.5).

**Table 3.1** Observed XRD data according to deposition rate ratio.

Deposition rate ratio $\text{PbI}_2:\text{MAI}$	FWHM of (110) peak	$\text{MAPbI}_3$ (110)/(220) ratio	$\text{PbI}_2$ peak/ $\text{MAPbI}_3$ (110) peak	LDP peak/ $\text{MAPbI}_3$ (110) peak
1:1	0.24	1.04	0.02115	-
1:2.5	0.17	1.41	0.01346	-
1:4	0.13	1.91	-	0.05

These diffractions are caused by the presence of low-dimensional perovskites (LDPs). When the concentration of MAI is too high, the zero-dimensional (0D) quantum dots of  $(\text{PbI}_6)^{4-}$  units in an MAI matrix is favored. As the concentration decreases, the formation changes to one-dimensional (1D) perovskite and consequently to 2D perovskite sheets through self-assembly. Finally, 3D perovskite is formed and the concentrations of MAI and  $\text{PbI}_2$  are compatible (Fig. 3.9). LDPs occur because corner-sharing  $(\text{PbI}_6)^{4-}$  units are sandwiched between intercalated organic cation bilayers [173]. Therefore, the spacing between  $(\text{PbI}_6)^{4-}$  is expanded by  $\sim 1.4 \text{ \AA}$  compared with those in 3D perovskite ( $d = 6.3 \text{ \AA}$ ), which have the XRD peaks of LDP shift to a lower angle.

Through the results of absorption spectra and XRD patterns, we can confirm that deposition of

$\text{MAPbI}_3$  with the rate ratio  $\text{PbI}_2:\text{MAI} = 1:2.5$  is the best-optimized condition. Fig. 3.8 (c) and (d) show the top view SEM and AFM image of  $\text{MAPbI}_3$  film on the glass. The grain size is around 270 nm, and the roughness is 9.3 nm.

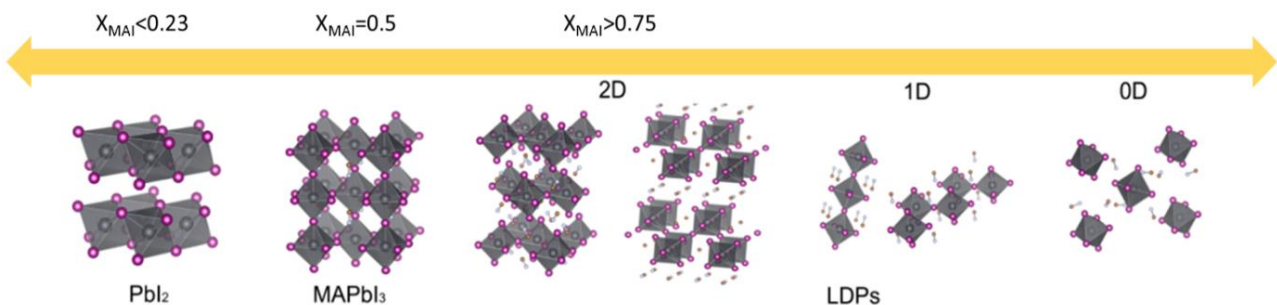


**Figure 3.9** Crystal structures of  $\text{PbI}_2$  and  $\text{MAPbI}_3$  perovskites in the form of 3D perovskite, 2D, 1D and 0D LDP where  $X_{\text{MAI}}$  defines the mole fraction of MAI in the mixture of MAI and  $\text{PbI}_2$  ( $X_{\text{MAI}}=n_{\text{MAI}}/(n_{\text{MAI}}+n_{\text{PbI2}})$ ) [173].

### 3.3.2 Impact of Rate of $\text{PbI}_2$ on $\text{MAPbI}_3$ Film Properties

Although the optimized deposition rate ratio of  $\text{PbI}_2 : \text{MAI}$  has been found, the overall rates of both  $\text{PbI}_2$  and MAI also need to be considered. The rate of  $\text{PbI}_2$ , which plays the role of a skeleton of  $\text{MAPbI}_3$  crystal structure, affects the morphology of  $\text{MAPbI}_3$  film [174], [175]. On the other hand, the rate of MAI strongly influences the chamber pressure, which is one of the important process parameters [176], [177]. Therefore, it is crucial to find the appropriate rates of  $\text{PbI}_2$  and MAI for the optimal morphology of  $\text{MAPbI}_3$  film. In this study,  $\text{PbI}_2$  was evaporated onto substrates with different deposition rates of 1, 1.5, and 2 Å/s with a fixed deposition rate ratio of  $\text{PbI}_2 : \text{MAI}$  (1:2.5). In addition, the  $\text{MAPbI}_3$  films with different rates of  $\text{PbI}_2$  and MAI were deposited on glass and PEDOT:PSS to investigate the crystalline properties of  $\text{MAPbI}_3$  according to the underlying layer.

Fig. 3.10 shows XRD patterns of  $\text{MAPbI}_3$  on glass according to the  $\text{PbI}_2$  rate. Detailed information on XRD peaks can be found in Table 3.2. With the increase of the  $\text{PbI}_2$  rate, the FWHM of the XRD (110) peak increases. This indicates that the crystallization of perovskite decreases and the quality of grains diminishes. In addition, the ratio of (110) to (220) decreases, and the (001) plane of  $\text{PbI}_2$  increases as the rate of  $\text{PbI}_2$  increases, which means the dominant plane of (110) in  $\text{MAPbI}_3$  is not fully formed, and the  $\text{PbI}_2$  phase remains. We guess it is more difficult for  $\text{PbI}_2$  to react with MAI at a higher rate.

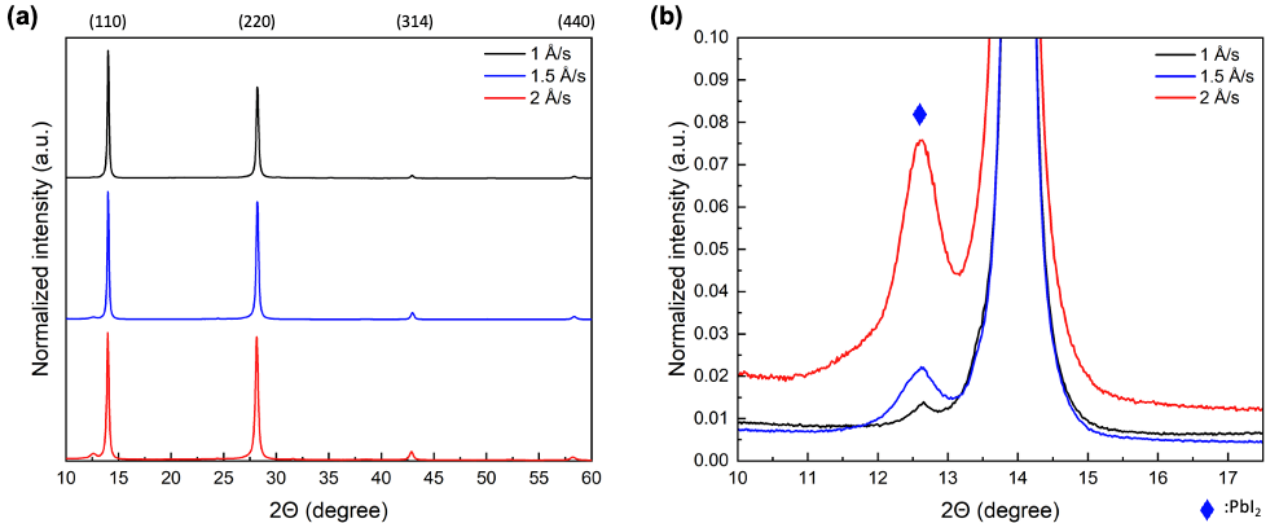


**Figure 3.10** (a) XRD patterns of perovskite thin films on glass with different PbI<sub>2</sub> rates of 1, 1.5, and 2 Å/s with the optimized deposition rate ratio. (b) Normalized XRD spectra of (110) diffraction peak with (001) plane of PbI<sub>2</sub> where blue diamond indicates (001) plane of PbI<sub>2</sub>.

**Table 3.2** Observed XRD data of MAPbI<sub>3</sub> on glass according to PbI<sub>2</sub> rates.

Rate of PbI <sub>2</sub>	FWHM of (110) peak	MAPbI <sub>3</sub> (110)/(220) ratio	PbI <sub>2</sub> peak/ MAPbI <sub>3</sub> (110) peak
1 Å/s	0.18	1.40	0.014
1.5 Å/s	0.20	1.08	0.022
2 Å/s	0.23	1.02	0.060

Before fabrication of standard PSCs, the crystalline property of MAPbI<sub>3</sub> on the hole transport layer is required to be considered. In the referential PSCs for this thesis, PEDOT:PSS is employed as HTL. MAPbI<sub>3</sub> films were deposited on PEDOT:PSS with different PbI<sub>2</sub> rates to investigate the property. XRD patterns of MAPbI<sub>3</sub> on PEDOT:PSS with detailed information are shown in Fig 3.11 and Table 3.3. When MAPbI<sub>3</sub> is deposited on PEDOT:PSS with PbI<sub>2</sub> rate of 1 Å/s, the FWHM of the XRD (110) peak is smaller than that of MAPbI<sub>3</sub> on glass with the same PbI<sub>2</sub> rate. PEDOT:PSS is a hydrophilic material, and the adhesion of MAI to PEDOT:PSS is higher than that to glass due to its hydrophilic nature. Because of the properties, the PbI<sub>2</sub> reacts more with MAI on PEDOT:PSS, and the crystallization of MAPbI<sub>3</sub> increases. The XRD results of MAPbI<sub>3</sub> on PEDOT:PSS, according to the PbI<sub>2</sub> rate, show patterns that are similar to those of MAPbI<sub>3</sub> on glass.

As the PbI<sub>2</sub> rate increases with the MAI rate at the same ratio, the (001) plane of PbI<sub>2</sub> increases for the same reason as those on glass. The (220) peak increases with the overall rate, and the peak is higher than the (110) peak at 2 Å/s of PbI<sub>2</sub>. The results indicate that the crystalline quality is worse than those on the glass when the rates of PbI<sub>2</sub> and MAI increase. Furthermore, the (001) plane of PbI<sub>2</sub> and LDP appear at the same time when the PbI<sub>2</sub> rate increases to 2 Å/s. It is worth noting that the reaction extent between PbI<sub>2</sub> and MAI is not uniform as the overall rate increases, so not only 3D

perovskite but also other phases including  $\text{PbI}_2$  and LDP are formed. Through these optimization processes with the variation of the overall deposition rate, we confirmed that the reaction of  $\text{PbI}_2$  and MAI into 3D  $\text{MAPbI}_3$  with dominated (110) is formed well at the low deposition rate.

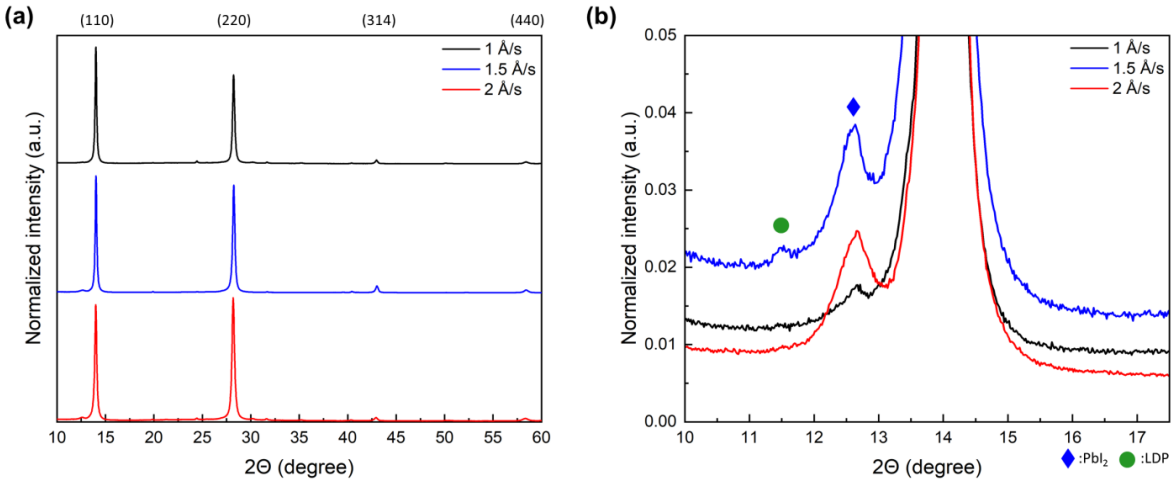


**Figure 3.11** (a) XRD patterns of perovskite thin films on PEDOT:PSS with different  $\text{PbI}_2$  rates of 1, 1.5, and 2  $\text{\AA/s}$  with the optimized deposition rate ratio. (b) Normalized XRD spectra of (110) diffraction peak with (001) plane of  $\text{PbI}_2$ .

**Table 3.3** Observed XRD data of  $\text{MAPbI}_3$  on PEDOT:PSS according to  $\text{PbI}_2$  rates.

Rate of $\text{PbI}_2$	FWHM of (110) peak	$\text{MAPbI}_3$ (110)/(220) ratio	$\text{PbI}_2$ peak/ $\text{MAPbI}_3$ (110) peak	LDP peak/ $\text{MAPbI}_3$ (110) peak
1 $\text{\AA/s}$	0.16	1.32	0.012	-
1.5 $\text{\AA/s}$	0.18	1.08	0.021	-
2 $\text{\AA/s}$	0.22	0.94	0.022	0.002

### 3.3.3 Impact of Hole Transport Layers on $\text{MAPbI}_3$ Film Properties

It is important to consider not only halide perovskite but also charge transport materials to achieve high photovoltaic efficiency in perovskite solar cells. Hole transport material (HTM) plays a variety of roles in the solar cells: (i) energetic barrier between anode and perovskite layer which prevents electrons from transferring to anode [178], (ii) enhancement of hole transfer efficiency [179], (iii) decision of the  $V_{oc}$  by controlling the splitting of the quasi Fermi-energy of halide perovskite [180]. In addition, the surface properties of HTMs in the inverted p-i-n structure PSCs affect the grain size, surface roughness, and crystal orientation of halide perovskite thin film [181]–[183]. The crystal orientation determines the type of surface defects in the perovskite and the interface quality between halide perovskite and top ETL.

Because of these reasons, it is crucial to find appropriate HTMs used in PSCs. Various hole transport

materials, including PEDOT:PSS, PTAA, and NiO, are used in this thesis, as shown in Fig.3.12. PEDOT:PSS is the first HTM used in the p-i-n structure PSCs, as mentioned in chapter 2, and it is also a typical HTM used in our laboratory. PTAA is another polymer HTM employed in PSCs. Both PEDOT:PSS and PTAA have higher hole mobility ( $1 \times 10^{-2} - 1 \times 10^{-3} \text{ cm}^2/\text{V}\cdot\text{s}$ ) compared with other polymers such as P3HT ( $3 \times 10^{-4} \text{ cm}^2/\text{V}\cdot\text{s}$ ) (Table 3.4). Compared to PEDOT:PSS, the solvent is hydrophobic, and the solution has lower acidity, which contributes to the higher stability of PSCs. NiO is an inorganic HTM with high transparency and deep valence band edge level, which matches well with those of  $\text{MAPbI}_3$  like PEDOT:PSS and PTAA [184]. Furthermore, its hole mobility is higher ( $1.4 \times 10^{-1} \text{ cm}^2/\text{V}\cdot\text{s}$ ) than polymer-based HTM. Additionally, the film can be deposited by a wet process such as thermal evaporation and sputtering which has the potential to achieve fully deposited PSCs.

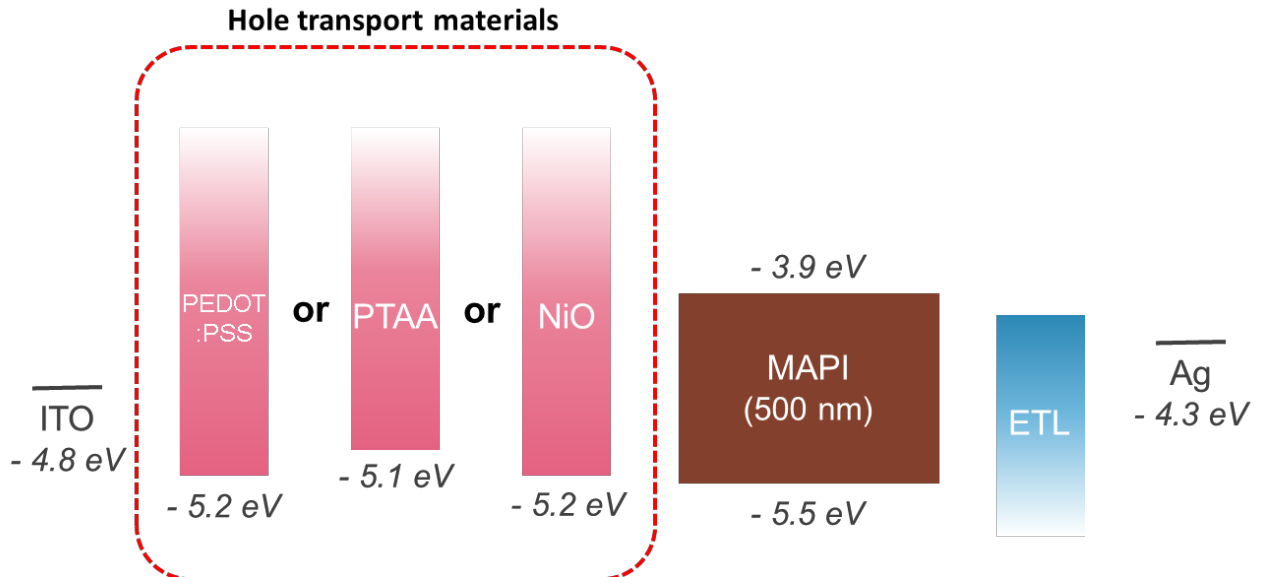


**Figure 3.12** Energy levels of HTMs including PEDOT:PSS, PTAA and NiO together with  $\text{MAPbI}_3$ , anode and cathode. Each valence band edge level of PEDOT:PSS, PTAA and NiO is referred to [184]–[186].

**Table 3.4** Hole mobility of HTM used in this thesis.

HTM	PEDOT:PSS	PTAA	NiO
Hole mobility ( $\text{cm}^2/\text{V}\cdot\text{s}$ )	$1 \times 10^{-2} - 1 \times 10^{-3}$ [187]	$1 \times 10^{-2} - 1 \times 10^{-3}$ [188]	$1.4 \times 10^{-1}$ [189]

However, the solution process used for NiO deposition in this study deteriorates the crystallinity of NiO and introduces defects that reduce hole extraction and increase carrier recombination [190], [191]. In addition, the defects cause rough contact with the perovskite layer, which deteriorates the crystalline quality and morphology of the halide perovskite layer. Therefore, to solve the problem, N4,N4,N4'',N4''-tetra([1,1'-biphenyl]-4-yl)-[1,1':4',1''-terphenyl]-4,4''- diamine (TaTm) is deposited between  $\text{MAPbI}_3$  and NiO as interlayer. TaTm has been recently used for interlayer in fully deposited PSCs with metal oxide-based HTMs [192].

Before fabrication of PSCs with these HTMs, 500 nm of MAPbI<sub>3</sub> layers on each HTM are characterized with optical measurements including SEM and XRD to investigate crystalline properties according to HTM underlayer.

Fig 3.13 (a) shows XRD patterns of MAPbI<sub>3</sub> on ITO/HTM where HTMs are PEDOT:PSS, PTAA, and NiO. Compared with the XRD pattern of MAPbI<sub>3</sub> on ITO/PEDOT:PSS, the patterns of MAPbI<sub>3</sub> on PTAA or NiO, include the amorphous bump of ITO. It implies that the intensity of (110) and (220) planes in MAPbI<sub>3</sub> on PEDOT:PSS is so high that the amorphous phase of ITO is negligible. In addition, ITO peaks in the XRD pattern of MAPbI<sub>3</sub> on NiO are more significant than those on PTAA. It is worth noting that the crystallinity of MAPbI<sub>3</sub> on PTAA and NiO is lower than on PEDOT:PSS. Especially, the intensity of perovskite crystalline planes is the weakest in those on PTAA. There is evidence to support the results. The (001) plane of PbI<sub>2</sub> at 12.6 ° is remarkable in MAPbI<sub>3</sub> on PTAA and NiO. The PbI<sub>2</sub> peak of MAPbI<sub>3</sub> on PTAA is higher than those of NiO. On the other hand, LDP appears in the spectra of MAPbI<sub>3</sub> on NiO, indicating that both the 3D phase and lower-dimensional phase also exist in MAPbI<sub>3</sub> deposited on NiO.

To improve the crystalline quality of MAPbI<sub>3</sub> on NiO, TaTm is inserted between MAPbI<sub>3</sub> and NiO. Fig. 3.13 (b) presents XRD patterns of MAPbI<sub>3</sub> on NiO without and with TaTm. When the interlayer is inserted, the (001) plane of PbI<sub>2</sub> at 12.07° decreases however, the perovskite phase, including (110), (222), and (314) peaks at 14.08 °, 31.68 °, and 42.95 °, noticeably increases. Through the XRD results, we confirmed that TaTm has a passivation effect with an enhancement of crystalline quality of MAPbI<sub>3</sub>.

The HTM underlayer makes an impact on the grain growth, as shown in SEM (Fig. 3.14). The MAPbI<sub>3</sub> film on PEDOT:PSS (Fig. 3.14(a)) is flat, uniform, pinhole-free, and covers the entire substrate. In addition, the grain is the biggest in all films prepared, with a size of around 400 nm. The result is coherent with the XRD result where (110) and (220) planes of MAPbI<sub>3</sub> are dominant. The hydrophilic surface of PEDOT:PSS and the optimal processing for deposition mentioned in section 3.3.2 promote grain growth.

In the case of the perovskite film on PTAA (Fig. 3.14(b)), the grain size is 200 nm. However, the grain size is not uniform, with small grains of ~100 nm. It is caused by the hydrophobic surface of PTAA. The adhesion of MAI to the surface is weak on the surface which disturbs the grain growth. The fact that the PbI<sub>2</sub> peak in the XRD pattern of MAPbI<sub>3</sub> on PTAA is the highest can also be explained by the surface property of PTAA. Through these results of PEDOT:PSS and PTAA, we confirmed that the surface wettability of HTM can primarily affect the grain size of the deposited MAPbI<sub>3</sub> films [193], [194]. In the SEM image of MAPbI<sub>3</sub> film on NiO (Fig. 3.14(c)), the grain size

is around 200 nm and much more uniform than those on PTAA. On the other hand, the grain size significantly increases when the TaTm layer is between MAPbI<sub>3</sub> and NiO. The grain size is around 350 nm. The results are consistent with the XRD results and demonstrate that TaTm can passivate the defect of NiO and improve the crystalline quality of MAPbI<sub>3</sub>.

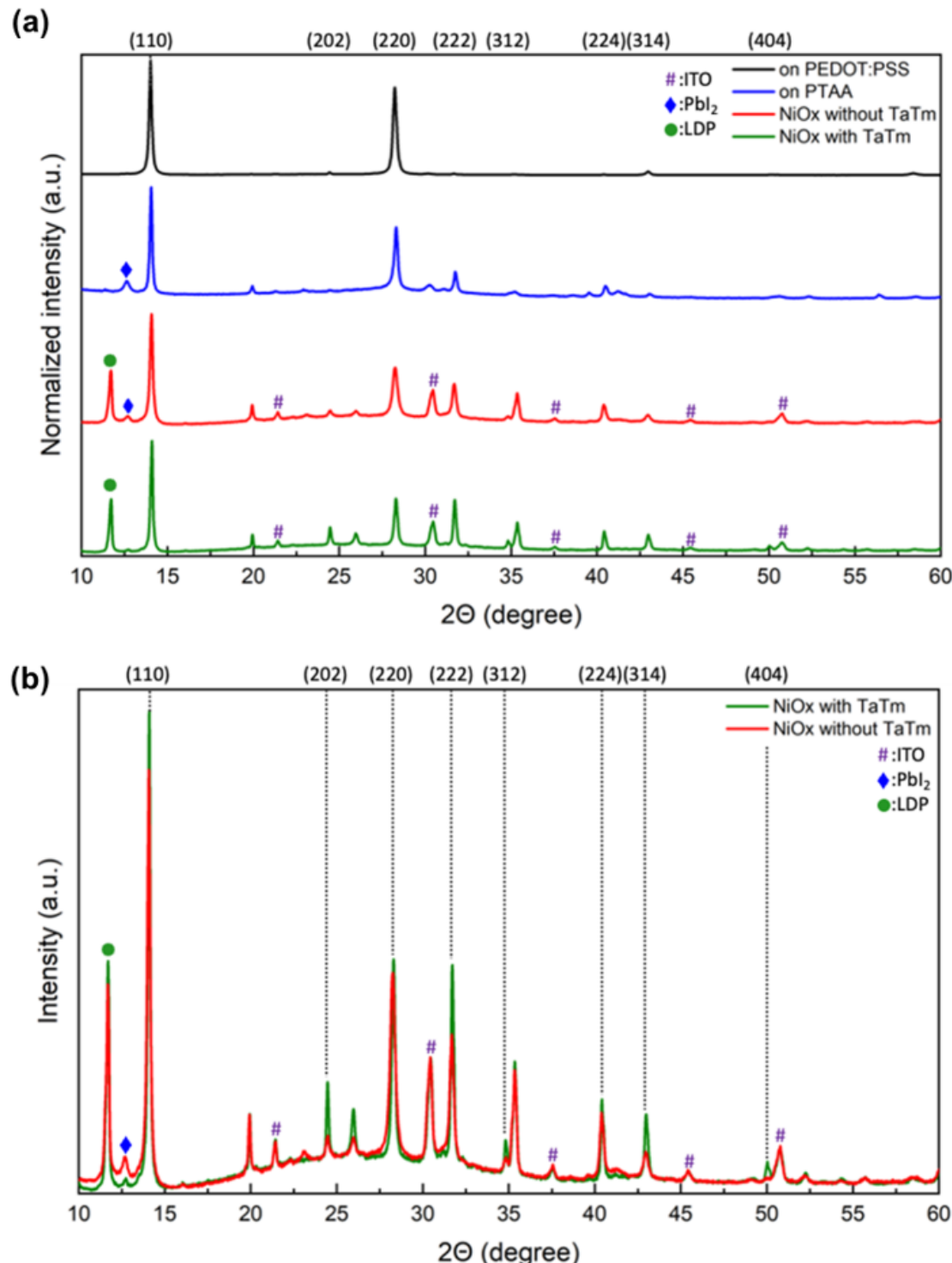


**Figure 3.13** (a) Characteristic peak intensity normalized XRD patterns of MAPbI<sub>3</sub> thin films on PEDOT:PSS, PTAA, and NiO with and without TaTm. (b) XRD patterns of MAPbI<sub>3</sub> thin films on NiO according to the presence of TaTm interlayer.

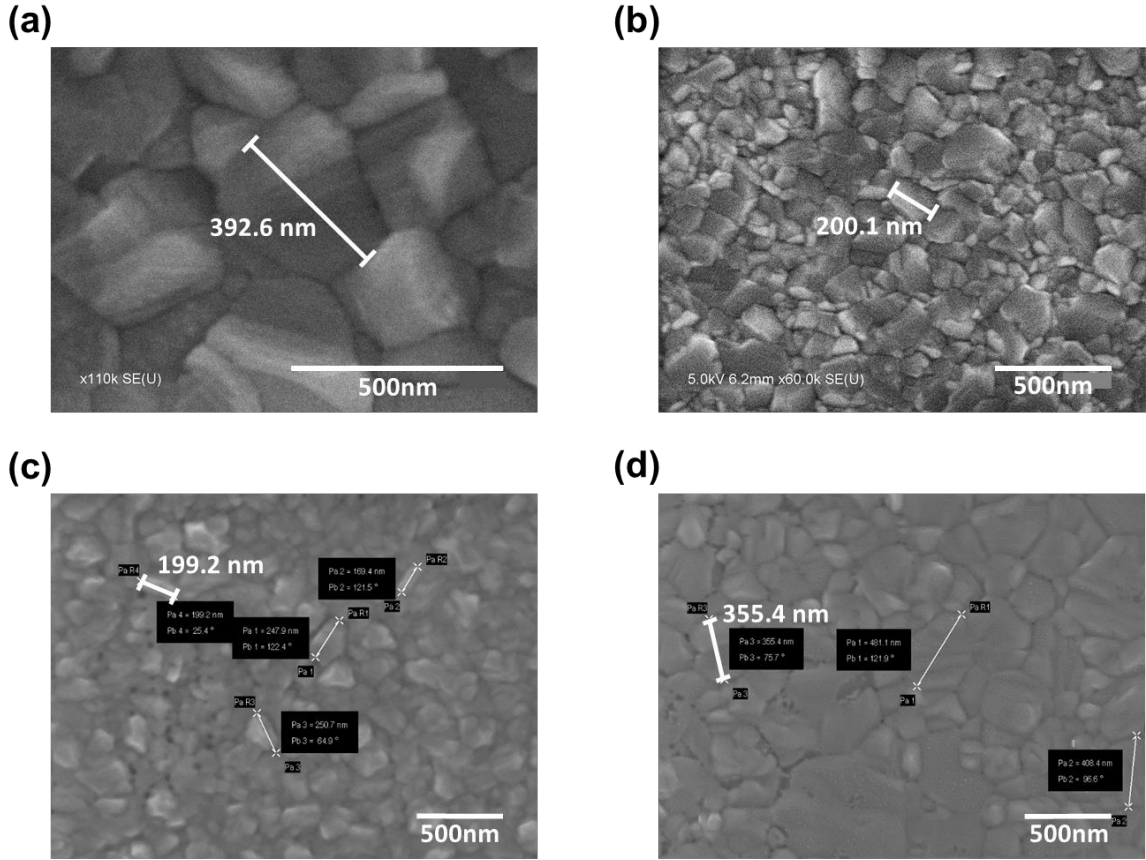


**Figure 3.14** Grain size analyses. Top-view SEM images of grains in the MAPbI<sub>3</sub> films on (a) PEDOT:PSS, (b) PTAA, (c) NiO, and (d) NiO with TaTm interlayer.

## 3.4 Photovoltaic Performances of MAPbI<sub>3</sub> Solar Cells

### 3.4.1 Photovoltaic Performance of Reference Solar Cells

In the section 3.3, the optimal processing of MAPbI<sub>3</sub> deposition by varying parameters in vacuum deposition was presented. Furthermore, the perovskite films were analyzed according to the underlying HTM layer through optical measurements such as XRD and SEM. Based on the optimal process of the thin film, we fabricated the PSCs with MAPbI<sub>3</sub> film based on co-evaporation and analyzed the electrical characteristics of solar cells through measurement of J-V performance and EQE.

Fig. 3.15 (a), (b), and (c) present a schematic illustration of the energy band diagram of the structure and a real cross-sectional SEM image of the MAPbI<sub>3</sub> solar cell, respectively. This MAPbI<sub>3</sub> solar cell

was employed as the reference sample in the thesis. An inverted planar structure of PSCs with a well-matched energy band was applied. The structure included PEDOT:PSS, C<sub>60</sub>, and BCP used as HTL, ETL, and HBL (Fig 3.15 (a), (b)) respectively. The cross-sectional SEM image (Fig 3.15 (c)) shows that the thickness of the vacuum deposited MAPbI<sub>3</sub> layer is 500 nm which consists of single-grain without any grain boundaries that would be profitable for charge transport.

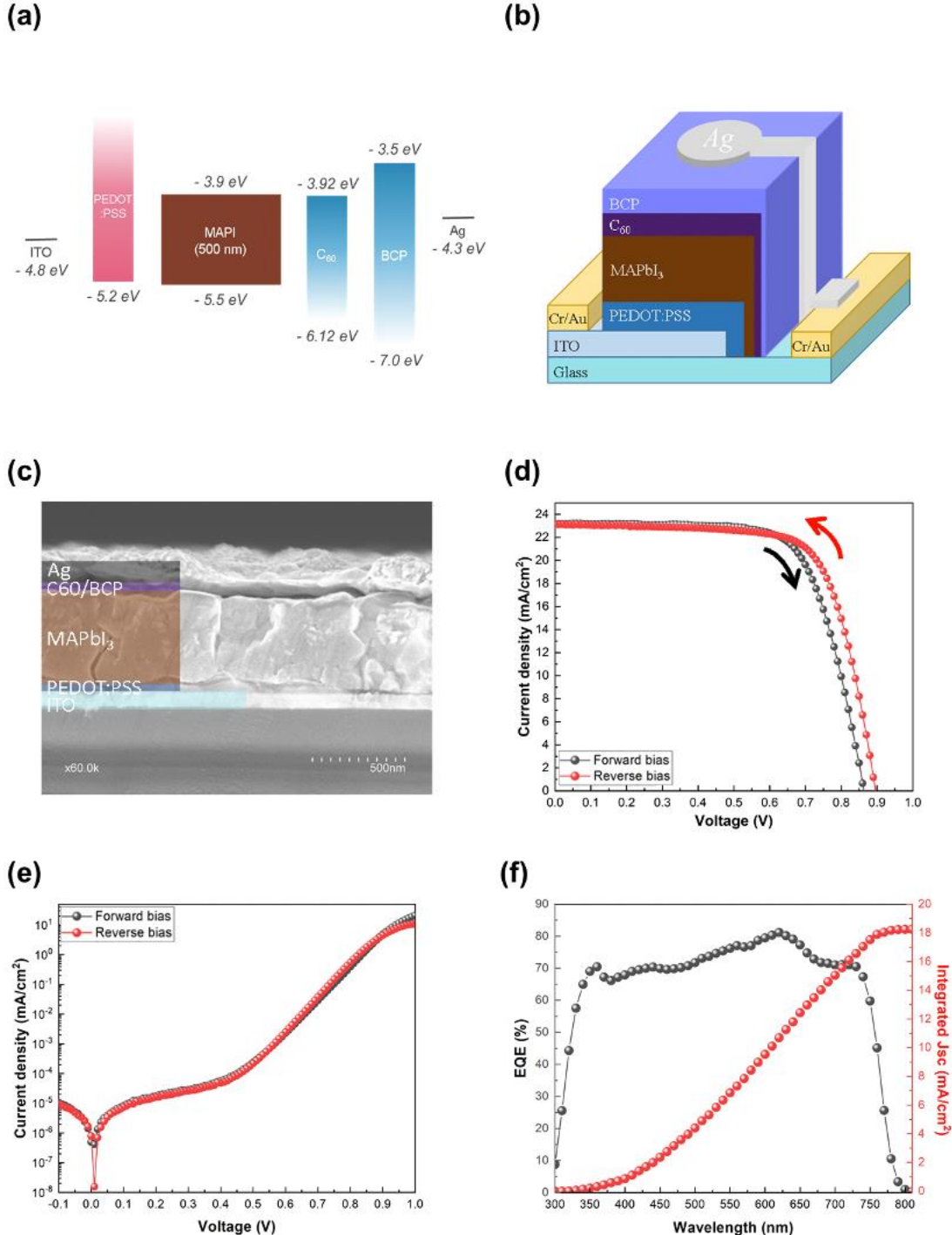


**Figure 3.15** (a) Energy diagram. (b) Device structure and (c) cross-sectional SEM image of the inverted p-i-n perovskite solar cells. Current density-voltage (J-V) curves of PSCs based on MAPbI<sub>3</sub> prepared by evaporation process measured (d) under 1-sun illumination, (e) under darkness. (f) The corresponding EQE spectrum.

**Table 3.5** Summary of photovoltaic parameters of the reference  $\text{MAPbI}_3$  solar cells according to scan direction.

	$V_{\text{OC}}$ (V)	$J_{\text{SC}}$ (mA/cm $^2$ )	FF (%)	$R_s$ (ohm)	$R_h$ (ohm)	PCE (%)	$J_{\text{SC}}$ (from EQE)
Forward scan	0.86	23.18	70.4	5.61	1.56k	14.10	
Reverse scan	0.90	23.14	71.4	4.93	1.42k	14.79	18.25

J-V characteristics of PSCs under the sun are described in Fig. 3.15 (d), where we obtained a  $J_{\text{SC}}$  of 23.14 mA/cm $^2$ , FF of 71.4 %, and a  $V_{\text{OC}}$  of 0.90 V, leading to a high PCE of 14.79 % (Table 3.5). To evaluate the hysteresis effect of the device, J-V curves were measured in the forward scan direction (from reverse bias to forward bias, R-F) and backward scan direction (from forward bias to reverse bias, F-R) at a scan rate of 10 mV/s. For the normal J-V hysteresis phenomenon in PSCs, the efficiency of F-R scan is higher than that of the R-F scan. Normal hysteresis is typically shown at pre-poling biases larger than the open circuit bias because of accumulated ionic and electronic polarization charges at the interfaces. On the other hand, inverted hysteresis is the opposite [195]. Hysteresis index can be calculated by Eq. 3.1

$$HI = \frac{PCE_{RB} - PCE_{FB}}{PCE_{RB}} \quad (3.1)$$

The hysteresis index is calculated to be 0.05 with inverted hysteresis, and its value is low enough.

Fig. 3.15 (e) shows the dark J-V curve of the solar cells, and it provides valuable information related to  $R_s$ ,  $R_{\text{SH}}$ , and FF. The dark current of the device under reverse bias is significantly low, suggesting that the reference PSC shows a low leakage current. In the forward bias region after 0.85 V, the injected current density is high, indicating that the injection barrier between the transport layer and perovskite is low. The results show that the device has high-quality interfaces between the perovskite layer and transport layers which is responsible for the high FF. EQE spectrum of the reference device is plotted in Fig. 3.15 (f). From the spectrum, we calculated the band gap since the EQE for photons with energy below the band gap should be ideally zero. 1.53 eV of the bandgap is obtained based on EQE, which is similar to the ideal value of the band gap of  $\text{MAPbI}_3$  (1.55 eV). In addition, short circuit current can be calculated from the spectrum and Eq. 3.2

$$J_{\text{SC}} = q \int_{\lambda_{\text{min}}}^{\lambda_{\text{max}}} \Phi(\lambda) \cdot EQE(\lambda) \cdot d\lambda \quad (3.2)$$

The current density calculated is 18.25 mA/cm $^2$ , which is lower than  $J_{\text{SC}}$  (23.14 mA/cm $^2$ ) obtained from J-V measurement under 1 sun illumination. Because the equipment for the EQE measurement is independent from that for the J-V measurement Zimmermann *et al.* explained that the actual irradiance of 100  $\mu\text{W}/\text{cm}^2$  used by the EQE machine is lower than AM 1.5G [196]. On that basis, these differences in irradiance between J-V and EQE measurement can be attributed to the error in

measurement of  $J_{SC}$ .

The device was stored in an  $N_2$  glove box and its J-V curves were measured periodically to assess the stability of the reference PSCs. Fig. 3.16 (a) presents the summary of PCE, and hysteresis index obtained from periodic measurements of the J-V curve done under illumination by a solar simulator. The reference device maintained more than 90% of its initial efficiency after eight weeks' storage in  $N_2$ . The results confirmed that PSCs based on evaporated  $MAPbI_3$  are more stable than those with solution-processed  $MAPbI_{3-x}Cl_x$  and triple cation perovskite ( $MA_{0.17}FA_{0.83})_{0.95}Cs_{0.05}Pb(I_{0.83}Br_{0.17})_3$  (3CP) fabricated in our laboratory. Solution-processed  $MAPbI_{3-x}Cl_x$  and 3CP solar cells fabricated in LPICM maintained less than 60 % after eight weeks' storage in  $N_2$  [197]. In addition, the hysteresis index also remained lower than 0.05, suggesting that  $MAPbI_3$  solar cells based on co-evaporation are stable under nitrogen. To check the reproducibility of  $MAPbI_3$  PSCs, a statistical histogram of PCE of 19 individual devices is shown in Fig. 3.16 (b). The average efficiency of the solar cells is  $12.51 \pm 2.28\%$ . The efficiency is reliable enough to study the phenomena in PSCs. High efficiency with high reproducibility through this optimization process of PSCs based on the results in section 3.3. We designate the PSCs achieved in this section as the reference PSCs in this thesis.

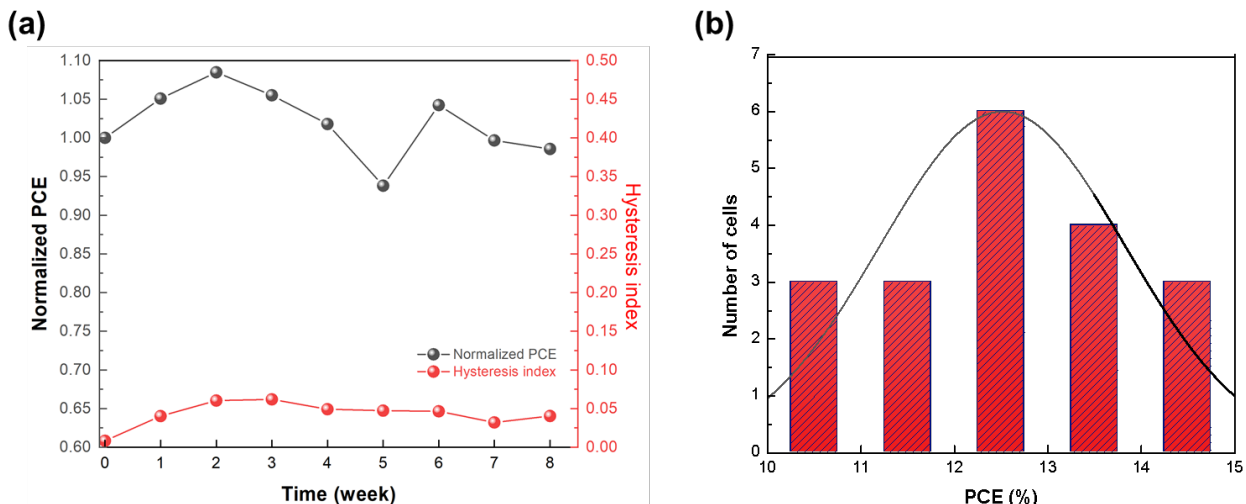


**Figure 3.16** (a) Summary of PCE and hysteresis index of perovskite solar cell stored in  $N_2$  and under darkness. (b) Statistical histogram of PCE of 19 individual devices.

### 3.4.2 Impact of Electron Transport Materials on Photovoltaic Performance

Electron transport materials (ETMs) extract photo-generated electrons from halide perovskite absorber layers and transport them to the cathode. Especially, the rough film of halide perovskite and grain boundary cause high leakage current. Upper ETL in the inverted structure PSCs improves

surface coverage compared to that of perovskite layer-only, and the ETL avoids the degradation at the interface between metal and halide perovskite interface [198]. In addition, the implementation of efficient hole blocking layers (HBLs) is also important for high efficiency in PSCs. HBLs permit charge separation and prevent the recombination of the electric charges by blocking hole transfer to the cathode. Therefore, appropriate ETMs and HBL materials are required for high-performance PSCs. C<sub>60</sub> and PCBM are representative fullerene derivatives used for ETM in the inverted structure PSCs. BCP is a typical material for HBL in PSCs.

In this section, the PSCs with C<sub>60</sub> and PCBM are presented, and their J-V performances are compared. The energy band and device structure of PSCs according to ETM are described in Fig. 3.17. C<sub>60</sub> is generally deposited on the halide perovskite layer by vacuum evaporation. PCBM consists of C<sub>60</sub> buckyball and an additional functional group that improves the solubility in organic solvents, including chlorobenzene. Therefore, PCBM is deposited by spin-coating. Conduction band maximum (CBM) of C<sub>60</sub> is -3.92 eV [199] and higher than that of PCBM (Fig. 3.17 (a) and (c)).

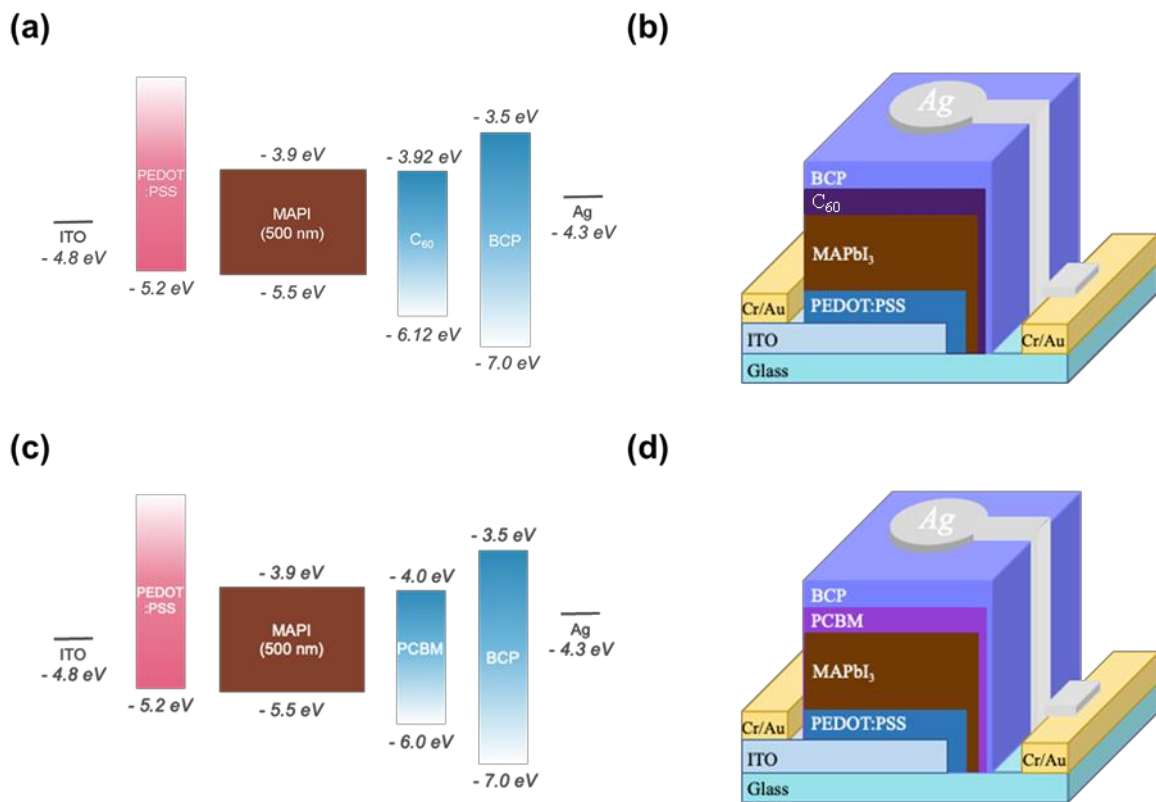


**Figure 3.17** The energy diagram of p-i-n MAPbI<sub>3</sub> solar cells with (a) C<sub>60</sub> and (c) PCBM. Device structure of PSCs (b) C<sub>60</sub> and (d) PCBM. MAPbI<sub>3</sub> was deposited between PEDOT:PSS and C<sub>60</sub> or PCBM by co-evaporation.

Fig. 3.18 shows J-V curves of PSCs with C<sub>60</sub> and PCBM measured under the standard condition (AM1.5G). Table 3.6 summarizes the photovoltaic performance of each PSC according to ETM and scanning direction. For the reference MAPbI<sub>3</sub> PSCs with C<sub>60</sub>, the photovoltaic performance is described in section 3.4.1. In the case of PSCs with PCBM, a J<sub>SC</sub> of 20.96 mA/cm<sup>2</sup>, FF of 68.7 %, a

$V_{OC}$  of 0.82 V, and a high PCE of 11.87 % are achieved in a reverse scanning direction. The HI calculated with Eq. 3.1 is 0.03, which is low enough to be negligible.

When two PSCs with  $C_{60}$  and PCBM are compared in a reverse scan, both  $V_{OC}$  and  $J_{SC}$  of the PSC with  $C_{60}$  were found to be higher than those of PCBM. The energy level of  $C_{60}$  is a better match with that of perovskite compared to PCBM (Fig. 3.17 (a) and (c)). This facilitates the electron transfer from perovskite to cathode more effectively, thus reducing the electron-hole recombination and increasing carrier lifetimes. In addition, the  $R_s$  of the PSC with  $C_{60}$  is lower, and its FF is higher than those of PCBM. These results could correspond to a solvent effect. After deposition of PCBM on vacuum deposited  $\text{MAPbI}_3$ , the residual chlorobenzene molecules are left after spin-coating of PCBM and act as defects at the interface between  $\text{MAPbI}_3$  and PCBM. In addition,  $\text{MAPbI}_3$  is damaged by the solvents. Therefore,  $C_{60}$  prepared by evaporation enables high interface quality which approaches high FF and low  $R_s$ . Through the fabrication of two PSCs with different ETMs and measurements, we confirmed that a solvent-free interface results in high efficiency and good stability in PSCs.

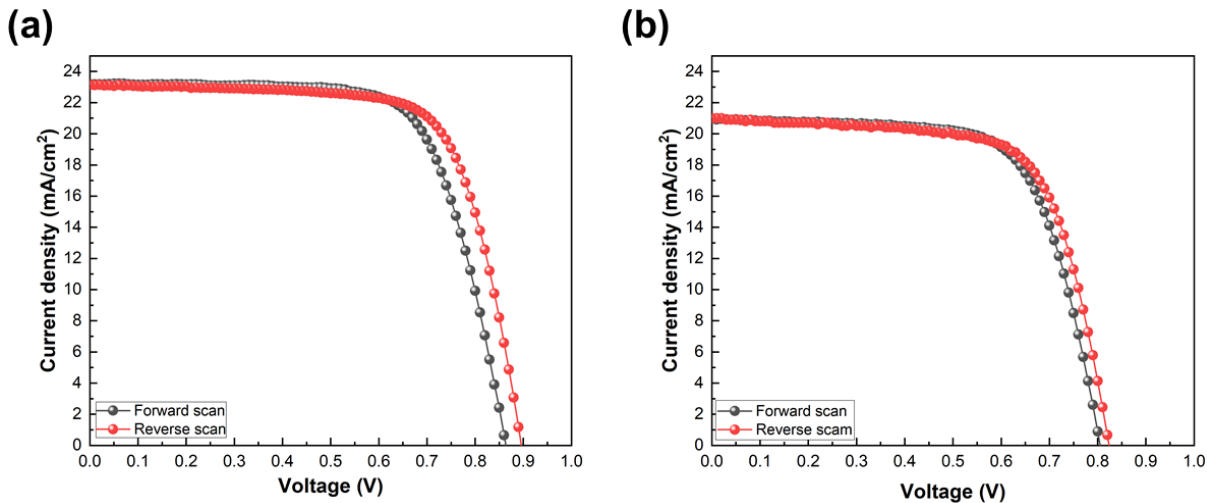


**Figure 3.18** J-V curves under 1-sun illumination of PSCs based on  $\text{MAPbI}_3$  with (a)  $C_{60}$  and (b) PCBM.

**Table 3.6** Output parameters of PSCs fabricated with  $C_{60}$  and PCBM according to scan direction.

ETM	Scan direction	$V_{OC}$ (V)	$J_{SC}$ ( $\text{mA}/\text{cm}^2$ )	FF (%)	$R_s$ (ohm)	$R_H$ (ohm)	PCE (%)
$C_{60}$	Forward scan	0.86	23.18	70.4	5.61	1.56k	14.10
	Reverse scan	0.90	23.14	71.4	4.93	1.42k	14.79
PCBM	Forward scan	0.81	20.97	68.5	5.73	1.63k	11.57
	Reverse scan	0.82	20.96	68.7	5.33	0.56k	11.87

### 3.4.3 Impact of Hole Transport Materials on Photovoltaic Performance

Based on the results of  $\text{MAPbI}_3$  thin film on different HTMs in section 3.3.3, PSCs with different HTMs were fabricated, and the photovoltaic performance was measured. Fig. 3.19 presents the structure of PSCs with different HTM, including PEDOT:PSS, PTAA, and NiO without and with the TaTm layer. In all structures, the thickness of  $\text{MAPbI}_3$  is 500 nm, and  $\text{C}_{60}$  and BCP are used for ETL and HBL, respectively.

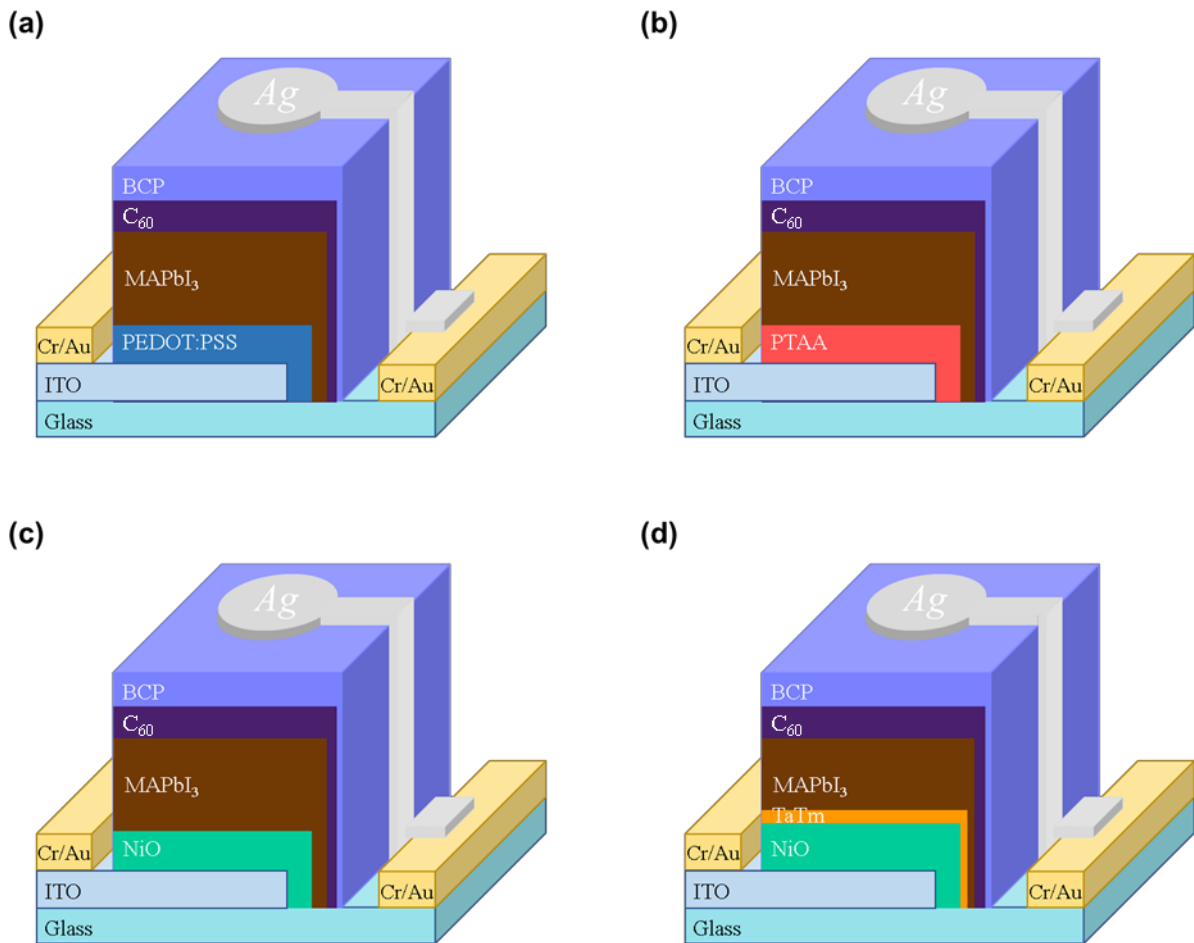


**Figure 3.19** Scheme of device structure of the PSCs with (a) PEDOT:PSS, (b) PTAA, and NiO (c) without and (d) with TaTm layer.

J-V curves of PSCs with different HTMs are reported in Fig 3.20. Photovoltaic parameters of the PSCs are described in Table 3.7. In the PSCs with PTAA, we obtained a  $J_{\text{SC}}$  of 21.10 mA/cm<sup>2</sup>, FF of 63.5 %, and a  $V_{\text{OC}}$  of 1.00 V, leading to a PCE of 13.39 % in a reverse scan.  $V_{\text{OC}}$  of the reference solar cell is lower than the PSC with PTAA, which originates from the potential loss and carrier recombination at the interface between  $\text{MAPbI}_3$  and PEDOT:PSS [200]–[203]. However, the FF of the PSCs with PTAA is lower than the reference solar cell. Because of the hydrophobic surface of PTAA, the grain size of  $\text{MAPbI}_3$  is smaller than the film on PEDOT:PSS (Fig. 3.14 (a) and (b)), which

increases the distribution of grain boundaries and deteriorates the interface between MAPbI<sub>3</sub> and PTAA with low FF. Additional process for enhancement of crystal quality of MAPbI<sub>3</sub> on PTAA is required.

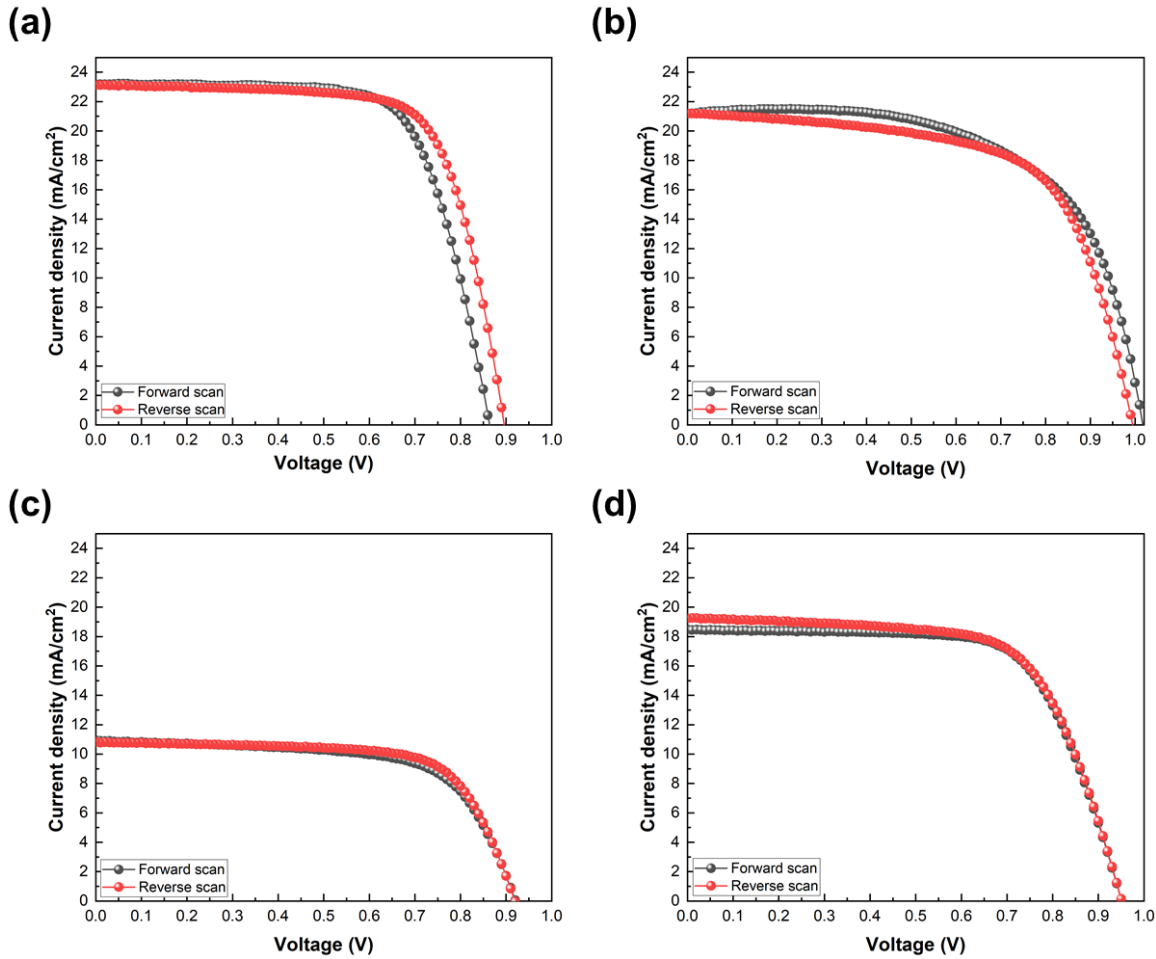


**Figure 3.20** J-V characteristics of MAPbI<sub>3</sub> PSCs with (a) PEDOT:PSS, (b) PTAA, and NiO (c) without and (d) with TaTm layer measured under the standard condition (AM1.5G).

**Table 3.7** Summary of photovoltaic parameters of MAPbI<sub>3</sub> solar cells with different HTMs according to scan direction

ETM	Scan direction	V <sub>OC</sub> (V)	J <sub>SC</sub> (mA/cm <sup>2</sup> )	FF (%)	R <sub>S</sub> (ohm)	R <sub>SH</sub> (ohm)	PCE (%)
PEDOT:PSS	Forward scan	0.86	23.18	70.4	5.61	1.56k	14.10
	Reverse scan	0.90	23.14	71.4	4.93	1.42k	14.79
PTAA	Forward scan	1.02	21.16	62.3	5.63	1.62k	13.40
	Reverse scan	1.00	21.20	63.5	6.69	0.52k	13.39
NiO w/o TaTm	Forward scan	0.92	10.94	65.5	11.1	0.53k	6.60
	Reverse scan	0.92	10.84	69.4	11.1	2.43k	6.92
NiO With TaTm	Forward scan	0.95	18.48	68.3	8.87	1.68k	12.01
	Reverse scan	0.95	19.23	65.9	8.68	1.05k	12.06

In the case of MAPbI<sub>3</sub> solar cell with NiO, a PCE of 6.92 % with a J<sub>SC</sub> of 10.84 mA/cm<sup>2</sup>, FF of 69.4 %, and a V<sub>OC</sub> of 0.92 V is obtained. The photovoltaic performance, especially J<sub>SC</sub>, is lower than those

of any other solar cells prepared. Interfacial vacancies and defects cause relatively low  $J_{SC}$  in the NiO thin film. The vacancies cause trap-assisted nonradiative recombination losses, which is demonstrated by the lower crystalline quality of  $\text{MAPbI}_3$  in XRD (Fig. 3.13 (b)) and the small grain size in the SEM image (Fig. 3.14 (c)). When the TaTm layer is between NiO and  $\text{MAPbI}_3$ , the  $J_{SC}$  almost doubles compared with those without TaTm. Furthermore, the  $R_s$  significantly decreases. With the XRD and SEM results (Fig. 3.13 (b) and Fig. 3.14(d)), it is worth noting that TaTm passivates the NiO surface and reduces the defects at the interface.

## **Chapter 4.**

# **Degradation in PSCs Caused by Electric Field and Exposure to Air Investigated with Impedance Spectroscopy**

---

<b>4.1 Introduction .....</b>	<b>91</b>
<b>4.2 Experimental Details.....</b>	<b>92</b>
4.2.1 Fabrication of Solar Cells for EIS measurement .....	92
4.2.2 Impedance Spectroscopy Measurement .....	95
4.2.3 Equivalent Circuit Modeling .....	96
<b>4.3 Analysis of Electric Field Induced Degradation.....</b>	<b>98</b>
4.3.1 EIS Results of the Reference MAPbI <sub>3</sub> PSCs.....	98
4.3.2 EIS Results by Applying the Electric Field.....	100
4.3.3 Presentation of the Hypothesis of Generation of Second Capacitance Caused by Electric Field.....	106
<b>4.4 Analysis of Degradation Caused by Air-Exposure.....</b>	<b>107</b>
4.4.1 EIS Results by Air Exposure.....	107
4.4.2 Application of Dielectric Modulus Spectroscopy to Study Degradation in PSCs.....	109
4.4.3 Discussion of Air Exposure Phenomena in the Reference PSCs .....	111

---

## **4.1 Introduction**

In chapter 2, we mentioned that EIS is a nondestructive electrical characterization method to measure the impedance response of a sample to an electric field as a frequency. EIS is employed to investigate dynamics such as relaxation times, energy storage, and dissipation energy processes in solid-state devices [204]–[206]. EIS has been verified to have an insight into the physical behavior of organic solar cells and dye-sensitized solar cells [132]. For example, Bisquert *et al.* applied EIS to achieve the information related to electro dynamics of dye-sensitized solar cells, including diffusion coefficient, electron recombination lifetime, diffusion length, and chemical capacitances [54], [132],

[207].

It has been reported that the high photovoltaic performance of PSCs is attributed to the properties of the halide perovskite structure, where component elements are connected by relatively weak chemical bonds, including ionic bonds, hydrogen bonds, and van der Waals interactions [208], [209]. This soft structure of halide perovskites involves not only electronic conduction but also ionic conduction, which causes ion migration. The two different carriers of electric and ionic charge carriers interact differently with the interface within PSCs, which plays a key role in device performance and stability. Therefore, it is crucial to understand the interfacial evolution under an operating environment. Meanwhile, the time scales of the motion of electronic charge and ionic charge carriers are totally different.

Because of these properties, EIS is a powerful technique for studying the property of charge distribution and the kinetic of charging processes in PSCs. For example, Park and Bisquert *et al.* first tried to apply EIS to PSCs to investigate the origin of hysteresis in PSCs [209], [210]. Studying the relaxation time of charge carriers in the frequency domain allows us to quantify the mobile ions in the halide perovskite at a given temperature. It leads to an understanding of the working mechanisms of PSCs. Furthermore, EIS allows operation under various environments, including different atmospheres, electrical bias, and temperatures, without damaging PSCs. Through EIS, interfacial and bulk processes can be studied separately.

In this chapter, we measured EIS and compared the results of PSCs with different halide perovskites, including  $\text{MAPbI}_3$  based on dry and wet processes, and  $\text{FAMACs}_{0.05}\text{Pb}(\text{I}_{0.83}\text{Br}_{0.17})_3$  prepared by spin-coating. In addition, we observed a second capacitance after applying an electrical bias to PSCs. Lastly, the EIS of the reference sample of PSCs is measured periodically to study the degradation mechanism in air. Through the measurement, we proposed a hypothesis that the degradation of grain promotes the accumulation of mobile ions at the interface.

## 4.2 Experimental Details

### 4.2.1 Fabrication of Solar Cells for EIS measurement

In order to study the influence of electrical bias by EIS measurements four kinds of PSC structures

were employed:

- i) ITO/PEDOT:PSS/MAPbI<sub>3</sub> [D]/C<sub>60</sub>/BCP/Ag
- ii) ITO/PTAA/MAPbI<sub>3</sub> [D]/PCBM/BCP/Ag
- iii) ITO/PEDOT:PSS/MAPbI<sub>3</sub> [W]/PCBM/Ag
- iv) ITO/PEDOT:PSS/(MA<sub>0.17</sub>FA<sub>0.83</sub>)<sub>0.95</sub>Cs<sub>0.05</sub>Pb(I<sub>0.83</sub>Br<sub>0.17</sub>)<sub>3</sub> (3CP)/PCBM/Ag

The structures and their energy band diagram are shown in Fig 4.1 and Fig. 4.2. Here i) is the reference sample of PSC in this thesis. This sample is also used for the study of degradation in air. In the structures, [D] of MAPbI<sub>3</sub> [D] indicates a dry process. MAPbI<sub>3</sub> [D] is deposited by co-evaporation. On the contrary, [W] of MAPbI<sub>3</sub> [W] means the wet process. MAPbI<sub>3</sub> [W] is formed by spin-coating. With two MAPbI<sub>3</sub> formed with different methods, we can confirm the properties of impedance according to the deposition process. (MA<sub>0.17</sub>FA<sub>0.83</sub>)<sub>0.95</sub>Cs<sub>0.05</sub>Pb(I<sub>0.83</sub>Br<sub>0.17</sub>)<sub>3</sub> (3CP) is created to enhance the stability by Saliba and his co-workers [29].

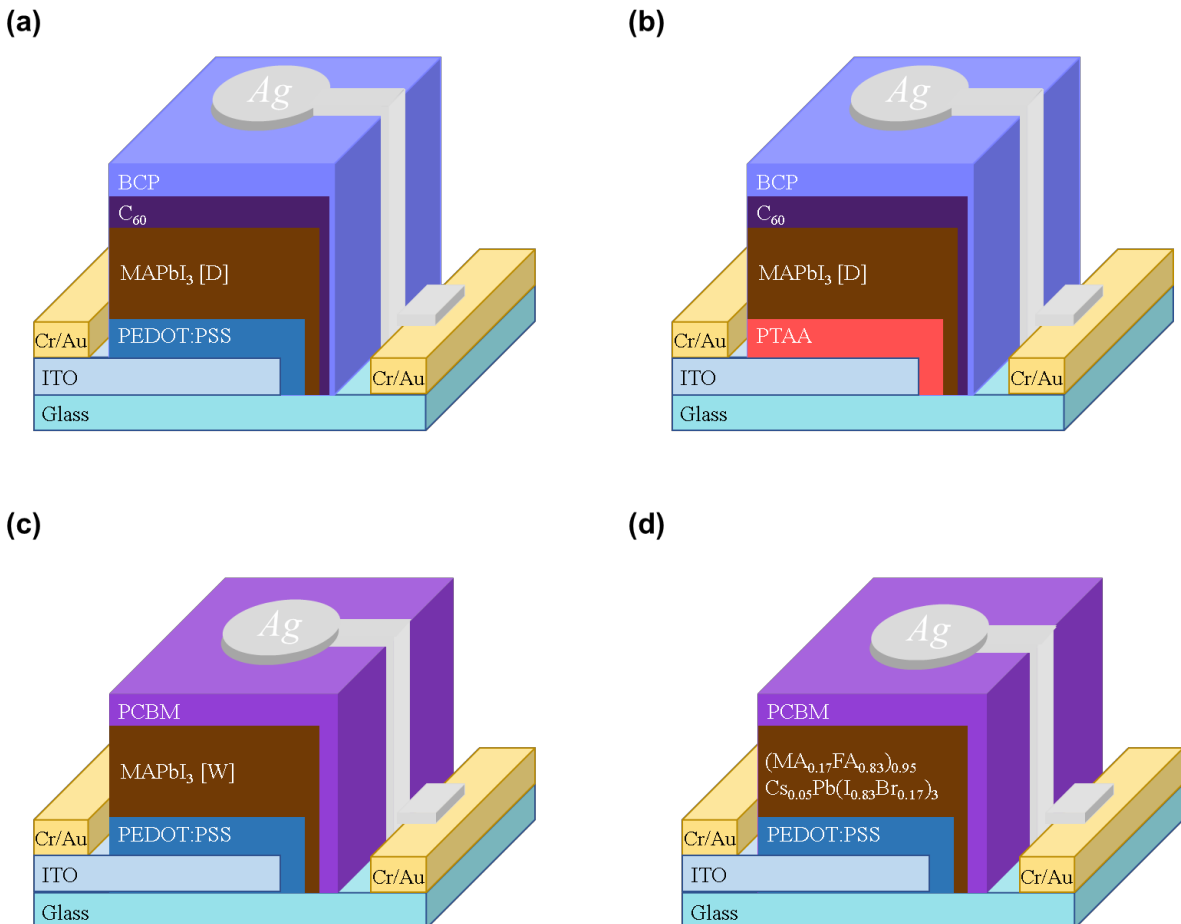


**Figure 4.1** Schematic illustration of PSCs structure: (a) The reference solar cells (i). PSCs with (b) co-evaporated MAPbI<sub>3</sub> (ii), PTAA (iii) and, (c) spin-coated MAPbI<sub>3</sub> and (d) (MA<sub>0.17</sub>FA<sub>0.83</sub>)<sub>0.95</sub>Cs<sub>0.05</sub>Pb(I<sub>0.83</sub>Br<sub>0.17</sub>)<sub>3</sub> (iv). Here, [D] of MAPbI<sub>3</sub> [D] means dry process, and [W] of MAPbI<sub>3</sub> [W] indicates wet process.

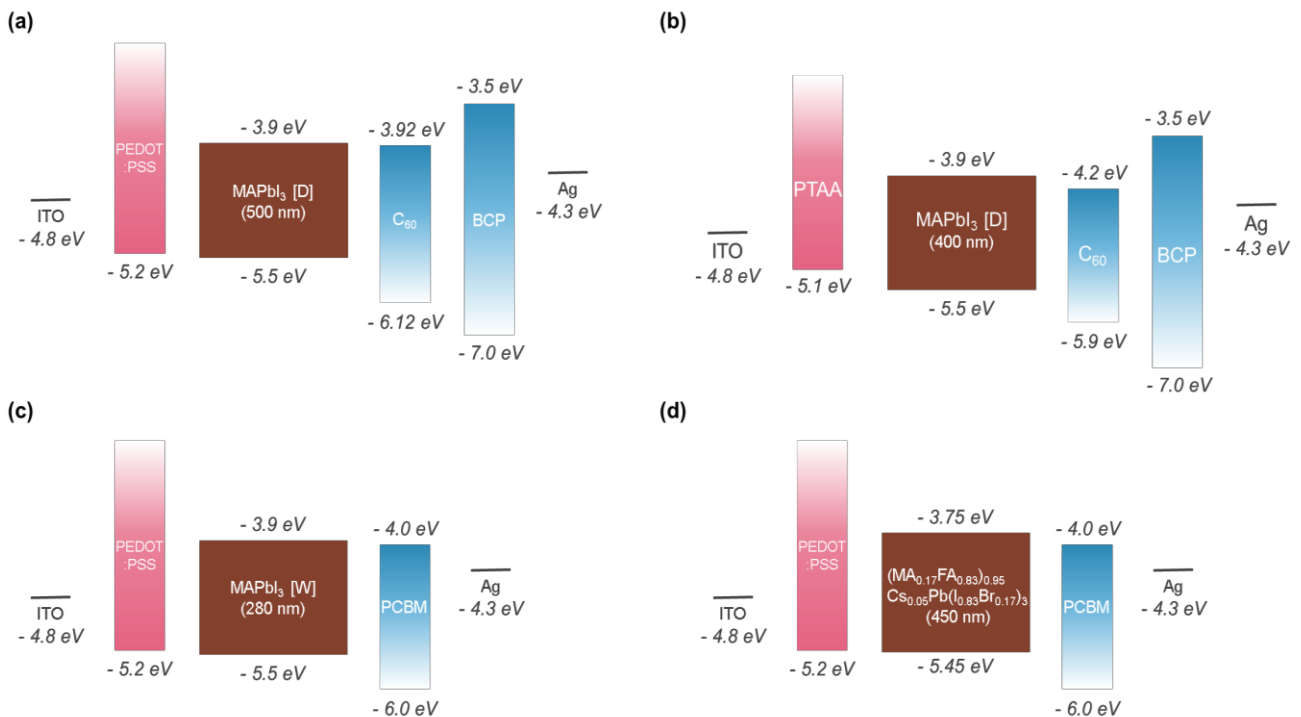


**Figure 4.2** The energy diagram of PSC (a) (i), (b) (ii), (c) (iii), and (d) (iv).

An organic cation of formamidinium (FA) has been proposed because the bandgap of FAPbI<sub>3</sub> is slightly smaller than those of MAPbI<sub>3</sub>, which is beneficial to the solar light-harvesting efficiency [211]. However, pure FAPbI<sub>3</sub> is divided into a non-perovskite hexagonal  $\delta$ -phase or a photoactive perovskite  $\alpha$ -phase which causes thermal and structural instability [28]. Therefore, a higher PCE of 18 % with a more thermally and structurally stability was obtained by mixing FA and a small amount of MA [212]. Furthermore, yellow phase impurities are suppressed, and highly uniform perovskite grains are formed by adding Cs to the mixtures of MA and FA. Through comparison of PSC with MAPbI<sub>3</sub> and those with 3CP, the impedance properties according to the stoichiometry of halide perovskite can be investigated.

The fabrication details of each layer in PSCs are explained as shown below.

**Hole transport layer (HTL)** In this chapter, PEDOT:PSS, and PTAA were employed as HTL. A full explanation of the deposition is described in section 3.2.2.

**Absorber layer** MAPbI<sub>3</sub> based on co-evaporation and spin-coating and 3CP are used in this chapter. The deposition of MAPbI<sub>3</sub> through co-evaporation is addressed in section 3.2.1. In the case of MAPbI<sub>3</sub> based on the wet process, the MAPbI<sub>3</sub> precursor solution (60  $\mu$ L) was spin-coated on PEDOT:PSS layer at 6000 rpm for 30 seconds in N<sub>2</sub> filled glove box. The film was annealed at 80 °C for 120 minutes in an N<sub>2</sub> environment. The precursor solution was a mixture of methylammonium iodide (MAI, Ossila), lead chloride (PbCl<sub>2</sub>, Aldrich), and lead iodide (PbI<sub>2</sub>, Alfa Aesar) at a molar

ratio ( $\text{PbCl}_2:\text{PbI}_2:\text{MAI}$ ) of 1:1:4 dissolved in anhydrous dimethylformamide (DMF, Aldrich). The solution (38 wt%) was stirred at 70 °C in a glove box for 12 hours.

For 3CP, 1.1 M of  $\text{PbI}_2$ , 0.2 M of  $\text{PbBr}_2$ , 1 M of FAI (formamidinium iodide), and 0.2 M of MABr (methylammonium bromide) are dissolved in 8:2 (v:v) mixture of N,N-dimethylformamide (DMF) and dimethyl sulfoxide (DMSO). After the dissolution, 2  $\mu\text{L}$  of CsI solution (1.5 M in DMSO) was then added to the solution. FAI was purchased from Sigma Aldrich; MABr from Solaronix;  $\text{PbI}_2$ , and CsI from Alfa Aesar. 100  $\mu\text{L}$  of the 3CP solution was deposited on PEDOT:PSS layer by spin-coating. The film on the substrate was then annealed at 80 °C for 60 minutes.

Electron transport layer (ETL), Hole blocking layer (HBL), and Cathode PCBM and  $\text{C}_{60}$  were used in PSCs as ETL. In addition, BCP and Ag were employed in PSCs as HBL and cathode, respectively. The detailed information is mentioned in section 3.2.2.

#### 4.2.2 Impedance Spectroscopy Measurement

EIS is a valuable diagnostic technique for the in-situ monitoring of transport and recombination processes at different points along the current-voltage (I-V) curve. In addition, it is used to identify device aging and performance loss under various environments and investigate the influence of variation in the fabrication process on photovoltaic performance.

In general, the equipment setup of EIS is carried out with a potentiostat, a Faraday cage, and dedicated software (Fig. 4.3). The potentiostat is electronic hardware required to control a three-electrode cell. A SP-200 potentiostat was used from Biologic for EIS measurement. The sample was placed in a Faraday cage to isolate the EIS results from electromagnetic radiation and noise. The EIS equipment has its dedicated software (EC-Lab software) for setting measurement parameters, analyzing data, and exporting the data.

EIS measurement was carried out by applying a small alternating voltage signal ( $V_{AC}$ ) across the sample and measuring the alternating current response ( $I_{AC}$ ). The small AC voltage was superposed on a DC voltage offset to examine different points along the J-V curve of the solar cells. For a constant DC voltage offset, the frequency of the alternating voltage was changed, and AC current with the transfer function  $Z$  was measured at each frequency. The range of frequency was from  $10^{-2}$  to  $10^6$  Hz. The Direct current (DC) bias was fixed to 0 V with 50 mV of the amplitude of an alternate current (AC).

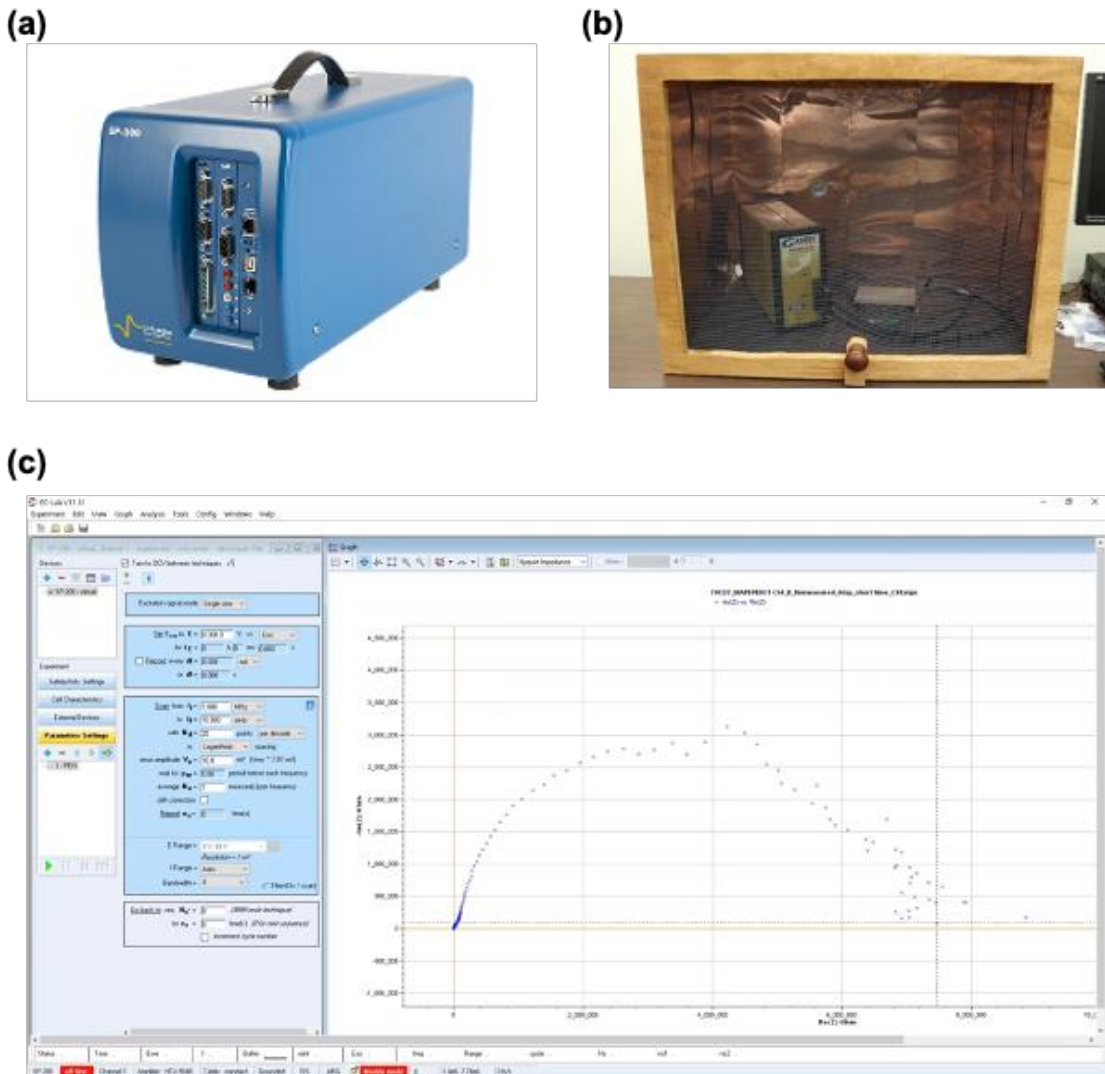


**Figure 4.3** (a) SP-200 potentiostat. (b) Faraday cage. (c) EC-Lab software.

### 4.2.3 Equivalent Circuit Modeling

The equivalent circuit model is one of the most widely applied approaches to analyzing the impedance data of solar cells. Equivalent circuit modeling quantifies the resistive and capacitive components in the impedance spectrum over the targeted frequency range. Because of this, equivalent circuit modeling is a relatively effective strategy for explaining the global sample response. To achieve meaningful results, the circuit model needs to be based on the basic physical parameter of the device. In the photovoltaic field, equivalent circuit models have been developed to explain the physical process of carrier diffusion and recombination in both darkness and illumination. Meanwhile, the Nyquist plot is widely used when equivalent circuit modeling is used to analyze data. As mentioned in chapter 2, the Nyquist plot is a polar plot where the magnitude and phase of the response to

frequency are expressed as polar coordinates. Through identification of the equivalent circuit for the Nyquist plot, the electrochemical properties of the solar cells can be analyzed. Furthermore, equivalent circuit modeling allows the impedance response of multilayer in solar cells to be quantified through a combination of circuit components, including capacitors inductors and Warburg impedance. Lastly, it allows rapid analysis and comparison of different frequency spectra.

Most equivalent circuit fitting programs are based on the Levenberg–Marquardt algorithm [213]. A Levenberg–Marquardt algorithm is a common approach to solving nonlinear least-squares problems. A parametrized function is fitted to the experimental data through the minimization of a sum of squares error between the simulated and the measured data points. Multiple iterations are used to minimize the object function  $S$  and optimize the fit parameters [213]

$$S = \sum_{i=1}^N \omega_i \left\{ [Z'_i - Z'_i(\omega_i, a_k)]^2 - [Z''_i - Z''_i(\omega_i, a_k)]^2 \right\} \quad (4.1)$$

where  $\omega_i$  is a weighting function,  $Z'_i - iZ''_i$  is the measured impedance data,  $Z_i(\omega_i, a_k) = Z'_i(\omega_i, a_k) - iZ''_i(\omega_i, a_k)$  is the fitting function, and  $a_k(k = 1, \dots, M)$  are the fitting parameters.  $Z_i(\omega_i, a_k)$  is linearized with a Taylor expansion, and the higher-order terms are neglected. The function can be expressed using circuit elements, including resistance, capacitance, and inductance. It is assumed that the impedance value of each element is linear, and therefore, a combination of the ideal circuit elements can be applied to explain the full spectrum of  $Z$  values.

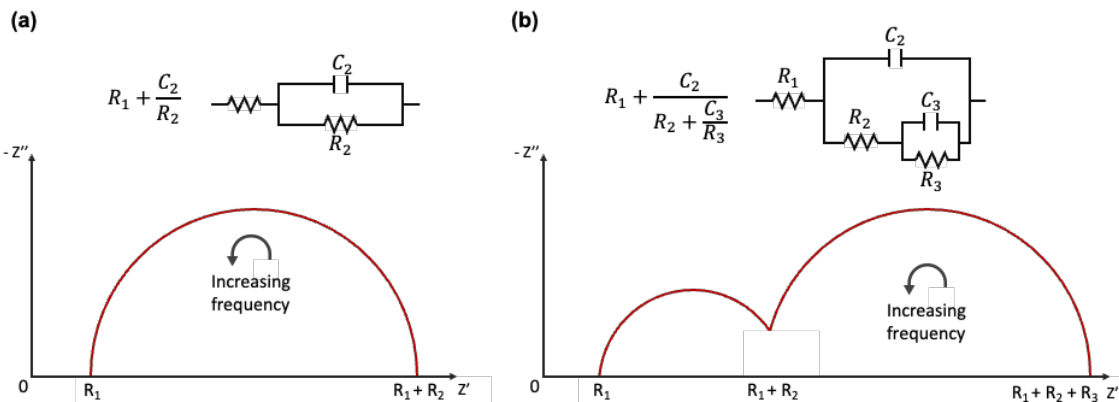


**Figure 4.4** Equivalent circuit model of (a)  $R_1 + C_2/R_2$  and (b)  $\{R_1 + C_2/(R_2 + C_3/R_3)\}$ .

A reasonable circuit model should be selected by users to achieve simulated data properly fitted with experimental data. The circuit model can be founded based on knowledge of the solar cells or established models from the literature. Starting value of the circuit elements is required to be validated by additional measurement. In our experiment,  $\{R_1 + C_2/R_2\}$  and  $\{R_1 + C_2/(R_2 + C_3/R_3)\}$  models are selected as shown in Fig. 4.4. After choosing the appropriate circuit model, EC-Lab fitting software from Biologics company is used to calculate each electric component (Fig. 4.5).

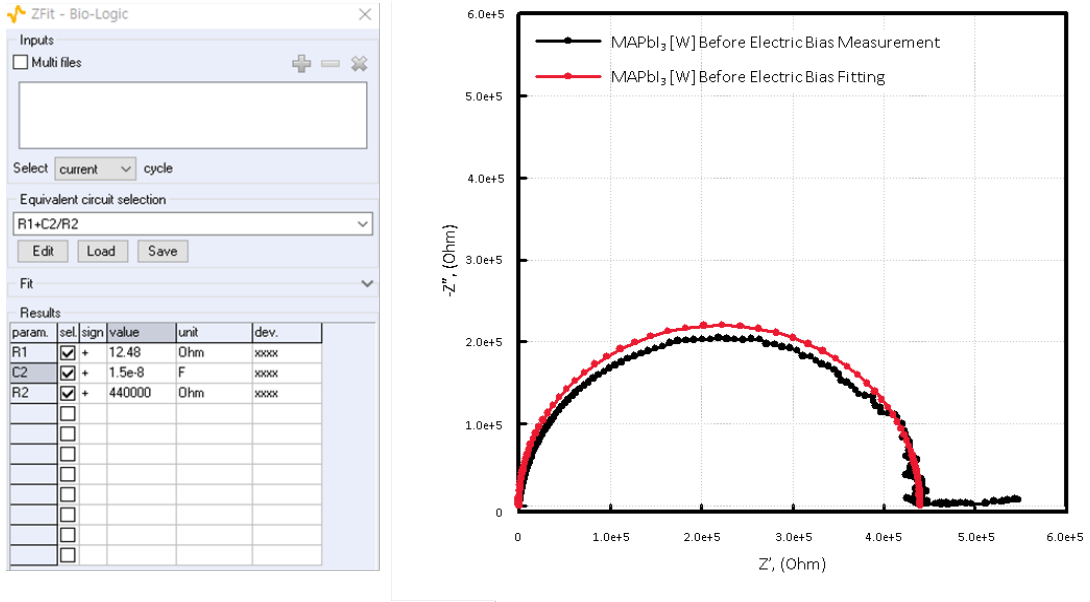


**Figure 4.5** One example of data fitting result according to Nyquist plot.

## 4.3 Analysis of Electric Field Induced Degradation

### 4.3.1 EIS Results of the Reference MAPbI<sub>3</sub> PSCs

Before studying the effect of electric bias and degradation under air in PSCs, EIS results of the reference solar cells (Fig. 4.1 (a) and Fig. 4.2 (a)) are shown to describe how to interpret the EIS results. Fig. 4.6 presents the EIS results of the optimized MAPbI<sub>3</sub> solar cell. Fig 4.6 (a) exhibits the Nyquist plot of the MAPbI<sub>3</sub> solar cell. EIS of the reference MAPbI<sub>3</sub> solar cell was measured under darkness in the air. An equivalent circuit was used to fit the impedance response in the figure. In the Nyquist plot of the measured MAPbI<sub>3</sub> solar cell, one big arc is observed and fitted with the simulated plot of R<sub>1</sub>+C<sub>2</sub>/R<sub>2</sub>.

In the equivalent circuit, the series resistance R<sub>1</sub> is contact resistance caused by the contact resistance of the electrical wire and contact metal, including ITO and Ag. It is deduced from a high-frequency intercept on the real axis. The value of R<sub>1</sub> extracted from the equivalent circuit modeling is 9.91 Ω. In the parallel resistor-capacitor (RC) element shown in the equivalent circuit, R<sub>2</sub> is related to the electron-hole charge recombination resistance (R<sub>rec</sub>), and the value of R<sub>2</sub> calculated by simulation is 4.1k Ω.

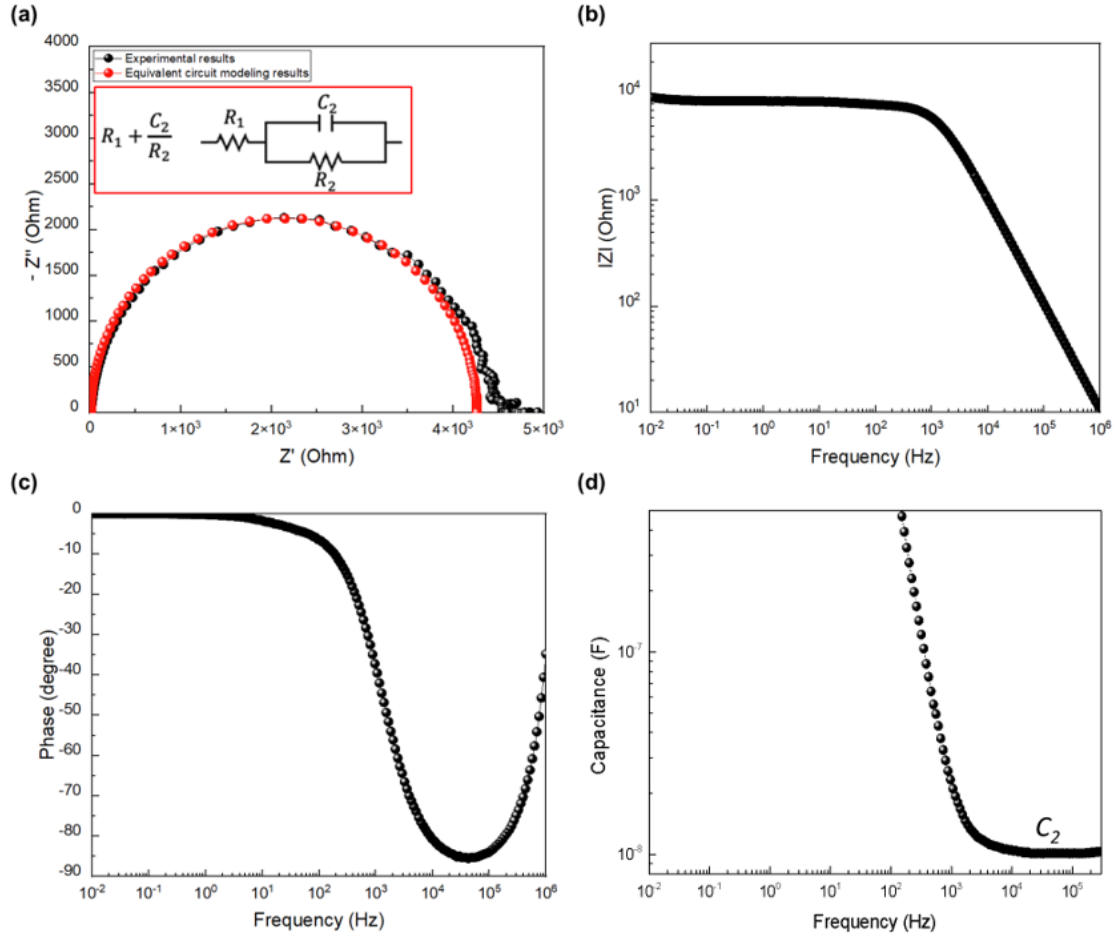


**Figure 4.6** (a) Nyquist plot of experimental results fitted with modeling results. Bode (b) impedance, (c) phase plot. (d) Capacitance versus frequency of the optimized MAPbI<sub>3</sub> solar cell under the dark condition.

Fig 4.6 (b) and (c) show Bode impedance and phase plots. In the Bode impedance plot (Fig. 4.6 (b)), the complex impedance ( $|Z|$ ) increases with a slope -1 at a high frequency which shows a pure capacitive behavior as the frequency decreases down to  $5 \times 10^3$  Hz. At lower frequencies than  $5 \times 10^3$  Hz,  $|Z|$  becomes independent of the frequency and reaches a plateau corresponding to a pure resistance. Accordingly, the phase Bode plots (Fig. 4.6 (c)) logically present a phase angle closed to -90 degrees at high frequency ( $6 \times 10^4$  Hz) and then drop to zero at a lower frequency.

In the capacitance curve versus frequency (Fig. 4.6 (d)), 10.1 nF of capacitance ( $C_2$ ) exists at a high-frequency region which is coherent with the Bode impedance and phase plots. The capacitance  $C_2$  is always present in the solar cells and indicates the geometrical capacitance ( $C_g$ ) of the planar solar cells. In the high-frequency region, the conductivity of halide perovskite is too low for the photovoltaic system to respond fast enough to the high-frequency AC excitation, which has the system behave like an insulator. Therefore, the geometrical capacitance is defined as:

$$C_g = \epsilon_0 \times \epsilon_r \times \frac{A}{t} \quad (4.2)$$

where  $\epsilon_0$  is the dielectric constant of vacuum ( $8.8541 \times 10^{-12}$  F/m),  $\epsilon_r$  is the relative dielectric constant,

$A$  is the area, and  $t$  is the thickness of the absorber layer. The relative dielectric constant of  $\text{MAPbI}_3$  calculated with the capacitance of  $9.64 \text{ nF}$  is 19, in agreement with the value deduced by other groups [140], [214]. Through the EIS measurement of the reference PSCs, we confirmed that the equivalent circuit of the fresh inverted p-i-n planar solar cell is  $R_1+C_2/R_2$ . In addition, each physical parameter in the PSCs can be quantified in the form of circuit parameters.

#### 4.3.2 EIS Results by Applying the Electric Field

Fig. 4.7 shows cross-section images of PSCs with dry processed  $\text{MAPbI}_3$ , wet-processed  $\text{MAPbI}_3$ , and 3CP, which is coherent with the schematics of PSC structure as shown in Fig. 4.1. These solar cells were employed in this study. In this section, the impact of HTL material, the deposition process, and the kind of halide perovskite on impedance properties are presented. The thicknesses of dry-processed  $\text{MAPbI}_3$  on PEDOT:PSS, PTAA, wet-processed  $\text{MAPbI}_3$ , and 3CP are 500 nm, 400 nm, 280 nm, and 450 nm, respectively. In all PSCs, any pinhole does not appear between the halide perovskite layer and the hole transport layer. Although the co-evaporation technique with the same condition is used for deposition of  $\text{MAPbI}_3$  on PEDOT:PSS and PTAA,  $\text{MAPbI}_3$  on PTAA consists of a relatively large number of grains as compared to those on PEDOT:PSS. If we consider the vertical axis of perpendicular to the interfaces of the different structures, spin-coated  $\text{MAPbI}_3$  on PEDOT:PSS, the layer is also composed of 1 grain. 3CP layer in the PSCs is made up of 2-3 grains.

The grain sizes of each halide perovskite are shown in Fig. 4.8. The average grain sizes of dry-processed  $\text{MAPbI}_3$  on PEDOT:PSS and PTAA, wet-processed  $\text{MAPbI}_3$  and 3CP are 400 nm, 200 nm, 500 nm, and 300 nm, respectively. Fig. 4.9 presents the XRD characterization of perovskite films. In all  $\text{MAPbI}_3$  films, the three tetragonal peaks  $\text{MAPbI}_3$  of (110), (220), and (310) peaks are shown with red stars at  $14.2^\circ$ ,  $28.6^\circ$ , and  $32.2^\circ$ . The 3CP film shares the same major perovskite peaks. However, (001) peak of  $\text{PbI}_2$  shown as a gray star at  $12.07^\circ$  remains in  $\text{MAPbI}_3$  film on PTAA and 3CP, which indicates that there still remains  $\text{PbI}_2$  that has not reacted with cation halide components. The grain size of co-evaporated  $\text{MAPbI}_3$  films on PEDOT:PSS and PTAA are explained in detail in section 3.3.3. spin-coated  $\text{MAPbI}_3$  film grain has a larger grain size than those of dry-processed  $\text{MAPbI}_3$  because of chloride. Liao *et al.* confirmed that the incorporation of minor chloride in  $\text{MAPbI}_3$  enhances film uniformity and grain growth [215]. Despite the incorporation of chloride, three tetragonal peaks of  $\text{MAPbI}_3$  are clearly shown in XRD results (Fig. 4.9 (c)). Therefore, the perovskite film is regarded as  $\text{MAPbI}_3$  in this study. For 3CP, the grain size of 3CP on PEDOT:PSS is smaller

than other MAPbI<sub>3</sub> films on the same HTM layer because of residual PbI<sub>2</sub> in the film.

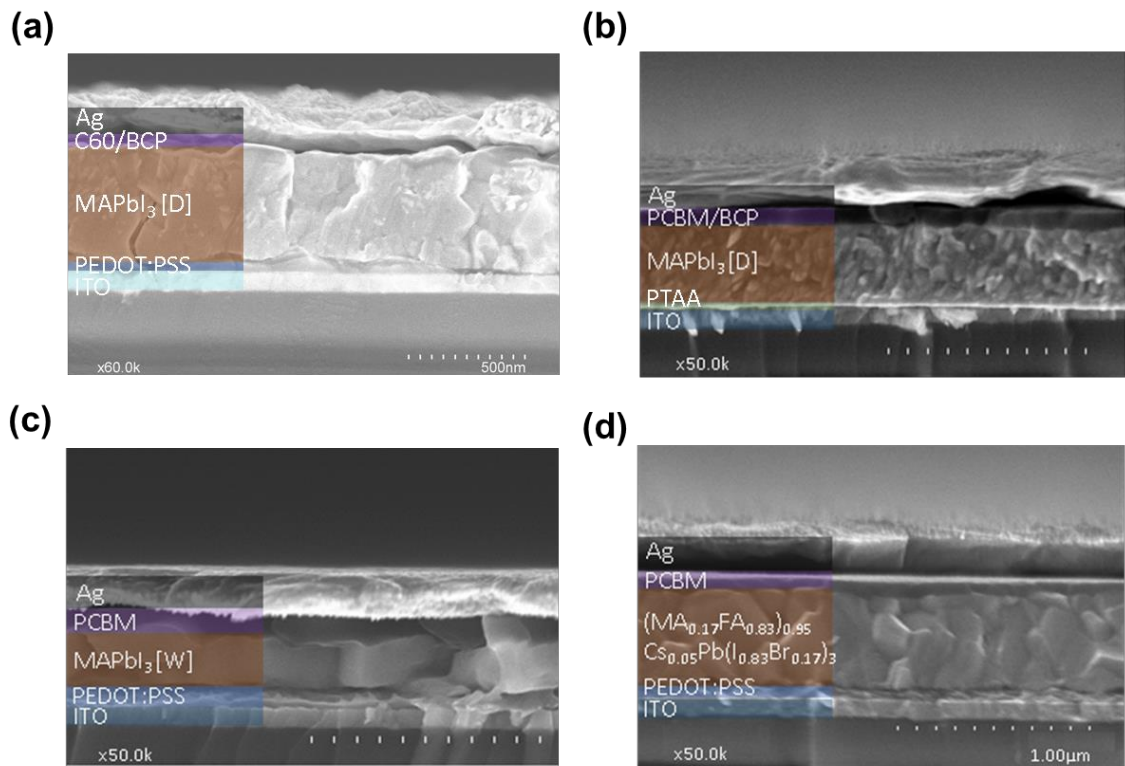


**Figure 4.7** Cross-section SEM images of the structures (a) dry MAPbI<sub>3</sub> with PEDOT:PSS (i), (b) dry MAPbI<sub>3</sub> with PTAA (ii), (c) wet MAPbI<sub>3</sub> (iii) and (d) 3CP (iv), respectively.

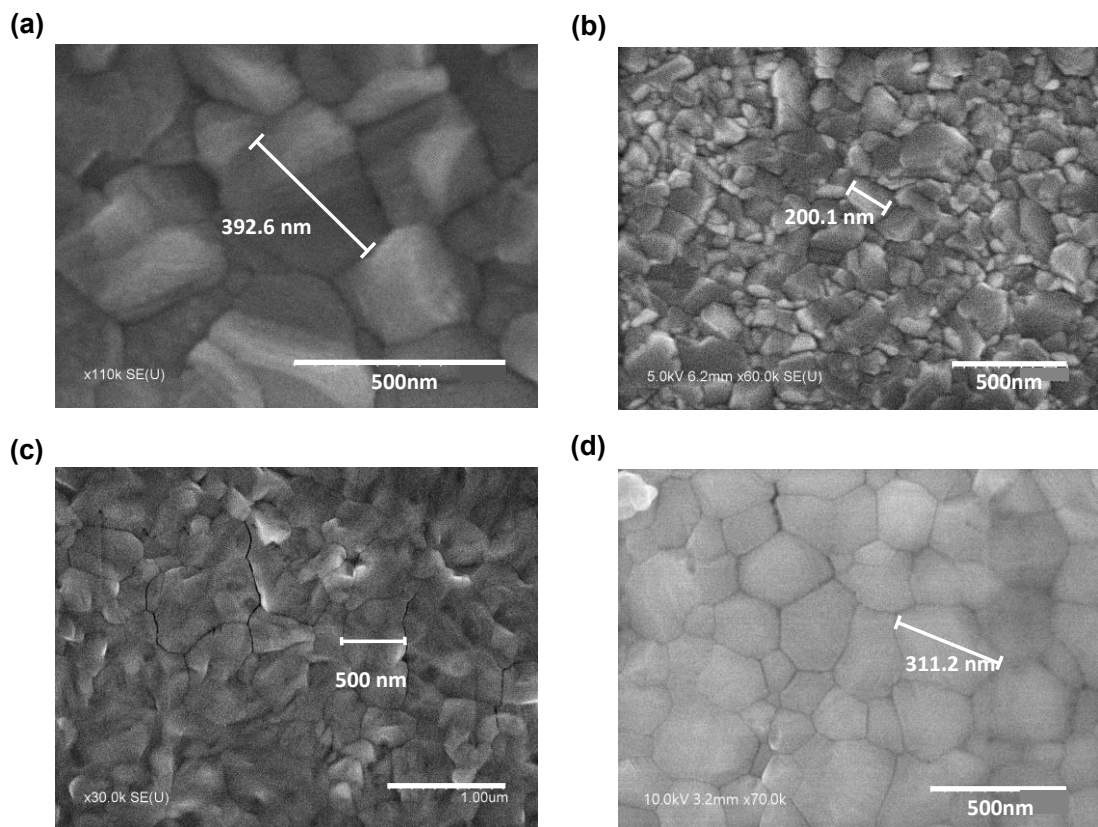


**Figure 4.8** Top view SEM images of MAPbI<sub>3</sub> [D] (a) on PEDOT:PSS, (b) on PTAA, (c) MAPbI<sub>3</sub> [W] and (d) 3CP.

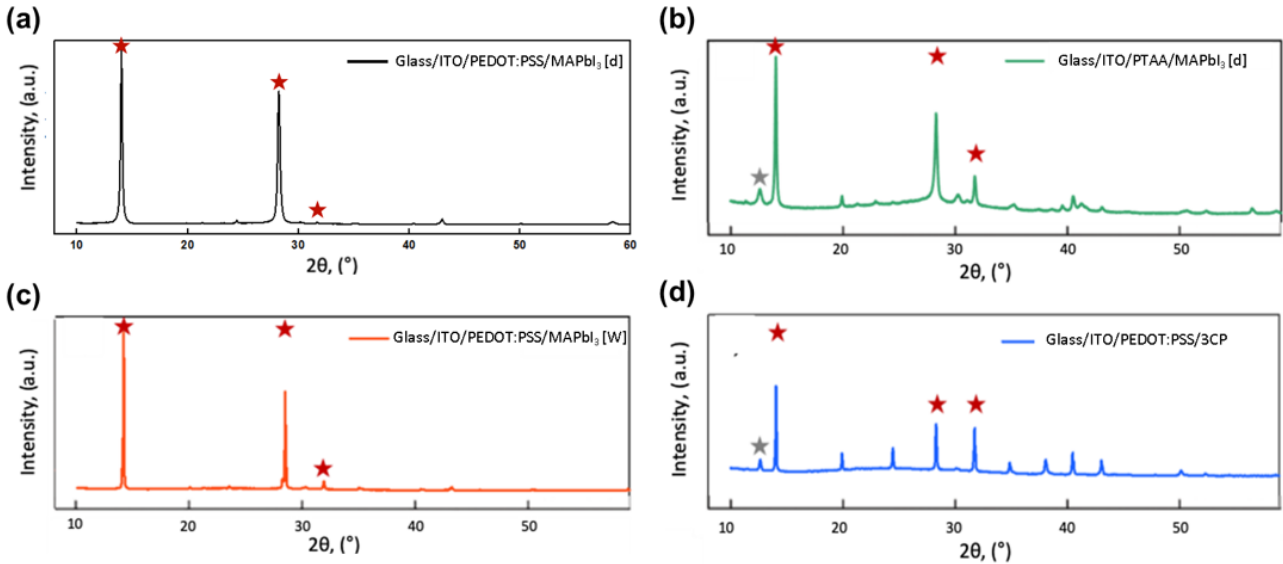


**Figure 4.9** X-ray diffraction results of  $\text{MAPbI}_3$  [D] on (a) PEDOT:PSS, (b) PTAA, (c)  $\text{MAPbI}_3$  [W] and 3CP. Red star indicated the peak of perovskite ( $2\theta = 14.2^\circ$ ,  $28.6^\circ$ , and  $32.2^\circ$ , respectively and the gray star means the peak of  $\text{PbI}_2$  ( $2\theta = 12.07^\circ$ ).

Based on the film properties, their photovoltaic performances are described in Fig. 4.10 and Table 4.1. The power conversion efficiencies of PSCs with dry-processed  $\text{MAPbI}_3$  on PEDOT:PSS and PTAA, wet-processed  $\text{MAPbI}_3$  and 3CP are 14.8%, 13.4 %, 11.9 % and 13.0 %, respectively. Detailed performances of PSCs with co-evaporated  $\text{MAPbI}_3$  are described in chapter 3. In the case of spin-coated  $\text{MAPbI}_3$  PSCs, a PCE of 11.9 % with a  $J_{\text{SC}}$  of  $19.2 \text{ mA/cm}^2$ , FF of 64.3 %, and a  $V_{\text{OC}}$  of 0.93 V is obtained. The hysteresis index was 0.015, which is negligible. The  $V_{\text{OC}}$  of PSCs with spin-coated  $\text{MAPbI}_3$  was higher than those of the reference PSCs. The incorporation of  $\text{Cl}^-$  slightly enlarges the perovskite bandgap and increases the peak intensity of (110) orientation with better carrier conductance which contributes to larger  $V_{\text{OC}}$ . [215], [216]. However, the fill factor was found to be lower, and the  $R_S$  was found to be higher than those of the reference PSCs. This could be the result of the solvent in the precursor solution of  $\text{MAPbI}_3$  that can damage the interface between  $\text{MAPbI}_3$  and PEDOT:PSS. For 3CP perovskite solar cells, a PCE of 13.0 % with a  $J_{\text{SC}}$  of  $22.19 \text{ mA/cm}^2$ , FF of 66.5 %, and a  $V_{\text{OC}}$  of 0.88 V is obtained. The 3CP also has a negligible hysteresis index (0.015). Compared to mono cation perovskite, rational composition engineering in triple cation-based perovskite suppresses the charge recombination, which enhances  $J_{\text{SC}}$  [217]. The  $V_{\text{OC}}$  is lower than that of wet-processed  $\text{MAPbI}_3$  PSCs because the  $\text{PbI}_2$  phase remains in perovskite and acts as a defect.

The EIS is measured for these different PSCs before and after applying an electric field by using J-V measurement (dry- and wet-processed  $\text{MAPbI}_3$  PSC) or shorting the device (3CP). When two contacts of the solar cell are connected, an internal electric field (built-in field) is formed due to the difference in Fermi levels of HTL and ETL [218], [219]. Fig. 4.11 presents the EIS results of the PSCs according to the effect of electric bias. It appears clearly that the impedance follows the same trends

independently of the device structure (different HTL/ETL), absorber material (MAPI or 3CP), or deposition process.

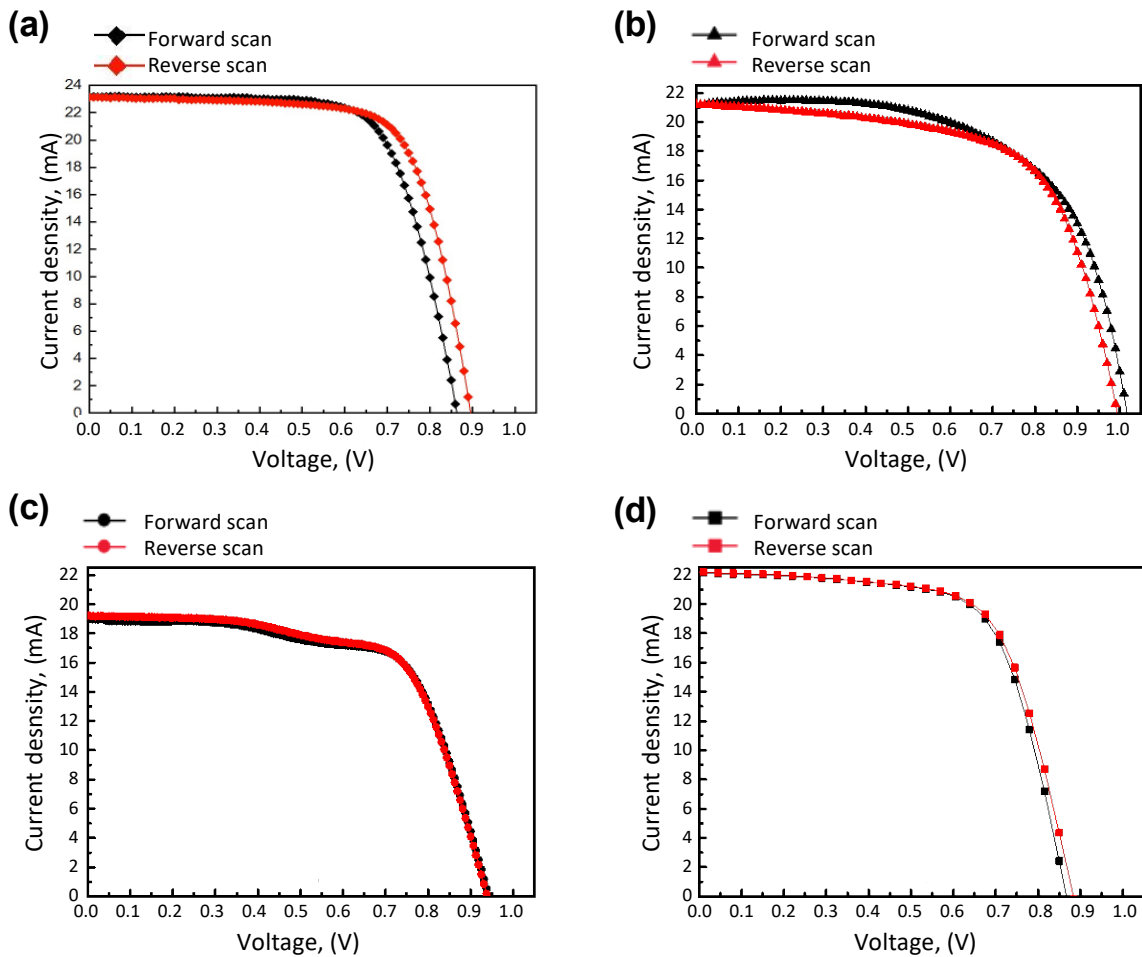


**Figure 4.10** J-V curves under 1-sun illumination of PSCs based on dry-processed MAPbI<sub>3</sub> on (a) PEDOT:PSS and (i) (b) PTAA (ii), wet-processed MAPbI<sub>3</sub> (iii), and (d) 3CP (iv).

**Table 4.1** Summary of photovoltaic parameters of MAPbI<sub>3</sub> solar cells with different HTM, deposition processes and kinds of perovskite.

Sample	Scan direction	V <sub>OC</sub> (V)	J <sub>SC</sub> (mA/cm <sup>2</sup> )	FF (%)	R <sub>S</sub> (ohm)	R <sub>SH</sub> (ohm)	PCE (%)
(i) MAPbI <sub>3</sub> [D] with PEDOT:PSS	Forward scan	0.86	23.18	70.4	5.61	1.56k	14.10
	Reverse scan	0.90	23.14	71.4	4.93	1.42k	14.79
(ii) MAPbI <sub>3</sub> [D] with PTAA	Forward scan	1.02	21.16	62.3	5.63	1.62k	13.40
	Reverse scan	1.00	21.20	63.5	6.69	0.52k	13.39
(iii) MAPbI <sub>3</sub> [W] with PEDOT:PSS	Forward scan	0.94	19.1	64.2	7.76	1.32k	11.72
	Reverse scan	0.93	19.2	64.3	8.12	1.12k	11.90
(iv) 3CP with PEDOT:PSS	Forward scan	0.86	22.13	66.9	6.51	1.21k	12.83
	Reverse scan	0.88	22.19	66.5	7.44	1.19k	13.03

Before applying electric bias, the complex impedance ( $|Z|$ ) and its phase of all samples follow the EIS results with the equivalent circuit of  $R_1+C_2/R_2$ . In the high-frequency region, the complex impedance ( $|Z|$ ) curve has a slope of -1 with a phase close to 90 degrees which implies pure capacitance in the high-frequency region. On the other hand, in the low-frequency region, there is a plateau of the complex impedance ( $|Z|$ ) with phase 0 degree, indicating a pure resistance. With Eq. 4.2, the geometric capacitance of each solar cell and the relative dielectric coefficients of each halide perovskite in PSCs can be calculated. The geometric capacitances ( $C_2$ ) of dry-processed MAPbI<sub>3</sub> on PEDOT:PSS and PTAA, wet-processed MAPbI<sub>3</sub> and 3CP are 10.1 nF, 10.4 nF, 15.0 nF, and 10.3 nF, respectively. In addition, their relative dielectric constants deduced from  $C_2$  are 19, 17, 17, and 19 for dry-processed MAPbI<sub>3</sub> on PEDOT:PSS and PTAA, wet-processed MAPbI<sub>3</sub> and 3CP, respectively. These values are similar to the value of references reported by other research groups [140], [214], [220], [221], and they fit well with the recommended value proposed by J. N. Wilson *et al.* [222].

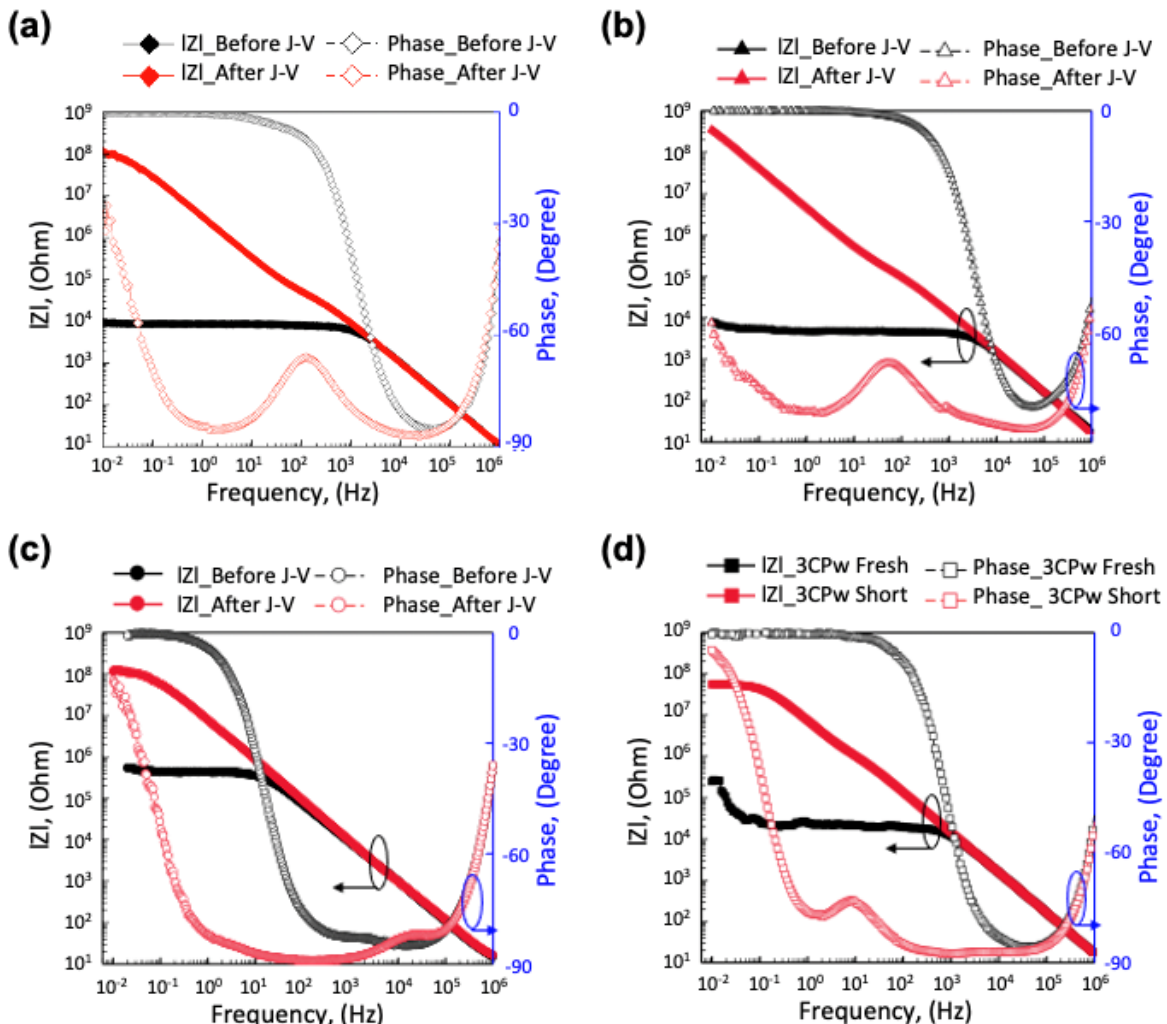


**Figure 4.11** Bode impedance and phase plot of the different devices before and after applied electric field under dark conditions; co-evaporated MAPbI<sub>3</sub> on (a) PEDOT:PSS (i) and (b) PTAA (ii), (c) spin-coated MAPbI<sub>3</sub> (iii) and (d) 3CP (iv) (Short means shorting conditions.).

When the PSCs are polarized by an electric field, the total impedance ( $|Z|$ ) at the low-frequency region

is significantly changed with the reduction of the resistive plateau and the formation of a second capacitive behavior. Another phase of - 90 degrees at low frequency supports the birth of a second capacitance. In order to analyze the impedance properties of each PSC in detail, the measurement data is fitted with the simulated data based on an equivalent circuit model. Fig. 4.12 shows the measured and simulated Nyquist plot of the reference PSCs before and after applying an electric field. The Nyquist plot of the polarized PSCs has another RC circuit connected with  $R_2$  in series compared with those of the fresh sample. The equivalent circuit of PSCs after applying the electric field is  $\{R_1+C_2/(R_2+C_3/R_3)\}$  and the EIS results of all biased samples are in agreement. The different circuit parameters, including  $R_1$ ,  $R_2$ ,  $C_2$ ,  $R_3$ , and  $C_3$  are extracted by fitting the experimental data and are reported in Table 4.2.

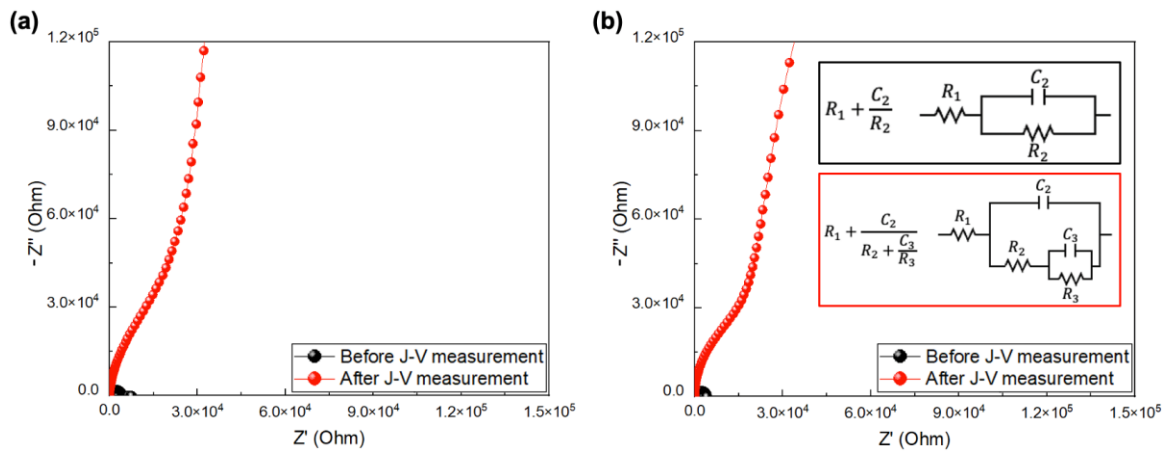


**Figure 4.12** (a) Measured Nyquist plot of the MAPbI<sub>3</sub> reference solar cells before and after applying an electric field. (b) Simulated Nyquist plot of the PSCs. Two inset figures are equivalent circuits of  $\{R_1+C_2/R_2\}$  and  $\{R_1+C_2/(R_2+C_3/R_3)\}$ .

**Table 4.2** Characteristic parameters extracted by fitting equivalent circuits. For each device, the first line is before polarization and the second line is after polarization.

Sample	Condition	$R_1$ (Ohm)	$R_2$ (Ohm)	$C_2$ (nF)	$R_3$ (Ohm)	$C_3$ (nF)
MAPbI <sub>3</sub> [D] with PEDOT:PSS	Before J-V measurement	9.91	$4.1 \times 10^3$	10.1	-	-
	After J-V measurement	9.98	$6.2 \times 10^4$	10.1	$1.7 \times 10^8$	7.3
MAPbI <sub>3</sub> [D] with PTAA	Before J-V measurement	10.1	$4.3 \times 10^3$	10.4	-	-
	After J-V measurement	10.1	$2.0 \times 10^4$	10.4	$3.4 \times 10^8$	23.8
MAPbI <sub>3</sub> [W] with PEDOT:PSS	Before J-V measurement	12.5	$4.4 \times 10^5$	15.0	-	-
	After J-V measurement	13.5	$\sim 10^5$	15.0	$1.2 \times 10^8$	5.0
3CP [W] with PEDOT:PSS	Before short	10.9	$1.9 \times 10^4$	10.3	-	-
	After short	10.3	$\sim 10^6$	10.4	$\sim 10^6$	9.1

The  $R_1$  is the contact resistance as mentioned in chapter 4.3.1 and is not significantly affected by the

electric effect. But  $R_1$  is strongly linked with  $R_S$  obtained by J-V measurement. As shown in Fig. 4.10 and Table 4.1,  $R_1$  is proportional to  $R_S$ , but greater. In J-V measurement,  $R_S$  is a contact resistance of contact metal in PSCs. On the other hand,  $R_1$  includes not only the resistance of contact metal but also the electrical wire in the EIS measurement system.

After applying the electric bias,  $R_2$  increases indicating that the charge carrier recombination is affected by the electrical field. On the other hand, the geometrical capacitance ( $C_2$ ) ignores the effect of electric bias. Wet-processed  $\text{MAPbI}_3$  PSC has the biggest  $C_2$ , followed by 3CP PSC, dry-processed  $\text{MAPbI}_3$  with PTAA and PEDOT:PSS. It is related to the thickness of the PSCs. In Eq. 4.2, the capacitance is inversely proportional to the thickness of the device. The thickness of the transport layer is a few ten nm which is negligible. However, the thicknesses of the absorber layer are 280 nm, 400 nm, 450 nm, and 500 nm for spin-coated  $\text{MAPbI}_3$ , 3CP, vacuum-deposited  $\text{MAPbI}_3$  on PTAA, and those on PEDOT:PSS, respectively. The capacitance ( $C_3$ ) observed in low frequency can be considered as electrode polarization caused by interfacial phenomena, i.e., by ionic charge accumulation at the interfaces of  $\text{MAPbI}_3$  [212], [221]–[223]. The next chapter describes a detailed explanation of the charge accumulation layer formation.

### 4.3.3 Presentation of the Hypothesis of Generation of Second Capacitance Caused by Electric Field

In the previous chapter, we confirmed that a second capacitance ( $C_3$ ) is observed at a low frequency ( $10^{-2}$  -10 Hz) after applying electric bias. We can interpret the capacitance as charge accumulation layers at both interfaces between halide perovskite and HTL and ETL. As noted earlier, it takes few seconds for the halide ions or halide vacancy to move toward the interfaces and then to accumulate under electric bias. The density of charge accumulated at the interfaces is high, which causes a large capacitance [61], [221]. However, the charges are promptly screened by mobile charges such as ions, electrons, and holes. Therefore, the charge accumulation layers transform into double layers called Debye layer with Debye screening length, which is observed in the electrolytes [218], [221], [224].

In other words, we can regard the perovskite layer as an ionic solution filling the space between HTL and ETL which is a parallel plate capacitor with a potential difference  $V$  as in electrolytes. Because Debye length at the interfaces is short (about 1 nm), a high built-in field is created, and the current density of electrons and holes can be controlled by the charged plane of high surface density (Fig.4.13 (a)). It means that the electric field formed inside the perovskite layer itself is too small to affect the

charge transport properties in the structure of PSCs [218].

We present a hypothesis that mobile halide ions and their ionic vacancies tend to migrate easily via grain boundaries, and the charge accumulation can be promoted by the presence of the grain boundaries (Fig. 4.13 (b)). Fig. 4.8 and Fig. 4.9 support the hypothesis. For example, wet-processed  $\text{MAPbI}_3$  has the largest grain size, followed by dry-processed  $\text{MAPbI}_3$  on PEDOT:PSS, 3CP, and dry-processed  $\text{MAPbI}_3$  on PTAA. In addition, the number of grains that comprises the vertical line of the absorber layer in wet- and dry-processed  $\text{MAPbI}_3$  PSCs with PEDOT:PSS is the smallest. The larger the grain size, the smaller the distribution of grain boundaries. The large distribution of grain boundaries promotes the accumulation of ions at the interface, which results in higher capacitance ( $C_3$ ). For the dry-processed  $\text{MAPbI}_3$  PSC with PTAA and the smallest grain size,  $C_3$  is the highest (Fig. 4.8 and Table 4.2), which can be provided as evidence for the hypothesis.

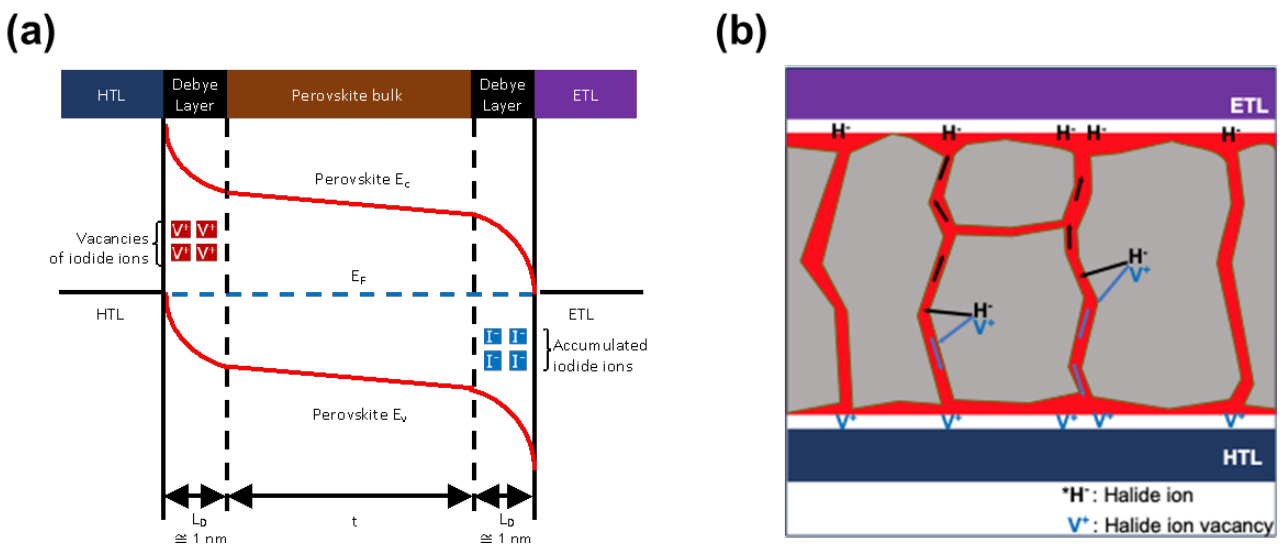


**Figure 4.13** (a) Scheme of band energy diagram in the perovskite after ion accumulation at the interfaces where  $t$  is the thickness of the perovskite absorber, and  $L_D$  is Debye layer thickness. (b) Scheme of phenomena of ion/vacancies accumulation at the interfaces between perovskite and charge transport layers. Ions and vacancies tend to migrate via grain boundary [225].

## 4.4 Analysis of Degradation Caused by Air-Exposure

### 4.4.1 EIS Results by Air Exposure

We prepared two reference samples of PSCs (Fig. 4.1 (a), Fig 4.2 (a), and Fig. 4.7 (a)) with the same

conditions. Two samples were stored in the air and in the dark. In one sample, EIS is measured periodically (without J-V measurement to prevent EIS results from being affected by the electric field from J-V measurement (as mentioned in chapter 4.3)), and in the other sample, the J-V curve is measured periodically. Fig. 4.14 shows impedance data collected from fresh and aged samples upon ageing time. In Bode plots (Fig. 4.14 (a) and (b)), the fresh sample shows a pure capacitance with a phase angle closed to -90 degrees at high frequency ( $10^4$ - $10^5$  Hz) and a resistive plateau at low frequency.

In the Bode impedance plot (Fig. 4.14 (a)), the complex impedance ( $|Z|$ ) shows a progressive change of the resistive behavior at low and intermediate frequency range with time, while no modification is observed at high frequency. At intermediate frequency ( $10^2$ - $10^3$  Hz),  $|Z|$  decreases gradually upon ageing. In the Bode phase plot (Fig. 4.14 (b)), there is a phase close to -90 degrees at 100 kHz in the fresh sample. At an ageing after five days, a second capacitive behavior emerges by the phase close to -90 degrees at a lower frequency range (1 Hz - 10 Hz). This feature at 1 Hz - 10 Hz is attributed to the charge accumulation layers occurring at the interfaces between  $\text{MAPbI}_3$  and selective contact layers. After that, the total impedance ( $|Z|$ ) and the magnitude of the phase decrease gradually from -90 to -80 degrees over time, indicating the loss of the pure capacitive property in the aged PSCs.

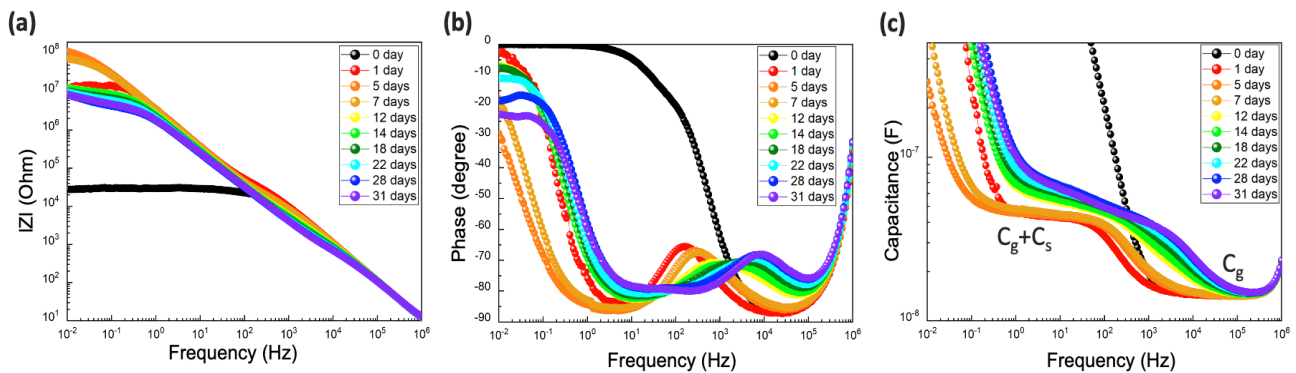


**Figure 4.14** EIS characteristics evolution as a function of ageing time for optimized  $\text{MAPbI}_3$  solar cell. (a) Complex impedance versus frequency. (b) Phase versus frequency. (c) Capacitance versus frequency

In Fig. 4.14 (c), only a single capacitance ( $C_2 = C_g \sim 14$  nF) is obtained at the high-frequency corresponding to the geometrical capacitance as mentioned previously for the fresh device. However, a second capacitance ( $C_3$ ) appears as a function of ageing time with a value around 31 nF, clearly identifiable until five days of ageing time (the measured value at lower frequency in Figure 4.14 (c) is the sum of  $C_g + C_3$ ). In addition, the transition point from geometrical capacitance to the sum of a geometrical capacitance ( $C_2$ ) and a capacitance caused by accumulated ions ( $C_3$ ) shifts to the right from  $10^2$  Hz to  $10^4$  Hz. After five days, the second capacitance increases gradually however, the property of pure capacitance behavior is lost.

#### 4.4.2 Application of Dielectric Modulus Spectroscopy to Study Degradation in PSCs

In EIS results of degraded PSCs caused by air, the analysis of the high-frequency region in  $Z'$ -versus  $-Z''$  Nyquist plot in EIS is difficult to interpret. So dielectric modulus is applied for studying the microscopic mechanism of charge transport upon exposure to air. Dielectric modulus ( $M$ ) is the inverse of the complex relative permittivity ( $\varepsilon$ ) with Eq. 4.3

$$M = \frac{1}{\varepsilon} = M' + iM'' \quad (4.3)$$

Dielectric modulus was first reported in 1967 by McCrum *et al.* to compare with the mechanical modulus in the viscoelastic relaxation of polymers, as shown in Table 4.3 [226]. Macedo and his co-workers first exploited the electric modulus to investigate electrical relaxation phenomena in the vitreous ionic conductors [227]. Hodge *et al.* verified that the dielectric modulus is useful for studying charge transport and dielectric polarization in electrolytes [228].

**Table 4. 3** Comparison of mechanical and dielectric modulus.

Mechanical modulus	Dielectric modulus
Stress $\sigma$	Electric field $E$
Strain $\gamma$	Displacement $D$
Elastic compliance $J$	Permittivity $\varepsilon$
$\gamma = J\sigma$	$D = \varepsilon E$
Elastic modulus $G$	Electric modulus $M$
$\sigma = G\gamma$	$D = MD$
$G = 1/J$	$M = 1/\varepsilon$

Furthermore, Bendahhou *et al.* confirmed that dielectric modulus spectroscopy can be used to study the effect of grain and grain boundary in  $\text{Ba}_5\text{CaTi}_{1.94}\text{Zn}_{0.06}\text{Nb}_8\text{O}_{30}$ , one of the dielectric materials, separately [229].

Based on the properties mentioned above of dielectric modulus, we applied dielectric modulus to analyze EIS results in-depth in a high-frequency region and investigate the change of grains and grain boundaries in  $\text{MAPbI}_3$  separately. A dielectric modulus is also a complex number like impedance. The real ( $M'$ ) and imaginary part ( $M''$ ) of dielectric modulus can be calculated with the imaginary and real part of impedance (Eq. 4.4 and Eq. 4.5).

$$M' = \frac{\varepsilon'}{\varepsilon'^2 + \varepsilon''^2} = \frac{\omega \cdot A \cdot \varepsilon_0}{l} \cdot (-Z'') \quad (4.4)$$

$$M'' = \frac{\varepsilon''}{\varepsilon'^2 + \varepsilon''^2} = \frac{\omega \cdot A \cdot \varepsilon_0}{l} \cdot (Z') \quad (4.5)$$

Fig. 4.15 (a) shows the typical  $M''(\omega)$  behavior of PSCs. For the fresh device, single  $M''$  peak exists at a high frequency. This peak is a relaxation peak caused by the hopping of electrons or holes. The charge carriers are mobile over long distances (hopping from one site to the neighboring site) at frequencies below the peak frequency, while the charges trapped in potential wells and can hop over a short distance at frequencies above the peak frequency [230], [231]. After exposure to air, two  $M''$  peaks at low and high frequencies are observed. The second  $M''$  peak is the relaxation peak of ions. Ions also have long and short hopping at frequencies below and above the second peak frequency, respectively. The modulus peak at high frequency exhibits a trend of the shift towards higher frequency upon ageing. Meanwhile, the peak at low-frequency shifts towards lower frequency for up to 7 days. After that, the shift in the peak towards higher frequency is observed.

Fig. 4.15 (b) illustrates the variation of the real part of the module  $M'$  as a function of frequencies with ageing time. In the fresh sample,  $M'$  is near zero in the low-frequency region, but as the frequency increases,  $M'$  continuously increases and closes to saturation at a particular frequency. The saturation in  $M'$  is caused by the conduction mechanism due to the motion of the electrons and holes. However, the stepwise transition from low to high values in  $M'$  appears after exposure to air. The first step at the low frequency is related to the conduction of ions and the other step indicates the electronic conduction. From 1 day to 7 days, the first step related to ionic conduction shifts to low frequency, and then it shifts to high frequency, which means that there are different mechanisms of the change in the conduction mechanism.

The complex modulus spectra of  $M''$  versus  $M'$  of PSCs upon ageing are shown in Fig. 4.15 (c). For the fresh sample, one big semicircle is observed. With time, the arc is divided into two semicircular arcs. The first semicircle at a higher frequency is because of grains, but the second semicircle at a lower frequency is due to the effect of grain boundaries [229], [232]. The first semicircle at high frequency decreases gradually, indicating that the conductivity in grains gradually decreases. On the other hand, the second semicircle at low frequency decreases until 11 days and increases thereon. It is worthy to note that the conductivity of carriers in grain boundary decreases until 11 days and then increases. In addition, we can guess that grain size decreases, and the proportion of grain boundaries increases with time in the air.

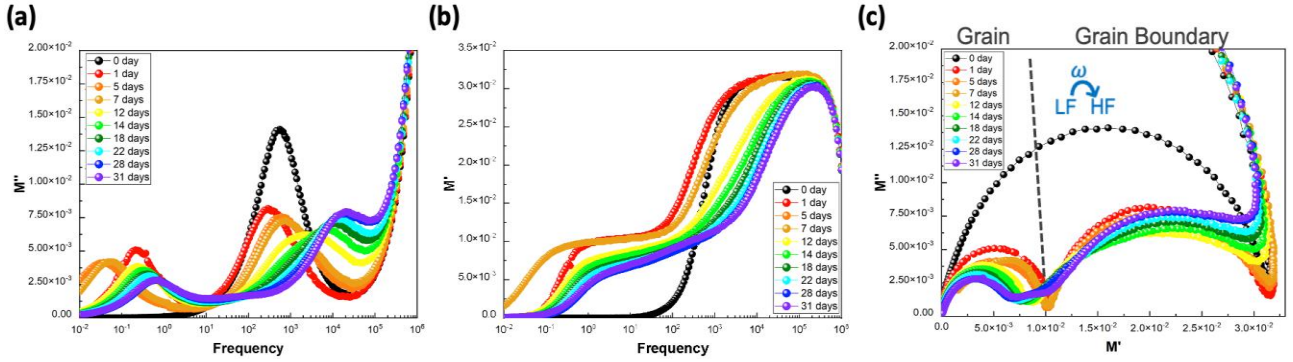


**Figure 4.15** (a) Imaginary and (b) real part of modulus versus frequency. (b) Complex modulus plots of optimized MAPbI<sub>3</sub> solar cell upon ageing in air.

#### 4.4.3 Discussion of Air Exposure Phenomena in the Reference PSCs

The relation of these results of impedance and modulus spectroscopy with the change of size of grain and grain boundary is not substantiated yet. Experimental evidence of the increase in the proportion of grain boundaries and the accumulation of ions is required. We estimate that the proportion of grain boundaries increases as MAPbI<sub>3</sub> film is degraded under exposure to air.

Grain boundaries may have more vacancy-type defects and contribute most importantly to the diffusion of I<sup>-</sup> ions. The results of J-V curves of other PSCs with the same condition stored in the same environment are coherent with those of EIS. Fig. 4.16 (a) shows J-V curves of F-R (Reverse scan) and R-F (Forward scan) upon ageing (from 0 days to 31 days). There is no big change in the results of R-F upon ageing. On the other hand, the FF of the J-V curve with F-R direction decreases gradually as time goes on. Accordingly, the magnitude of the hysteresis index also increases, which means the amount of accumulated mobile I<sup>-</sup> ions increases upon ageing in air Fig. 4.16 (b).

We propose a hypothesis of the degradation mechanism of MAPbI<sub>3</sub> in the inverted p-i-n PSCs through linking dielectric modulus results and J-V measurements. Fig 4.17 illustrates the mechanism of degradation of MAPbI<sub>3</sub> with ageing time from fresh to 31 days. In the fresh sample (Fig. 4.17 (a)), the hysteresis is negligible in the J-V curve, and one big arc is shown in complex modulus spectra, which indicates that only the electronic conduction exists, and any mobile ion is not observed. From 1 day to 7 days (Fig. 4.17 (b)), the J<sub>SC</sub> of a reverse scan is lower than those of a forward scan. In addition, the one big arc in modulus spectra is divided into two semicircles. It implies that the bonding of some halides in grains is weak, and mobile halide ions are formed, which induces the appearance of ionic conduction in the dielectric modulus spectroscopy.

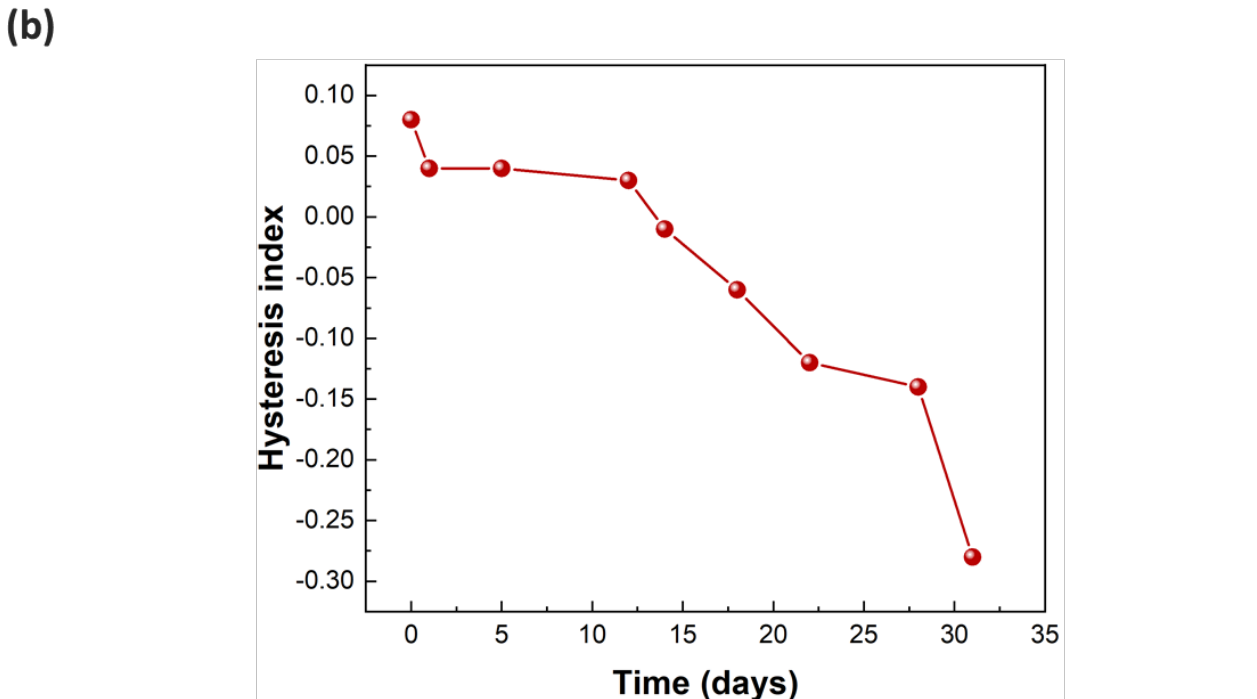
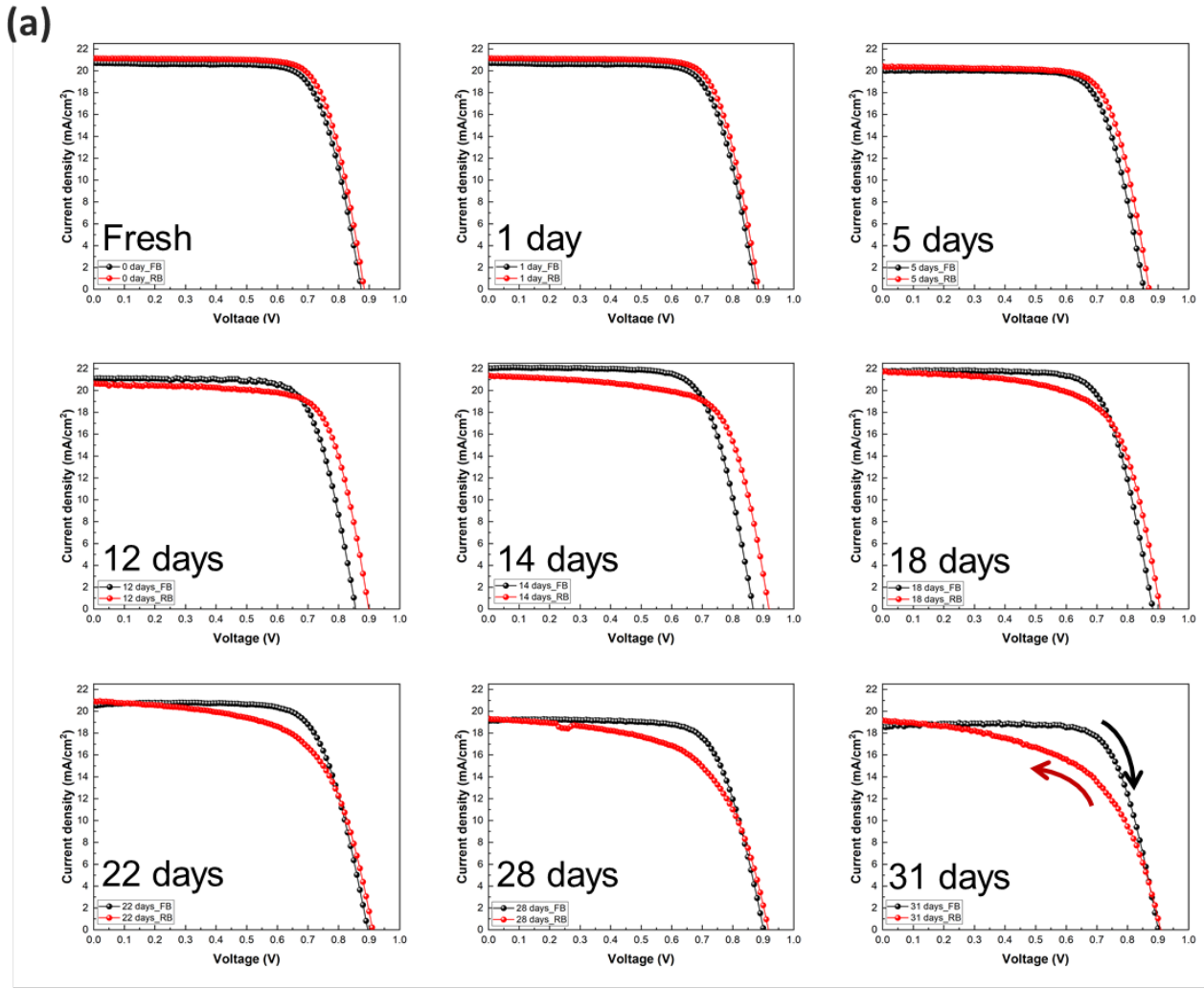


**Figure 4.16** (a) Current density-voltage (J-V) curves of PSCs as a function of ageing time: fresh - 31 days. (b) Summary of hysteresis index.

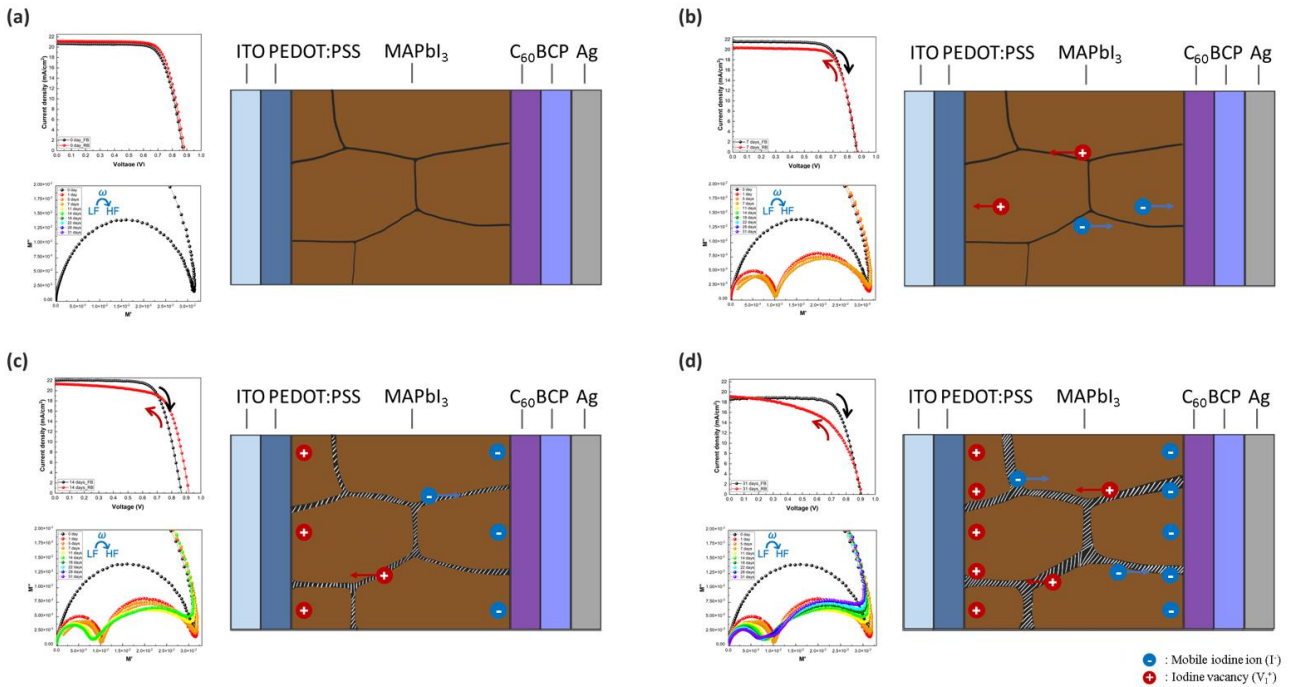


**Figure 4.17** Schematic illustration of the behavior of mobile halide ions and ionic vacancies in MAPbI<sub>3</sub> with aged time: (a) fresh, (b) 1 - 7 days, (c) 11- 14 days, and (d) 18-31 days.

In the period from 11 to 14 days (Fig. 4.17 (c)), inverted hysteresis with higher PCE of forward scan than those of reverse scan is observed. Furthermore, the radius of both arcs gradually decreases. We can explain that the conductivity of both electronic and ionic carriers increases. Especially, the number of mobile ions increases, and they are accumulated at the interfaces. After 14 days (Fig. 4.17 (d)), it was observed that the hysteresis gets stronger, the radius of arc at high-frequency decreases, and those at low-frequency increases. It is worth noting that the grain degraded, which induced a decrease in electronic conductivity. On the contrary, the proportion of grain boundaries becomes higher, which promotes ion accumulation at interfaces. While this hypothesis is reasonable, it is required to be verified by providing experimental evidence.

Experimental evidence of change in grain size under air is still not enough. However, there is evidence of ion migration and the reaction of iodine with the contact layer. In one of the previous studies in our laboratory (LPICM), Lee *et al.* investigated the change of the atomic composition in MAPbI<sub>3</sub> PSCs with ageing under air using glow discharge optical spectroscopy technique (GD-OES). Fig. 4.18 (a) presents the GD-OES line profiles of iodine as a function of ageing time under dark conditions and without applied bias. In GD-OES results, the position in PSCs can be defined by plasma etching direction and the sputtering time. The silver is located at the shortest sputtering time, and the position of ITO corresponds to the longest sputtering time [233]. In Fig. 4.18 (d), a significant motion of iodide ions upon ageing is observed while the other components, including nitrogen, lead, and chloride (Fig 4.18 (a), (b), and (c)), are stable. The intensity of the iodine peak at a sputtering time, indicating the MAPbI<sub>3</sub> layer decreases significantly, and a shoulder increases gradually toward

the Ag electrode with time. After four weeks, the iodine signal starts at 20 s of sputtering time (50 s for the fresh device), corresponding to the silver position. It indicates that the iodine atom goes through the PCBM layer and approach to Ag electrode in ageing condition.

The GD-OES results are proved by Fig. 4.18 (e), where the color variation of the top electrode from silver to yellow is observed after two weeks of ageing. The color indicates the chemical reaction of iodide ions with Ag, which results in AgI [225]. After four weeks, the perovskite film is completely degraded only around the silver electrode showing a yellow PbI<sub>2</sub> compound. Through GD-OES results, we verified that halide ions not only migrate in halide perovskite but also approach charge transport layers, which causes a chemical reaction. They are related to the change of impedance in PSCs.

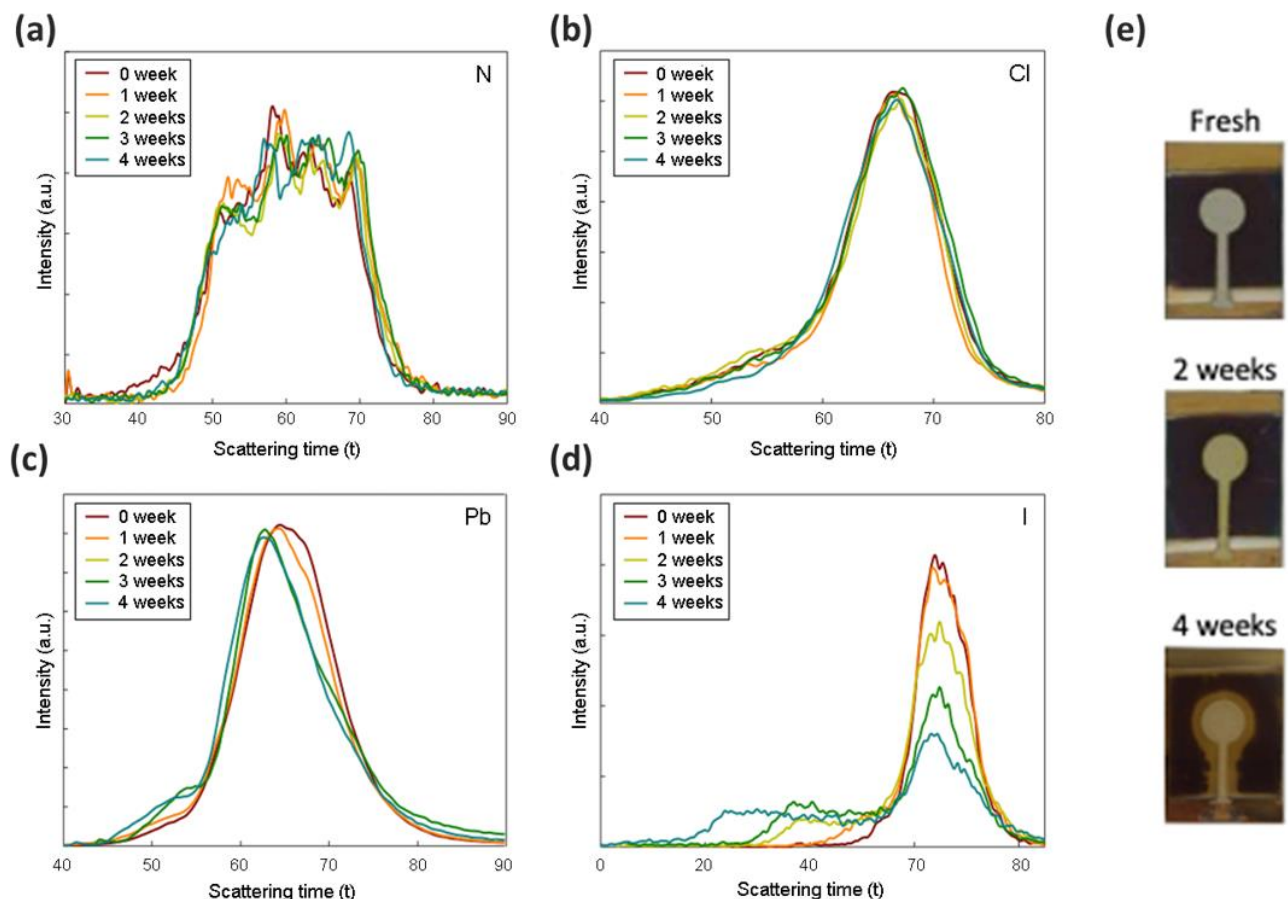


**Figure 4.18** MAPbI<sub>3</sub> PSCs aged under dark conditions; GD-OES profile lines of (a) nitrogen, (b) chloride, (c) lead and (d) iodine versus ageing time. (e) Photographs of the fresh, 2 weeks and 4 weeks aged PSCs [225].

## **Chapter 5.**

# **Study of Electric Field-induced Degradation in Perovskite Films and Solar Cells with Scanning Transmission X-ray Microscopy**

---

<b>5.1 Introduction .....</b>	<b>115</b>
<b>5.2 Experimental Details.....</b>	<b>116</b>
5.2.1 Preparation of Films of Components Forming Halide Perovskites and PSCs .....	116
5.2.2 Instruments for Synchrotron-based Characterization .....	119
5.2.3 Specialized In-situ Electric Biasing System from Norcada Inc.....	120
<b>5.3 Utility of STXM for Chemical Characterization of Halide Perovskites.....</b>	<b>122</b>
5.3.1 Identification of Components and By-products in Halide Perovskites.....	122
5.3.2 Characterization of MAPbI <sub>3</sub> using STXM .....	125
5.3.3 Evaluation of Homogeneity of MAPbI <sub>3</sub> based on STXM .....	128
<b>5.4 Degradation of Halide Perovskite Film and Solar Cells under In-situ Biasing .....</b>	<b>129</b>
5.4.1 Degradation of MAPbI <sub>3</sub> Film under In-situ Electric Bias .....	129
5.4.2 Degradation of MAPbI <sub>3</sub> Solar Cells Induced by Ex-situ Electric Field .....	134
5.4.3 Proposal to Explain Electric Field-induced Degradation Mechanism in MAPbI <sub>3</sub> Solar Cells through the Correlation between STXM and EIS Results .....	139

---

## **5.1 Introduction**

As mentioned in chapter 1, the detailed mechanism of the degradation phenomena in PSCs needs to be understood to improve the stability and photovoltaic performance. To study the mechanism, the chemical and electronic parameters changed by a specific environment need to be analyzed at the micro- and nano- scales. Furthermore, organic-inorganic hybrid perovskites consist of organic molecules, inorganic atoms, and halide atoms. The measurements that can characterize both organic and inorganic materials at the nanoscale are necessary.

STXM is one of the promising measurement techniques which satisfies these requirements. STXM is a characterization technique based on synchrotron radiation. It focuses monochromatic X-rays to a spot size of about 30-50 nm on a sample that is raster scanned. Transmitted photons are detected simultaneously to obtain an absorption image that captures the chemical and structural characteristics of the sample. Furthermore, the soft X-ray regime for STXM includes not only the outer shell X-ray absorption edges of Pb and I but also the inner shell X-ray absorption edges of carbon and nitrogen. This energy range provides the opportunity to investigate the organic component of the organic halide perovskites in conjunction with the lead halide component. It could be particularly used to investigate changes in the spectroscopic fine structure of the N K-edge at 405.5 eV, to explore the chemical changes in interfaces to the active layers [234], as well as ion migration in the active layer [235].

In this chapter, we focused on the impact of the electric field, among various factors, in operating conditions in PSCs, on  $\text{MAPbI}_3$  film and solar cells based on STXM. To achieve the above objectives, we systematically demonstrated the sensitivity of STXM to various elements/components contained in halide perovskites and various aging or oxidation by-products. Furthermore,  $\text{MAPbI}_3$  samples with different  $\text{PbI}_2:\text{MAI}$  ratios and of various thicknesses were prepared and compared to highlight the chemical and thickness sensitivity of STXM. After the functional verification of STXM for studying halide perovskites, we employed a special electric biasing system for studying the degradation of  $\text{MAPbI}_3$  film caused by the electric field. Through the electric biasing test, we analyzed which chemical components are mobile in  $\text{MAPbI}_3$  under an electric field.

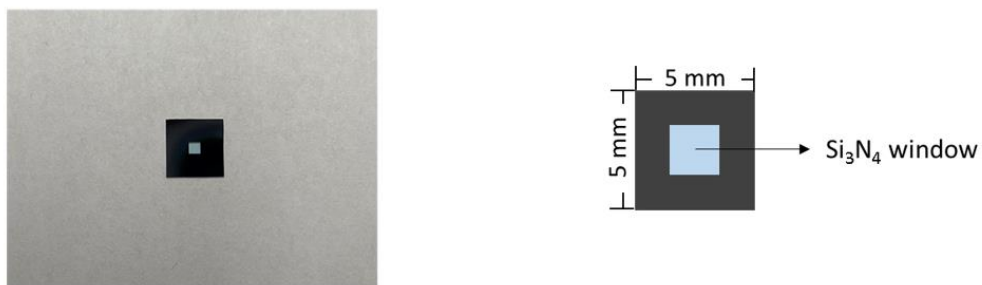
Furthermore, the reference PSC in this thesis (ITO/PEDOT:PSS/ $\text{MAPbI}_3/\text{C}_{60}/\text{BCP}/\text{Ag}$ ) were prepared, and an electric field was applied to the solar cells. Subsequently, FIB (Focused ion beam) sections of the complete devices were investigated using STXM to obtain spatially resolved information on ion migration and chemical changes in the bulk and interface of various transport layers. Lastly, we tried to explain the mechanism of the electric field-induced degradation in  $\text{MAPbI}_3$  solar cells by correlating the results of STXM with EIS results described in chapter 4.

## 5.2 Experimental Details

### 5.2.1 Preparation of Films of Components Forming Halide Perovskites and PSCs

*PbI<sub>2</sub>, MAI, PbCl<sub>2</sub>, KI, PbO, and MAPbI<sub>3</sub>, CsPbIxBr<sub>3-x</sub> films* To validate the utility of STXM for its sensitivity to various elements/components that are contained in halide perovskites, films of PbI<sub>2</sub>, MAI, PbCl<sub>2</sub>, KI, PbO, and MAPbI<sub>3</sub> were prepared onto a Si<sub>3</sub>N<sub>4</sub> window (50 nm thickness of Si<sub>3</sub>N<sub>4</sub> window, 200  $\mu$ m thickness of Si, frame size of 5  $\times$  5 mm<sup>2</sup>, and fabricated by Norcada Inc., Edmonton, Canada). In addition, CsPbIxBr<sub>3-x</sub> was prepared to characterize all-inorganic perovskite and compare the change of perovskites, including inorganic cation with those of MAPbI<sub>3</sub>, under an electric field. Si<sub>3</sub>N<sub>4</sub> window (Fig. 5.1) is an X-ray and electron transparent sample holder. It is optimized for various applications such as X-ray and electron microscopy, spectroscopy, interferometry, atomic force microscopy, etc.

(a)



(b)

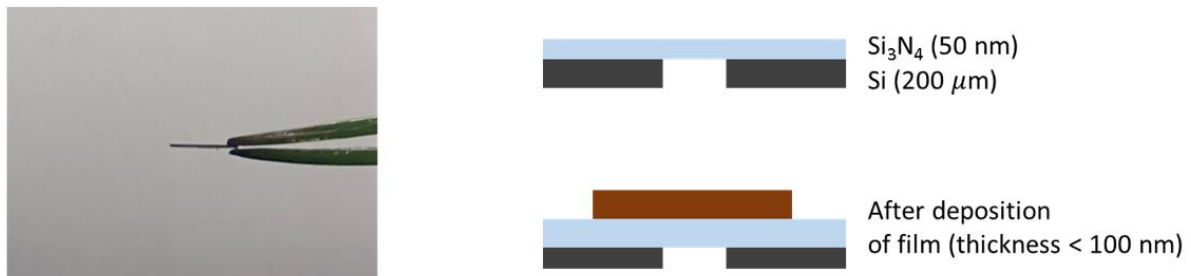


**Figure 5.1** Real images and schemes of (a) top view and (b) cross-section view Si<sub>3</sub>N<sub>4</sub> window.

STXM results, including microscope images or spectra, are recorded in transmission mode. Therefore, the thickness of the sample is recommended to be thin (< 100 nm) enough so that the transmitted photon can be counted by the detector (photomultiplier tube). For the preparation of the films, MAI, PbCl<sub>2</sub>, KI, and PbO were deposited by spin-coating. On the other hand, PbI<sub>2</sub> and MAPbI<sub>3</sub> were based on vacuum deposition. MAI (Greatcell Solar, >99.99 %) solution was prepared by dissolving MAI into N, N-Dimethylformamide (DMF, Sigma Aldrich, anhydrous, 99.8 %) with a concentration of 0.125 M. Both PbCl<sub>2</sub> (Alpha Aesar, ultra-dry, 99.99 %) and KI (Sigma Aldrich,  $\geq$  99 %) solutions were prepared with a concentration of 0.025 g/ml in DMF. The 0.05 M of PbO (Sigma Aldrich, 99 %) was dissolved in deionized water. All films of MAI, PbCl<sub>2</sub>, KI, and PbO were spin-coated at 3000 rpm in an N<sub>2</sub> environment.

50 nm thick PbI<sub>2</sub> film was prepared by dry process. The source of PbI<sub>2</sub> was located at the same evaporator for MAPbI<sub>3</sub>. PbI<sub>2</sub> was sublimated in a vacuum chamber at 300 °C, and the deposition rate of PbI<sub>2</sub> was 1 Å/s. During the deposition, the vacuum level was  $1.6 \times 10^{-6}$  mbar. MAPbI<sub>3</sub> films with different ratios of PbI<sub>2</sub>:MAI and thicknesses were prepared to characterize MAPbI<sub>3</sub> in detail using STXM and evaluate whether STXM is a useful measurement technique for analyzing halide perovskite. The PbI<sub>2</sub> rate was fixed to 1 Å/s. The MAI rates used were 0.5 Å/s, 1 Å/s and 2.5 Å/s. In the optimized deposition condition of MAPbI<sub>3</sub>, the rate of PbI<sub>2</sub> and MAI are 1 Å/s and 2.5 Å/s, respectively. The detailed process is explained in section 3.2.1. With this optimized condition, MAPbI<sub>3</sub> of 25 nm, 50 nm, and 75 nm thicknesses were prepared. CsPbI<sub>X</sub>Br<sub>3-X</sub> of 75 nm thickness was also prepared by vacuum deposition in IPVF. The CsBr and PbI<sub>2</sub> were sublimated at 380 °C and 270 °C, respectively. Each rate of CsBr and PbI<sub>2</sub> were Å/s and Å/s.

**FIB section of MAPbI<sub>3</sub> solar cells** Three reference MAPbI<sub>3</sub> PSCs with different conditions of applying electric bias were prepared. The fabrication details of MAPbI<sub>3</sub> PSCs (ITO/PEDOT:PSS/MAPbI<sub>3</sub>/C<sub>60</sub>/BCP/Ag) are described in section 3.2.2. After fabrication of the PSCs, + 2.5 V was applied to one PSC for 15 minutes. Secondly, - 2.5 V was applied to another PSC for 15 minutes. Lastly, the other PSC was kept without applying an electric field.

After applying the electric field to the PSCs with different conditions, cross-section lamellas of the three PSCs were prepared by using the FIB technique on the PSCs. Before the milling process with the FIB dual beam microscope chamber (Scios DualBeam), several preprocesses are required. Firstly, a thin carbon layer was deposited by a carbonic pen to prevent any electron and ionic beam charge effects that appear during the milling process. Secondly, a platinum layer was deposited on a target area to avoid excessive ion damage, and the area was etched by the gallium ion beam. When the selected area was isolated, the milling process began in the FIB chamber using an ion beam. In the process, the ion beam current is low to obtain a very thin lamella (150-200 nm). The lamella formed was fixed to the TEM grid as shown in Fig. 5.2.

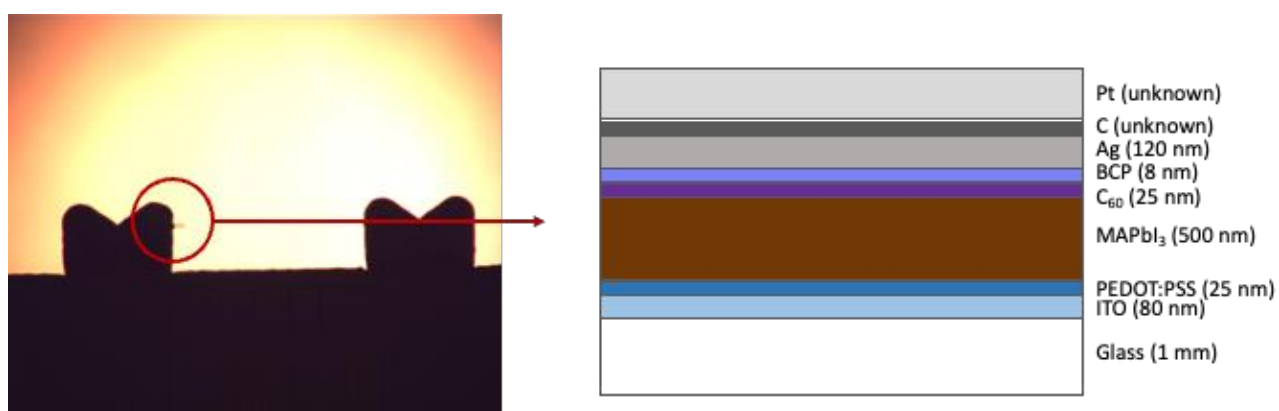
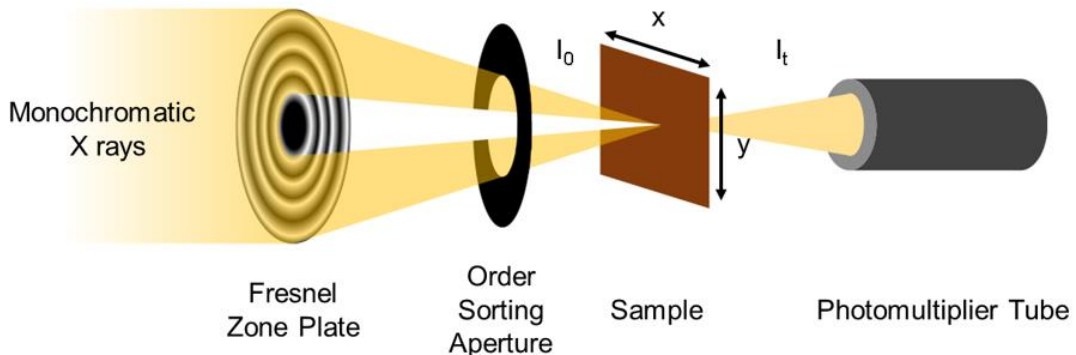


**Figure 5.2** Microscopy image of MAPbI<sub>3</sub> PSC lamella fixed to TEM grid and scheme of the lamella.

## 5.2.2 Instruments for Synchrotron-based Characterization

STXM measurements were performed at the HERMES beamline of synchrotron SOLEIL. The details of the beamline are mentioned in the reference [155]. Fig. 5.3 (a) and (b) present the scheme of STXM and a close-up view of the STXM with transmission detection in the vacuum chamber at the HERMES beamline. The STXM measurement was performed under a pressure of  $10^{-6}$  mbar. A Fresnel zone plate of 25 nm outer zone width (Applied Nanotools Inc., Canada) was used to focus the monochromatic X-rays to a spot size of (30 nm) which contributes to high-resolution images. The sample is raster scanned across the X-ray spot with the help of an interferometrically stabilized piezoelectric stage. A photomultiplier tube (PMT) positioned behind the sample measures the flux of the transmitted X-rays after being converted to visible photons by the phosphorous screen.

(a)



(b)

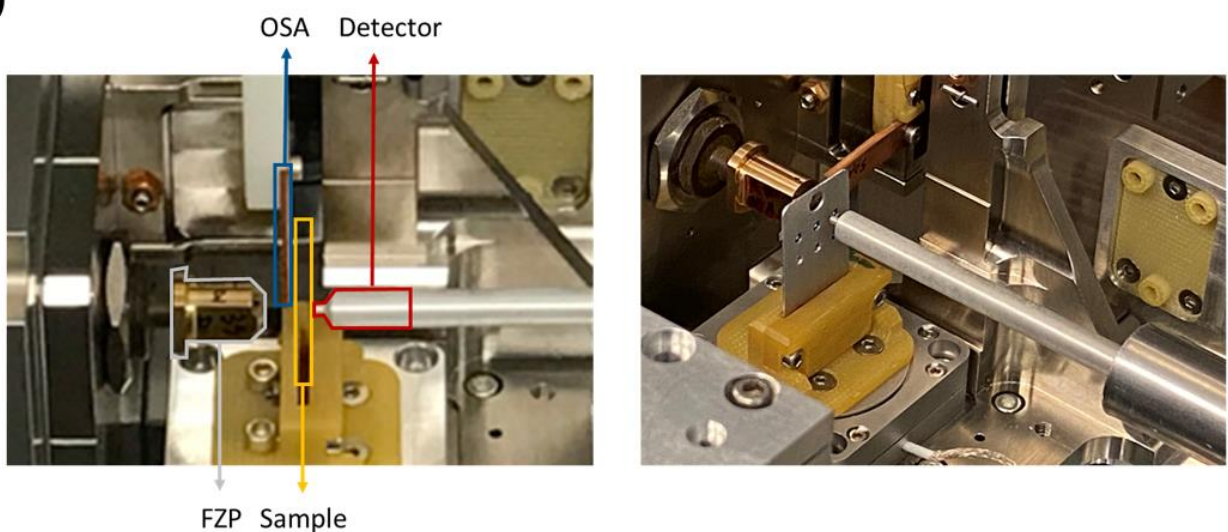


**Figure 5.3** Scheme of the STXM technique. (b) Close-up interior view of the STXM instrument.

The following protocol is recommended in order to perform studies in a reproducible fashion: (a) clean beamline optics is essential for investigating organic species, (b) if possible, in order to avoid

contamination and degradation of the samples during transportation, a vacuum environment or isolated environment with minimum exposure to light is recommended. Spectral data presented in this section are primarily obtained from a stack of very low-resolution images measured at a range of predetermined energies. Each spectral point in these cases is obtained by integrating over each image.

The energy range investigated for each sample is from 270 to 750 eV covering C K-edge, N K-edge, O K-edge, I M-edge, Cs M-edge, and Pb N-edge. To avoid any mechanical drift and focusing issues due to long-range travel of the zone plate, we split the scans into four partially overlapping sections from 270 to 390 eV, 370 to 450 eV, 430 to 570 eV, and 550 to 750 eV.

Focus corrections and beam alignment were performed between each chosen energy range. High spectral resolution (0.1 eV energy step) was used near the absorption edges of C, N, O, I, and Cs. In the intermediate energy ranges, an energy step of up to 5 eV was used. Before real measurement, a radiation damage study is recommended. To obtain spatially resolved spectra, energy stacks were obtained over an area of  $2 \times 2 \mu\text{m}^2$  by raster scanning the sample with a step size of 30 nm with the same energy definition as described above. The focal length of FZP is proportional to the energy of the incident X-ray. During the acquisition of a stack, the distance between the FZP and the sample changed to keep the sample in focus as the incident X-ray energy changed.

### 5.2.3 Specialized In-situ Electric Biasing System from Norcada Inc.

A special electric biasing system is required to obtain an in-depth understanding degradation mechanism of  $\text{MAPbI}_3$  under electrical bias using STXM. Fig. 5 (a) shows the in-situ electric biasing system designed by Norcada company in Canada in collaboration with MAX IV (Sweden). The system consists of an electric biasing chip, its holder, an electric biasing controller, and software. The electric biasing controller provides I-V measurement in the mA/mV range with the software “Blaze”. Additionally, the controller and the software can measure not only current-voltage but also resistance. Fig. 5 (b) presents the electric biasing chip and holder. The holder has four-point probes, and the biasing chip can be customized with two-point or four-point probes according to the objective of the research.

$\text{MAPbI}_3$  film on biasing chip is shown in Fig. 5 (c). The biasing chip is a  $\text{Si}_3\text{N}_4$  membrane with 50 nm-thick Au electrodes. The shadow mask was used for the deposition of  $\text{MAPbI}_3$ .  $\text{MAPbI}_3$  was deposited between the two electrodes. Furthermore,  $\text{CsPbI}_x\text{Br}_{3-x}$  film on the electric biasing chip was

also prepared to investigate the migration under electric bias according to chemical components, including organic or inorganic cation and halide anion. The thicknesses of both  $\text{MAPbI}_3$  and  $\text{CsPbI}_x\text{Br}_{3-x}$  film are 75 nm.

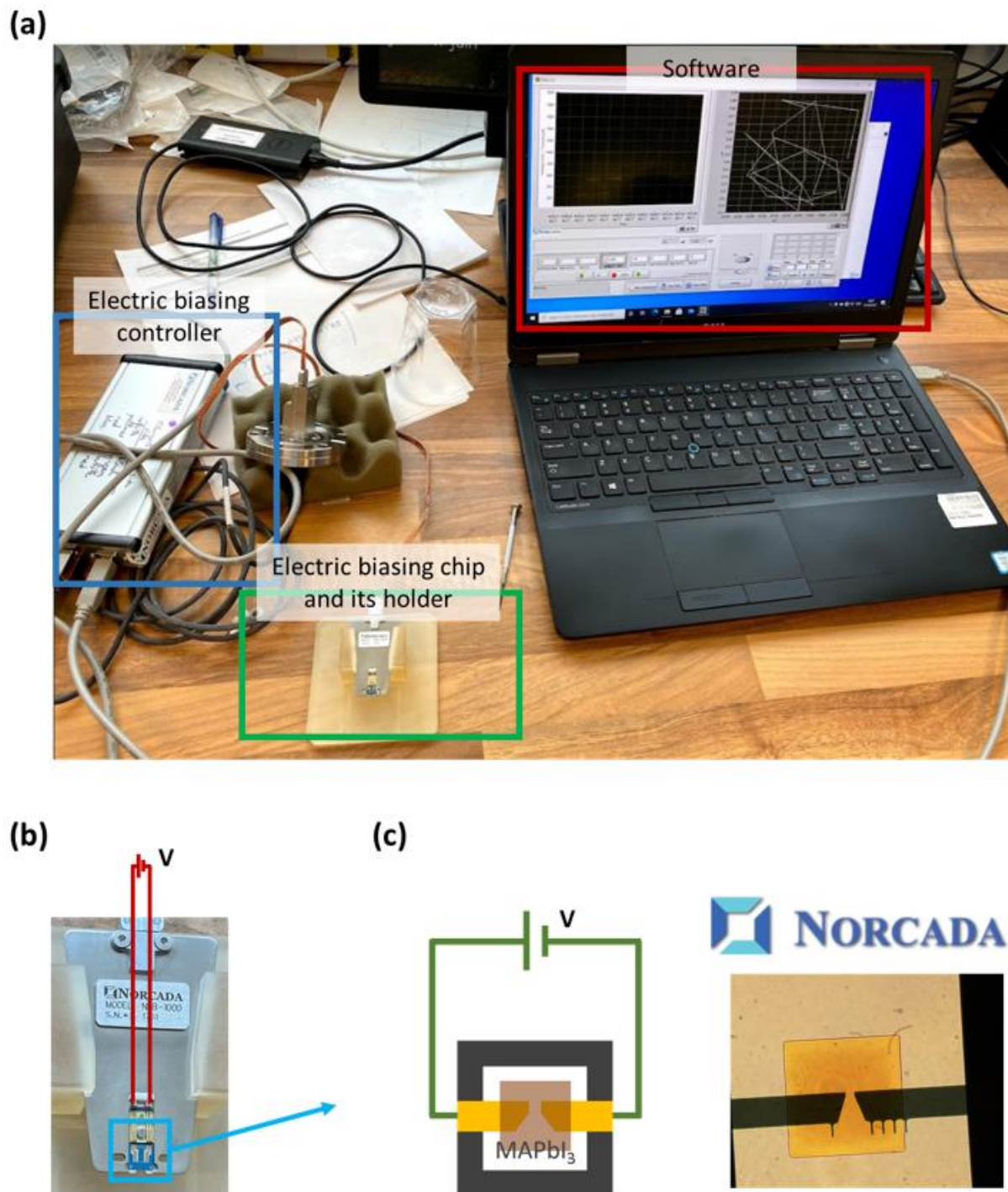


**Figure 5.4** (a) Electric biasing system including electric biasing chip, its holder, electric biasing controller, and software. (b) Close-up electric biasing chip and holder. (c) Schematic and microscope image of  $\text{MAPbI}_3$  film on the electric biasing chip.

After the preparation of the halide perovskite film on the electric biasing chip, the biasing holder with the chip was installed inside the STXM instrument (Fig. 5.5). To keep the high vacuum in the chamber

of STXM, the electrical connections are made through special feedthrough installed on the STXM chamber. The film is biased in-operando during the STXM measurement.

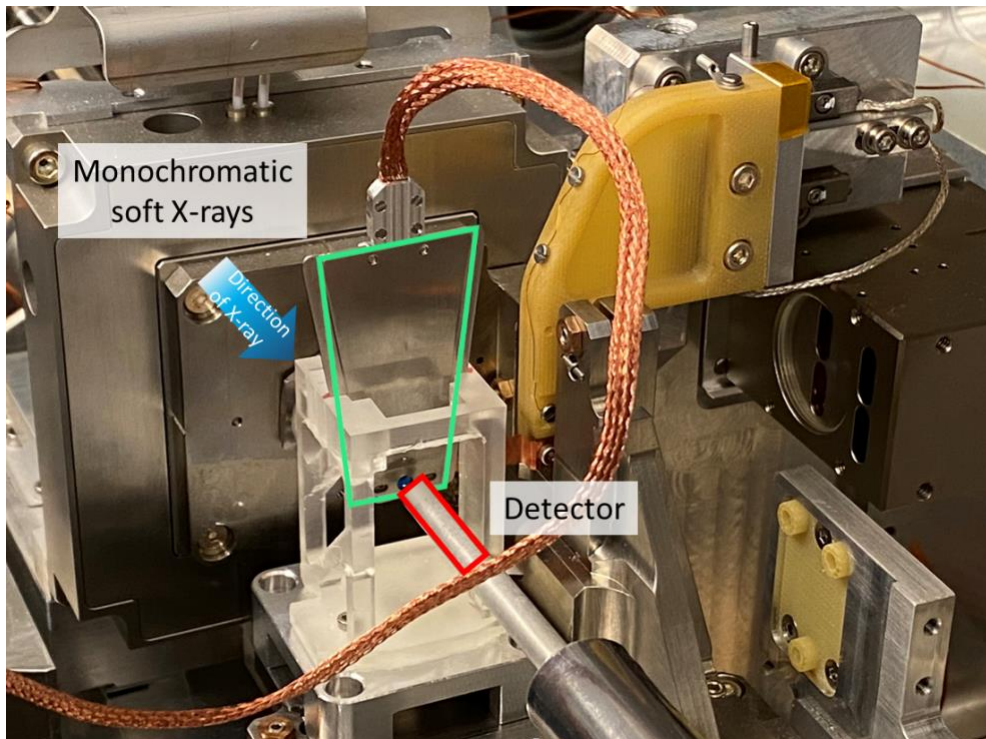


**Figure 5.5** Close-up interior view of the STXM instrument equipped with the in-situ electric biasing system.

## 5.3 Utility of STXM for Chemical Characterization of Halide Perovskites

### 5.3.1 Identification of Components and By-products in Halide Perovskites

As mentioned in section 5.2.2, the soft X-ray regime from 270 to 750 eV is used to research the chemical changes at interfaces between perovskite active layers and charge transport layers as well as ion migration in the perovskite film itself. Fig 5.6 presents the simulated spectra of  $\text{MAPbI}_3$  and the chemical elements that make up the perovskite, including C, N, Pb, and I. In the simulated spectra, there are inner shell X-ray absorption edges of carbon and nitrogen (C K-edge and N K-edge) and the outer shell X-ray absorption edges of I M-edge and Pb N-edge. NEXAFS spectrum of  $\text{MAPbI}_3$  includes all absorption edges of C, N, Pb, and I. Here, we would like to notice that the I M absorption edge in our study has 20 eV higher energy ( $\sim 640$  eV) than that indicated in the Henke database (619

eV) [236]. As pointed out by Hansen [237] and Comes *et al.* [238], studies about the energy of the absorption edges are needed. The energy value of I M-edge has been blue-shifted by 20 eV in the range of 620-700 eV to overcome the discrepancy before simulating the spectra using the software aXis2000 [239].

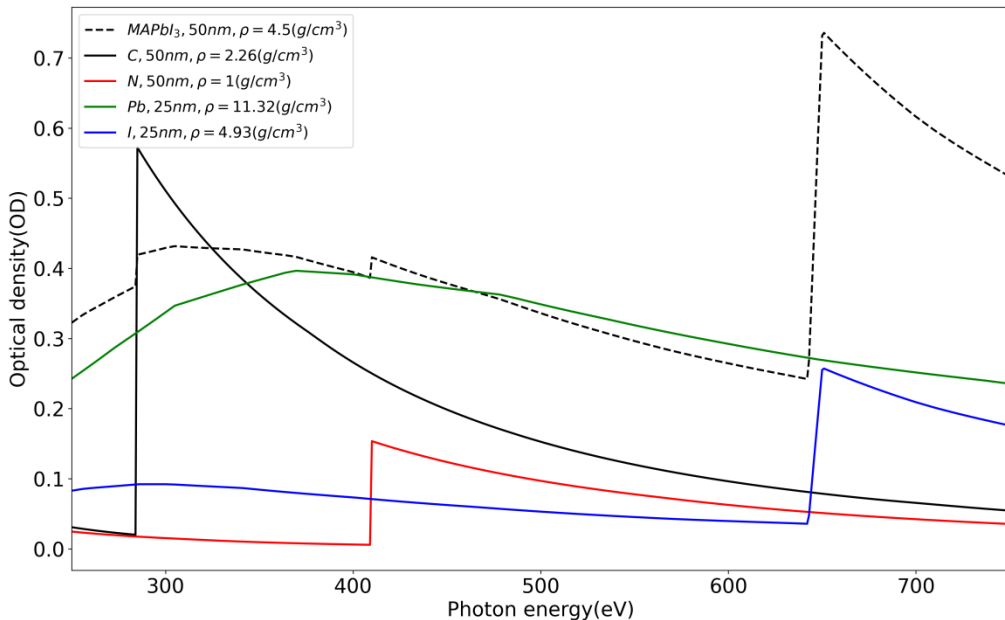


**Figure 5.6** Simulations for the X-ray absorption spectrum of  $\text{MAPbI}_3$  (top) and the different perovskite elements including C, N, Pb, and I (bottom) in soft X-ray region using aXis2000 [239].

In order to demonstrate the utility of soft X-ray STXM for the characterization of halide perovskites, NEXAFS of MAI and  $\text{PbI}_2$ , which form  $\text{MAPbI}_3$ , were measured. Additionally,  $\text{PbCl}_2$  and KI were also characterized to verify the ability to identify halide and organic components and distinguish them from other components. NEXAFS spectra of  $\text{PbI}_2$ , MAI,  $\text{PbCl}_2$ , and KI, covering the C K-edge, N K-edge, O K-edge, I M-edge, and Pb N-edge are shown in Fig. 5.7. In the spectrum of  $\text{PbI}_2$ , a broad Pb N-edge in the form of a “bump” can be observed at around 370 eV. A strong I M-edge at 631 eV is also observed. The spectrum of MAI presents three edges at  $\sim 285$  eV,  $\sim 395$  eV, and  $\sim 631$  eV, which correspond to the C K-edge, N K-edge, and I M-edge, respectively. In the case of KI, the I M-edge at  $\sim 631$  eV and K L-edge at  $\sim 295$  eV are observed in the spectra. The spectra of  $\text{PbCl}_2$  match well with the simulated spectrum.

In comparison to the simulated spectrum, the experimental MAI spectrum appears with an inhibited I M-edge. This fact is supported by energy-dispersive X-ray spectroscopy (EDX) analysis of MAI films in Table 5.1, wherein the iodine atomic percent was observed to be small compared with those of carbon and nitrogen. The experimental percentages of each element, including carbon, nitrogen, and iodine, are described in the table. The atomic ratio of all components obtained by the measurement is different from the ratio in the chemical formula of  $\text{CH}_3\text{NH}_3\text{I}$ . The atomic percentage

of iodide is much smaller than those of carbon and nitrogen, indicating that most iodine is volatilized after deposition on the sample substrate.

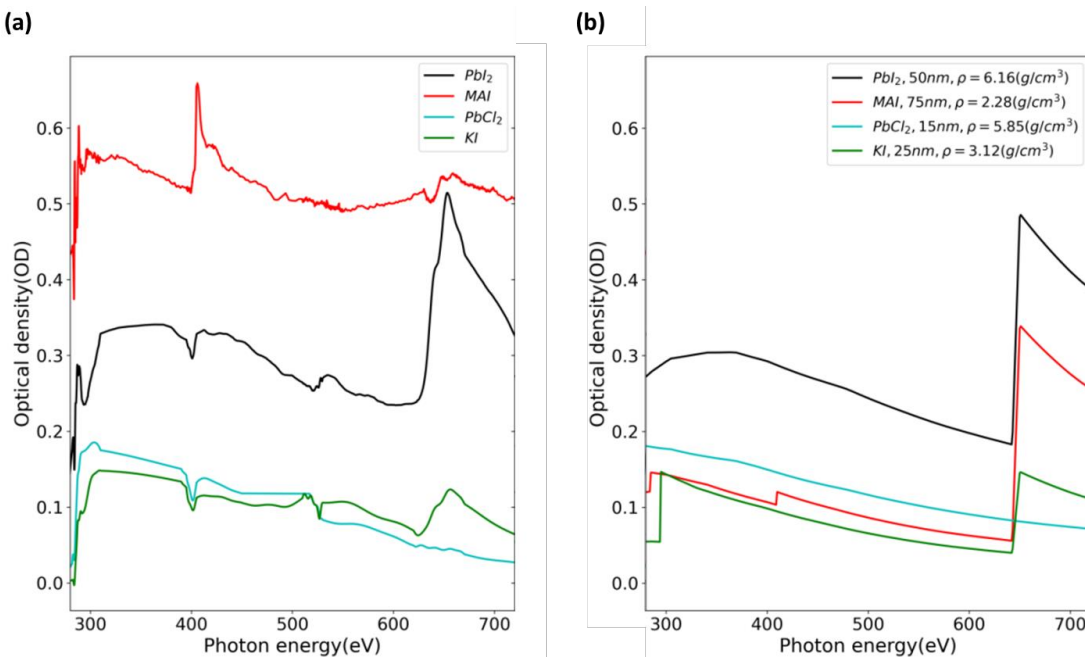


**Figure 5.7** (a) Experimental XAS spectra. (b) Simulated spectra of  $\text{PbI}_2$ ,  $\text{MAI}$ ,  $\text{PbCl}_2$ , and  $\text{KI}$  in the range of 280–720 eV.

**Table 5.1** Energy-dispersive X-ray spectroscopy (EDX) analysis of carbon (C), nitrogen (N), and iodine (I) in  $\text{MAI}$  film.

Element line	Net counts	Atom %
C K	4217	10.82
N K	6305	20.43
I L	572	0.17

It is important to identify not only components of perovskite but also by-products from the film processing and degradation processes to investigate physical and chemical phenomena in PSCs using STXM. For example, in the study of stability in  $\text{MAPbI}_3$ , the major by-products of aged perovskite are  $\text{PbI}_2$  and  $\text{PbO}$  [239]–[243]. Fig. 5.8 shows their corresponding XAS spectra. We confirm that  $\text{PbI}_2$  and  $\text{PbO}$  have broad Pb N-edge at 370 eV in common. However, I M-edge only exists in the OD spectrum of  $\text{PbI}_2$  while the  $\text{PbO}$  spectrum is relatively flat at 640 eV. Furthermore, in the OD spectrum of  $\text{PbO}$ , oxygen K-edge at 543 eV is clearly shown. The presence of oxygen moieties can also be detected in the  $\text{PbI}_2$  spectra, highlighting the sensitivity of these techniques to degradation by-products of aging in air.

These two results in Fig. 5.7 and Fig. 5.8 confirm that each component of  $\text{MAPbI}_3$ , such as  $\text{MAI}$  and  $\text{PbI}_2$ , can be detected and distinguished from other components. The absorption spectra of  $\text{KI}$  (pure iodine, no lead) and  $\text{PbCl}_2$  (only lead, no iodine) in Fig. 5.7 show that we are able to reliably attribute I and Pb contributions to spectra of films that contain both elements. Similarly, the absorption spectra

of  $\text{PbI}_2$  and  $\text{PbO}$  presented in Fig. 5.8 are compared to their 1 nm equivalent simulated spectra to assure the reliable detection of these by-products of aged  $\text{MAPbI}_3$  in the soft X-ray region. The low energy anomaly observed in  $\text{PbO}$  in the C K-edge region (280-310 eV) in Fig. 5.8 (a) could be due to bad normalization or beamline optics contamination.

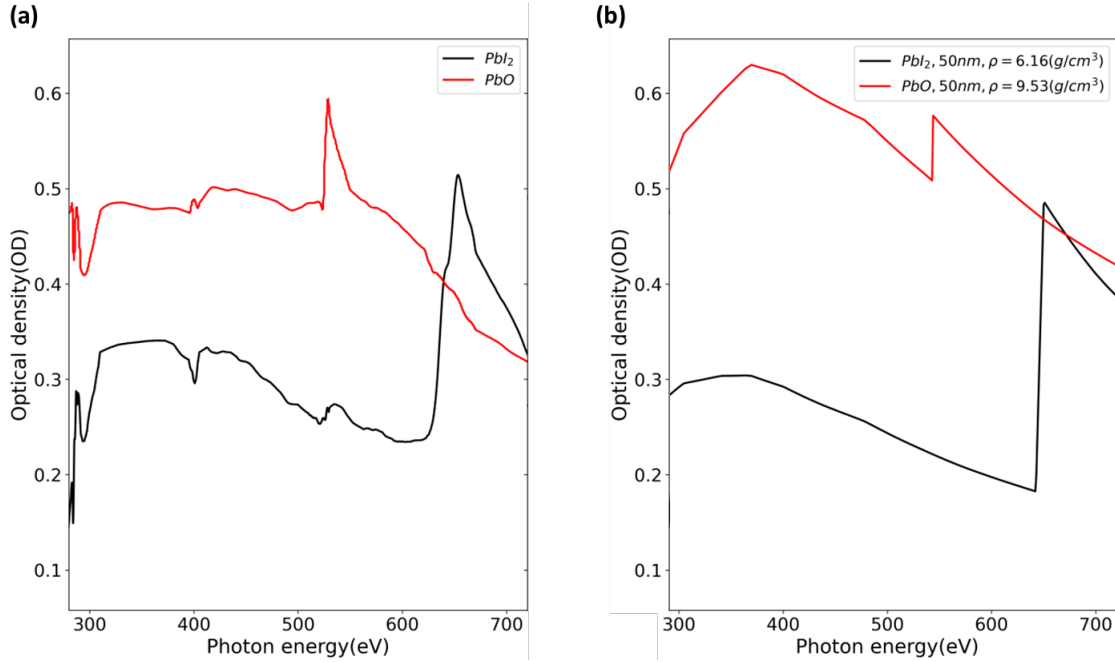


**Figure 5.8** (a) Experimental NEXAFS spectra. (b) Simulated spectra of  $\text{PbI}_2$  and  $\text{PbO}$  in the range of 280-720 eV.

### 5.3.2 Characterization of $\text{MAPbI}_3$ using STXM

In general,  $\text{MAPbI}_3$  is synthesized by the reaction of  $\text{PbI}_2$  and MAI. The large grain size with a small portion of grain boundaries in  $\text{MAPbI}_3$  is generally considered to result in high photovoltaic performance with a low recombination rate [244], [245]. The relative ratio of  $\text{PbI}_2$  to MAI in the vacuum deposition process considerably affects the grain size in  $\text{MAPbI}_3$ , as mentioned in section 3.3.2. Fig. 5.9 illustrates the use of STXM to characterize  $\text{MAPbI}_3$  with different  $\text{PbI}_2$  to MAI ratios. STXM images of  $\text{MAPbI}_3$  with  $\text{PbI}_2$  to MAI ratio of 1:0.5, 1:1 and 1:2.5 at 662 eV are shown in Fig. 5.9 (a), (b) and (c), respectively. Similar to other studies [246], [247], we observe that as the amount of MAI increases, the grain size increases, which is coherent with the results in section 3.3.2. The increase in grain size can be interpreted in Fig. 5.9 (a) to Fig. 5.9 (c) from the increase in domain size (dimension of regions of similar intensity) and decrease in image “roughness”.

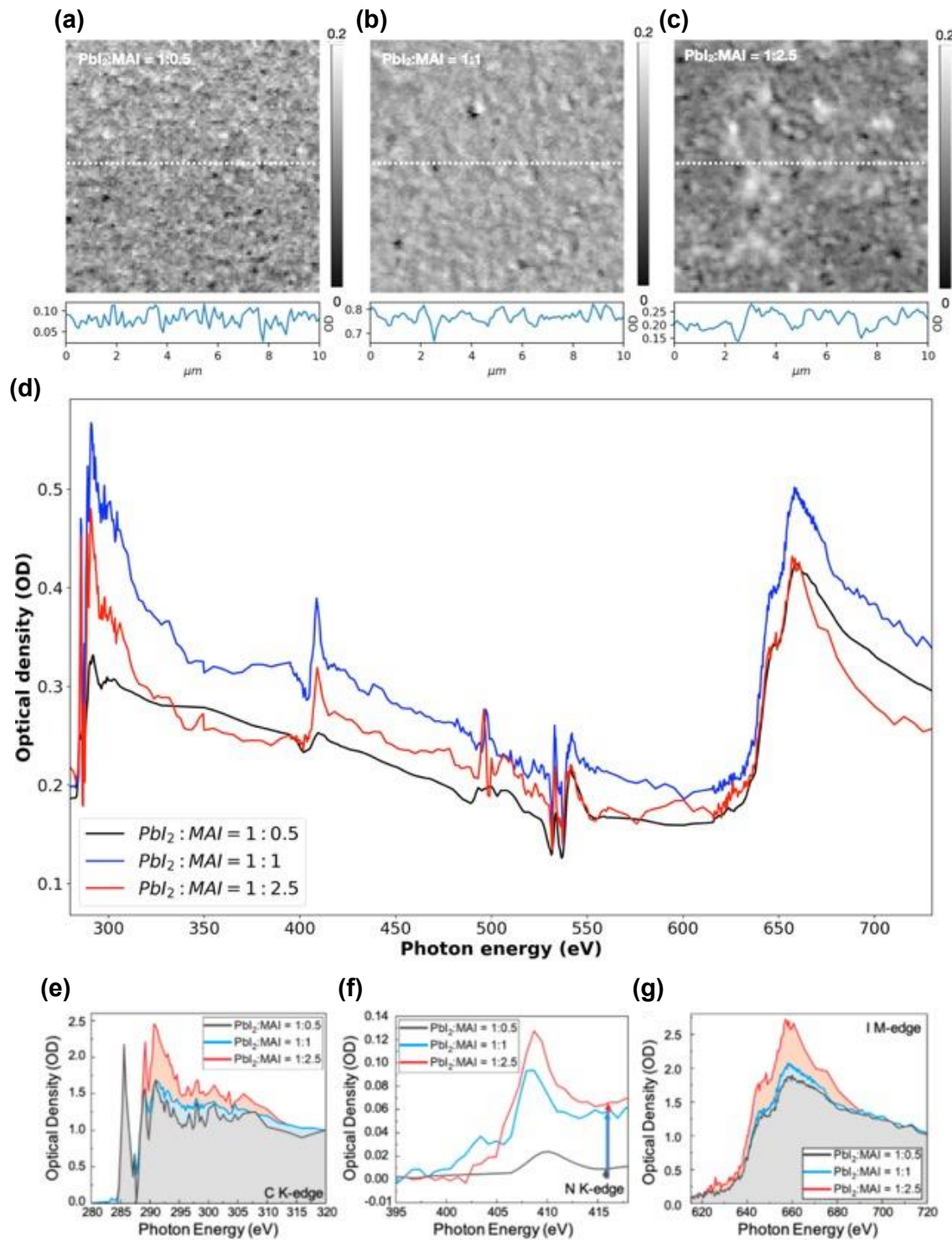


**Figure 5.9** STXM images and spectra of  $\text{MAPbI}_3$  with different  $\text{PbI}_2$  to MAI ratios. STXM images and line profile (taken from white dotted line in the image) at 662 eV with the ratio of (a) 1:0.5 (b) 1:1 (c) 1:2.5. (d) NEXAFS spectra in the entire energy region (280–730 eV), edge normalized (e) C K-edge, (f) N K-edge, and (g) I M-edge region of  $\text{MAPbI}_3$  with different  $\text{PbI}_2$  to MAI ratios. The shaded regions in (e) and (g) indicate the integrated C K-edge spectra and I M-edge spectra, and the arrows in (f) represent the N K-edge jumps.

Fig. 5.9 (d) indicates spectra of  $\text{MAPbI}_3$  with the different ratios that cover N K-edge, O K-edge, I M-edge, and Pb N-edge energy range. The overall difference in the OD of the three spectra, especially that with the  $\text{PbI}_2$  to MAI ratio of 1:1, arises from the difference in film thickness. In order to compare

the spectra and to obtain a semi-quantitative (relative) measure of organic molecules, the integrated area under the edge-normalized C K-edge NEXAFS spectra (Fig. 5.9 (e)), the edge-jump in N K-edge NEXAFS spectra (Fig. 5.9 (f)) and the integrated area under the edge-normalized I M-edge NEXAFS spectra (Fig. 5.9 (g)) are presented in Table 5.2. Investigations related to semi-quantitative studies using NEXAFS spectra often use edge-normalized spectra [248]–[251]. The integrated area under both the C K-edge spectra and the I M-edge spectra, as well as the edge jump in N K-edge spectra (Table 5.2), can be clearly seen to be increasing for samples with higher MAI content.

**Table 5.2** Integrated area under the edge-normalized C K-edge NEXAFS, the edge jump in N K-edge NEXAFS spectra, and the integrated area under the edge-normalized I M-edge of various MAPbI<sub>3</sub> samples.

PbI <sub>2</sub> : MAI deposition ratio in MAPbI <sub>3</sub>	Area under the edge-normalized C K-edge NEXAFS spectra (OD <sup>2</sup> )	Edge jump (OD) in N K-edge NEXAFS	Area under the edge-normalized I K-edge NEXAFS spectra (OD <sup>2</sup> )
1:0.5	35	0.008	149
1:1	39	0.058	153
1:2.5	45	0.065	169

Fig. 5.10 shows XAS obtained from STXM measurements of MAPbI<sub>3</sub> with optimized ratio (PbI<sub>2</sub> : MAI = 1:2.5) and two different thicknesses. The two spectra of MAPbI<sub>3</sub> with 25 nm and 50 nm thicknesses have similar features with the expected difference in OD that corresponds to the difference in thickness. The clearly observed essential absorption edges (C K-edge, N K-edge, O K-edge, and I M-edge) further confirm the reliability of STXM in detecting thickness variations in MAPbI<sub>3</sub> films with similar chemical compositions. The sharp drop observed in the C K-edge region is possibly due to incorrect normalization in this region or carbon contamination on the beamline optics during these particular measurements.

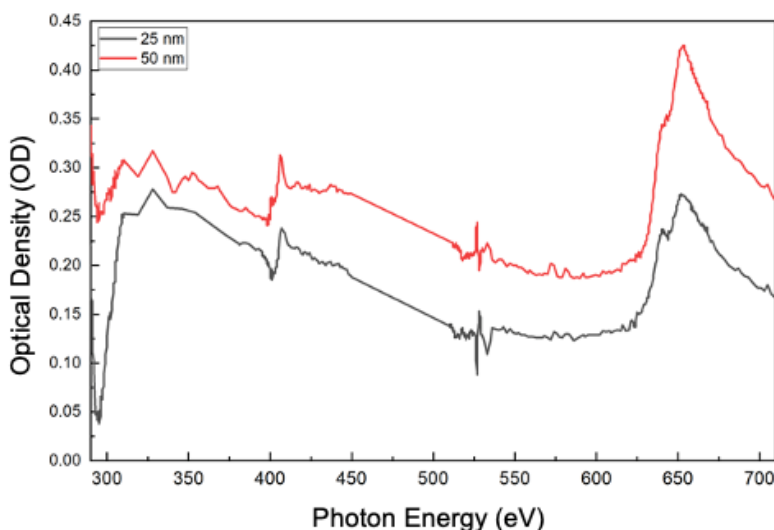


**Figure 5.10** Experimental NEXAFS spectra of MAPbI<sub>3</sub> with different thicknesses.

### 5.3.3 Evaluation of Homogeneity of MAPbI<sub>3</sub> based on STXM

Inhomogeneous morphology was observed in MAPbI<sub>3</sub> with 1:2.5, and consequently, a spatially resolved analysis was performed to investigate the chemical homogeneity in MAPbI<sub>3</sub>. Fig 5.11 (a) shows a STXM image of MAPbI<sub>3</sub> with the ratio of 1:2.5 at 662 eV. Fig 5.11 (b), (c), and (d) indicate the C, N, and I cluster maps of MAPbI<sub>3</sub> for the same region obtained from cluster analysis performed by the software MANTIS [252]. Fig 5.11 (e), (f), and (g) are corresponding background removed XAS spectra for different clusters represented in the cluster maps. In all cases, the shape of spectra according to the clusters can be considered the same, and the variation observed arises only from the overall intensity. The intensities of spectra arising from clusters 1 and 2 are almost identical but vary in each case with the spectra of cluster 3. Considering the similarity in maps and spectra of clusters 1 and 2, the morphological and chemical homogeneities are obvious.

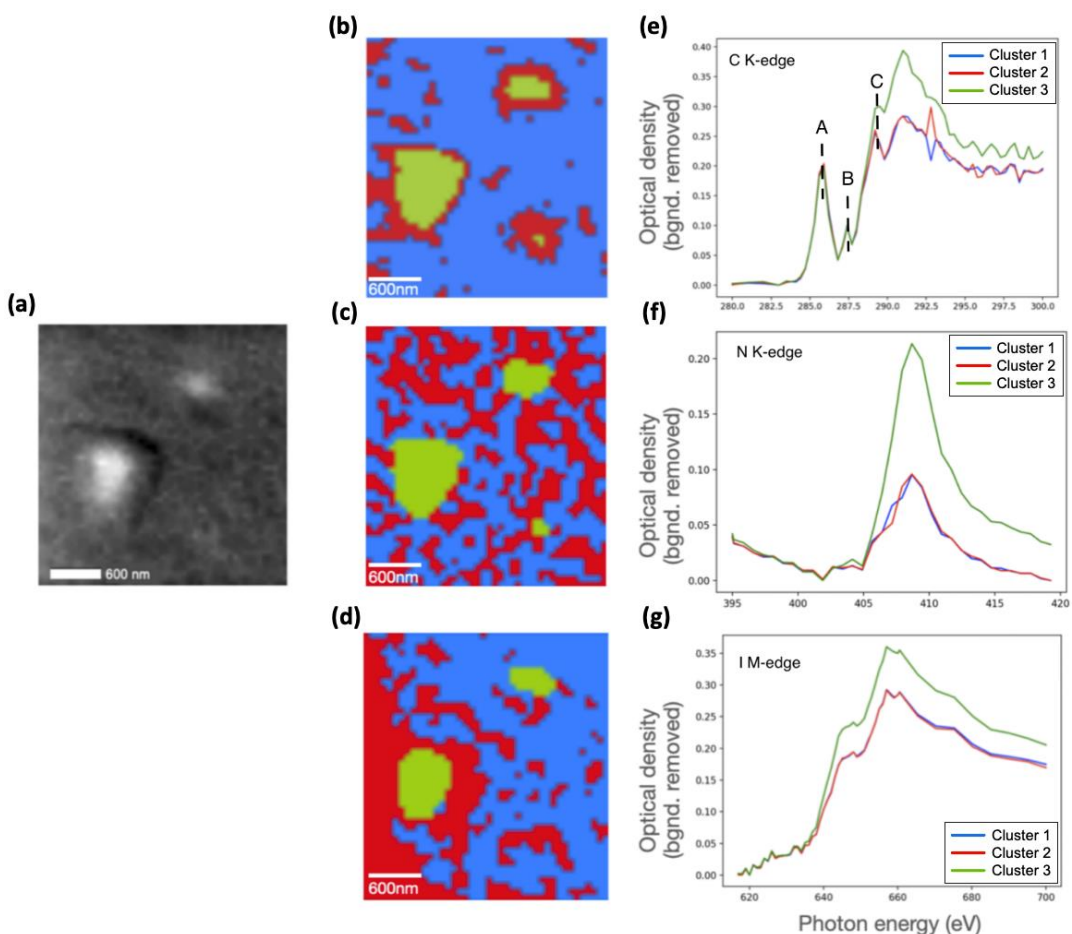


**Figure 5.11** (a) STXM image-at 662 eV of MAPbI<sub>3</sub> with PbI<sub>2</sub> to MAI ratio of 1:2.5. Cluster images of MAPbI<sub>3</sub> in the (b) C K-edge, (c) N K-edge, and (d) I M-edge region. Corresponding average cluster XAS spectra of cluster analysis in the (e) C K-edge, (f) N K-edge, and (g) I M-edge region (Color of each spectrum corresponds to the color of each cluster on the map).

In C K-edge spectra (Fig. 5.11 (e)), the pre-edge spectral features of A (286 eV) and B (~287.5 eV) are related to  $\text{C}1\text{s}\rightarrow\pi^*(\text{C}=\text{C})$  and  $\text{C}1\text{s}\rightarrow\pi^*(\text{C}=\text{O})$  transitions respectively [253]. In this first study, we guess that these features indicate the presence of oxidation and/or degradation products due to the samples being exposed to air. The feature C at 289.5 eV and the shoulder just below it are most likely caused by  $\text{C}1\text{s}\rightarrow\sigma^*$  (C-H)/Rydberg peak [254]. Higher energy features in C K-edge (> 290 eV) and in N K-edge (> 405 eV) accord with  $\text{C}1\text{s}\rightarrow\sigma^*$  and  $\text{N}1\text{s}\rightarrow\sigma^*$  transitions. The sensitivity of these two absorption edges, along with O K-edge (not fully utilized in this study due to beamtime constraints) to chemical moieties, is well-known [255], and spectral features in these edges could be utilized to identify various functional groups in different halide perovskite.

The increase in OD of cluster 3 spectra indicates that while the chemical homogeneity persists on the grain, the thickness is higher. These cluster maps obtained from STXM provide spatially resolved spectra of not only the halide component but also organic components. They could be valuable in accessing chemical changes that could arise from aging or different kinds of stress on the nanometer scale.

## 5.4 Degradation of Halide Perovskite Film and Solar Cells under In-situ Biasing

### 5.4.1 Degradation of MAPbI<sub>3</sub> Film under In-situ Electric Bias

In the previous sections, we demonstrated that STXM has a high sensitivity to chemical composition and homogeneity in halide perovskites. In addition, we verified that it is a useful characterization technique for an in-depth analysis of physical and chemical phenomena in PSCs. As mentioned in section 1.2.3, halide perovskites have outstanding optoelectric properties, which contribute to the high-power conversion efficiency in PSCs. However, low operational stability is one of the main issues challenging commercialization. Among the various operational environments, including light, heat, and electric field, which affect the degradation of PSCs, the influence of the electric field on the degradation of PSCs has not been systematically studied. For a systematic study of the effect of the electric field on the degradation of PSCs, a multimethod approach is necessary.

Here, degradation phenomena caused by the electric bias are investigated using STXM. In this section, the changes in the bulk of perovskite films were observed by using STXM. For this study,  $\text{MAPbI}_3$  thin film of 75 nm thickness was deposited on a special electrical biased chip. Fig. 5.12 (a), (b) shows STXM OD (optical density) images of  $\text{MAPbI}_3$  on the electric biasing chip with two Au electrodes taken at 662 eV. *A relatively thin film (75nm) along with a large inter-electrode distance (4  $\mu\text{m}$ ) implies a high resistance of the film along with a low current.* To increase the current passing through  $\text{MAPbI}_3$ , we applied a higher voltage of 15 V than that applied to solar cells under operation. The current detected by the blaze software is 7  $\mu\text{A}$ .

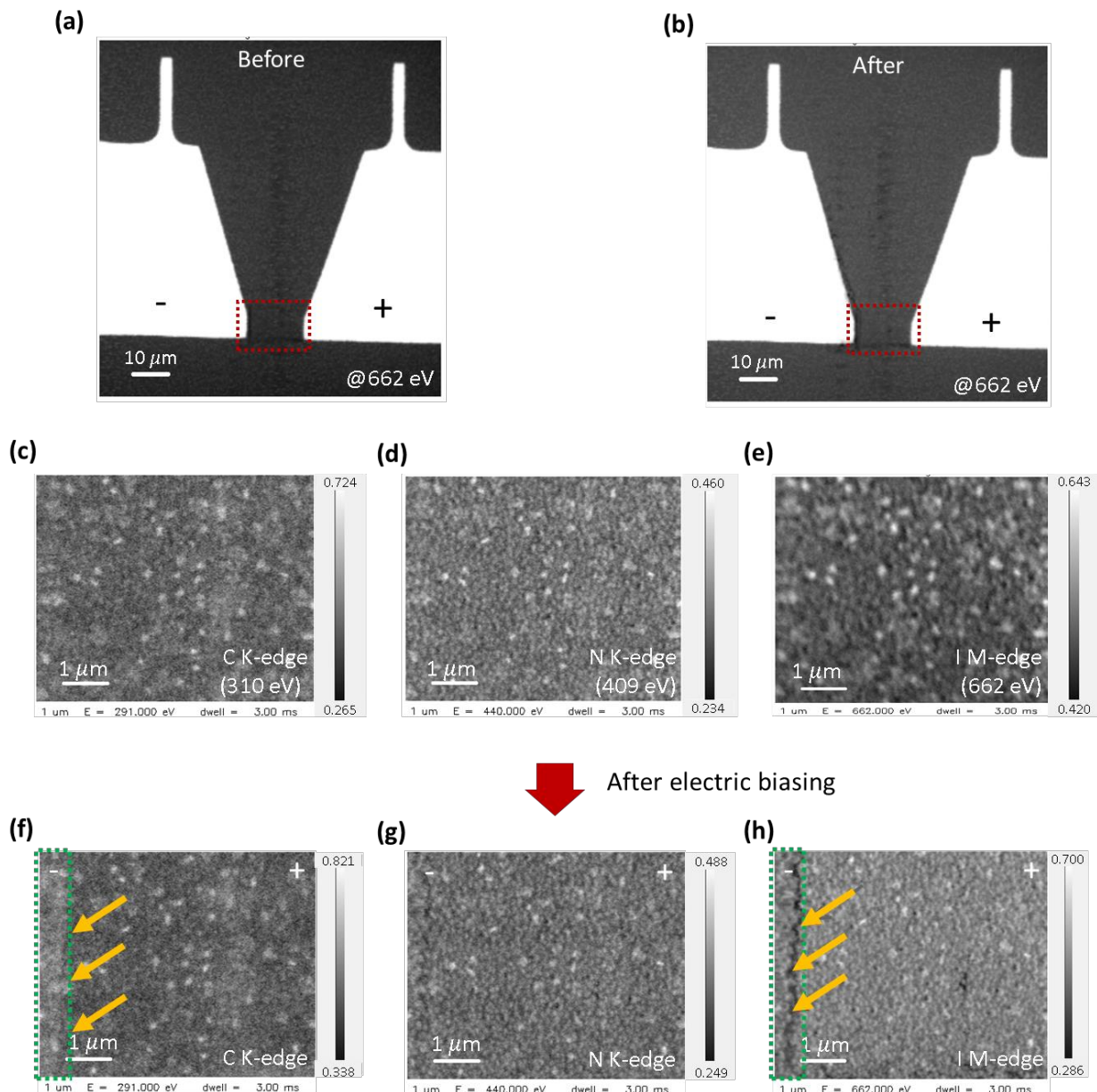


**Figure 5.12** STXM images at 662 eV of  $\text{MAPbI}_3$  (a) before and (b) after applying an electric field. Red dotted regions in (a) and (b) indicate the region of  $\text{MAPbI}_3$  between two Au electrodes with the shortest distance. Zoomed-in STXM images of the red dotted region before biasing at (c) 310 eV (C K-edge), (d) 409 eV (N K-edge), and (e) 662 eV (I M-edge). Zoomed-in STXM images of the red dotted region after biasing at (f) 310 eV (C K-edge), (g) 409 eV (N K-edge), and (h) 662 eV (I M-edge).

The red dotted square region in Fig. 5.12 (a) and (b) was chosen as the region of interest and investigated closely. Fig. 5.12 (c), (d), and (e) indicate STXM images taken before biasing at C K-edge, N K-edge, and I M-edge, respectively. These three images clearly imply that carbon, nitrogen, and iodine are homogeneously distributed before biasing. Upon the application of the electric field, the MAPbI<sub>3</sub> film, significant changes can be observed near the cathode. In Fig. 5.12 (f), the OD of carbon near the cathode (green dotted region) is much relatively higher than in other regions. On the other hand, the OD of iodine (Fig. 5.12 (h)) near the cathode is much smaller. Negative ions of iodine have migrated to the anode under an electric field, as has also been observed in other studies [39], [40], [140].

It is interesting to note that only a small change was observed in nitrogen OD (marked in red in Fig. 5.12 (g)) under electric bias, although the OD of carbon near the cathode increases relatively significantly. To analyze the change of MA<sup>+</sup> under electric bias in detail, the spectra that cover the I M-edge (Fig. 5.13 (c)), C K-edge (Fig. 5.13 (d)), and N K-edge (Fig. 5.13 (e)) are extracted from the region of MAPbI<sub>3</sub> near the cathode (Fig. 5.13 (a) and (b)). In the three spectra, the red lines indicate the XAS spectra before applying an electric field, while the green lines indicate the XAS spectra before applying the electric field.

In Fig. 5.13 (c), the OD intensity of I M-edge at 662 eV significantly decreases after applying an electric field, which indicates that the iodine ions near the cathode migrate in the direction of the anode. In the case of carbon, there is a change in the opposite direction implying that there is indeed a migration of carbon atoms towards the cathode as well (Fig. 5.13 (d)). The spectra show additional changes in the C K pre-edge. The minor peak related to C1s→σ\* (C-H) at 289.5 eV slightly increases.

In addition, the pre-edge spectral features of C1s→π\* (C=C), which are negligible before applying electric bias, appear after applying the electric field. On the other hand, minor peak of C1s→π\* (C=O) disappears after electric bias. With the changes in peaks in the C K pre-edge region, we can guess that the electric field results in the change of chemical bond in MA<sup>+</sup>. This increase in carbon content is accompanied by an increase the nitrogen content as well, indicated by the overall edge jump (440 eV) for the spectrum of the biased sample as compared to the unbiased sample. This comparatively smaller shift (0.001 OD) could be due to incorrect normalization.

While it is evident that there is indeed a relative increase in C content near the cathode, in order to investigate the relative changes in the region of interest (as opposed to an average visualization from the spectra), the STXM OD images at 285 eV are subtracted from those at 291 eV for the biasing experiment.

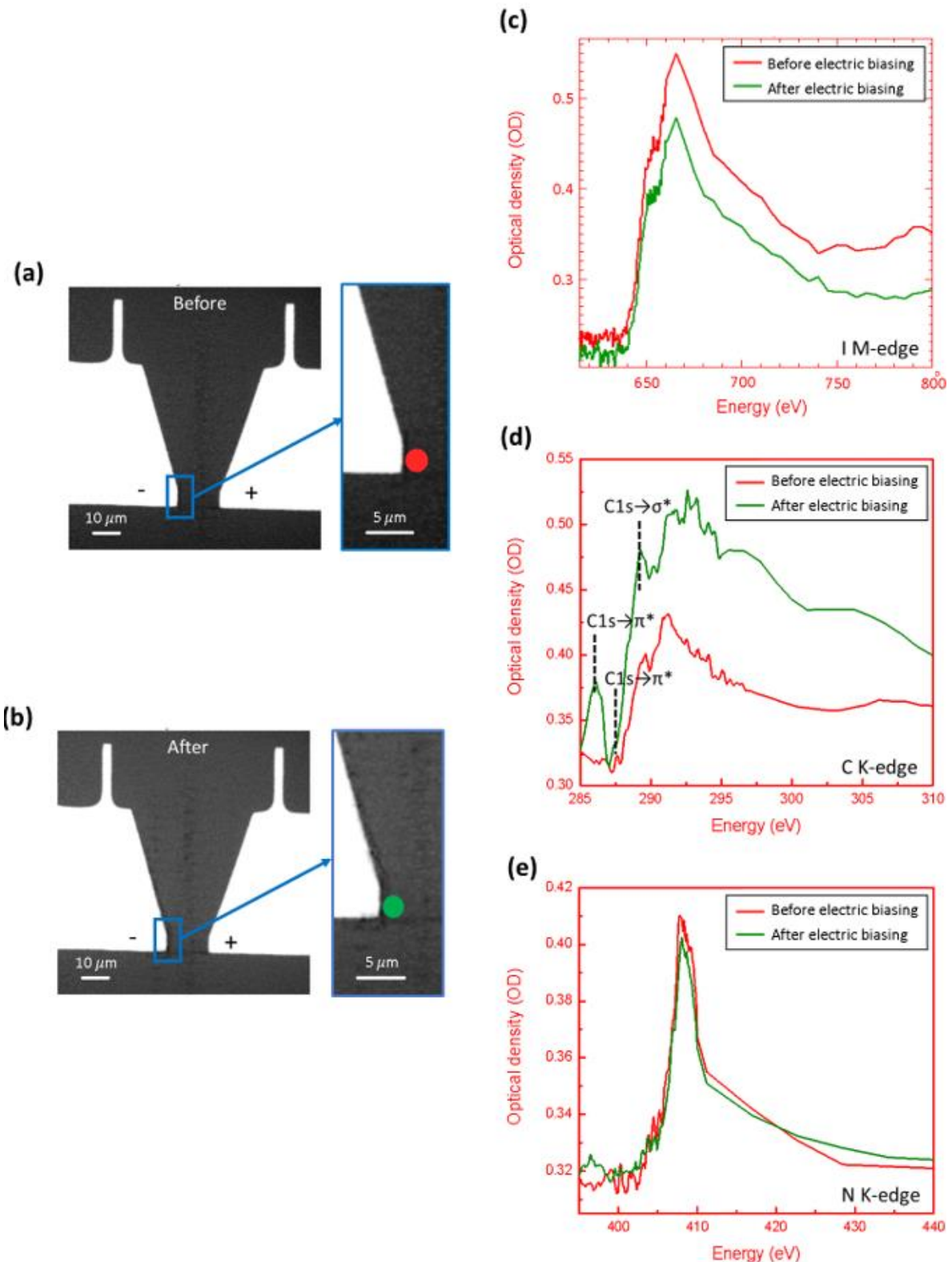


**Figure 5.13** STXM OD images at 662 eV of  $\text{MAPbI}_3$  (a) before and (b) after applying an electric bias. The region of interest near the cathode has been marked in red and green in (a) and (b). I M-edge (c) C K-edge, and (d) N K-edge NEXAFS spectra of  $\text{MAPbI}_3$  before and after electric biasing as extracted from the ROI.

Fig. 5.14 (a) shows STXM images before C K-edge energy (at 285 eV) and Fig. 5.14 (b) presents STXM images after C K-edge energy (291 eV). The images are measured under the electric field every ten minutes. Compared with the fresh image (0 minute), the changes in the OD of  $\text{MAPbI}_3$  near

the cathode, both 285 eV and 291 eV, are shown after 10 minutes. Furthermore, the OD of the region and the area of increased region increase with time. When the STXM image at 285 eV is deducted from that at 291 eV, the difference between STXM images at two energies is constant regardless of the time. For the images taken after 10 minutes, the observed bright regions around the anode and bottom of the cathode in the image difference are artifacts of the image alignment procedure and not the result of an actual change in OD.

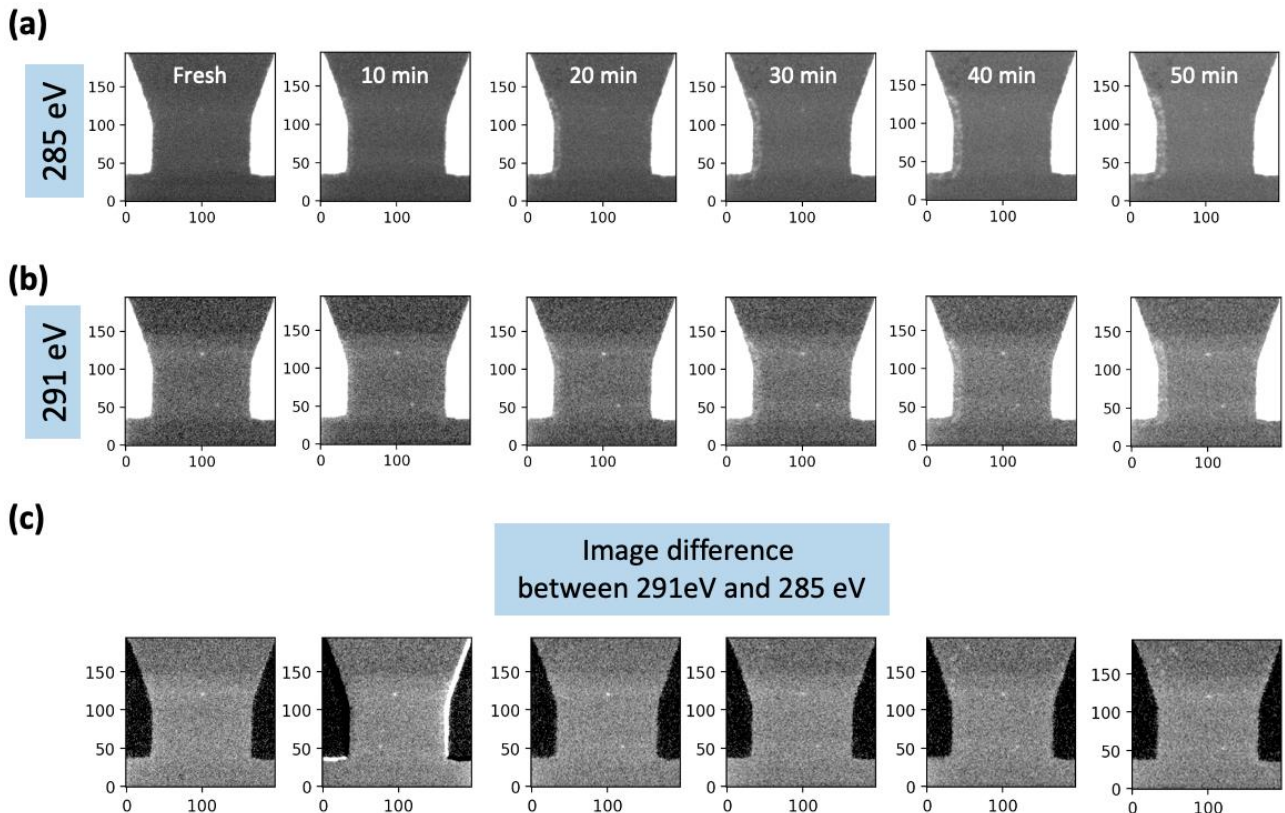


**Figure 5.14** STXM images at (a) 285 eV (before C K-edge) and (b) 291 eV (after C K-edge) measured every 10 minutes under electric field. (c) Image difference between STXM image at 291 eV and that at 285 eV.

For clarity, below is the point-wise summary of observations:

1. Iodine is observed to migrate away from the cathode. Spectral data also indicate that the average iodine content decreases near the cathode. OD images at 662 eV show a systematic decrease in the OD near the cathode.
2. Spectral data and OD image at 291 eV indicate a clear increase in the carbon content near the cathode. This increase is an overall increase in the carbon content, i.e., not a particular bond-specific species, and can be ascertained from the difference between the 291 eV and 285 eV images.
3. While there is an increase in carbon content, a similar increase is not clearly observed in the nitrogen content in figure 5.12 (g) but is seen in figure 5.13 (e). This indicates a breakdown or decomposition of the  $\text{MA}^+$  ions under an electric field.

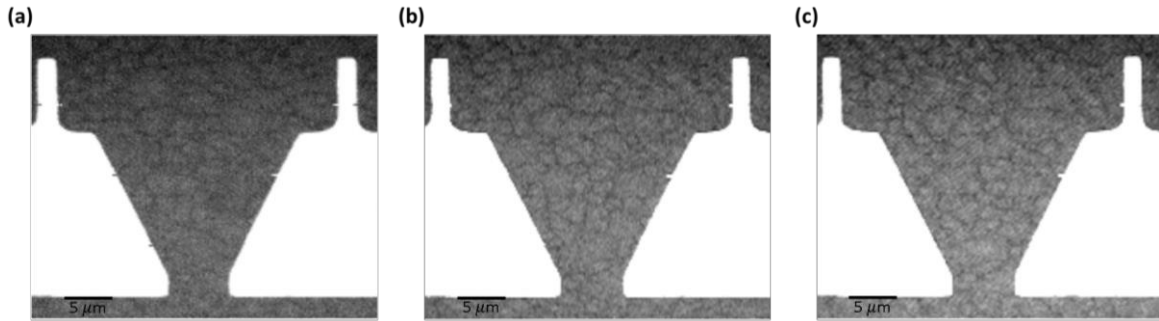


**Figure 5.15** STXM images of  $\text{CsPbIxBr}_{3-x}$  at Cs M-edge (750.8 eV) (a) fresh, under in-situ electric bias for (b) 15 minutes and (c) 60 minutes.

Additionally, preliminary STXM measurements of  $\text{CsPbIxBr}_{3-x}$  film on the electric biasing chip under in-situ biasing were also performed.  $\text{CsPbIxBr}_{3-x}$  is all inorganic perovskite compared to  $\text{MAPbI}_3$  with organic cation ( $\text{MA}^+$ ). In the STXM measurement of  $\text{CsPbIxBr}_{3-x}$ , Cs M-edge at 740 eV is required to be considered. Fig. 5.15 presents the STXM images of fresh and biased  $\text{CsPbIxBr}_{3-x}$  film at 750.8 eV. In the energy region, the information of both iodine and cesium atoms can be obtained at the same time. In Fig. 5.15, the  $\text{CsPbIxBr}_{3-x}$  film in all regions is homogeneous regardless of applying the electric field. It implies that not only cesium ions but also iodine ions do not migrate under an electric field which emphasizes more stability than  $\text{MAPbI}_3$ . However, more studies, including measurement of the spectrum from all regions, including lead and bromine, are required to investigate the detailed change of chemical bond under the electric field.

#### 5.4.2 Degradation of $\text{MAPbI}_3$ Solar Cells Induced by Ex-situ Electric Field

The influence of the electric field on the bulk of  $\text{MAPbI}_3$  is investigated in the earlier section. Through the experiment, the chemical change of  $\text{MAPbI}_3$ , including the relative amount of atoms and the chemical bond after applying an electric field, can be understood in detail. In this section, the degradation behavior of  $\text{MAPbI}_3$  in PSCs caused by an electric field is studied. The difference between the experiment in this section and that in section 5.4.1 is that the chemical reaction between  $\text{MAPbI}_3$  and charge transport layers (HTL/ETL) also needs to be considered in this section. In this experiment, five reference  $\text{MAPbI}_3$  PSCs (ITO/PEDOT:PSS/ $\text{MAPbI}_3/\text{C}_{60}/\text{BCP/Ag}$ ) are prepared. Among them, the J-V characteristics of two PSCs with different directions of the applied electric field are measured to study electrical properties. The other PSCs are employed in the form of a FIB section to analyze from the chemical point of view using STXM.

Fig. 5.16 shows the changes in J-V characteristics after applying positive/negative bias voltage, and Table 5.3 summarizes the photovoltaic performance of PSCs with each condition. The PCE of two

fresh solar cells is 14.74 % and 11.79 %, respectively. Although the PCE of the two reference solar cells is different, they are in the normal range of PCE of the reference PSCs described in chapter 3 (Fig. 3.16 (b)). When the positive bias of 2.5 V is applied in one of the PSCs, a PCE of 11.02 % with a  $J_{SC}$  of  $22.55 \text{ mA/cm}^2$ , a FF of 61.4 %, a  $V_{OC}$  of 0.80 V, and high hysteresis is obtained (Fig. 5.16 (a)). There is a noticeable decrease in  $J_{SC}$ ,  $V_{OC}$ , and  $R_{SH}$ , leading to a decrease in FF and PCE. Especially, the decrease in  $R_{SH}$  and FF implies the formation of defects at the interfaces after applying the electric field. Furthermore, J-V hysteresis behavior with HI of 0.46 indicates that the electric bias causes ion migration in PSCs. On the other hand, the shorted circuit in PSC after applying the negative bias to the other PSC. As shown in Fig. 3.15 (f) of chapter 3, PSC has diode J-V characteristics. In the PSCs, the diode breakdown occurs at high negative voltages (Fig. 5.16 (b)). In these J-V measurements of PSCs after applying electric bias, we confirm that the change of electric properties induced by the negative electric bias is bigger than those caused by the positive voltage despite the same magnitude of applied voltage.

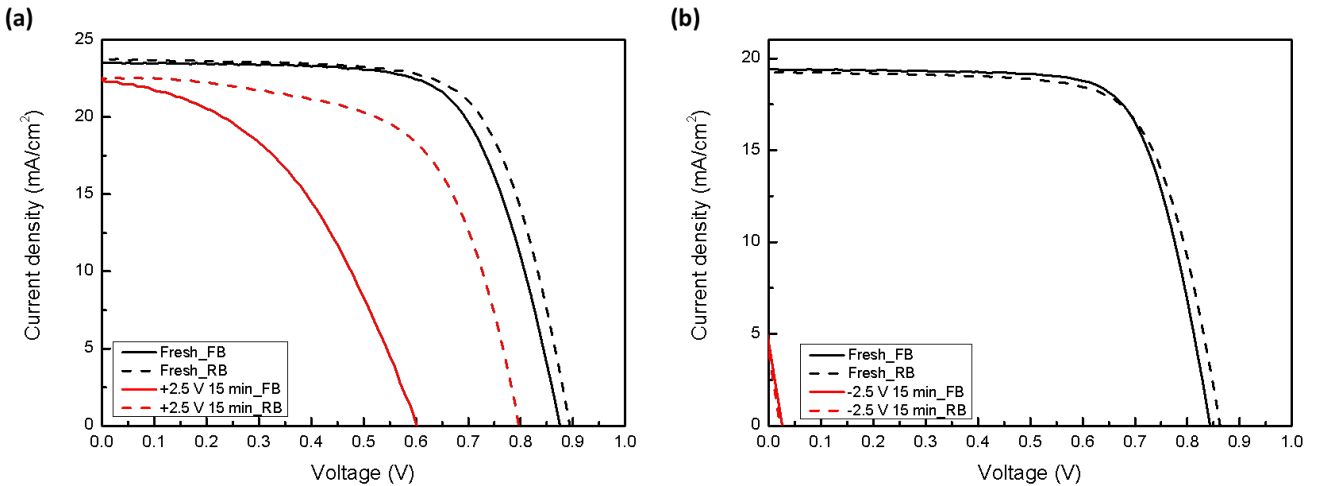


**Figure 5.16** J-V characteristics of MAPbI<sub>3</sub> PSCs (a) before and after applying an electric field of +2.5 V for 15 minutes and (b) before and after applying an electric bias of -2.5 V for 15 minutes.

**Table 5.3** Summary of photovoltaic parameters of MAPbI<sub>3</sub> PSCs with the fresh condition and applying the electric bias of +5 V and -5 V

	Scan direction	$V_{OC}$ (V)	$J_{SC}$ (mA/cm <sup>2</sup> )	FF (%)	$R_S$ (ohm)	$R_{SH}$ (ohm)	PCE (%)
Fresh	Forward scan	0.88	23.51	68.5	5.89	1.26k	14.09
	Reverse scan	0.89	23.74	69.4	5.26	2.56k	14.74
+2.5 V 15 minutes	Forward scan	0.60	22.39	43.8	10.7	273	5.9
	Reverse scan	0.80	22.55	61.4	5.58	861	11.02
Fresh	Forward scan	0.84	19.40	72.5	5.71	2.89k	11.86
	Reverse scan	0.86	19.27	70.9	5.69	2.01k	11.79
-2.5 V 15 minutes	Forward scan	0.03	4.57	25.0	5.75	5.71	0.03
	Reverse scan	0.03	4.10	22.1	5.20	5.46	0.02

The three remained PSCs whose J-V characteristics were not measured were prepared with three different biasing conditions fresh (0 V), +2.5 V for 15 minutes, and -2.5 V for 15 minutes, respectively). After that, cross-section samples of each device were prepared with FIB. Fig. 5.17 (a), (b), and (c) presents cross-section STXM images of MAPbI<sub>3</sub> PSCs without electrical biasing and after applying an electric field of +2.5 V and -2.5 V, respectively. Fig 5.17 (d), (e), and (f) correspond to XAS spectra at the I M-edge of the middle part of the MAPbI<sub>3</sub> layer and the layer near PEDOT:PSS and C<sub>60</sub> in each sample.

In the fresh sample (Fig 5.17 (a) and (d)), the form and the intensity of the spectra in a whole region, including the middle part (green) and two interfaces between MAPbI<sub>3</sub> and charge transport layers (PEDOT:PSS (blue) and C<sub>60</sub> (red)), are the same. The same spectra indicate that the morphological and chemical properties of the full MAPbI<sub>3</sub> layer are homogeneous. After applying the positive voltage of +2.5 V, the shapes of the I M-edge in all the regions are the same however, the OD intensity of I decreases from PEDOT:PSS to C<sub>60</sub> (Fig 5.17 (b) and (e)). It shows that negative iodine ions migrate toward PEDOT:PSS under positive electric bias. In addition, small resonance features at the pre-edge region (below 640 eV) are found in MAPbI<sub>3</sub> near PEDOT:PSS after electric bias, which is not found in the experiment of in-situ biasing MAPbI<sub>3</sub> on Norcada biasing chip (in section 5.4.1). The features imply that the electric field induces a chemical change of MAPbI<sub>3</sub> or reaction with PEDOT:PSS. On the contrary, the OD intensity of I decreases from C<sub>60</sub> to PEDOT:PSS when the positive voltage of -2.5 V is applied (Fig 5.17 (c) and (f)), re-emphasizing I<sup>-</sup> ion migration under an electric field. Under the negative electric bias, the small resonance features at the pre-edge region also appear. However, the peaks at 623 eV and 632 eV are conspicuous, and the overall spectra include noise compared with other PSCs, including the fresh one and the device after applying the positive voltage. As mentioned in the analysis of J-V characteristics of PSCs before and after applying the positive voltage, the current at - 2.5V is higher than that at +2.5 V, or the breakdown occurs, which indicates that applying the negative voltage is stronger for PSCs to be changed or degraded than the positive voltage.

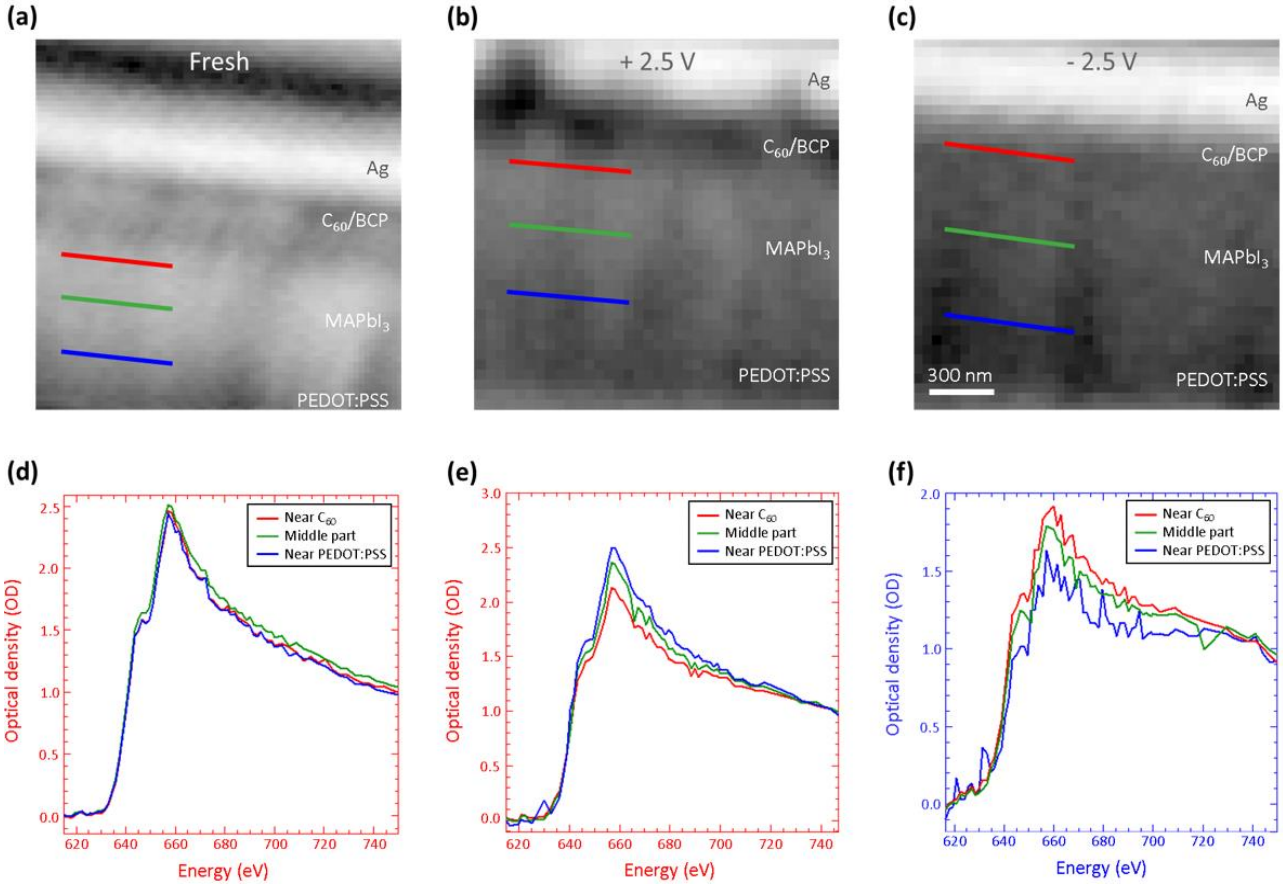


**Figure 5.17** STXM images of FIB sections of (a) fresh MAPbI<sub>3</sub> PSCs and the PSCs after applying (b) +2.5 V and (c) -2.5 V for 15 minutes. The STXM images were measured at 616.5 eV. I M-edge NEXAFS spectra of (d) fresh MAPbI<sub>3</sub> layers between PEDOT:PSS and C<sub>60</sub>, and the layer after applying (e) +2.5 V and (f) -2.5 V. The colors of the NEXAFS spectrum line in (d), (e), and (f) accord with those marked in the regions of STXM images (a), (b), and (c) where each absorption spectrum was obtained.

In order to further understand the electric field-induced degradation of the MAPbI<sub>3</sub> layer in the device, XAS at the C K-edge of MAPbI<sub>3</sub> for the fresh sample and for the sample that was negatively biased was measured. For the fresh sample, the various spectra are overlapping, underlying the homogeneity of the deposition (Fig. 5.18 (a) and (b)). The C1s→π\* feature is much more pronounced than in figure 5.13 (d), especially relative to the σ\* region (high energy). We think that this could be because this particular sample (fresh) is slightly thicker than rest of the samples. This saturates the signal above the absorption edge (>287 eV). Consequently, the relative difference between the pre-edge and post-edge features is not comparable to figure 5.13 (d). For the negatively biased sample (Fig. 5.18 (c) and (d)), the OD intensity of C K-edge at 291 eV decreases from PEDOT:PSS to C<sub>60</sub>, which is the opposite direction of I<sup>-</sup> migration under the electric bias and coherent with the results of an in-situ biasing test of MAPbI<sub>3</sub> on the Norcada biasing chip (Fig. 5.13 (d)). Furthermore, there are changes in C K pre-edge. The pre-edge spectral feature of C1s→π\* (C=C) at 286 eV is higher, and that of C1s→σ\* (C-H) at 289.5 eV is lower at the interfaces than those of the middle part of MAPbI<sub>3</sub>. It

means that C-H bonds in methylammonium are broken after applying electric bias, and new bonds are formed at the interface. In addition, the OD intensity of C1s $\rightarrow\pi^*$  (C=O) at  $\sim$ 287.5 eV is much stronger at the interface between MAPbI<sub>3</sub> and PEDOT:PSS. It is worth noting that we observe not only the migration of the ions (also observed in the in-situ biasing chip) but we also observe the changes in the resonance of iodine and the chemical bonds in MA<sup>+</sup> at the interfaces between MAPbI<sub>3</sub> and HTL/ETL using STXM. A detailed explanation of the phenomena occurring in MAPbI<sub>3</sub> between PEDOT:PSS and C<sub>60</sub> are described in the next section. Note that we were unable to obtain reasonable noise-free spectra of the positively biased sample due to a lack of sufficient beamtime.

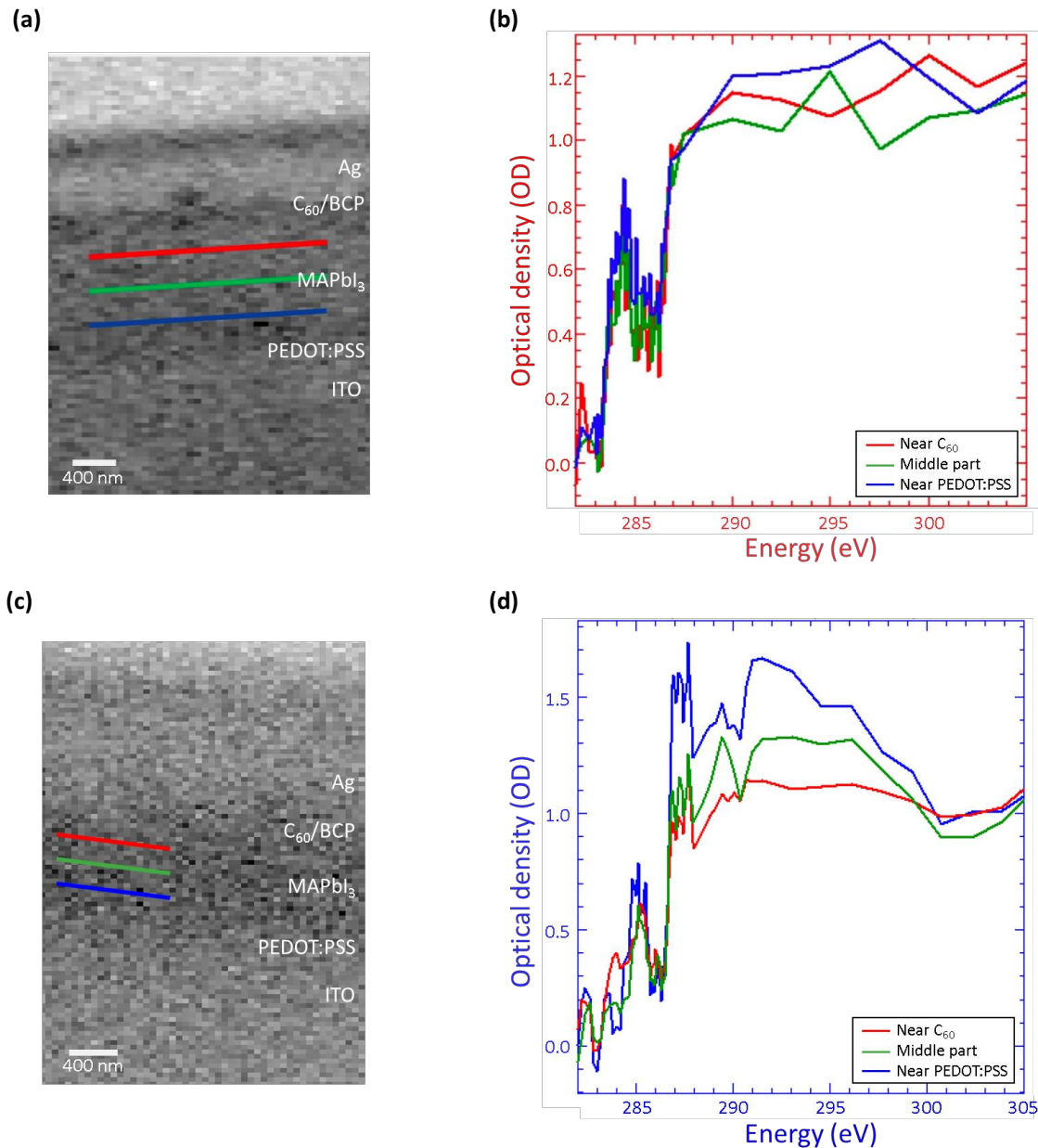


**Figure 5.18** (a) Cross-section STXM images and (b) C K-edge NEXAFS spectra of fresh MAPbI<sub>3</sub> PSCs. (a) Cross-section STXM images and (b) C K-edge NEXAFS spectra of MAPbI<sub>3</sub> PSCs after applying -2.5 V for 15 minutes. The colors of the NEXAFS spectrum line in (b) accord with those marked in the regions of STXM images (a) where each absorption spectrum was achieved.

### 5.4.3 Proposal to Explain Electric Field-induced Degradation Mechanism in MAPbI<sub>3</sub> Solar Cells through the Correlation between STXM and EIS Results

In chapter 4 and this chapter, the influence of the electric field on the MAPbI<sub>3</sub> PSCs is studied using EIS (Fig. 4.11 in section 4.3.2), J-V characteristics (Fig. 5.16), and STXM (Fig. 5.13, Fig. 5.17 and Fig. 5.18). In this section, we analyze the change in electrical properties of the PSCs by correlating J-V characteristics with EIS results obtained in chapter 4. Furthermore, we try to propose the mechanism of the electric field-induced degradation in MAPbI<sub>3</sub> PSCs, which has a decisive influence on the change in impedance properties in PSCs.

As mentioned in section 4.3.2, R<sub>1</sub> and C<sub>2</sub> in all PSCs with different perovskite materials, including the reference solar cells, are not affected by the electric field. The R<sub>1</sub> indicates a contact resistance of contact metal which also determines R<sub>s</sub> in J-V characteristics. C<sub>2</sub> means geometrical capacitance, which is determined by the thickness of PSCs. Based on two electrical parameters, we confirm that the contact resistance and geometrical capacitance of PSCs are not influenced by the electric field. In the J-V curves of the PSCs (Fig. 5.16 (a)), R<sub>SH</sub> and FF decrease due to defects formed at the interfaces after biasing. The defects at the interface accelerate the charge carrier recombination with the increase in R<sub>2</sub> of EIS results. In addition, the appearance of C<sub>3</sub> and R<sub>3</sub> upon the electric bias in EIS results cannot be matched with electrical parameters such as V<sub>OC</sub> and J<sub>SC</sub>. However, the J-V hysteresis is observed (Fig. 5.16 (a)) before being a dead cell (Fig. 5.16 (b)).

A mechanism of electric field-induced degradation in MAPbI<sub>3</sub> is proposed to describe the origin of the defect at the interface, which contributes to the increase in R<sub>2</sub> and ion migration which contributes to the appearance of R<sub>3</sub> and C<sub>3</sub> in EIS results based on the STXM results (Fig. 5.13, Fig. 5.17 (d) and (f), and Fig. 5.18 (b) and (d)). Herein, the phenomena in the PSCs are explained in three parts including the middle part of MAPbI<sub>3</sub> layer, MAPbI<sub>3</sub> near C<sub>60</sub> and PEDOT:PSS (Fig. 5.19). In Fig. 5.19 (a), mobile iodine ions (I<sup>-</sup>) with iodine vacancies (V<sub>I</sub><sup>+</sup>) are formed upon an electric bias. The negative iodine ions migrate toward the C<sub>60</sub> layer under the electric field. In the case of MA<sup>+</sup>, two decomposition pathways are more favorable rather than decomposition into simple MA<sup>+</sup> from MAPbI<sub>3</sub> [Ref 1, 16, 18]. One is CH<sub>3</sub>NH<sub>2</sub> with HI, which is formed with H from MA<sup>+</sup> and mobile I<sup>-</sup>. The other one is NH<sub>3</sub> and CH<sub>3</sub><sup>+</sup>. The positive ion CH<sub>3</sub><sup>+</sup> can be reacted with I<sup>-</sup> forming CH<sub>3</sub>I, or the ion can migrate into PEDOT:PSS. In the case of nitrogen, CH<sub>3</sub>NH<sub>2</sub> and NH<sub>3</sub> are neutral and do not migrate under an electric field, which enables the homogeneous XAS spectra of N in all regions (Fig. 5.13 (e)).

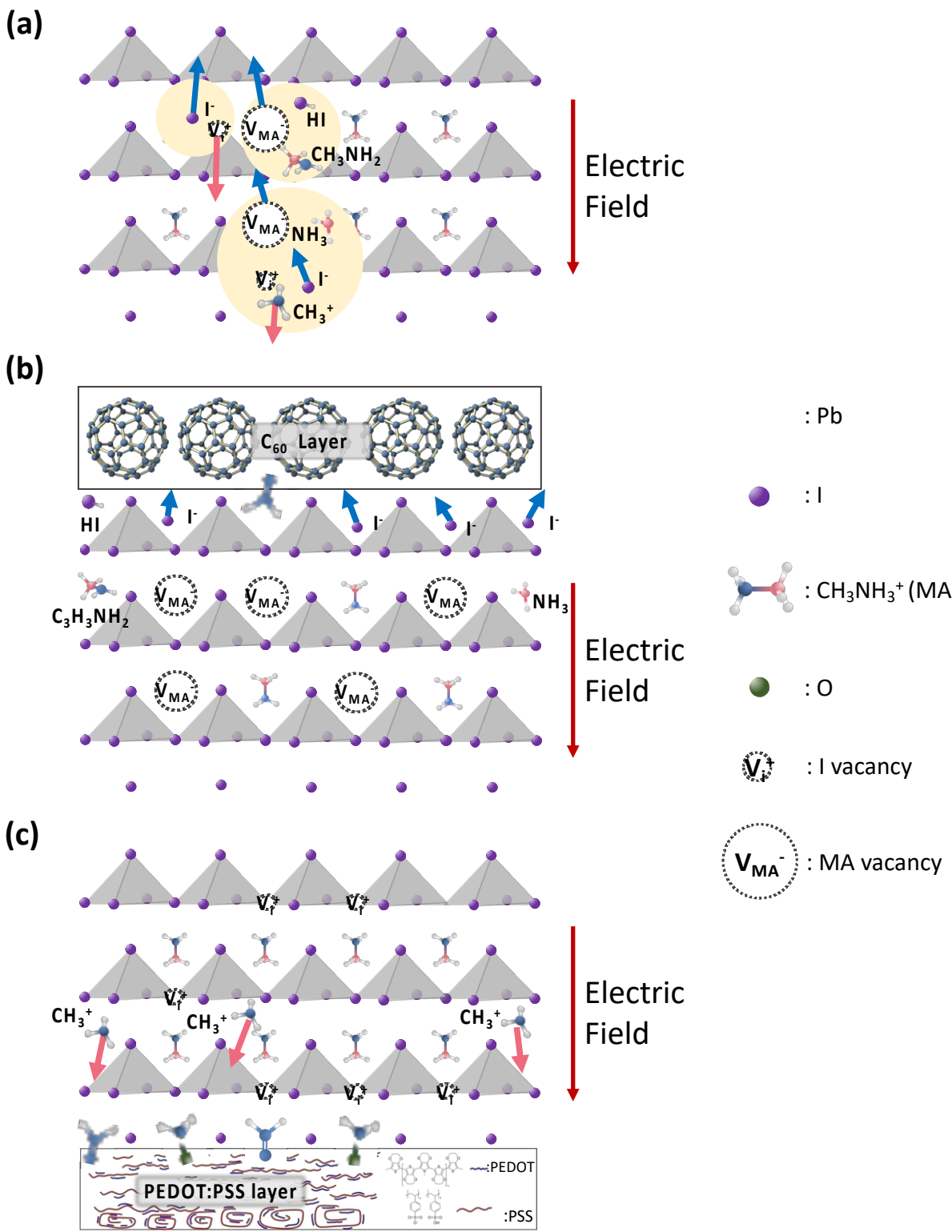


**Figure 5.19** Schemes of the electric field-induced degradation process in MAPbI<sub>3</sub> (a) in the middle part, (b) near C<sub>60</sub> (ETL), and (c) near PEDOT:PSS. In the PSCs of the illustrations, negative electric bias is applied.

In MAPbI<sub>3</sub> near C<sub>60</sub> (Fig. 5.19 (b)), the same chemical reactions of iodine and organic cation caused by an electric field occur. In addition, the mobile iodine ions and methylammonium vacancies (MA<sup>+</sup>) are accumulated at the interface between MAPbI<sub>3</sub> and C<sub>60</sub>. The ions and vacancies lead to the formation of R<sub>3</sub> and C<sub>3</sub> and J-V hysteresis in J-V curves. Furthermore, CH<sub>3</sub><sup>+</sup> ions formed by the electric field react with the adjacent C<sub>60</sub>/BCP layer, and H<sub>2</sub>C=M (M is an atom or a molecule from

$C_{60}$  and BCP) formed, which contributes to the increase in the peak of  $C1s \rightarrow \pi^*$  ( $C=C$ ) at 286 eV and decrease in  $C1s \rightarrow \sigma^*$  ( $C-H$ ) at 289.5 eV in XAS spectra (Fig. 5.18 (b)). The formation including the  $C=C$  double bond at the interface plays a role as a defect leading to an increase in  $R_3$  of EIS results and a decrease in  $R_{SH}$  measured by J-V characteristics.

Lastly, in the  $MAPbI_3$  layer near PEDOT:PSS (Fig. 5.19 (c)), the formation of mobile iodine and the decomposition of organic cation also occurs. Upon the negative bias, the positive ions of  $CH_3^+$  and  $V_I^+$  are accumulated at the interface, which contributes to  $R_3$  and  $C_3$  in EIS results. At the interface between  $MAPbI_3$  and PEDOT:PSS, the single bond of C-N is broken, and  $C=C$  bond are formed through reaction of  $CH_3^+$  ions with the PEDOT:PSS. Furthermore, PEDOT and PSS are divided through methanol treatment to enhance the conductivity of PEDOT:PSS, as mentioned in chapter 2. Here, PSS divided from PEDOT has  $O^-$  bond. The oxygen ion in PSS reacts with  $CH_3^+$  and the  $C=O$  bond forms leading to the increase in the peak of  $C1s \rightarrow \pi^*$  ( $C=O$ ) at 287.5 eV. In addition, the diffusion of oxygen from ITO under thin PEDOT:PSS can also react with  $CH_3^+$  forming  $C=O$ . The products formed by the reactions at the interface act as defects which affects the electrical properties in PSCs.

Through this correlation between the results electrical characterization including EIS and J-V curves and STXM results, we can propose a reliable hypotheses of electric field-induced degradation in PSCs. During the degradation process, ion migration and the formation of defects at the interface occurs. They affect the electrical characteristics including deterioration of photovoltaic performance and appearance of another impedance parameter which is shown in the J-V curves and EIS results. Through the STXM results, we can propose to identify the mobile ions which is not only iodine but also  $CH_3^+$ . In addition, the form of defect at the interface can be explained based on change in the chemical bonds of organic component at interface in the STXM spectra.

# **Chapter 6.**

## **General Conclusion and Perspectives**

The main goal of the thesis was to study degradation in MAPbI<sub>3</sub> solar cells caused by an electric field and explain the electric field-induced degradation mechanism through a multimethod approach. Degradation of PSCs during operation is a hindrance to the achievement of the PSCs with long-term stability. Therefore, it is important to systematically understand the degradation mechanism so that the solutions to the problems can be found. In this study, various methods for the characterization of PSCs were employed, including J-V characteristics and EIS.

To study physical phenomena in PSCs, the high crystalline perovskite films and PSCs with high efficiency and reproducibility are required. In the study, MAPbI<sub>3</sub> was deposited by vacuum deposition. By varying the deposition rate ratio of PbI<sub>2</sub> and MAI, the rate of PbI<sub>2</sub>, and hole transport material under MAPbI<sub>3</sub>, high crystalline MAPbI<sub>3</sub> film without the PbI<sub>2</sub> phase was achieved. Based on the optimized film, MAPbI<sub>3</sub> solar cells with different ETL and HTL were fabricated. PCE of all PSCs fabricated is over 11 %, with a low hysteresis index, which is appropriate for studying physical phenomena in PSCs. Among them, a high PCE of 14.79 % with a low hysteresis index of 0.05 was achieved in the reference MAPbI<sub>3</sub> solar cell in this study (ITO/PEDOT:PSS/MAPbI<sub>3</sub>/C<sub>60</sub>/BCP/Ag).

Using the reference solar cell, we have studied the change in the MAPbI<sub>3</sub> bulk and the interfaces between MAPbI<sub>3</sub> and charge transport layers caused by an electric field from an electrical and chemical point of view. Firstly, the influence of the electric field on the impedance of PSCs with various activation layers (wet- and dry-processed MAPbI<sub>3</sub> and 3CP) was investigated using EIS. After applying an electric field, R<sub>2</sub> resistance determined by nonradiative charge recombination increases, and a second capacitance (C<sub>3</sub>) at a low frequency is observed. The second capacitance is interpreted as a charge accumulation layer at interfaces. These results are coherent with the J-V curves of MAPbI<sub>3</sub> solar cells after applying an electric field that the shunt resistance decreases, and the hysteresis index increases. Additionally, the evolution of the reference solar cells under exposure to air was studied with J-V curves, impedance, and dielectric modulus spectroscopy. It is worthy to note that the conductivity of grain decreases and that of grain boundary increases with time which promotes ion migration with J-V hysteresis.

Secondly, we investigated the effect of the electric field on the degradation in bulk MAPbI<sub>3</sub> film and PSCs with STXM. Before studying the effect, we demonstrated the possibility that STXM is spectroscopy as well as microscopy for studying halide perovskite by identifying various components of MAPbI<sub>3</sub> and MAPbI<sub>3</sub> with different conditions. After that, an electric field was applied to bulk MAPbI<sub>3</sub> film on a special electric biasing chip during the STXM measurement (in-situ biasing). After applying bias, not only I<sup>-</sup> migration but also carbon migration with deformation of carbon bonding were observed. Furthermore, the various deformation of carbon bonding was observed at the interface between MAPbI<sub>3</sub> and charge transport layers (PEDOT:PSS or C<sub>60</sub>) in the FIB section of biased MAPbI<sub>3</sub> solar cells.

Through the correlation between electrical characterization, including EIS and J-V curve results and STXM, we can propose an hypothesis to explain the degradation mechanism in MAPbI<sub>3</sub> solar cells. We highlight that ion migration of I<sup>-</sup>, V<sub>I</sub><sup>+</sup>, CH<sub>3</sub><sup>+</sup> and V<sub>MA</sub><sup>-</sup> is observed with STXM, and the results support the J-V hysteresis and EIS results under the electric field. In addition, the chemical reactions at the interface between MAPbI<sub>3</sub> and charge transport layers are analyzed using STXM, and the defects at the interfaces that affect impedance properties can be identified. This study emphasized the utility of STXM for a detailed understanding of phenomena in PSCs.

In perspective, the hypothesis suggested that for a complete analysis, further investigation with a wider range of techniques, including other synchrotron techniques such as photoelectron microscopy for surface and interface effects, grazing incidence X-ray scattering for observing changes in crystallinity, and hard X-ray fluorescence measurements for observing changes in ion migration are needed. As a part of this PhD work, it is important to note that preliminary investigations on other synchrotron-based techniques such as GIWAXS and nano-XRF have already been performed with especially interesting results that need further analysis. In addition, STXM measurement with a more systematic condition and additional measurements are required to establish the hypothesis. Furthermore, we plan to study electric field-induced degradation in other PSCs with different active layers such as FAPbI<sub>3</sub>, MA<sub>0.5</sub>FA<sub>0.5</sub>PbI<sub>3</sub>, (MA<sub>0.17</sub>FA<sub>0.83</sub>)<sub>0.95</sub>Cs<sub>0.05</sub>Pb(I<sub>0.83</sub>Br<sub>0.17</sub>)<sub>3</sub> using STXM to understand the chemical change according to components in halide perovskite under an electrical field. Meanwhile, we observed the change in the conductivity of grain and grain boundary with ageing, and it implies that the increase in the conductivity of grain boundary promotes ion migration. Therefore, the changes in grain boundaries under various environments from the chemical points of view will be studied with STXM to understand the relation between grain boundaries and ion migration in detail.

## Appendix A.

### List of Publication

1. C. Dindault, **H. Jun**, D. Tondelier, B. Geffroy, J. E. Bourée, Y. Bonnassieux, P. Schulz, and S. Swaraj, “Metal halide perovskite layers studied by scanning transmission X-ray microscopy,” *RSC Adv.*, vol. 12, pp. 25570-25577, Sep. 2022.
2. **H. Jun**, H. R. Lee, D. Tondelier, B. Geffroy, P. Schulz, J. E. Bourée, Y. Bonnassieux, and S. Swaraj, “Soft X-ray characterization of halide perovskite film by scanning transmission X-ray microscopy,” *Sci. Rep.*, vol. 12, no. 1, pp. 1-11, Mar. 2022.
3. M. Kim, **H. Jun**, H. Lee, H. Nahdi, D. Tondlier, Y. Bonnassieux, J. E. Bourée, and B. Geffroy, “Halide ion migration and its role at the interfaces in perovskite solar cells,” *Eur. J. Inorg. Chem.*, vol. 2021, no. 46, pp. 4781-4789, Oct. 2021. (1<sup>st</sup> co-author)
4. J. An, Z. Zheng, R. Gong, T. Nguyen, **H. Jun**, M. Chrostowski, J. Maurice, W. Chen, P. R. i Cabarrocas, “Interfacial hydrogen incorporation in epitaxial silicon for layer transfer,” *Appl. Surf. Sci.*, vol. 518, no. 10, pp. 146057, Mar. 2020.
5. E. Moyen, **H. Jun**, H. Kim and J. Jang, “Surface engineering of room temperature grown inorganic perovskite quantum dots for highly efficient inverted light emitting diodes,” *ACS Appl. Mater. Interfaces*, vol. 10, no. 49, pp. 42647-42656, Nov. 2018.
6. E. Moyen, A. Kanwat, S. Cho, **H. Jun**, R. Aad and J. Jang, “Ligand removal and photo-activation of CsPbBr<sub>3</sub> quantum dots for enhanced optoelectronic devices,” *Nanoscale*, vol. 10, no. 18, pp. 8591-8599, Apr. 2018.
7. M. Mativenga, **H. Jun**, Y. Choi, J. UM, and J. Jang, “Circular structure for high mechanical bending stability of a-IGZO TFTs,” *IEEE J. Electron Devices Soc.*, vol. 5, no. 6, pp. 453-457, Sep. 2017.

## **Appendix B.**

# **Conferences, Training, and Scholarships**

## **Conferences**

1. **H. Jun**, D. Tondelier, P. Schulz, J. E. Bourée, B. Geffroy, Y. Bonnassieux, and S. Swaraj, “Soft X-ray Spectromicroscopy of Organic Inorganic Halide Perovskites”, 15<sup>th</sup> X-ray Microscopy (XRM2022), Hsinchu, Taiwan, Jun. 2022. **Oral**
2. **H. Jun**, A. Loncle, K. Medjoubi, D. Tondelier, F. Oswald, P. Schulz, J. E. Bourée, B. Geffroy, S. Swaraj and Y. Bonnassieux, “Preliminary Study on Migration of Halide Ions in Metal Halide Perovskite induced by Electrical Field based on Nano X-ray Fluorescence”, 16<sup>th</sup>, Sunset User Meeting (SUM 2022), Online, Jan. 2022. **Oral**
3. **H. Jun**, D. Tondelier, B. Geffroy, J. E. Bourée, S. Swaraj and Y. Bonnassieux, “Study of degradation mechanism in halide perovskite solar cells using impedance and modulus spectroscopy”, MRS Fall meeting 2021, Boston, USA, Dec. 2021. **Oral**
4. **H. Jun**, D. Tondelier, B. Geffroy, J. E. Bourée, S. Swaraj and Y. Bonnassieux, “Study of Chemical Composition in Perovskite Thin Films by Scanning Transmission X-ray Microscopy”, Journées Nationales du Photovoltaïque (JNPV2020), Online, Dec. 2021. **Poster**
5. J. Baik, **H. Jun**, H. Nahdi, B. Geffroy, D. Tondlier and Y. Bonnassieux, “Modeling the Perovskite Solar Cells and the Ion Migration with Physical Approach based on FEM from Silvaco”, Journées Nationales du Photovoltaïque (JNPV2020), Online, Dec. 2021. **Poster**
6. **H. Jun**, D. Tondelier, B. Geffroy, J. E. Bourée, S. Swaraj and Y. Bonnassieux, “Utility of STXM to Investigate Chemical Composition in Vacuum Deposited Perovskite Thin Films”, Perovskite Evaporation Conference (PEC 2020), Online. Nov. 2020. **Oral**
7. **H. Jun**, A. Foti, M. Chrostowski, R. Ossikowski, and P. R. i Cabarrocas, “Molecular Hydrogen and Blistering in c-Si:H Epitaxial Thin Films”, 28<sup>th</sup> International Conference on Amorphous and Nano-crystalline Semiconductors (ICANS 2019), Palaiseau, France, Aug. 2019. **Poster**

8. **H. Jun**, E. Moyen, H. Kim, J. Jang, “Interfacial Improvement Using Solution Processed Interlayer on Inverted Perovskite Quantum-Dot Light Emitting Diodes”, 25<sup>th</sup> International Display Workshops (IDW 2017), Sendai, Japan, Dec. 2017. **Oral**

## Training

1. 1<sup>st</sup> Nanoperando2022 school, September 2022, Gif-sur-Yvette and Palaiseau, France
2. 5<sup>th</sup> Photovoltaic Systems Summer School, August 2022, Delft, Netherland.

## Scholarship

1. Ecole Doctoral: Institute Polytechnique de Paris, Oct. 2019 – Oct. 2022

# Bibliography

- [1] J. Curtin, C. McInerney, B. Ó Gallachóir, C. Hickey, P. Deane, and P. Deeney, “Quantifying stranding risk for fossil fuel assets and implications for renewable energy investment: A review of the literature,” *Renew. Sustain. Energy Rev.*, vol. 116, no. September, p. 109402, 2019.
- [2] X. Yang, J. Pang, F. Teng, R. Gong, and C. Springer, “The environmental co-benefit and economic impact of China’s low-carbon pathways: Evidence from linking bottom-up and top-down models,” *Renew. Sustain. Energy Rev.*, vol. 136, no. 12, p. 110438, 2021.
- [3] A. G. Olabi *et al.*, “Assessment of the pre-combustion carbon capture contribution into sustainable development goals SDGs using novel indicators,” *Renew. Sustain. Energy Rev.*, vol. 153, no. 10, p. 111710, 2022.
- [4] BP, “Statistical review of world energy,” no. 69, 2020.
- [5] REN21, “Renewables 2022 global status report,” 2022.
- [6] A. Sahu, N. Yadav, and K. Sudhakar, “Floating photovoltaic power plant: A review,” *Renew. Sustain. Energy Rev.*, vol. 66, pp. 815–824, 2016.
- [7] A. Modi, F. Bühlér, J. G. Andreasen, and F. Haglind, “A review of solar energy based heat and power generation systems,” *Renew. Sustain. Energy Rev.*, vol. 67, pp. 1047–1064, 2017.
- [8] L. Friedman, *Starsailing, solar sails and inter-stellar travel*. Wiley, 1988.
- [9] IEA, “Global energy review 2020,” 2020.
- [10] C. E. Fritts, “On a new form of selenium cell, and some electrical discoveries made by its use,” *Am. J. Sci.*, vol. s3-26, no. 156, pp. 465–472, 1883.
- [11] D. M. Chapin, C. S. Fuller, and G. L. Pearson, “A new silicon p-n junction photocell for converting solar radiation into electrical power,” *J. Appl. Phys.*, vol. 25, no. 5, pp. 676–677, 1954.
- [12] A. Slade and V. Garboushian, “27.6% efficient silicon concentrator solar cells for mass production,” *Tech. Dig. 15th Int. ...*, no. 1, pp. 1–2, 2005.
- [13] M. A. Green, “Thin-film solar cells: Review of materials, technologies and commercial status,” *J. Mater. Sci. Mater. Electron.*, vol. 18, no. Suppl. 1, pp. 15–19, 2007.
- [14] “NREL efficiency chart.” [Online]. Available: <https://www.nrel.gov/pv/cell-efficiency.html>.
- [15] A. Pivrikas, N. S. Sariciftci, G. Juška, and R. Österbacka, “A review of charge transport and recombination in polymer/fullerene organic solar cells,” *Prog. Photovoltaics Res. Appl.*, vol.

15, pp. 677–696, 2007.

- [16] P. Docampo, S. Guldin, T. Leijtens, N. K. Noel, U. Steiner, and H. J. Snaith, “Lessons learned: From dye-sensitized solar cells to all-solid-state hybrid devices,” *Adv. Mater.*, vol. 26, no. 24, pp. 4013–4030, 2014.
- [17] M. Yuan, M. Liu, and E. H. Sargent, “Colloidal quantum dot solids for solution-processed solar cells,” *Nat. Energy*, vol. 1, no. 3, p. 16016, 2016.
- [18] H. Cho *et al.*, “Overcoming the electroluminescence efficiency limitations of perovskite light-emitting diodes,” *Science*, vol. 350, no. 6265, pp. 1222–1225, 2015.
- [19] H. Wei *et al.*, “Sensitive X-ray detectors made of methylammonium lead tribromide perovskite single crystals,” *Nat. Photonics*, vol. 10, no. 5, pp. 333–339, 2016.
- [20] F. Haque, N. T. T. Hoang, J. Ji, and M. Mativenga, “Effect of Precursor Composition on Ion Migration in Hybrid Perovskite  $\text{CH}_3\text{NH}_3\text{PbI}_3$ ,” *IEEE Electron Device Lett.*, vol. 40, no. 11, pp. 1756–1759, 2019.
- [21] P. Umari, E. Mosconi, and F. De Angelis, “Relativistic GW calculations on  $\text{CH}_3\text{NH}_3\text{PbI}_3$  and  $\text{CH}_3\text{NH}_3\text{SnI}_3$  Perovskites for Solar Cell Applications,” *Sci. Rep.*, vol. 4, pp. 1–7, 2014.
- [22] M. J. P. Alcocer, T. Leijtens, L. M. Herz, A. Petrozza, and H. J. Snaith, “Electron-hole diffusion lengths exceeding trihalide perovskite absorber,” *Science*, vol. 342, no. October, pp. 341–344, 2013.
- [23] K. Galkowski *et al.*, “Determination of the exciton binding energy and effective masses for methylammonium and formamidinium lead tri-halide perovskite semiconductors,” *Energy Environ. Sci.*, vol. 9, no. 3, pp. 962–970, 2016.
- [24] L. Meng, J. You, and Y. Yang, “Addressing the stability issue of perovskite solar cells for commercial applications,” *Nat. Commun.*, vol. 9, no. 1, pp. 1–4, 2018.
- [25] Z. Li *et al.*, “Cost analysis of perovskite tandem photovoltaics,” *Joule*, vol. 2, no. 8, pp. 1559–1572, 2018.
- [26] A. Kojima, K. Teshima, Y. Shirai, and T. Miyasaka, “Organometal halide perovskites as visible-light sensitizers for photovoltaic cells,” *J. Am. Chem. Soc.*, vol. 131, no. 17, pp. 6050–1, 2009.
- [27] J. Burschka *et al.*, “Sequential deposition as a route to high-performance perovskite-sensitized solar cells,” *Nature*, vol. 499, no. 7458, pp. 316–319, 2013.
- [28] N. J. Jeon *et al.*, “Compositional engineering of perovskite materials for high-performance solar cells,” *Nature*, vol. 517, no. 7535, pp. 476–480, 2015.
- [29] M. Saliba *et al.*, “Cesium-containing triple cation perovskite solar cells: Improved stability, reproducibility and high efficiency,” *Energy Environ. Sci.*, vol. 9, no. 6, pp. 1989–1997, 2016.
- [30] J. Jeong *et al.*, “Pseudo-halide anion engineering for  $\alpha\text{-FAPbI}_3$  perovskite solar cells,” *Nature*,

vol. 592, no. 7854, pp. 381–385, 2021.

- [31] J. Bisquert and E. J. Juarez-Perez, “The causes of degradation of perovskite solar cells,” *J. Phys. Chem. Lett.*, vol. 10, no. 19, pp. 5889–5891, 2019.
- [32] H. J. Jung, D. Kim, S. Kim, J. Park, V. P. Dravid, and B. Shin, “Stability of halide perovskite solar cell devices: In situ observation of oxygen diffusion under biasing,” *Adv. Mater.*, vol. 30, no. 39, p. 1802769, 2018.
- [33] A. Uddin, M. B. Upama, H. Yi, and L. Duan, “Encapsulation of organic and perovskite solar cells: A review,” *Coatings*, vol. 9, no. 2, p. 65, 2019.
- [34] A. M. A. Leguy *et al.*, “Experimental and theoretical optical properties of methylammonium lead halide perovskites,” *Nanoscale*, vol. 8, no. 12, pp. 6317–6327, 2016.
- [35] A. Senocrate *et al.*, “Interaction of oxygen with halide perovskites,” *J. Mater. Chem. A*, vol. 6, no. 23, pp. 10847–10855, 2018.
- [36] C. C. Boyd, R. Cheacharoen, T. Leijtens, and M. D. McGehee, “Understanding degradation mechanisms and improving stability of perovskite photovoltaics,” *Chem. Rev.*, vol. 119, no. 5, pp. 3418–3451, 2019.
- [37] D. J. Slotcavage, H. I. Karunadasa, and M. D. McGehee, “Light-induced phase segregation in halide-perovskite absorbers,” *ACS Energy Lett.*, vol. 1, no. 6, pp. 1199–1205, 2016.
- [38] M. García-Batlle *et al.*, “Moving ions vary electronic conductivity in lead bromide perovskite single crystals through dynamic doping,” *Adv. Electron. Mater.*, vol. 6, no. 10, pp. 1–9, 2020.
- [39] C. Li *et al.*, “Iodine migration and its effect on hysteresis in perovskite solar cells,” *Adv. Mater.*, vol. 28, no. 12, pp. 2446–2454, 2016.
- [40] C. Li *et al.*, “Real-time observation of iodide ion migration in methylammonium lead halide perovskites,” *Small*, vol. 13, no. 42, pp. 1–10, 2017.
- [41] Y. Luo *et al.*, “Direct observation of halide migration and its effect on the photoluminescence of methylammonium lead bromide perovskite single crystals,” *Adv. Mater.*, vol. 29, no. 43, pp. 1–7, 2017.
- [42] K. Higgins *et al.*, “Exploration of electrochemical reactions at organic–inorganic halide perovskite interfaces via machine learning in in situ time-of-flight secondary ion mass spectrometry,” *Adv. Funct. Mater.*, vol. 30, no. 36, p. 2001995, Sep. 2020.
- [43] Q. Jeangros *et al.*, “In situ TEM analysis of organic-inorganic metal-halide perovskite solar cells under electrical bias,” *Nano Lett.*, vol. 16, no. 11, pp. 7013–7018, 2016.
- [44] T. Duong *et al.*, “Light and electrically induced phase segregation and its impact on the stability of quadruple cation high bandgap perovskite solar cells,” *ACS Appl. Mater. Interfaces*, vol. 9, no. 32, pp. 26859–26866, 2017.
- [45] M. Kim *et al.*, “Imaging real-time amorphization of hybrid perovskite solar cells under

- electrical biasing,” *ACS Energy Lett.*, vol. 6, no. 10, pp. 3530–3537, 2021.
- [46] A. J. Steckl *et al.*, “Review of focused ion beam implantation mixing for the fabrication of GaAs-based optoelectronic devices,” *J. Vac. Sci. Technol. B Microelectron. Nanom. Struct.*, vol. 13, no. 6, pp. 2570–2575, 1995.
  - [47] R. D. Dupius, “Epitaxial growth of III-V nitride semiconductors by metalorganic chemical vapor deposition,” *J. Cryst. Growth*, vol. 178, pp. 56–73, 1997.
  - [48] W. Shan *et al.*, “Optical properties of  $\text{In}_x\text{Ga}_{1-x}\text{N}$  alloys grown by metalorganic chemical vapor deposition,” *J. Appl. Phys.*, vol. 4452, no. 11, pp. 3315–3317, 1998.
  - [49] K. Domanski *et al.*, “Not all that glitters is gold: Metal-migration-induced degradation in perovskite solar cells,” *ACS Nano*, vol. 10, no. 6, pp. 6306–6314, 2016.
  - [50] M. Abdi-Jalebi *et al.*, “Maximizing and stabilizing luminescence from halide perovskites with potassium passivation,” *Nature*, vol. 555, no. 7697, pp. 497–501, 2018.
  - [51] T. Fuqiang and O. Yoshimichi, “Electric modulus powerful tool for analyzing dielectric behavior,” *IEEE Trans. Dielectr. Electr. Insul.*, vol. 21, no. 3, pp. 929–931, 2014.
  - [52] A. I. Zia and S. C. Mukhopadhyay, *Electrochemical Sensing: Carcinogens in Beverages*, vol. 20, 2016.
  - [53] A. Sacco, “Electrochemical impedance spectroscopy: Fundamentals and application in dye-sensitized solar cells,” *Renew. Sustain. Energy Rev.*, vol. 79, no. 8, pp. 814–829, 2017.
  - [54] F. Fabregat-Santiago, J. Bisquert, G. Garcia-Belmonte, G. Boschloo, and A. Hagfeldt, “Influence of electrolyte in transport and recombination in dye-sensitized solar cells studied by impedance spectroscopy,” *Sol. Energy Mater. Sol. Cells*, vol. 87, no. 1–4, pp. 117–131, 2005.
  - [55] Y. Zhao, W. Zhou, Z. Han, D. Yu, and Q. Zhao, “Effects of ion migration and improvement strategies for the operational stability of perovskite solar cells,” *Phys. Chem. Chem. Phys.*, vol. 23, no. 1, pp. 94–106, 2021.
  - [56] E. L. Unger *et al.*, “Hysteresis and transient behavior in current-voltage measurements of hybrid-perovskite absorber solar cells,” *Energy Environ. Sci.*, vol. 7, no. 11, pp. 3690–3698, 2014.
  - [57] D. A. Egger, L. Kronik, and A. M. Rappe, “Theory of hydrogen migration in organic-inorganic halide perovskites,” *Angew. Chemie*, vol. 127, no. 42, pp. 12614–12618, 2015.
  - [58] X. Qin, Z. Zhao, Y. Wang, J. Wu, Q. Jiang, and J. You, “Recent progress in stability of perovskite solar cells,” *J. Semicond.*, vol. 38, no. 1, pp. 1–9, 2017.
  - [59] S. Heo *et al.*, “Origins of high performance and degradation in the mixed perovskite solar cells,” *Adv. Mater.*, vol. 31, no. 8, pp. 1–5, 2019.
  - [60] H. S. Kim *et al.*, “Mechanism of carrier accumulation in perovskite thin-absorber solar cells,”

*Nat. Commun.*, vol. 4, pp. 1–7, 2013.

- [61] R. S. Sanchez *et al.*, “Slow dynamic processes in lead halide perovskite solar cells. Characteristic times and hysteresis,” *J. Phys. Chem. Lett.*, vol. 5, no. 13, pp. 2357–2363, 2014.
- [62] J. Dhar, S. Sil, A. Dey, D. Sanyal, and P. P. Ray, “Investigation of ion-mediated charge transport in methylammonium lead iodide perovskite,” *J. Phys. Chem. C*, vol. 121, no. 10, pp. 5515–5522, 2017.
- [63] E. J. Juarez-Perez *et al.*, “Role of the selective contacts in the performance of lead halide perovskite solar cells,” *J. Phys. Chem. Lett.*, vol. 5, no. 4, pp. 680–685, 2014.
- [64] M. Ulfa, T. Pauperté, T. T. Bui, and F. Goubard, “Impact of organic hole transporting material and doping on the electrical response of perovskite solar cells,” *J. Phys. Chem. C*, vol. 122, no. 22, pp. 11651–11658, 2018.
- [65] P. M. Bertsch and D. B. Hunter, “Applications of synchrotron-based X-ray microprobes,” *Chem. Rev.*, vol. 101, no. 6, pp. 1809–1842, 2001.
- [66] B. M. West *et al.*, “X-ray fluorescence at nanoscale resolution for multicomponent layered structures: A solar cell case study,” *J. Synchrotron Radiat.*, vol. 24, no. 1, pp. 288–295, 2017.
- [67] P. Sedigh Rahimabadi, M. Khodaei, and K. R. Koswattage, “Review on applications of synchrotron-based X-ray techniques in materials characterization,” *X-Ray Spectrom.*, vol. 49, p. 348, May 2020.
- [68] M. Kodur *et al.*, “X-Ray microscopy of halide perovskites: Techniques, applications, and prospects,” *Adv. Energy Mater.*, vol. 10, no. 26, pp. 1–25, 2020.
- [69] L. Oesinghaus *et al.*, “Toward tailored film morphologies: The origin of crystal orientation in hybrid perovskite thin films,” *Adv. Mater. Interfaces*, vol. 3, no. 19, 2016.
- [70] G. W. P. Adhyaksa *et al.*, “Understanding detrimental and beneficial grain boundary effects in halide perovskites,” *Adv. Mater.*, vol. 30, no. 52, 2018.
- [71] E. L. Unger *et al.*, “Chloride in lead chloride-derived organo-metal halides for perovskite-absorber solar cells,” *Chem. Mater.*, vol. 26, no. 24, pp. 7158–7165, 2014.
- [72] J. P. Correa-Baena *et al.*, “Homogenized halides and alkali cation segregation in alloyed organic-inorganic perovskites,” *Science*, vol. 363, no. 6427, pp. 627–631, 2019.
- [73] J. R. Poindexter *et al.*, “High tolerance to iron contamination in lead halide perovskite solar cells,” *ACS Nano*, vol. 11, no. 7, pp. 7101–7109, 2017.
- [74] C. Hartmann *et al.*, “Spatially resolved insight into the chemical and electronic structure of solution-processed perovskites—Why to (not) worry about pinholes,” *Adv. Mater. Interfaces*, vol. 5, no. 5, pp. 1–9, 2018.
- [75] W. S. Drisdell *et al.*, “Determining atomic-scale structure and composition of organo-lead halide perovskites by combining high-resolution X-ray absorption spectroscopy and first-

- principles calculations,” *ACS Energy Lett.*, vol. 2, no. 5, pp. 1183–1189, 2017.
- [76] J. R. A. Beale, *Solid State Electronic Devices*, vol. 24, no. 3. Prentice-Hall Englewood Cliffs, NJ, 1995.
- [77] A. R. Jordehi, “Parameter estimation of solar photovoltaic (PV) cells: A review,” *Renew. Sustain. Energy Rev.*, vol. 61, no. July, pp. 354–371, 2016.
- [78] G. Hashmi, M. A. R. Akand, M. K. Basher, M. Hoq, and M. H. Rahman, “Fabrication of crystalline silicon solar cell in Bangladesh: Limitations and remedies,” *Int. J. Sci. Eng. Res.*, vol. 7, no. 5, pp. 581–586, 2016.
- [79] J. Poortmans and V. Arkhipov, *Thin Film Solar Cells: Fabrication, Characterization and Applications*. 2006.
- [80] S. R. Scully and M. D. McGehee, “Effects of optical interference and energy transfer on exciton diffusion length measurements in organic semiconductors,” *J. Appl. Phys.*, vol. 100, no. 3, 2006.
- [81] S. D. Stranks *et al.*, “Electron-hole diffusion lengths exceeding 1 micrometer in an organometal trihalide perovskite absorber,” *Science*, vol. 342, no. 10, pp. 341–345, 2013.
- [82] J. örn Rostalski and D. Meissner, “Monochromatic versus solar efficiencies of organic solar cells,” *Sol. Energy Mater. Sol. Cells*, vol. 61, no. 1, pp. 87–95, 2000.
- [83] N. G. Park, “Halide perovskite photovoltaics: History, progress, and perspectives,” *MRS Bull.*, vol. 43, no. 7, pp. 527–533, 2018.
- [84] M. A. Green, A. Ho-Baillie, and H. J. Snaith, “The emergence of perovskite solar cells,” *Nat. Photonics*, vol. 8, no. 7, pp. 506–514, 2014.
- [85] R. H. Mitchell, M. D. Welch, and A. R. Chakhmouradian, “Nomenclature of the perovskite supergroup: A hierarchical system of classification based on crystal structure and composition,” *Mineral. Mag.*, vol. 81, no. 3, pp. 411–461, 2017.
- [86] W. A. Wooster and C. K. M, “Crystal structure and photoconductivity of cæsium plumbohalides,” *Proc. Arner. Acad.*, vol. 93, no. 1955, p. 131, 1958.
- [87] C. R. Kagan, D. B. Mitzi, and C. D. Dimitrakopoulos, “Organic-inorganic hybrid materials as semiconducting channels in thin- film field-effect transistors,” *Science*, vol. 286, no. 5441, pp. 945–947, 1999.
- [88] J. H. Im, C. R. Lee, J. W. Lee, S. W. Park, and N. G. Park, “6.5% efficient perovskite quantum-dot-sensitized solar cell,” *Nanoscale*, vol. 3, no. 10, pp. 4088–4093, 2011.
- [89] A. Jamshaid *et al.*, “Atomic-scale insight into the enhanced surface stability of methylammonium lead iodide perovskite by controlled deposition of lead chloride,” *Energy Environ. Sci.*, vol. 14, no. 8, pp. 4541–4554, 2021.
- [90] H. S. Kim *et al.*, “High efficiency solid-state sensitized solar cell-based on submicrometer

- rutile  $\text{TiO}_2$  nanorod and  $\text{CH}_3\text{NH}_3\text{PbI}_3$  perovskite sensitizer," *Nano Lett.*, vol. 13, no. 6, pp. 2412–2417, 2013.
- [91] N. G. Park and H. Segawa, "Research direction toward theoretical efficiency in perovskite solar cells," *ACS Photonics*, vol. 5, no. 8, pp. 2970–2977, 2018.
- [92] T. M. Brenner, D. A. Egger, L. Kronik, G. Hodes, and D. Cahen, "Hybrid organic-inorganic perovskites: Low-cost semiconductors with intriguing charge-transport properties," *Nat. Rev. Mater.*, vol. 1, no. 1, 2016.
- [93] S. De Wolf *et al.*, "Organometallic halide perovskites: Sharp optical absorption edge and its relation to photovoltaic performance," *J. Phys. Chem. Lett.*, vol. 5, no. 6, pp. 1035–1039, 2014.
- [94] I. Chung, B. Lee, J. He, R. P. H. Chang, and M. G. Kanatzidis, "All-solid-state dye-sensitized solar cells with high efficiency," *Nature*, vol. 485, no. 7399, pp. 486–489, 2012.
- [95] C. C. Stoumpos, C. D. Malliakas, and M. G. Kanatzidis, "Semiconducting tin and lead iodide perovskites with organic cations: Phase transitions, high mobilities, and near-infrared photoluminescent properties," *Inorg. Chem.*, vol. 52, no. 15, pp. 9019–9038, 2013.
- [96] O. Oni, K. Sujit, S. Kasemsuwan, T. Sakpuaram, and D. U. Pfeiffer, "Organometal halide perovskite solar cell materials rationalized: Ultrafast charge generation, high and microsecond-long balanced mobilities, and slow recombination," *Vet. Rec.*, vol. 160, no. 11, pp. 368–371, 2007.
- [97] H. S. Kim *et al.*, "Lead iodide perovskite sensitized all-solid-state submicron thin film mesoscopic solar cell with efficiency exceeding 9%," *Sci. Rep.*, vol. 2, pp. 1–7, 2012.
- [98] M. Liu, M. B. Johnston, and H. J. Snaith, "Efficient planar heterojunction perovskite solar cells by vapour deposition," *Nature*, vol. 501, no. 7467, pp. 395–398, 2013.
- [99] L. Etgar *et al.*, "Mesoscopic  $\text{CH}_3\text{NH}_3\text{PbI}_3/\text{TiO}_2$  heterojunction solar cells," *J. Am. Chem. Soc.*, vol. 134, no. 42, pp. 17396–17399, 2012.
- [100] R. S. Sanchez and E. Mas-Marza, "Light-induced effects on Spiro-OMeTAD films and hybrid lead halide perovskite solar cells," *Sol. Energy Mater. Sol. Cells*, vol. 158, pp. 189–194, 2016.
- [101] Q. Zhang, C. S. Dandeneau, X. Zhou, and C. Cao, "ZnO nanostructures for dye-sensitized solar cells," *Adv. Mater.*, vol. 21, no. 41, pp. 4087–4108, 2009.
- [102] C. Wehrenfennig, G. E. Eperon, M. B. Johnston, H. J. Snaith, and L. M. Herz, "High charge carrier mobilities and lifetimes in organolead trihalide perovskites," *Adv. Mater.*, vol. 26, no. 10, pp. 1584–1589, 2014.
- [103] T. Leijtens, G. E. Eperon, S. Pathak, A. Abate, M. M. Lee, and H. J. Snaith, "Overcoming ultraviolet light instability of sensitized  $\text{TiO}_2$  with meso-superstructured organometal trihalide perovskite solar cells," *Nat. Commun.*, vol. 4, pp. 1–8, 2013.
- [104] D. Liu, M. K. Gangishetty, and T. L. Kelly, "Effect of  $\text{CH}_3\text{NH}_3\text{PbI}_3$  thickness on device

- efficiency in planar heterojunction perovskite solar cells,” *J. Mater. Chem. A*, vol. 2, no. 46, pp. 19873–19881, 2014.
- [105] W. Ke *et al.*, “Low temperature solution-processed tin oxide as an alternative electron transporting layer for efficient perovskite solar cells,” *J. Am. Chem. Soc.*, vol. 137, no. 21, pp. 6730–6733, 2015.
- [106] L. Zuo *et al.*, “Enhanced photovoltaic performance of  $\text{CH}_3\text{NH}_3\text{PbI}_3$  perovskite solar cells through interfacial engineering using self-assembling monolayer,” *J. Am. Chem. Soc.*, vol. 137, no. 7, pp. 2674–2679, 2015.
- [107] L. M. Peter, D. J. Riley, E. J. Tull, and K. G. U. Wijayantha, “Photosensitization of nanocrystalline  $\text{TiO}_2$  by self-assembled layers of CdS quantum dots,” *Chem. Commun.*, vol. 10, pp. 1030–1031, 2002.
- [108] R. A. Sinton and A. Cuevas, “Contactless determination of current-voltage characteristics and minority-carrier lifetimes in semiconductors from quasi-steady-state photoconductance data,” *Appl. Phys. Lett.*, vol. 69, no. 17, pp. 2510–2512, 1996.
- [109] J. H. Heo, H. J. Han, D. Kim, T. K. Ahn, and S. H. Im, “Hysteresis-less inverted  $\text{CH}_3\text{NH}_3\text{PbI}_3$  planar perovskite hybrid solar cells with 18.1% power conversion efficiency,” *Energy Environ. Sci.*, vol. 8, no. 5, pp. 1602–1608, 2015.
- [110] Q. Zhao *et al.*, “Achieving efficient inverted planar perovskite solar cells with nondoped PTAA as a hole transport layer,” *Org. Electron.*, vol. 71, pp. 106–112, 2019.
- [111] W. Yu *et al.*, “Ultrathin  $\text{Cu}_2\text{O}$  as an efficient inorganic hole transporting material for perovskite solar cells,” *Nanoscale*, vol. 8, no. 11, pp. 6173–6179, 2016.
- [112] H. Rao *et al.*, “A 19.0% efficiency achieved in  $\text{CuO}_x$ -based inverted  $\text{CH}_3\text{NH}_3\text{PbI}_{3-x}\text{Cl}_x$  solar cells by an effective Cl doping method,” *Nano Energy*, vol. 27, pp. 51–57, 2016.
- [113] F. Xie *et al.*, “Vertical recrystallization for highly efficient and stable formamidinium-based inverted-structure perovskite solar cells,” *Energy Environ. Sci.*, vol. 10, no. 9, pp. 1942–1949, 2017.
- [114] H. J. Snaith *et al.*, “Anomalous hysteresis in perovskite solar cells,” *J. Phys. Chem. Lett.*, vol. 5, no. 9, pp. 1511–1515, 2014.
- [115] E. J. Juarez-Perez *et al.*, “Photoinduced giant dielectric constant in lead halide perovskite solar cells,” *J. Phys. Chem. Lett.*, vol. 5, no. 13, pp. 2390–2394, 2014.
- [116] Y. Deng, Z. Xiao, and J. Huang, “Light-induced self-poling effect on organometal trihalide perovskite solar cells for increased device efficiency and stability,” *Adv. Energy Mater.*, vol. 5, no. 20, pp. 1–6, 2015.
- [117] Y. Yuan and J. Huang, “Ion migration in organometal trihalide perovskite and its impact on photovoltaic efficiency and stability,” *Acc. Chem. Res.*, vol. 49, no. 2, pp. 286–293, 2016.

- [118] M. Yashima, K. Nomura, H. Kageyama, Y. Miyazaki, N. Chitose, and K. Adachi, “Conduction path and disorder in the fast oxide-ion conductor  $(La_{0.8}Sr_{0.2})(Ga_{0.8}Mg_{0.15}Co_{0.05})O_{2.8}$ ,” *Chem. Phys. Lett.*, vol. 380, no. 3–4, pp. 391–396, 2003.
- [119] J. Mizusaki, K. Arai, and K. Fueki, “Ionic conduction of the perovskite-type halides,” *Solid State Ionics*, vol. 11, no. 3, pp. 203–211, 1983.
- [120] C. Eames, J. M. Frost, P. R. F. Barnes, B. C. O’Regan, A. Walsh, and M. S. Islam, “Ionic transport in hybrid lead iodide perovskite solar cells,” *Nat. Commun.*, vol. 6, no. May, pp. 2–9, 2015.
- [121] Y. Yuan *et al.*, “Photovoltaic switching mechanism in lateral structure hybrid perovskite solar cells,” *Adv. Energy Mater.*, vol. 5, no. 15, pp. 1–7, 2015.
- [122] H. Yu, H. Lu, F. Xie, S. Zhou, and N. Zhao, “Native defect-induced hysteresis behavior in organolead iodide perovskite solar cells,” *Adv. Funct. Mater.*, vol. 26, no. 9, pp. 1411–1419, 2016.
- [123] A. Buin *et al.*, “Materials processing routes to trap-free halide perovskites,” *Nano Lett.*, vol. 14, no. 11, pp. 6281–6286, 2014.
- [124] A. Walsh, D. O. Scanlon, S. Chen, X. G. Gong, and S. H. Wei, “Self-regulation mechanism for charged point defects in hybrid halide perovskites,” *Angew. Chemie - Int. Ed.*, vol. 54, no. 6, pp. 1791–1794, 2015.
- [125] Z. Xiao *et al.*, “Giant switchable photovoltaic effect in organometal trihalide perovskite devices,” *Nat. Mater.*, vol. 14, no. 2, pp. 193–197, 2015.
- [126] Y. Zhang *et al.*, “Charge selective contacts, mobile ions and anomalous hysteresis in organic-inorganic perovskite solar cells,” *Mater. Horizons*, vol. 2, no. 3, pp. 315–322, 2015.
- [127] A. Mei *et al.*, “A hole-conductor-free, fully printable mesoscopic perovskite solar cell with high stability,” *Science*, vol. 345, no. 6194, pp. 295–298, 2014.
- [128] E. T. Hoke, D. J. Slotcavage, E. R. Dohner, A. R. Bowring, H. I. Karunadasa, and M. D. McGehee, “Reversible photo-induced trap formation in mixed-halide hybrid perovskites for photovoltaics,” *Chem. Sci.*, vol. 6, no. 1, pp. 613–617, 2015.
- [129] R. J. Meredith, *Engineers Handbook Of Industrial Microwave Heating*. UK: Stevenage, 1998.
- [130] B. Greenebaum and F. Barnes, *Bioengineering and Biophysical Aspects of Electromagnetic Fields*. USA: CRC Press: Boca Raton, 2019.
- [131] P. Mehrotra, B. Chatterjee, and S. Sen, “EM-wave biosensors: A review of RF, microwave, mm-wave and optical sensing,” *Sensors*, vol. 19, no. 5, 2019.
- [132] F. Fabregat-Santiago, G. Garcia-Belmonte, I. Mora-Seró, and J. Bisquert, “Characterization of nanostructured hybrid and organic solar cells by impedance spectroscopy,” *Phys. Chem. Chem. Phys.*, vol. 13, no. 20, pp. 9083–9118, 2011.

- [133] B. Ecker, H. J. Egelhaaf, R. Steim, J. Parisi, and E. Von Hauff, “Understanding S-shaped current-voltage characteristics in organic solar cells containing a  $\text{TiO}_x$  interlayer with impedance spectroscopy and equivalent circuit analysis,” *J. Phys. Chem. C*, vol. 116, no. 31, pp. 16333–16337, 2012.
- [134] W. Tress, “Metal halide perovskites as mixed electronic-ionic conductors: Challenges and opportunities - From hysteresis to Memristivity,” *J. Phys. Chem. Lett.*, vol. 8, no. 13, pp. 3106–3114, 2017.
- [135] F. Ma *et al.*, “Optoelectronic perovskite synapses for neuromorphic computing,” *Adv. Funct. Mater.*, vol. 30, no. 11, pp. 1–9, 2020.
- [136] S. Ahmad, C. George, D. J. Beesley, J. J. Baumberg, and M. De Volder, “Photo-rechargeable organo-halide perovskite batteries,” *Nano Lett.*, vol. 18, no. 3, pp. 1856–1862, 2018.
- [137] J. Carrillo *et al.*, “Ionic reactivity at contacts and aging of methylammonium lead triiodide perovskite solar cells,” *Adv. Energy Mater.*, vol. 6, no. 9, pp. 1–7, 2016.
- [138] S. Bai *et al.*, “Planar perovskite solar cells with long-term stability using ionic liquid additives,” *Nature*, vol. 571, no. 7764, pp. 245–250, 2019.
- [139] T. Y. Yang, G. Gregori, N. Pellet, M. Grätzel, and J. Maier, “The significance of ion conduction in a hybrid organic-inorganic lead-iodide-based perovskite photosensitizer,” *Angew. Chemie - Int. Ed.*, vol. 54, no. 27, pp. 7905–7910, 2015.
- [140] A. Senocrate *et al.*, “The nature of ion conduction in methylammonium lead iodide: A multimethod approach,” *Angew. Chemie - Int. Ed.*, vol. 56, no. 27, pp. 7755–7759, 2017.
- [141] K. Yamada, K. Isobe, T. Okuda, and Y. Furukawa, “Successive phase transitions and high ionic conductivity of trichlorogermanate(II) salts as studied by  $^{35}\text{Cl}$  NQR and powder X-ray diffraction,” *Zeitschrift fur Naturforsch. - Sect. A*, vol. 49, no. 1–2, pp. 258–266, 1994.
- [142] K. Yamada, Y. Kuranaga, K. Ueda, S. Goto, T. Okuda, and Y. Furukawa, “Phase transition and electric conductivity of  $\text{ASnCl}_3$  ( $\text{A} = \text{Cs}$  and  $\text{CH}_3\text{NH}_3$ ),” *Bulletin of the Chemical Society of Japan*, vol. 71, no. 1, pp. 127–134, 1998.
- [143] D. Meggiolaro, E. Mosconi, and F. De Angelis, “Formation of surface defects dominates ion migration in lead-halide perovskites,” *ACS Energy Lett.*, vol. 4, no. 3, pp. 779–785, 2019.
- [144] Y. Zou and R. J. Holmes, “Temperature-dependent bias poling and hysteresis in planar organo-metal halide perovskite photovoltaic cells,” *Adv. Energy Mater.*, vol. 6, no. 7, 2016.
- [145] S. Reichert, Q. An, Y. W. Woo, A. Walsh, Y. Vaynzof, and C. Deibel, “Probing the ionic defect landscape in halide perovskite solar cells,” *Nat. Commun.*, vol. 11, no. 1, 2020.
- [146] M. H. Futscher, M. K. Gangishetty, D. N. Congreve, and B. Ehrler, “Manganese doping stabilizes perovskite light-emitting diodes by reducing ion migration,” *ACS Appl. Electron. Mater.*, vol. 2, no. 6, pp. 1522–1528, 2020.

- [147] O. Almora, M. García-Batlle, and G. Garcia-Belmonte, “Utilization of temperature-sweeping capacitive techniques to evaluate band gap defect densities in photovoltaic perovskites,” *J. Phys. Chem. Lett.*, vol. 10, no. 13, pp. 3661–3669, 2019.
- [148] O. Almora, A. Guerrero, and G. Garcia-Belmonte, “Ionic charging by local imbalance at interfaces in hybrid lead halide perovskites,” *Appl. Phys. Lett.*, vol. 108, no. 4, 2016.
- [149] I. Bukreeva *et al.*, “Virtual unrolling and deciphering of Herculaneum papyri by X-ray phase-contrast tomography,” *Sci. Rep.*, vol. 6, no. June, pp. 1–7, 2016.
- [150] “Electromagnetic spectrum.” [Online]. Available: [targetedindividualscanada.files.wordpress.com/2011/06/spectrum.jpg](http://targetedindividualscanada.files.wordpress.com/2011/06/spectrum.jpg).
- [151] M. Kunz *et al.*, “A beamline for high-pressure studies at the Advanced Light Source with a superconducting bending magnet as the source,” *J. Synchrotron Rad.*, vol. 12, pp. 650–658, 2005.
- [152] E. Mitchell, P. Kuhn, and E. Garman, “Demystifying the synchrotron trip: A first time user’s guide,” *Structure*, vol. 7, no. 5, pp. 111–121, 1999.
- [153] A. Bharti and N. Goyal, “Fundamental of synchrotron radiations,” in *Synchrotron Radiation - Useful and Interesting Applications*, 2019, pp. 1–10.
- [154] S. Sabchevski, E. Di Palma, I. Spassovsky, and G. Dattoli, “Gyrotrons as high-frequency drivers for undulators and high-gradient accelerators,” *Appl. Sci.*, vol. 12, no. 12, p. 6101, 2022.
- [155] R. Belkhou *et al.*, “HERMES: A soft X-ray beamline dedicated to X-ray microscopy,” *J. Synchrotron Radiat.*, vol. 22, pp. 968–979, 2015.
- [156] J. Kowalska and S. DeBeer, “The role of X-ray spectroscopy in understanding the geometric and electronic structure of nitrogenase,” *Biochim. Biophys. Acta - Mol. Cell Res.*, vol. 1853, no. 6, pp. 1406–1415, 2015.
- [157] J. Yano and V. K. Yachandra, “X-ray absorption spectroscopy,” *Photosynth. Res.*, vol. 102, no. 2, pp. 241–254, 2009.
- [158] J. E. Penner-Hahn, “X-ray Absorption Spectroscopy,” *Compr. Coord. Chem. II*, vol. 2, pp. 159–186, 2003.
- [159] B. Rösner *et al.*, “7 nm spatial resolution in soft X-ray microscopy,” vol. 24, no. Suppl 2, pp. 270–271, 2018.
- [160] R. C. Moffet, A. V Tivanski, and M. K. Gilles, *Scanning Transmission X-ray Microscopy: Applications in Atmospheric Aerosol Research*, vol. 2011. Berkeley, California: Ernest Orlando Lawrence Berkeley National Laboratory, 2011.
- [161] L. Muntean, R. Planques, A. L. D. Kilcoyne, L. Muntean, R. Planques, and S. R. Leone, “Chemical mapping of polymer photoresists by scanning transmission x-ray microscopy,” vol. 1630, no. 2005, 2010.

- [162] J. M. Ball, M. M. Lee, A. Hey, and H. J. Snaith, “Low-temperature processed meso-superstructured to thin-film perovskite solar cells,” *Energy Environ. Sci.*, vol. 6, no. 6, pp. 1739–1743, 2013.
- [163] W. S. Yang *et al.*, “High-performance photovoltaic perovskite layers fabricated through intramolecular exchange,” *Science*, vol. 348, no. 6240, pp. 1234–1237, 2015.
- [164] J. H. Heo, M. H. Lee, M. H. Jang, and S. H. Im, “Highly efficient  $\text{CH}_3\text{NH}_3\text{PbI}_{3-x}\text{Cl}_x$  mixed halide perovskite solar cells prepared by re-dissolution and crystal grain growth via spray coating,” *J. Mater. Chem. A*, vol. 4, no. 45, pp. 17636–17642, 2016.
- [165] F. Di Giacomo *et al.*, “Up-scalable sheet-to-sheet production of high efficiency perovskite module and solar cells on 6-in. substrate using slot die coating,” *Sol. Energy Mater. Sol. Cells*, vol. 181, no. October, pp. 53–59, 2018.
- [166] J. Ávila, C. Momblona, P. P. Boix, M. Sessolo, and H. J. Bolink, “Vapor-deposited perovskites: The route to high-performance solar cell production?,” *Joule*, vol. 1, no. 3, pp. 431–442, 2017.
- [167] H. Gaonkar, J. Zhu, R. Kottokkaran, B. Bhageri, M. Noack, and V. Dalal, “Thermally stable, efficient, vapor deposited inorganic perovskite solar cells,” *ACS Appl. Energy Mater.*, vol. 3, no. 4, pp. 3497–3503, 2020.
- [168] M. M. Tavakoli, A. Simchi, Z. Fan, and H. Aashuri, “Chemical processing of three-dimensional graphene networks on transparent conducting electrodes for depleted-heterojunction quantum dot solar cells,” *Chem. Commun.*, vol. 52, no. 2, pp. 323–326, 2016.
- [169] S. Wang, X. Li, J. Wu, W. Wen, and Y. Qi, “Fabrication of efficient metal halide perovskite solar cells by vacuum thermal evaporation: A progress review,” *Curr. Opin. Electrochem.*, vol. 11, pp. 130–140, 2018.
- [170] S. Y. Hsiao *et al.*, “Efficient all-vacuum deposited perovskite solar cells by controlling reagent partial pressure in high vacuum,” *Adv. Mater.*, vol. 28, no. 32, pp. 7013–7019, 2016.
- [171] D. Zhao *et al.*, “Annealing-free efficient vacuum-deposited planar perovskite solar cells with evaporated fullerenes as electron-selective layers,” *Nano Energy*, vol. 19, pp. 88–97, 2016.
- [172] D. Alemu, H. Y. Wei, K. C. Ho, and C. W. Chu, “Highly conductive PEDOT:PSS electrode by simple film treatment with methanol for ITO-free polymer solar cells,” *Energy Environ. Sci.*, vol. 5, no. 11, pp. 9662–9671, 2012.
- [173] Z. Song, S. C. Watthage, A. B. Phillips, B. L. Tompkins, R. J. Ellingson, and M. J. Heben, “Impact of processing temperature and composition on the formation of methylammonium lead iodide perovskites,” *Chem. Mater.*, vol. 27, no. 13, pp. 4612–4619, 2015.
- [174] K. Li *et al.*, “An efficient, flexible perovskite solar module exceeding 8% prepared with an ultrafast  $\text{PbI}_2$  deposition rate,” *Sci. Rep.*, vol. 8, no. 1, pp. 1–8, 2018.
- [175] T. Abzieher *et al.*, “Efficient all-evaporated pin-perovskite solar cells: A promising approach

- toward industrial large-scale fabrication," *IEEE J. Photovoltaics*, vol. 9, no. 5, pp. 1249–1257, 2019.
- [176] T. Gallet, R. G. Poeira, E. M. Lanzoni, T. Abzieher, U. W. Paetzold, and A. Redinger, "Co-evaporation of  $\text{CH}_3\text{NH}_3\text{PbI}_3$ : How growth conditions impact phase purity, photostriction, and intrinsic stability," *ACS Appl. Mater. Interfaces*, vol. 13, no. 2, pp. 2642–2653, 2021.
- [177] L. K. Ono, S. Wang, Y. Kato, S. R. Raga, and Y. Qi, "Fabrication of semi-transparent perovskite films with centimeter-scale superior uniformity by the hybrid deposition method," *Energy Environ. Sci.*, vol. 7, no. 12, pp. 3989–3993, 2014.
- [178] W. Tress, N. Marinova, O. Inganas, M. K. Nazeeruddin, S. M. Zakeeruddin, and M. Graetzel, "The role of the hole-transport layer in perovskite solar cells - Reducing recombination and increasing absorption," *2014 IEEE 40th PVSEC*, pp. 1563–1566, 2014.
- [179] L. Zhu *et al.*, "Efficient  $\text{CH}_3\text{NH}_3\text{PbI}_3$  perovskite solar cells with 2TPA-n-DP hole-transporting layers," *Nano Res.*, vol. 8, no. 4, pp. 1116–1127, 2015.
- [180] S. Chen *et al.*, "Exploring the limiting open-circuit voltage and the voltage loss mechanism in planar  $\text{CH}_3\text{NH}_3\text{PbBr}_3$  perovskite solar cells," *Adv. Energy Mater.*, vol. 6, no. 18, pp. 1–9, 2016.
- [181] C. H. Chiang and C. G. Wu, "Bulk heterojunction perovskite-PCBM solar cells with high fill factor," *Nat. Photonics*, vol. 10, no. 3, pp. 196–200, 2016.
- [182] S. H. Chang *et al.*, "Effects of the washing-enhanced nucleation process on the material properties and performance of perovskite solar cells," *J. Alloys Compd.*, vol. 808, p. 151723, 2019.
- [183] X. Liu *et al.*, "Triple cathode buffer layers composed of PCBM,  $\text{C}_{60}$ , and LiF for high-performance planar perovskite solar cells," *ACS Appl. Mater. Interfaces*, vol. 7, no. 11, pp. 6230–6237, 2015.
- [184] M. D. Irwin, D. B. Buchholz, A. W. Hains, R. P. H. Chang, and T. J. Marks, "p-Type semiconducting nickel oxide as an efficiency-enhancing anode interfacial layer in polymer bulk-heterojunction solar cells," *Proc. Natl. Acad. Sci.*, vol. 105, no. 8, pp. 2783–2787, 2008.
- [185] Z. H. Bakr, Q. Wali, A. Fakharuddin, L. Schmidt-Mende, T. M. Brown, and R. Jose, "Advances in hole transport materials engineering for stable and efficient perovskite solar cells," *Nano Energy*, vol. 34, no. November 2016, pp. 271–305, 2017.
- [186] Q. Bin Ke, J. Wu, C. Lin, and S. H. Chang, "Understanding the PEDOT:PSS, PTAA and P3CT-X Hole-Transport-Layer-Based Inverted Perovskite Solar Cells," *Polymers (Basel)*, vol. 14, no. 4, p. 823, 2022.
- [187] S. A. Rutledge and A. S. Helmy, "Carrier mobility enhancement in poly(3,4-ethylenedioxythiophene)- poly(styrenesulfonate) having undergone rapid thermal annealing," *J. Appl. Phys.*, vol. 114, no. 13, p. 133708, 2013.

- [188] J. H. Heo *et al.*, “Efficient inorganic-organic hybrid heterojunction solar cells containing perovskite compound and polymeric hole conductors,” *Nat. Photonics*, vol. 7, no. 6, pp. 486–491, 2013.
- [189] S. Liu, R. Liu, Y. Chen, S. Ho, J. H. Kim, and F. So, “Nickel oxide hole injection/transport layers for efficient solution-processed organic light-emitting diodes,” *Chem. Mater.*, vol. 26, no. 15, pp. 4528–4534, 2014.
- [190] A. Corani *et al.*, “Ultrafast dynamics of hole injection and recombination in organometal halide perovskite using nickel oxide as p-type contact electrode,” *J. Phys. Chem. Lett.*, vol. 7, no. 7, pp. 1096–1101, 2016.
- [191] R. Fan, Y. Huang, L. Wang, L. Li, G. Zheng, and H. Zhou, “The progress of interface design in perovskite-based solar cells,” *Adv. Energy Mater.*, vol. 6, no. 17, pp. 1–32, 2016.
- [192] C. Dindault, “Development of coevaporated perovskite thin films for tandem solar cells applications.,” 2020.
- [193] H. Lee, S. Rhee, J. Kim, C. Lee, and H. Kim, “Surface coverage enhancement of a mixed halide perovskite film by using an UV-ozone treatment,” *J. Korean Phys. Soc.*, vol. 69, no. 3, pp. 406–411, 2016.
- [194] K. M. Lee *et al.*, “Thickness effects of thermally evaporated C<sub>60</sub> thin films on regular-type CH<sub>3</sub>NH<sub>3</sub>PbI<sub>3</sub> based solar cells,” *Sol. Energy Mater. Sol. Cells*, vol. 164, no. February, pp. 13–18, 2017.
- [195] S. N. Habisreutinger, N. K. Noel, and H. J. Snaith, “Hysteresis index: A figure without merit for quantifying hysteresis in perovskite solar cells,” *ACS Energy Lett.*, vol. 3, no. 10, pp. 2472–2476, 2018.
- [196] E. Zimmermann, P. Ehrenreich, T. Pfadler, J. A. Dorman, J. Weickert, and L. Schmidt-Mende, “Erroneous efficiency reports harm organic solar cell research,” *Nat. Photonics*, vol. 8, no. 9, pp. 669–672, 2014.
- [197] M. Kim, D. Tondelier, J. Bouréé, Y. Bonnassieux, and B. Geffroy, “Comparison of MAPI and triple-cations perovskites based solar cells,” in *JNPV 2018*, 2018.
- [198] B. Chen, P. Wang, N. Ren, R. Li, and Y. Zhao, “Tin dioxide buffer layer-assisted efficiency and stability of wide- bandgap inverted perovskite solar cells,” vol. 43, no. 5, pp. 1674–4926, 2022.
- [199] L. Hu *et al.*, “Unravelling the role of C<sub>60</sub> derivatives as additives into active layer for achieving high-efficiency planar perovskite solar cells,” *Carbon N. Y.*, vol. 167, pp. 160–168, 2020.
- [200] Q. Wang, C. Bi, and J. Huang, “Doped hole transport layer for efficiency enhancement in planar heterojunction organolead trihalide perovskite solar cells,” *Nano Energy*, vol. 15, pp. 275–280, 2015.

- [201] M. Hu, C. Bi, Y. Yuan, Y. Bai, and J. Huang, “Stabilized wide bandgap MAPbBr<sub>x</sub>I<sub>3-x</sub> perovskite by enhanced grain size and improved crystallinity,” *Adv. Sci.*, vol. 3, no. 6, pp. 6–11, 2015.
- [202] J. Haddad *et al.*, “Analyzing interface recombination in lead-halide perovskite solar cells with organic and inorganic hole-transport layers,” *Adv. Mater. Interfaces*, vol. 7, no. 16, p. 2000366, 2020.
- [203] D. Głowienka *et al.*, “Role of surface recombination in perovskite solar cells at the interface of HTL/CH<sub>3</sub>NH<sub>3</sub>PbI<sub>3</sub>,” *Nano Energy*, vol. 67, p. 104186, 2020.
- [204] M. Adil Afroz, K. K. Sonigara, T. Bhim Raju, S. S. Soni, and P. Krishnan Iyer, “Effect of fluorine substitution and position on phenylene spacer in carbazole based organic sensitizers for dye sensitized solar cells,” *Phys. Chem. Chem. Phys.*, vol. 19, no. 42, pp. 28579–28587, 2017.
- [205] E. Von Hauff, “Impedance spectroscopy for emerging photovoltaics,” *J. Phys. Chem. C*, vol. 123, no. 18, pp. 11329–11346, 2019.
- [206] T. B. Raju, J. V. Vaghasiya, M. A. Afroz, S. S. Soni, and P. K. Iyer, “Effect of mono- and di-anchoring dyes based on o,m-difluoro substituted phenylene spacer in liquid and solid state dye sensitized solar cells,” *Dye. Pigment.*, vol. 174, no. 10, p. 108021, 2020.
- [207] J. Bisquert, “Theory of the impedance of electron diffusion and recombination in a thin layer,” *J. Phys. Chem. B*, vol. 106, no. 2, pp. 325–333, 2002.
- [208] J. Liang *et al.*, “An all-inorganic perovskite solar capacitor for efficient and stable spontaneous photocharging,” *Nano Energy*, vol. 52, no. 6, pp. 239–245, 2018.
- [209] Y. Wang *et al.*, “Stabilizing heterostructures of soft perovskite semiconductors,” *Science (80-. ).*, vol. 365, no. 6454, pp. 687–691, 2019.
- [210] L. K. Ono, S. R. Raga, S. Wang, Y. Kato, and Y. Qi, “Temperature-dependent hysteresis effects in perovskite-based solar cells,” *J. Mater. Chem. A*, vol. 3, no. 17, pp. 9074–9080, 2015.
- [211] W. Shockley and H. J. Queisser, “Detailed balance limit of efficiency of p-n junction solar cells,” *J. Appl. Phys.*, vol. 32, no. 3, pp. 510–519, 1961.
- [212] J. P. Correa Baena *et al.*, “Highly efficient planar perovskite solar cells through band alignment engineering,” *Energy Environ. Sci.*, vol. 8, no. 10, pp. 2928–2934, 2015.
- [213] B. A. Boukamp, “Impedance spectroscopy, strength and limitations,” *tm - Tech. Mess.*, vol. 71, no. 9, pp. 454–459, 2004.
- [214] J. M. Frost, K. T. Butler, and A. Walsh, “Molecular ferroelectric contributions to anomalous hysteresis in hybrid perovskite solar cells,” *APL Mater.*, vol. 2, no. 8, 2014.
- [215] H. C. Liao *et al.*, “Enhanced efficiency of hot-cast large-area planar perovskite solar cells/modules having controlled chloride incorporation,” *Adv. Energy Mater.*, vol. 7, no. 8, pp.

1–9, 2017.

- [216] J. Chae, Q. Dong, J. Huang, and A. Centrone, “Chloride incorporation process in  $\text{CH}_3\text{NH}_3\text{PbI}_3\text{-xCl}_x$  perovskites via nanoscale bandgap maps,” *Nano Lett.*, vol. 15, no. 12, pp. 8114–8121, 2015.
- [217] J. Chen and N. G. Park, “Causes and solutions of recombination in perovskite solar cells,” *Adv. Mater.*, vol. 31, no. 47, 2019.
- [218] G. Richardson *et al.*, “Can slow-moving ions explain hysteresis in the current-voltage curves of perovskite solar cells?,” *Energy Environ. Sci.*, vol. 9, no. 4, pp. 1476–1485, 2016.
- [219] J. S. Yun *et al.*, “Critical role of grain boundaries for ion migration in formamidinium and methylammonium lead halide perovskite solar cells,” *Adv. Energy Mater.*, vol. 6, no. 13, pp. 1–8, 2016.
- [220] J. M. Frost and A. Walsh, “What is moving in hybrid halide perovskite solar cells?,” *Acc. Chem. Res.*, vol. 49, no. 3, pp. 528–535, 2016.
- [221] C. Aranda, J. Bisquert, and A. Guerrero, “Impedance spectroscopy of perovskite/contact interface: Beneficial chemical reactivity effect,” *J. Chem. Phys.*, vol. 151, no. 12, 2019.
- [222] J. N. Wilson, J. M. Frost, S. K. Wallace, and A. Walsh, “Dielectric and ferroic properties of metal halide perovskites,” *APL Mater.*, vol. 7, no. 1, 2019.
- [223] W. Tress, N. Marinova, T. Moehl, S. M. Zakeeruddin, M. K. Nazeeruddin, and M. Grätzel, “Understanding the rate-dependent J-V hysteresis, slow time component, and aging in  $\text{CH}_3\text{NH}_3\text{PbI}_3$  perovskite solar cells: The role of a compensated electric field,” *Energy Environ. Sci.*, vol. 8, no. 3, pp. 995–1004, 2015.
- [224] O. Almora, C. Aranda, E. Mas-Marzá, and G. Garcia-Belmonte, “On Mott-Schottky analysis interpretation of capacitance measurements in organometal perovskite solar cells,” *Appl. Phys. Lett.*, vol. 109, no. 17, 2016.
- [225] M. Kim *et al.*, “Halide ion migration and its role at the interfaces in perovskite solar cells,” *Eur. J. Inorg. Chem.*, vol. 2021, no. 46, pp. 4781–4789, 2021.
- [226] N. G. Mccrum, B. E. Read, and G. Williams, “Anelastic and dielectric effects in polymeric solids,” *J. Appl. Polym. Sci.*, vol. 13, pp. 397–397, 1969.
- [227] P. B. Macedo, C. T. Moynihan, and R. Bose, “The role of ionic diffusion in polarization in vitreous ionic conductors,” *Phys. Chem. Glas.*, vol. 13, no. 1976, pp. 125–143, 1972.
- [228] I. M. Hodge, M. D. Ingram, and A. R. West, “Impedance and modulus spectroscopy of polycrystalline solid electrolytes,” *J. Electroanal. Chem.*, vol. 74, no. 2, pp. 125–143, 1976.
- [229] A. Bendahhou, K. Chourti, R. El Bouayadi, S. El Barkany, and M. Abou-Salama, “Structural, dielectric and impedance spectroscopy analysis of  $\text{Ba}_5\text{CaTi}_{1.94}\text{Zn}_{0.06}\text{Nb}_8\text{O}_{30}$  ferroelectric ceramic,” *RSC Adv.*, vol. 10, no. 47, pp. 28007–28018, 2020.

- [230] I. M. Hodge, K. L. Ngai, and C. T. Moynihan, “Comments on the electric modulus function,” *J. Non. Cryst. Solids*, vol. 351, no. 2, pp. 104–115, 2005.
- [231] A. A. Saif and P. Poopalan, “AC conductivity and dielectric relaxation behavior of sol-gel  $\text{Ba}_x\text{Sr}_{1-x}\text{TiO}_3$  thin films,” *J. Mater. Sci. Technol.*, vol. 27, no. 9, pp. 802–808, 2011.
- [232] S. Rani, N. Ahlawat, R. Punia, K. M. Sangwan, and P. Khandelwal, “Dielectric and impedance studies of La and Zn co-doped complex perovskite  $\text{CaCu}_3\text{Ti}_4\text{O}_{12}$  ceramic,” *Ceram. Int.*, vol. 44, no. 18, pp. 23125–23136, 2018.
- [233] H. Lee *et al.*, “Direct experimental evidence of halide ionic migration under bias in  $\text{CH}_3\text{NH}_3\text{PbI}_{3-x}\text{Cl}_x$  based perovskite solar cells using GD-OES analysis,” *ACS Energy Lett.*, vol. 2, no. 4, pp. 943–949, 2017.
- [234] L. M. Wheeler *et al.*, “Targeted ligand-exchange chemistry on cesium lead halide perovskite quantum dots for high-efficiency photovoltaics,” *J. Am. Chem. Soc.*, vol. 140, no. 33, pp. 10504–10513, 2018.
- [235] H. Lee *et al.*, “Effect of halide ion migration on the electrical properties of methylammonium lead tri-iodide perovskite solar cells,” *J. Phys. Chem. C*, vol. 123, no. 29, pp. 17728–17734, 2019.
- [236] B. L. Henke, E. M. Gullikson, and J. C. Davis, “X-ray interactions: Photoabsorption, scattering, transmission, and reflection at  $E = 50\text{--}30,000 \text{ eV}$ ,  $Z = 1\text{--}92$ ,” *Atomic Data and Nuclear Data Tables*, vol. 54, no. 2, pp. 181–342, 1993.
- [237] H. Hansen, “Die Schwächung monochromatischer Röntgenstrahlen in flüssigem und gasförmigem  $\text{CS}_2$ ,  $\text{CH}_2\text{Cl}_2$  und  $\text{C}_2\text{H}_5\text{Br}$  sowie in gasförmigem  $\text{CH}_3\text{J}$  zwischen 0,1623 und 1,933 Å \*,” *Ann. Phys. (N. Y.)*, vol. 427, pp. 524–546, 1939.
- [238] F. J. Comes, R. Haensel, U. Nielsen, and W. H. E. Schwarz, “Spectra of the xenon fluorides  $\text{XeF}_2$  and  $\text{XeF}_4$  in the far uv region,” *J. Chem. Phys.*, vol. 58, no. 2, pp. 516–529, 1973.
- [239] “aXis2000.” [Online]. Available: <http://unicorn.chemistry.mcmaster.ca/axis/aXis2000-download.html>.
- [240] G. Niu, W. Li, F. Meng, L. Wang, H. Dong, and Y. Qiu, “Study on the stability of  $\text{CH}_3\text{NH}_3\text{PbI}_3$  films and the effect of post-modification by aluminum oxide in all-solid-state hybrid solar cells,” *J. Mater. Chem. A*, vol. 2, no. 3, pp. 705–710, 2014.
- [241] Y. H. Kye, C. J. Yu, U. G. Jong, Y. Chen, and A. Walsh, “Critical role of water in defect aggregation and chemical degradation of perovskite solar cells,” *J. Phys. Chem. Lett.*, vol. 9, no. 9, pp. 2196–2201, 2018.
- [242] J. Yang *et al.*, “Oxygen- and water-induced energetics degradation in organometal halide perovskites,” *ACS Appl. Mater. Interfaces*, vol. 10, no. 18, pp. 16225–16230, 2018.
- [243] Y. Ouyang *et al.*, “Photo-oxidative degradation of methylammonium lead iodide perovskite:

- Mechanism and protection,” *J. Mater. Chem. A*, vol. 7, no. 5, pp. 2275–2282, 2019.
- [244] Q. Sun *et al.*, “Role of microstructure in oxygen induced photodegradation of methylammonium lead triiodide perovskite films,” *Adv. Energy Mater.*, vol. 7, no. 20, p. 1700977, 2017.
- [245] R. Long, J. Liu, and O. V. Prezhdo, “Unravelling the effects of grain boundary and chemical doping on electron-hole recombination in  $\text{CH}_3\text{NH}_3\text{PbI}_3$  perovskite by time-domain atomistic simulation,” *J. Am. Chem. Soc.*, vol. 138, no. 11, pp. 3884–3890, 2016.
- [246] M. Nukunudompanich, G. Budiatama, K. Suzuki, K. Hasegawa, and M. Ihara, “Dominant effect of the grain size of the  $\text{MAPbI}_3$  perovskite controlled by the surface roughness of  $\text{TiO}_2$  on the performance of perovskite solar cells,” *CrystEngComm*, vol. 22, no. 16, pp. 2718–2727, 2020.
- [247] H.-S. Yun, Y. H. Jang, and D.-K. Lee, “Enhancement open-circuit voltage of methylammonium lead halide perovskite solar cells via non-stoichiometric precursor,” *Curr. Photovolt. Res.*, vol. 6, no. 1, pp. 12–16, 2018.
- [248] S. Sanders *et al.*, “Showerhead-assisted chemical vapor deposition of perovskite films for solar cell application,” *MRS Adv.*, vol. 5, no. 8–9, pp. 385–393, 2020.
- [249] S. Swaraj, U. Oran, A. Lippitz, R. D. Schulze, J. F. Friedrich, and W. E. S. Unger, “Surface analysis of plasma-deposited polymer films, 2,” *Plasma Process. Polym.*, vol. 1, no. 2, pp. 134–140, 2004.
- [250] S. Swaraj, U. Oran, A. Lippitz, J. F. Friedrich, and W. E. S. Unger, “Surface analysis of plasma deposited polymer films, 6,” *Plasma Process. Polym.*, vol. 2, no. 7, pp. 572–580, 2005.
- [251] S. Swaraj, U. Oran, A. Lippitz, J. F. Friedrich, and W. E. S. Unger, “Aging of plasma-deposited films prepared from organic monomers,” *Plasma Process. Polym.*, vol. 4, no. SUPPL.1, pp. 784–789, 2007.
- [252] S. Swaraj, U. Oran, A. Lippitz, and W. E. S. Unger, “Surface chemical analysis of plasma-deposited copolymer films prepared from feed gas mixtures of ethylene or styrene with allylamine,” *Plasma Process. Polym.*, vol. 5, no. 1, pp. 92–104, 2008.
- [253] M. Lerotic, R. Mak, S. Wirick, F. Meirer, and C. Jacobsen, “Mantis: A program for the analysis of x-ray spectromicroscopy data,” *J. Synchrotron Radiat.*, vol. 21, no. 5, pp. 1206–1212, 2014.
- [254] S. Swaraj and H. Ade, “Differences in NEXAFS of odd/even long chain n-alkane crystals,” *J. Electron Spectros. Relat. Phenomena*, vol. 191, pp. 60–64, 2013.
- [255] S. G. Urquhart and H. Ade, “Trends in the carbonyl core ( $\text{C} 1\text{S}$ ,  $\text{O} 1\text{S}$ )  $\rightarrow \pi^*\text{c=O}$  transition in the near-edge X-ray absorption fine structure spectra of organic molecules,” *J. Phys. Chem. B*, vol. 106, no. 34, pp. 8531–8538, 2002.